LOCAL AND REMOTE FORCING OF THE OCEAN BY THE MADDEN-JULIAN OSCILLATION AND ITS PREDICTABILITY

by

Eric C. J. Oliver

Submitted in partial fulfillment of the requirements
for the degree of Doctor of Philosophy

at

Dalhousie University
Halifax, Nova Scotia
August 2011

DALHOUSIE UNIVERSITY

DEPARTMENT OF OCEANOGRAPHY

The undersigned hereby certify that they have read and recommend to the Faculty of Graduate Studies for acceptance a thesis entitled "LOCAL AND REMOTE FORCING OF THE OCEAN BY THE MADDEN-JULIAN OSCILLATION AND ITS PREDICTABILITY" by Eric C. J. Oliver in partial fulfillment of the requirements for the degree of Doctor of Philosophy.

Dated: August 24, 2011

External Examiner: ____________________

Research Supervisor: ____________________

Examining Committee: ____________________

____

____

____

Departmental Representative: ____________________

DALHOUSIE UNIVERSITY

DATE: August 24, 2011

AUTHOR: Eric C. J. Oliver

TITLE: LOCAL AND REMOTE FORCING OF THE OCEAN BY THE MADDEN-JULIAN OSCILLATION AND ITS PREDICTABILITY

DEPARTMENT OR SCHOOL: Department of Oceanography

DEGREE: PhD CONVOCATION: October YEAR: 2011

Signature of Author

TABLE OF CONTENTS

List of Tables . . . . **ix**

List of Figures . . . . **x**

Abstract . . . . **xiv**

List of Abbreviations and Symbols Used . . . . **xv**

Acknowledgements . . . . **xix**

Chapter 1 Introduction **1**
- 1.1 Weather, Climate, and Intraseasonal Variability 1
- 1.2 Modes of Variability in the Ocean-Atmosphere System 3
- 1.3 The Madden-Julian Oscillation 5
- 1.4 Dynamical Theories and Models of the MJO 9
- 1.5 The MJO and the Extratropical Atmosphere 11
- 1.6 The MJO and the Tropical Ocean 12
- 1.7 Statement of Problem, Objectives, and Outline of Thesis 13

Chapter 2 Statistical Techniques and Models **14**
- 2.1 Relationships Within a Set of Random Variables 14
  - 2.1.1 Empirical Orthogonal Function Analysis 15
  - 2.1.2 Frequency Dependent EOF Analysis 15
  - 2.1.3 Dynamical Modal Analysis 16
- 2.2 Relationships Between Sets of Random Variables 19
  - 2.2.1 Partial Correlation 19
  - 2.2.2 Multiple Coherence 20
  - 2.2.3 Frequency Independent Measures of Fit 20
  - 2.2.4 Assessing Statistical Significance 22
- 2.3 Autoregressive Models 22
  - 2.3.1 Damped Harmonic Oscillator Model in Continuous Time 22

2.3.2 Damped Harmonic Oscillator Model in Discrete Time 23
2.3.3 Damped Harmonic Oscillator Model With Autoregressive Forcing 24
2.3.4 Statistical Properties of the Damped Harmonic Oscillator Model . 25

Chapter 3 Ocean Dynamics and Models 28
3.1 Equations of Motion 28
3.2 Vertical Normal Modes 29
3.3 Equatorial Waves 30
3.3.1 Equatorial β-plane 30
3.3.2 Equatorially Trapped Kelvin Waves 31
3.3.3 Equatorially Trapped Rossby, Gravity, and Yanai Waves 32
3.3.4 Reflection and Transmission at an Eastern Boundary 36
3.4 Numerical Models 37
3.4.1 Princeton Ocean Model (POM) 37
3.4.2 Nucleus for European Modelling of the Ocean (NEMO) 38

Chapter 4 Response of the Global Ocean to the Madden-Julian Oscillation 40
4.1 Introduction 40
4.2 Data 42
4.2.1 The Madden-Julian Oscillation 42
4.2.2 Global Observations of Sea Level 42
4.2.3 Coastal Observations of Sea Level 43
4.2.4 Global Observations of Surface Wind 43
4.3 Statistical Methods 46
4.3.1 Relationships Between Sea Level and the MJO 46
4.3.2 Modes of Sea Level Variability in the MJO Band 47
4.4 Global Response of Sea Level to the MJO 47
4.5 Regional Responses of Sea Level to the MJO 48
4.5.1 The Equatorial Pacific and Coastal American Waveguides 48
4.5.2 Gulf of Carpentaria 53
4.5.3 Northeastern Indian Ocean 58
4.6 Summary and Discussion 62

Chapter 5 The Gulf of Carpentaria: Local Response to the MJO and Remote Forcing from the Pacific Ocean . . . 64
5.1 Introduction . . . 64
5.2 Observations of Sea Level, the MJO, and Surface Wind . . . 66
 5.2.1 The Madden-Julian Oscillation Index . . . 66
 5.2.2 Sea Level from Altimeters . . . 66
 5.2.3 Sea Level from Tide Gauges . . . 66
 5.2.4 Surface Wind . . . 67
5.3 Intraseasonal Variability in Observed Sea Level and Surface Wind . . . 70
5.4 Numerical Model . . . 74
5.5 Comparison of Observed and Predicted Sea Level . . . 76
 5.5.1 Dynamical Response of the Gulf to Wind Forcing . . . 76
 5.5.2 Seasonality and Intraseasonal Variability in Observed and Predicted Sea Level . . . 77
 5.5.3 Influence of the MJO on Circulation and Sea Level . . . 78
5.6 Cause of Low-Frequency Sea Level Variability . . . 80
 5.6.1 Correlations of Sea Level with Climatalogical Indices . . . 82
 5.6.2 Regional Sea Level Correlations . . . 82
 5.6.3 Hovmöller Diagrams . . . 83
5.7 Summary and Discussion . . . 86

Chapter 6 The Northeastern Indian Ocean: Local and Remote Response to the MJO . . . 89
6.1 Introduction . . . 89
6.2 Observations of Sea Level, Currents, MJO Index, and Surface Wind . . . 91
 6.2.1 The Madden-Julian Oscillation Index . . . 91
 6.2.2 Sea Level from Altimeters . . . 93
 6.2.3 Sea Level from Tide Gauges . . . 93
 6.2.4 Zonal and Meridional Currents from ADCPs . . . 94
 6.2.5 Atmospheric Forcing Fields . . . 94
6.3 Intraseasonal Variability of Observed Sea Level, Currents and Atmospheric Variables . . . 95
6.4 Numerical Model . . . 100

6.5 Validation and Analysis of the FULL Run 102
    6.5.1 Validation of Predicted Sea Level and Currents 102
    6.5.2 Response of the Ocean to the MJO 103
    6.5.3 Physical Interpretation in Terms of Dynamical Wave Modes . . . 107
6.6 Physical Causes of Variability 113
    6.6.1 Momentum Versus Buoyancy Forcing 113
    6.6.2 Role of Local and Remote Forcing by the MJO 115
6.7 Summary and Discussion 116

Chapter 7 Historical Reconstruction of the Madden-Julian Oscillation and an Examination of its Predictability 119
7.1 Introduction 119
7.2 Data and Preliminary Analysis 121
    7.2.1 The Madden-Julian Oscillation Index, $\boldsymbol{I}_t^{\mathrm{WH}}$ 121
    7.2.2 Global Surface Pressure 121
    7.2.3 Observed Records of Precipitation, Air Temperature, Sea Level, and Surface Pressure 122
7.3 Reconstructing the MJO 123
    7.3.1 Location of Pressures Chosen for Inclusion in the Regression Model 124
    7.3.2 The Reconstructed Historical Index 125
7.4 Validity of Reconstructed Low Frequency Variability 130
    7.4.1 Stability of the Relationship Between the MJO and Environmental Variables 131
    7.4.2 Reconstructing MJO Variability from Long Land-Based Records . 135
7.5 Predictability of the MJO Index 136
    7.5.1 Empirical Measures of Predictability 136
    7.5.2 Predictability and the Damped Harmonic Oscillator 141
7.6 Summary and Discussion 143

Chapter 8 Summary and Discussion 146
8.1 Summary 146
8.2 Discussion and Future Work 150

Appendix A A Monte Carlo Method for the Calculation of Statistical Significance 153

Appendix B Equations for Incompressible and Inviscid Flow 155

B.1 Three Dimensional Equations of Motion 155

B.2 The Shallow Water Equations 157

Appendix C Reflection and Transmission of Equatorial Waves at an Eastern Boundary 158

C.1 Meridional boundary 159

C.2 Nonmeridional boundary 161

Appendix D Restriction of Pressures for Inclusion in the Historical Reconstruction 162

D.1 Strength of Linear Relationship with the MJO 162

D.2 Accuracy of the Reanalysis Pressure 163

D.3 Pressure Decorrelation Lengthscales 165

Appendix E Calculating the Posterior Distribution 168

Bibliography 170

LIST OF TABLES

Table 4.1 Details on the tide gauge records 49

Table 5.1 Details of the tide gauge records 67
Table 5.2 Comparison of observed and predicted sea level 78

Table 6.1 Details on the tide gauge records 91
Table 6.2 Correlations between observed and predicted sea level, zonal current and meridional current and their relationship to the MJO 96
Table 6.3 Details on model runs 102
Table 6.4 The first ten baroclinic wave speeds 110
Table 6.5 Quality of fit for individual dynamical wave modes 111

Table 7.1 The long meteorological and oceanographic records used for validation of the reconstructed MJO index 122

Table D.1 Longitudinal decorrelation lengthscales of surface pressure 166

LIST OF FIGURES

Figure 1.1 Select modes of variability in the Ocean-Atmosphere system . . . 4

Figure 1.2 MJO lifecycle and index 6

Figure 1.3 Wavenumber-frequency spectra for outgoing longwave radiation . 8

Figure 2.1 Locations of stations for three dynamical modal analysis case studies 17

Figure 2.2 Damped harmonic oscillator model with autoregressive stochastic forcing 25

Figure 2.3 Spectral properties of the damped harmonic oscillator model . . . 27

Figure 3.1 Dispersion curves for waves on an equatorial β-plane 33

Figure 3.2 Meridional structure of equatorially trapped waves 34

Figure 3.3 Relationship between critical latitude, frequency, coastline angle, and the behaviour of waves near ocean boundaries 36

Figure 3.4 Vertical coordinates used in general circulation models: σ-levels and z-levels 38

Figure 3.5 Arrangement of ocean variables on model grids 39

Figure 4.1 Global map of the proportion of sea level variability related to the MJO 44

Figure 4.2 Global map of the proportion of sea level variability related to the MJO 45

Figure 4.3 Coherence between the MJO and sea level 49

Figure 4.4 Proportion of sea level variability accounted for by the MJO near the Americas 50

Figure 4.5 Total spectral density of sea level accounted for by the FDEOF as a function of the number of FDEOF modes included 52

Figure 4.6 The first mode of the FDEOF analysis for the Pacific-Americas waveguide (75 day period) 54

Figure 4.7 Maps of the first FDEOF mode in the Gulf of Carpentaria region (75 day period) 55

Figure 4.8 Sea level and local wind set-up in the Gulf of Carpentaria 56

Figure 4.9 Maps of the first FDEOF mode in the northeastern Indian Ocean (75 day period) 59

Figure 4.10 Modified Hovmöller diagram for the northeastern Indian Ocean . . 61

Figure 5.1 Power spectrum of the MJO and its relationship to wind over the Gulf of Carpentaria 65

Figure 5.2 Observed and predicted sea level for a typical two-year period . . 68

Figure 5.3 The model domain and bathymetry 69

Figure 5.4 Annual cycle of observed sea level 69

Figure 5.5 Maps of the amount of sea level variability in the Gulf of Carpentaria that is related to the MJO 70

Figure 5.6 Power spectrum of the MJO and coherence between the MJO and coastal sea level 71

Figure 5.7 Wind statistics over the Gulf of Carpentaria as a function of wind direction 72

Figure 5.8 MJO Composites of sea level, wind, and surface current anomalies 73

Figure 5.9 Seasonal variation of the spectral properties of the Gulf-mean wind 74

Figure 5.10 Seasonal variation of the spectral density of observed and predicted sea level 75

Figure 5.11 Observed and predicted sea level at Groote Eylandt 79

Figure 5.12 Time series and correlations of low frequency sea level 81

Figure 5.13 Connections between the Indian and Pacific Oceans and the Gulf of Carpentaria 84

Figure 5.14 Propagation of signals along pathways originating in the Indian Ocean and the Pacific Ocean and terminating in the Gulf 85

Figure 6.1 The model bathymetry for the high resolution nest 92

Figure 6.2 Observed and predicted sea level at three locations in the northeastern Indian Ocean 93

Figure 6.3 Observed and predicted zonal current at (0°N,90°E) and depths of 41 m, 93 m, and 160 m 94

Figure 6.4 Maps of the amount of sea level variability in the tropical Indian Ocean that is related to the MJO 95

Figure 6.5 The MJO response of observed sea level for the eight MJO phases 97

Figure 6.6 The MJO response of 10 m wind for the eight MJO phases 99

Figure 6.7 The MJO response of modelled sea level and horizontal velocity at 3 m for the eight MJO phases 104

Figure 6.8 The MJO response of modelled vertical and horizontal velocity at 200 m depth for the eight MJO phases 105

Figure 6.9 The MJO response of modelled velocity at 1000 m for the eight MJO phases 106

Figure 6.10 Sea level variability and phase propagation speeds for model predictions and dynamical modal fits 108

Figure 6.11 Vertical profiles of absolute salinity, conservative temperature, buoyancy frequency, and vertical normal modes 109

Figure 6.12 MJO response of sea level for various model runs 114

Figure 6.13 Relationship between the MJO index and sea level, upwelling, and temperature at (97.3°E,0°N) 118

Figure 7.1 Relationship between the MJO index and surface pressure 124

Figure 7.2 Comparison of MJO index and reconstruction over the period 2000 to 2002 125

Figure 7.3 Comparison of the two components of the reconstructed MJO index over the periods 2000 to 2002 and 1920 to 1922 126

Figure 7.4 Cross-spectral analysis of MJO index and reconstruction 127

Figure 7.5 Frequency-wavenumber spectra of tropical surface pressure 128

Figure 7.6 Hovmöller diagram of MJO-reconstructed tropical surface pressure 129

Figure 7.7 Variance and spectral content of reconstruction over the last century 131

Figure 7.8 Relationship of Australian DJF surface air temperature to the MJO 132

Figure 7.9 Relationship between the MJO and three independent environmental variables 132

Figure 7.10 Stability of the relationship between the reconstructed index and three environmental variables 133

Figure 7.11 Running three-year variance of $\boldsymbol{I}_t^{\mathrm{WH}}$, $\boldsymbol{I}_t^{\mathrm{OT}}$, and $\boldsymbol{I}_t^{\mathrm{EV}}$ for December to January 135

Figure 7.12 Evolution of the MJO in phase space given an imperfectly observed initial condition 138

Figure 7.13 Predictability measures for the Wheeler and Hendon MJO index and damped harmonic oscillator model 139

Figure 7.14 Time scales for loss of predictability of a canonical MJO event . . 140

Figure A.1 The calculation of statistical significance of $\bar{\kappa}$. 154

Figure C.1 Coastal coordinate system 159

Figure D.1 Relative error of Twentieth Century Reanalysis pressure at selected locations 164

Figure D.2 Mean and trend in relative error of surface pressure 165

Figure D.3 Fit of the regression model 166

ABSTRACT

The Madden-Julian Oscillation (MJO) is the dominant mode of intraseasonal variability in the tropical atmosphere and provides global predictability on timescales that bridge the gap between weather and climate. The influence of the MJO on the ocean is explored with a combination of statistical analysis of observations using multivariate time series techniques, dynamical theory, and general circulation models with realistic forcing and bathymetry.

The MJO is shown to have a significant and predictable influence on global sea level. Three main regions of influence are identified: (i) the equatorial Pacific and the west coast of the Americas, (ii) the Gulf of of Carpentaria, and (iii) the northeastern Indian Ocean. In the equatorial Pacific, equatorially trapped Kelvin waves are forced by MJO-related surface winds in the western Pacific and propagate eastward. These remotely forced waves then transform into coastal trapped waves that propagate poleward along the west coast of the Americas (consistent with previous work). By way of contrast, in the Gulf of Carpentaria it is shown that the connection with the MJO is due to local wind forcing through simple set-up of sea level. In the northeastern Indian Ocean, a complex sea level pattern involving equatorially trapped Kelvin waves, coastal trapped waves along Sumatra, Java and the Bay of Bengal, and reflected Rossby waves along 5.5°N is shown to be caused by a combination of local and remote forcing by MJO-related surface winds.

To examine the predictability of the MJO, and the stability of MJO variability on multi-decadal time scales, the MJO index is reconstructed over the last century. The reconstructed index is verified by comparing it with independently observed environmental variables. Three predictability time scales are proposed and estimated from the MJO index. A simple forced damped harmonic oscillator model is used to explain the complex relationship amongst the predictability time scales and also gain insight into the predictability of the MJO.

LIST OF ABBREVIATIONS AND SYMBOLS USED

Abbreviation	Definition
20CR	Twentieth Century Reanalysis Project
ADCP	Acoustic Doppler Current Profiler
AGRIF	Adaptive Grid Refinement in Fortran
AR	Autoregressive
CFL	Courant-Friedrichs-Levy
CIAF	Corrected Inter-Annual Forcing
CNYF	Corrected Normal-Year Forcing
CORE	Common Ocean-Ice Reference Experiments
CSIRO	Commonwealth Scientific and Industrial Research Organisation
DMA	Dynamical Modal Analysis
DJF	December-January-February
ENSO	El Niño-Southern Oscillation
EOF	Empirical Orthogonal Function
FDEOF	Frequency-dependent Empirical Orthogonal Function
GRACE	Gravity Recovery and Climate Experiment
GSW	Gibbs SeaWater
MJO	Madden-Julian Oscillation
NAO	North Atlantic Oscillation
NCAR	National Center for Atmospheric Research
NCEP	National Centers for Environmental Prediction
NEMO	Nucleus for European Modelling of the Ocean
NOAA	National Oceanic and Atmospheric Administration
OLR	Outgoing Longwave Radiation
POM	Princeton Ocean Model
RAMA	Research Moored Array for African-Asian-Australian Monsoon Analysis and Prediction

Abbreviation	Definition
RMS	Root Mean Square
SAT	Surface Air Temperature
SOND	September-October-November-December
SST	Sea Surface Temperature
TAO	Tropical Atmosphere Ocean
WH04	*Wheeler and Hendon* (2004)

Symbol	Description	Units
t	Time	s
x, y, z	Spatial coordinates	m
ω	Frequency	radians s^{-1}
k	Wavenumber	radians m^{-1}
λ_i	Eigenvalues	
$\boldsymbol{e}_i$	Eigenvectors	
$\boldsymbol{\Sigma}_{\boldsymbol{xx}}$	Covariance matrix of x	various
$\boldsymbol{f}_{\boldsymbol{xx}}$	Cross-spectral matrix of x	various
σ_x^2	Variance	various
σ_{xy}	Covariance	various
ρ_{xy}	Correlation	
$\rho_{xy\cdot z}$	Partial correlation	
κ_{xy}	Coherence	
$\bar{\kappa}_{xy}$	Averaged coherence	
$\bar{\kappa}_{5\%}$	5% significance level for $\bar{\kappa}$	
$\mathbf{I}$	Identity matrix	
$\boldsymbol{M}$	Dynamical mode matrix	various
Q	Quality of fit	
ϵ, ε	Error term	various
u, v, w	Zonal, meridional, and vertical velocity	m s^{-1}
η	Sea level height	m
$\boldsymbol{U}$	Depth-averaged velocity	m s^{-1}
Ω	Rotation rate of the Earth	7.3×10^{-5} radians s^{-1}
f	Coriolis parameter	radians s^{-1}

Symbol	Description	Units
β	β-plane coefficient	2.3×10^{11} m^{-1} s^{-1}
p	Pressure	Pa
p_0	Equilibrium pressure	Pa
p_p	Perturbation pressure	Pa
ρ	Fluid density	kg m^{-3}
ρ_0	Equilibrium fluid density	kg m^{-3}
ρ_p	Perturbation fluid density	kg m^{-3}
g	Gravitational acceleration	9.8 m s^{-2}
N^2	Buoyancy *or* BruntVäisälä frequency squared	radians^2 s^{-2}
$\hat{p}_m$, $\hat{h}_m$	Vertical structure functions	
S_A	Absolute salinity	g kg^{-1}
Θ	Conservative temperature	°C
c	Wave speed	m s^{-1}
H	Fluid depth	m
η'_a	Altimeter sea level anomaly	m
η'_c	Tide gauge sea level anomaly	m
η_H	Observed sea level at head of Gulf of Carpentaria	m
$\hat{\eta}_\mathrm{H}$	Predicted sea level at head of Gulf of Carpentaria	m
L	Length of the Gulf of Carpentaria	m
τ	Wind stress	kg m^{-1} s^{-2}
c_d	Drag coefficient	
η_o	Observed sea level in the Gulf of Carpentaria	m
η_m	Predicted sea level in the Gulf of Carpentaria	m
$\bar{\eta}_\mathrm{o-m}$	Dewinded sea level in the Gulf of Carpentaria	m
η_sh	Sea level on the shelf edge (NW Australia)	m
I_EN	Niño 3.4 Index	
I_DMI	Dipole Mode Index	
$I_{1,t}$	First component of the MJO index	
$I_{2,t}$	Second component of the MJO index	
η^MJO	MJO-reconstructed sea level	m
$\boldsymbol{I}_t^\mathrm{WH}$	*Wheeler and Hendon* (2004) MJO index	

Symbol	Description	Units
$\boldsymbol{I}_t^{\mathrm{OT}}$	Historical reconstruction of $\boldsymbol{I}_t^{\mathrm{WH}}$	
$\boldsymbol{I}_t^{\mathrm{EV}}$	Environmental variable-based reconstruction of $\boldsymbol{I}_t^{\mathrm{WH}}$	
p_{ijt}	Reanalysis pressure ensemble mean	Pa
p_{ijt}^{a}	Filtered p_{ijt}	Pa
Δp_{ijt}	Reanalysis pressure ensemble spread	Pa
Δ_{ijt}	Relative reanalysis pressure ensemble spread	
s_{ij}	Standard deviation of p_{ijt}^{a} through time	Pa
α_{0ij}	Mean relative error (Δ_{ijt})	
α_{1ij}	Relative error (Δ_{ijt}) trend	days^{-1}
$\boldsymbol{y}_{\mathrm{obs}}$	MJO index observation mean	
σ_{obs}	MJO index observation error variance	
$\boldsymbol{\mu}_{t_0}$	Mean of MJO index at time t_0	
$\boldsymbol{\Sigma}_{t_0,t_0}$	Covariance matrix of MJO index at time t_0	
$\sigma_{t_0}^2$	Total variance of MJO index at time t_0	
$\sigma_{\mathrm{prior}}^2$	Variance of prior probability distribution	
$\boldsymbol{x}_t$	Damped harmonic oscillator model state vector	
$\boldsymbol{A}$	Damped harmonic oscillator model transition matrix	
θ	Oscillation rate	radians
γ_1	Oscillation decay parameter	
γ_2	Autoregressive decay parameter	
P	Oscillation period	days
τ_1	Oscillation decay time scale	days
τ_2	Autoregressive forcing time scale	days

ACKNOWLEDGEMENTS

I would like to thank the following people and organizations:

. . .

My family (Mom, Dad, and Jason) for always being there for me.

Friends, roommates, and graduate students in Oceanography and other departments including Jenny, Mark, Adam, Jean-Pierre, Bryan, Clark, Simon, Mike Casey, Mike Brown, Jeff, Paul, Karl, Faez, Lee, Vasily, Jorge, Shan, Yimin, Megan, Sinziana, Trajce, Doris, Steph, Xu, Yang (and more!) for so many good times.

Todd for innumerable lunchtime conversations.

Ping pong, Judo, Friday beer, and Tuesday trivia for maintaining my sanity!

. . .

Youyu Lu, Shannon Nudds, Yimin Liu for their help with numerical modelling.

My supervisor, Keith Thompson, for always being positive, supportive, and encouraging. My advisory committee (Youyu Lu, Barry Ruddick, Hal Ritchie, and Ian Folkins) for helpful comments and discussions.

. . .

Dalhousie University, CFCAS, GOAPP, and the Nunatsiavut Government for funding and supporting my studies.

. . .

Finally, I would like to thank Cecilia for her love, encouragement, and patience.

CHAPTER 1

INTRODUCTION

The Madden-Julian Oscillation (MJO) is the dominant mode of intraseasonal variability in the tropical atmosphere. The MJO provides predictability on timescales that bridge the gap between weather and climate. By modulating surface wind stress, precipitation, and the amount of solar radiation that reaches the sea surface, among other variables, the MJO can influence the state of the ocean as well. The Madden-Julian Oscillation is therefore an important source of intraseasonal variability in the world ocean. In this thesis I will explore the influence of the MJO on ocean variability and explore the consequences for the predictability of the ocean on intraseasonal time scales.

1.1 Weather, Climate, and Intraseasonal Variability

The prediction of the atmosphere and the ocean over the short-term (*weather forecasting*) and over the long-term (*climate prediction*) have been studied extensively for centuries (e.g., see Aristotle's 4^{th} century *Meteorologica*, or Ibn Wahshiyya's 10^{th} century *Nabatean Agriculture*). However, throughout most of our history weather prediction has involved little more than *weather lore*, such as the old mariner's rhyme

> *Red sky at night, sailor's delight*
> *Red sky at morning, sailors take warning*

indicating how one may interpret the colour of a sunrise or sunset (i.e., the observed state of the atmosphere) in terms of the severity of forthcoming weather conditions. Items of weather lore such as this were effectively empirical weather prediction tools. The technological achievements of the industrial revolution led to more accurate observations of the environment and the ability to signal changes in weather patterns across large distances as our ability to communicate improved. The greatest leap came when we were able to understand the dynamics of the atmosphere in terms of fluid motion and thermodynamics; by the twentieth century, technology had advanced to the point that we were able to simulate the atmosphere and ocean using general circulation models. These last developments can be considered the beginning of contemporary weather and climate prediction.

After Edward Lorenz laid the theoretical foundations for what would become Chaos Theory, rapid advances were made in our understanding of the dynamics of weather and climate. He postulated that the dynamical system describing the atmosphere was *chaotic*, implying that there existed a time scale beyond which predictions based on similar initial conditions would evolve into considerably different states. Unless the initial condition is known exactly it is impossible to predict the state of the system beyond this time scale (*Lorenz*, 1963). Based on a simple mathematical model of the atmosphere, the limiting time scale for weather prediction was estimated to be about one or two weeks (*Lorenz*, 1965). These ideas provided the framework for our early understanding of weather and climate. Weather was defined as the variability that occurs on time scales less than two weeks and could be predicted using the appropriate dynamical equations and a given initial state. In practice, modern weather prediction is effectively a series of short initial condition problems with observations assimilated into the numerical model to correct the model state as it drifts from reality. Climate prediction is focussed on the statistical properties of the atmosphere on seasonal time scales or longer and relies on predicting average conditions using atmospheric dynamics.

The classic division of weather and climate and its practical implications have been described concisely by John von Neumann (*von Neumann*, 1960):

> *"It seems quite plausible from general experience that in any mathematical problem it is easiest to determine the solution for shorter periods, over which the extrapolation parameter is small. The next most difficult problem to solve is that of determining the asymptotic conditions – that is, the conditions that exist over periods for which the extrapolation parameter is very large, say near infinity. Finally, the most difficult is the intermediate range problem, for which*

> *the extrapolation parameter is neither very small nor very large. In this case the neglect of either extreme is forbidden. On the basis of these considerations, it follows that there is a perfectly logical approach to any computational treatment of the problem of weather prediction. The approach is to try first short-range forecasts, then long range forecasts of those properties of the circulation that can perpetuate themselves over arbitrarily long periods of time, and only finally to attempt forecasts for medium time periods which are too long to treat by simple hydrodynamic theory and too short to treat by the general principles of equilibrium theory."*

This view effectively divided the prediction of weather, climate, and the intermediate time scales into three distinct problems of increasing difficulty. A different point of view is that there are essentially two problems. The more complicated problem is that of predicting the statistical behaviour of the atmosphere over long time scales (i.e., climate prediction). The more tractable problem consists of predicting weather and other similar phenomena within the limits set by their predictability time scales. Weather prediction using numerical models has been an active field of research for more than a century and our skill at predicting weather is quite advanced. Recent research has now begun to tackle the problem of predicting on intermediate, or *intraseasonal*, time scales that span a few weeks to a few months. The Madden-Julian Oscillation has a predictability time scale longer than the "two-week limit" and therefore a better understanding of this phenomenon, and how it influences the ocean, may allow us to bridge the gap between short-term weather predictions and long-term climate predictions and help with the development of a seamless forecasting framework.

1.2 Modes of Variability in the Ocean-Atmosphere System

Recurring patterns of variability in the atmosphere and ocean are known as "modes of variability". El Niño is a well-known example that occurs in the tropical eastern Pacific Ocean and is associated with variations in sea surface temperature and sea level height (e.g., *Clarke* (2008)). El Niño, and its opposite phase La Niña, tend to repeat every 3 to 8 years. In addition to El Niño-La Niña, there exist numerous other modes of variability affecting all aspects of the atmosphere and ocean with various time scales and spatial patterns.

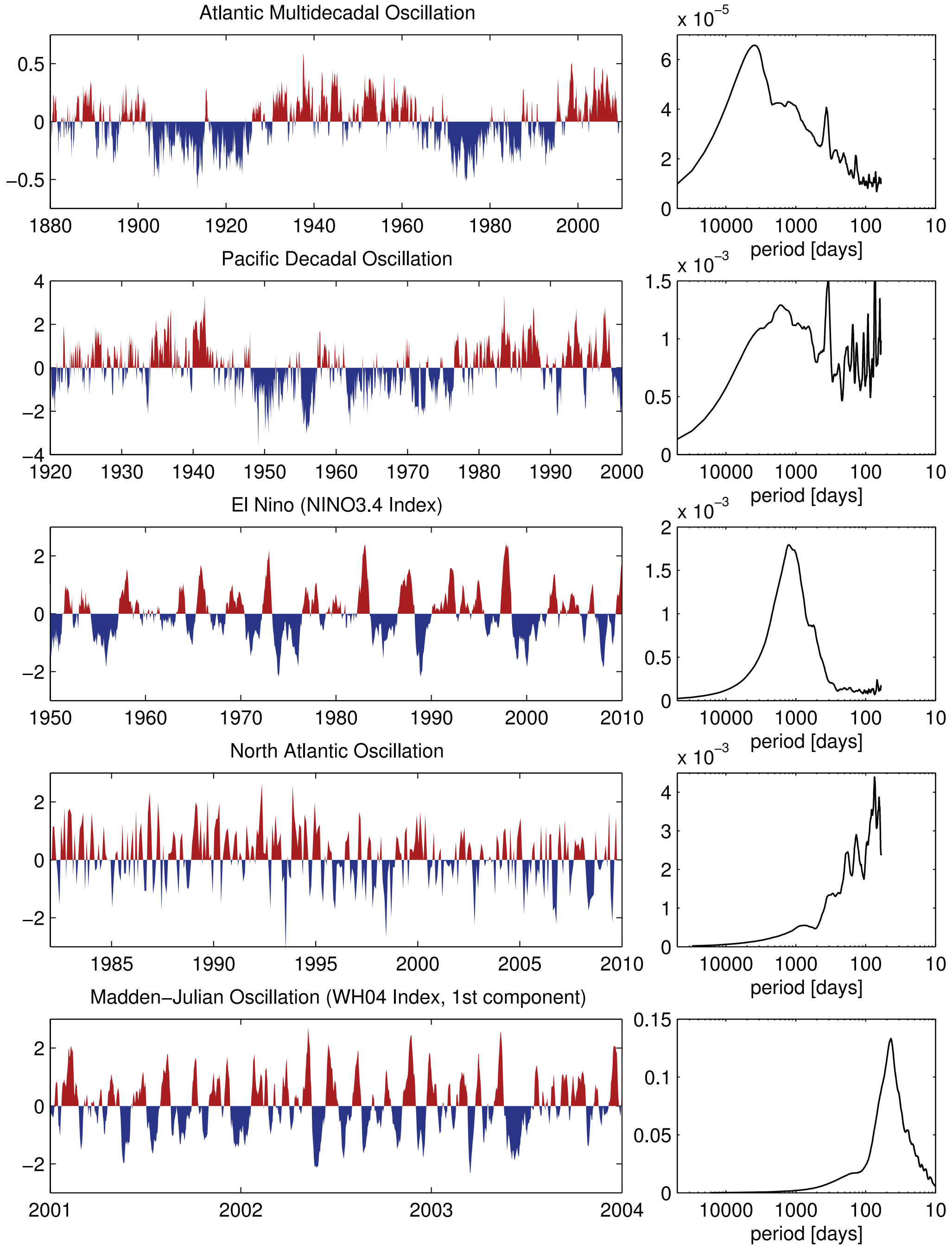

Figure 1.1: Indices describing the time variation of selected modes of variability of the ocean-atmosphere system. Each row corresponds to a given index, specifically (from top to bottom) the Atlantic Multidecadal Oscillation, the Pacific Decadal Oscillation, El Niño-La Niña (Niño 3.4 index), the North Atlantic Oscillation, and the Madden Julian Oscillation (first component only). Time series are shown on the left and power spectral densities are shown on the right. The y-axis is the product of frequency and power and x-axis is the logarithm of frequency leading to a variance preserving form for the power spectral density.

Examples include the North Atlantic Oscillation (e.g., *Gill* (1982)), the Pacific Decadal Oscillation (*Mantua and Hare*, 2002), the Atlantic Multidecadal Oscillation (*Schlesinger and Ramankutty*, 1994), and the Indian Ocean Dipole (*Saji et al.*, 1999). The time variation of these modes is often characterized by a time series, known as an index, that captures the most important features of its temporal variability. Indices for selected phenomena are shown in Figure 1.1 to illustrate the diverse time scales on which different modes of variability operate.

The ability to predict the modes of variability can be used to help predict local climatic conditions. For example, a strong El Niño is associated with enhanced rainfall in coastal South America, warmer and drier winters over much of northern North America, and dry conditions over Southeast Asia (*Ropelewski and Halpert*, 1987, 1986). Therefore, the predictability inherent in the index describing El Niño allows enhanced predictability of environmental conditions in these regions.

The MJO is a mode of variability in the tropical atmosphere that operates on intraseasonal time scales (between 30 and 90 days, Figure 1.1). Therefore, the Madden-Julian Oscillation (MJO) is a prime candidate for improving the quality of long-range weather predictions.

1.3 The Madden-Julian Oscillation

The phenomenon now known as the Madden-Julian Oscillation was discovered accidentally during a study of tropical wind. The details were first published in 1971 by Roland Madden and Paul Julian:

> *"[. . .] we stumbled upon an apparent long-period oscillation in the station pressure and zonal wind components at Canton Island (3°S, 172°W). The frequency of this oscillation is much lower than that of any wave mode yet hypothesized, but is higher than can be expected from any component of a seasonal variation."* (*Madden and Julian*, 1971)

They also observed a similar phenomenon in high-level zonal wind that was out of phase with the signal in low level zonal wind, indicating a baroclinic structure. The initial discovery and subsequent investigations identified many characteristics of the MJO that continue to be areas of study today including its time scale, seasonality, nonlinearity, questions about wavelike or non-wavelike nature, and the dynamics (which are as yet

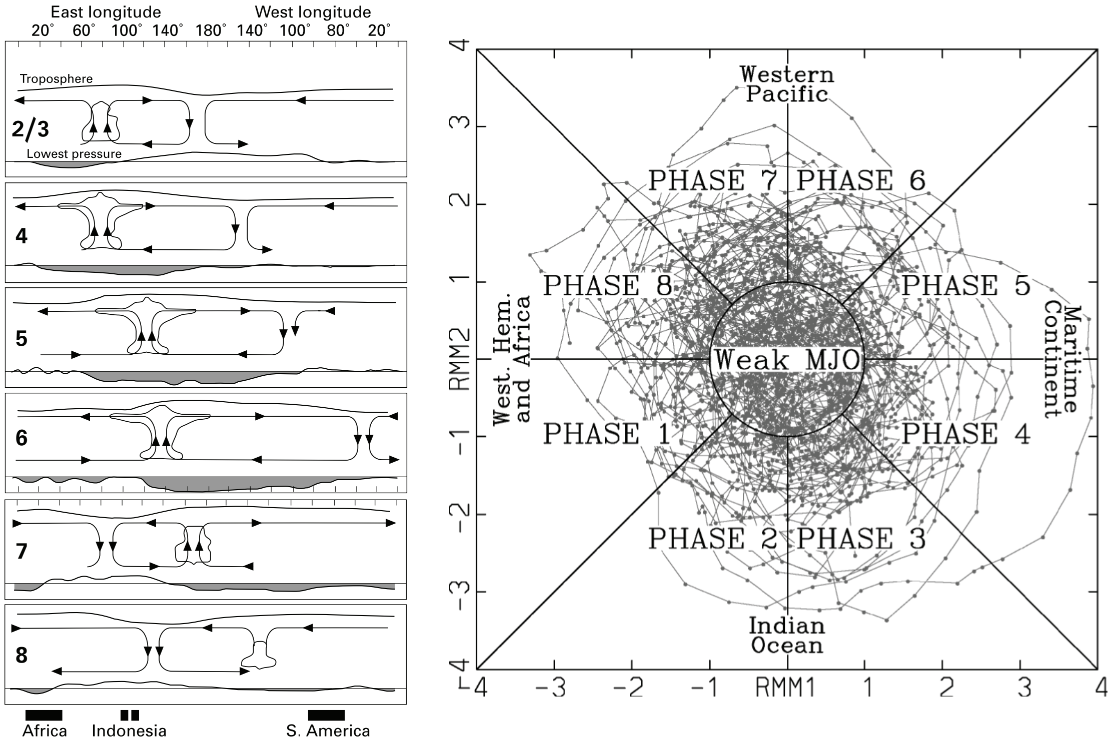

Figure 1.2: MJO event lifecycle and index. Left: Schematic showing the lifecycle of a single MJO event (*Madden and Julian*, 2005). A convection cell develops over the Indian Ocean, perturbing the troposphere and zonal wind at both low and high levels. This "MJO event" then propagates eastward before dissipating over the eastern Pacific and Atlantic Oceans. Right: MJO Index as developed by *Wheeler and Hendon* (2004). The radius and angle of a particular point represent the strength and phase (zonal position of active convection as indicated around the edge of the plot) of the MJO, respectively. The numbered phases roughly correspond between the left and right panels.

unexplained by theory and improperly resolved by models). Madden and Julian continued the study of this phenomenon in their follow-up paper in which they examined the spatial and temporal structure of the MJO (*Madden and Julian*, 1972). They reduced the complex behaviour of the MJO in space and time (along the equator) down to the simple schematic reproduced here in Figure 1.2. In short, the MJO consists of an eastward propagating region of deep convection with associated anomalies in precipitation, surface pressure, and zonal wind at both low and high vertical heights which occurs approximately every 40-50 days along with seasonal variations in strength, meridional structure, and timescale (*Zhang and Dong*, 2004). This behaviour represents the dominant mode (but by no means the only source) of intraseasonal variability in the tropical atmosphere.

The Madden-Julian Oscillation is a complex beast. As described above, the primary phenomenon is an eastward moving region of deep atmospheric convection and precipitation centred about the equator. However, it also has poleward propagating features over Southeast Asia that are often considered separately as the Boreal Summer Intraseasonal Oscillation (*Madden and Julian*, 1994). The deep convection drives a baroclinic wind structure whereby the lower troposphere (below about 1.5 km) experiences anomalous convergence of zonal wind and the upper troposphere (above about 10 km) experiences anomalous divergence. Near the surface and over land this is expressed as anomalous easterly and then westerly winds as the active region of convection passes over. It has been speculated that the ancient Polynesians may have used knowledge of these "westerly wind bursts" to navigate the large distances between islands in the Pacific Ocean (*Finney*, 1994). The active region of the MJO moves at an average speed of about 5 m s^{-1} until it reaches the eastern Pacific after which its speed increases and its strength decreases.

Wheeler and Kiladis (1999) summarized the unique, and largely unexplained, characteristics of the MJO using wavenumber-frequency spectra of equatorial outgoing longwave radiation (OLR, used as a proxy for precipitation). They detected dynamically predicted modes of variability (e.g., convectively coupled Kelvin waves, Rossby waves, inertio-gravity waves, see *Matsuno* (1966) and Section 3.3 for details on these modes) as well as variability which fit the characteristics of the MJO (Figure 1.3). Their spectral approach gave a clear picture as to how the MJO compares with the dispersion relations of dynamically based modes of variability; it is notable that the MJO lies off the dispersion curves for known equatorial wave types.

Over the last few years the MJO has been of increasing interest to the research community. The number of articles containing the text "intraseasonal" has increased rapidly since the 1970s when there were only a handful per year. Over the last five years this number has increased to between 400 and 500 such articles published per year. Since its naming in the mid-1980s, the number of articles containing the text "madden-julian oscillation" has increased to nearly 200 annually over the last few years[1]. The topics covered by these articles have branched out from simple observational studies of the intraseasonal oscillation in the tropics in the early years to theoretical studies of the dynamics of the MJO, how the MJO is represented in numerical models, its connections with ENSO, and

---

[1] These figures were generated by searching Google Scholar (scholar.google.com) for specific phrases and publication dates.

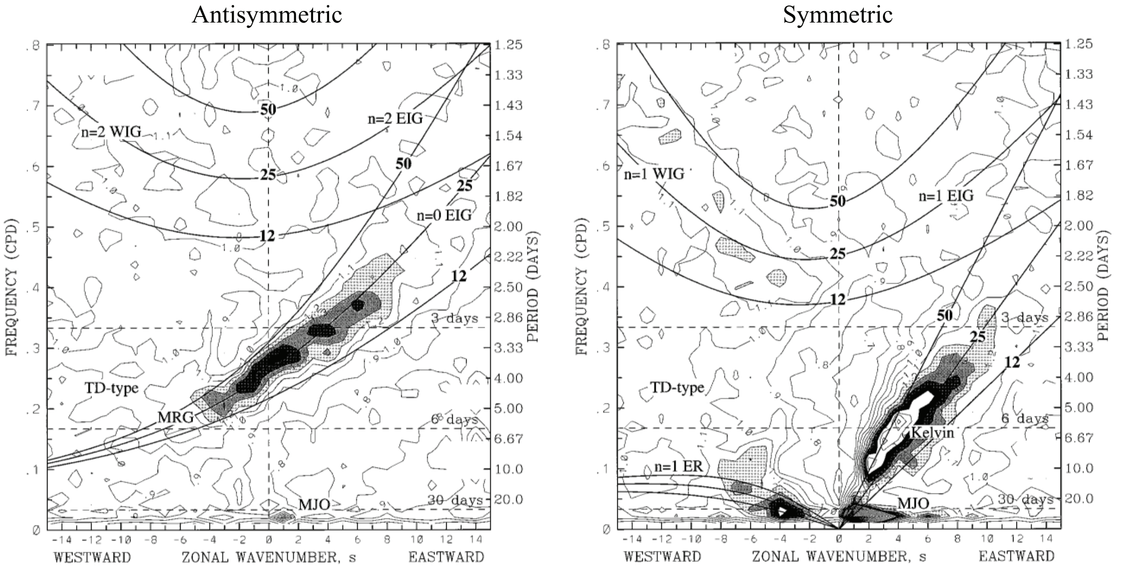

Antisymmetric

Symmetric

Figure 1.3: Wavenumber-frequency spectra for outgoing longwave radiation (OLR) in the atmosphere. The spectra, based on averages of OLR in the tropics between 15°S and 15°N, are shown for variability which is antisymmetric (left) and symmetric (right) about the equator. The MJO is clearly distinguishable in both panels for periods between 30 and 90 days and for zonal wavenumbers 1 to 4. The signal is strongest in the symmetric spectrum which is consistent with observations which show the MJO to be predominantly symmetric about the equator. The thin solid lines show the dispersion curves for Kelvin waves, gravity waves (EIG), Rossby waves (ER), and mixed Rossby-gravity waves (MRG). Figure reproduced from *Wheeler and Kiladis* (1999).

teleconnections with the extratropical ocean and atmosphere.

The MJO, like weather, has an inherent predictability time scale which is independent of the MJO oscillation period. *Waliser* (2005) suggested that this time scale is between 20 to 30 days. Other studies have estimated the time scale to be 2 weeks using a coupled ocean-atmosphere circulation model (*Vitart et al.*, 2007), 15 days using autoregressive models (*Lo and Hendon*, 2000; *Maharaj and Wheeler*, 2005), 15 days using a multivariate lag-regression model (*Jiang et al.*, 2008), and 10 days using an atmospheric circulation model (*Lin et al.*, 2008). *Woolnough et al.* (2007) found that coupling an ocean general circulation model to an atmospheric model can add several days over results from modeling the atmosphere alone. The predictability of the MJO (20–30 days) is longer than the predictability limit attributed to weather variability (1–2 weeks) and therefore the MJO has potential to add true value to long range atmospheric forecasting.

Until recently there was no widely accepted index for the MJO. In fact, there were nearly as many ways of characterizing the MJO as there were independent studies. Recently, the definition developed by *Wheeler and Hendon* (2004) has become the effective standard index for the MJO. This index is bivariate and consists of the first two principal components of an EOF analysis of tropically averaged (15°S to 15°N) fields of OLR (as a proxy for precipitation) and zonal wind at two heights (200 hPa and 850 hPa). The intraseasonal signals in each of these three variables are primary indicators of the MJO and their combination into the Wheeler Hendon index further suppresses high frequencies signals which are incoherent amongst these three variables.

The two components of the index can be visualized in a two-dimensional plot where the x and y axes correspond to the two components. This will be referred to as *MJO space*. The radius and angle of a particular point represents the strength and phase of the MJO, respectively (Figure 1.2). The angle can also be interpreted as the region over which the active convection associated with the MJO is situated (as indicated in Figure 1.2). MJO events typically follow counterclockwise paths in MJO space as they propagate eastward around the globe. (The two components are approximately in quadrature.) The centre of convection is over the Western Hemisphere and Africa during phases 8 and 1, the Indian Ocean during phases 2 and 3, the Maritime Continent during phases 4 and 5, and the Western Pacific during phases 6 and 7.

1.4 Dynamical Theories and Models of the MJO

The Madden-Julian Oscillation has proven itself to be a difficult phenomenon to describe theoretically. The properties which an effective theoretical model of the MJO must reproduce include (1) coupled planetary-scale circulation and large-scale convection, (2) horizontal atmospheric circulation along the equator made up of both eastward propagating Kelvin waves and westward propagating Rossby waves, (3) eastward propagation speed of about 5 m s^{-1} in the Eastern Hemisphere and faster elsewhere, and (4) northward and westward propagation in the Asian monsoon region during northern summer. It has been determined that the principal process which must be modeled theoretically in order to properly reproduce the properties listed above is the interaction between large-scale motion and moist atmospheric processes. Thus far, models based on wave-CISK (conditional instability of the second kind), WISHE (wind-induced surface heat exchange), and friction-induced moisture-convergence feedback have been the most successful. However, to date most models have only been able to reproduce a subset of the properties listed above (*Wang*, 2005).

Numerical models have had mixed results when attempting to resolve intraseasonal variability in the ocean and atmosphere. Approaches have ranged from simplifying the mathematical model down to a forced rotating fluid on a β-plane (*Wedi and Smolarkiewicz*, 2008) to assessing how a complex ensemble of fifteen different global atmospheric circulation models behave on intraseasonal timescales (*Slingo et al.*, 1996). Part of the conclusions in the latter study is summarized by the following statement:

> *"[An] accurate simulation of the intraseasonal oscillation may be a demanding test of a General Circulation Model, because it has so many requirements, and that these may include good simulations of the basic climate, the seasonal cycle, higher frequency modes of tropical variability, and interactions with the extratropics."*

Often, models are able to capture some of the characteristics of the MJO such as eastward propagation speed and zonal structure while lacking others such as coherence between zonal wind and precipitation or seasonal variations (*Zhang et al.*, 2006). One of the main factors that may improve how models handle the MJO and intraseasonal variability is proper parameterization of subgrid-scale convection (*Lin et al.*, 2008; *Grabowski*, 2006).

The importance of ocean-atmosphere coupling is potentially an important aspect of modeling the MJO. Air-sea interactions are certainly necessary in order to resolve oceanic expressions of the MJO. However, it is not clear if two-way air-sea coupling is critical for fully resolving the MJO itself or if one-way coupling alone is sufficient. The effect of air-sea coupling in models is inconsistent from study to study; some show improved resolution of the MJO and others show no effect or an improvement of some features and not others (*e.g.*, *Hendon* (2000), *Zhang et al.* (2006), *Newman et al.* (2009), and the aforementioned *Slingo et al.* (1996)). This inconsistency may depend on factors such as the particular oceanic or atmospheric model, the coupling mechanism, specific parameterizations or the initialization state. Two-way coupling is currently an active field of research.

1.5 The MJO and the Extratropical Atmosphere

In the extratropical atmosphere, intraseasonal variability is not dominated by the MJO and other phenomena have a strong influence (e.g.,the North Atlantic Oscillation). However, the MJO is such a strong source of variability that it affects the global atmosphere-ocean system leading to detectable signatures in some extratropical regions. A qualitative description of how the global atmosphere is affected by the MJO can be found in *Meehl et al.* (1996) where global patterns of wind anomalies and pressure systems are mapped for different phases of the MJO. These maps show the effects of tropical intraseasonal variability being felt at all levels of the troposphere as well as the tropics and extratropics.

Rainfall in the Pacific Northwest of the USA is known to be modulated by the MJO during the northern autumn (*Bond and Vecchi*, 2003). Tropical cyclones, though not strictly an extratropical phenomenon, exert a strong influence when they move into the extratropics and it has been shown that the generation rate of tropical cyclones is strongly influenced by the MJO in all ocean basins (*Hall et al.*, 2001; *Maloney and Hartmann*, 2000a,b; *Ho et al.*, 2006; *Bessafi and Wheeler*, 2006). Furthermore, there is strong evidence that there are links with surface air temperature (SAT) at high latitudes (*Vecchi and Bond*, 2004; *Lin and Brunet*, 2009). Anomalies in SAT associated with the MJO are on the order of 5°C in regions such as Northern Ontario and Central Siberia.

Recent research has pointed to strong links between two major modes of variability in the ocean-atmosphere system: the MJO and the North Atlantic Oscillation (NAO) (*Cassou*, 2008; *Lin et al.*, 2009). *Cassou* (2008) categorized the NAO by four regimes: NAO+, NAO-, Atlantic ridge and Scandinavian blocking. The first two describe variability in the zonal flow of the region and the latter two describe specific positioning of pressure systems over Europe and the eastern Atlantic. *Cassou* (2008) presents statistical evidence that phases 3 and 6 of the MJO (Figure 1.2) are precursors to NAO+ and NAO- regimes respectively, and proposes that it may be due to timescale resonance or possibly direct forcing from the eastern Pacific. *Lin et al.* (2009) revealed the connection between the MJO and NAO by examining lagged composites of the NAO index with MJO phase.

1.6 The MJO and the Tropical Ocean

The Madden-Julian Oscillation is an atmospheric phenomenon but the associated precipitation, convection, and wind anomalies also interact with the ocean surface. Zonal wind anomalies affect ocean mixed layer depth and zonal currents at various depths (*Kessler*, 2005). For example, *Han et al.* (2001) found that a large portion of the variability in the intraseasonal zonal flow anomalies in the interior of the Indian Ocean is associated with the MJO. They also observed that the ocean response to the MJO tends to be expressed on longer timescales within the intraseasonal band (90 days in the Indian Ocean, 70 days in the Pacific Ocean). This tendency towards longer timescales is often found when analysing the oceanic response to intraseasonal forcing and may be an indication of nonlinear processes influencing the interaction between the two fluids.

Sea level variability on intraseasonal time scales has been studied more than other ocean variables. Broad scale patterns of intraseasonal sea level anomalies have been detected worldwide (*Fu*, 2003) but the most interesting (and numerous) results have been on ocean waves. *Hendon et al.* (1998) presented a general study on the MJO and Kelvin waves and there have been numerous studies focussed on specific regions (e.g., *Zhang et al.* (2009) focus on the equatorial Pacific Ocean). Coastally trapped waves with intraseasonal periods of oscillation have been detected along the eastern boundaries of both the Pacific (*Spillane et al.*, 1987) and the Indian Oceans (*Iskandar et al.*, 2005). They are believed to be generated by eastward propagating equatorially trapped waves, driven by the MJO and originating in the Western Pacific, impinging on the eastern boundary which then excite a response which travels poleward along the coast (*Enfield*, 1987; *Clarke and Liu*, 1993).

Sea surface temperatures (SSTs) have been observed to undergo modulations due to the MJO (*e.g.*, *Woolnough et al.* (2000); *Shinoda et al.* (1998); *Maloney et al.* (2008)) and it is known that SST signatures propagate eastward across the Pacific Ocean along with the MJO (*Zhang*, 2005). In fact, temperature variability in the mixed layer, along with sea level, may be one of the best oceanic indicators of the MJO. Feedbacks with ENSO are a major area of study (*Kessler*, 2005) and it has been observed that the MJO is particularly strong in the time leading up to the onset of El Niño. It has been proposed that MJO-driven equatorially trapped Kelvin waves may play a role in triggering El Niño events (e.g., *Harrison and Vecchi* (1997); *Zhang* (2005)).

1.7 Statement of Problem, Objectives, and Outline of Thesis

This study attempts to answer two fundamental questions:

1. How does the MJO impact the ocean?
2. Is the MJO a potentially useful source of oceanic predictability?

To answer those questions the following objectives have been set:

1. Identify the temporal and spatial patterns of ocean response to the MJO.
2. Identify the physical processes governing the oceanic response.
3. Quantify the impact of the MJO on oceanic predictability and exploit the predictability in the design of ocean forecast systems.

The structure of the thesis is as follows. Statistical, dynamical, and numerical methods are outlined in Chapters 2 and 3. An analysis of the impact of the MJO on global sea level is described in Chapter 4 and three regions in which the MJO-ocean connection is particularly strong are identified: the equatorial Pacific and Coastal Americas, the Gulf of Carpentaria, and the northeastern Indian Ocean. The MJO-ocean connections in the Gulf of Carpentaria and the northeastern Indian Ocean are explored further using numerical ocean models in Chapter 5 and Chapter 6, respectively. Chapter 7 describes a reconstruction of the MJO index over the last century and also sheds some light on the predictability time scale of the MJO. A summary of the main conclusions of this study, and their implications, are presented in Chapter 8.

CHAPTER 2

STATISTICAL TECHNIQUES AND MODELS

The advanced statistical techniques that are used in this thesis are outlined below. Techniques that explore the relationship within a set of random variables are presented in Section 2.1 and techniques that explore the relationships between sets of random variables are presented in Section 2.2. Autoregressive models, including a stochastically forced damped harmonic oscillator used to examine the predictability of the MJO, are presented in Section 2.3.

2.1 Relationships Within a Set of Random Variables

The techniques outlined below are concerned with relationships that exist within a set of random variables. In practice, this typically amounts to identifying *modes of variability* and the amount of variability accounted for by such modes. At this point the distinction between *statistical modes* and *dynamical modes* should be made. Statistical modes are a set of empirically determined modes that account for observed variability, e.g., the eigenmodes of a covariance or cross-spectral matrix (see Sections 2.1.1 and 2.1.2 below). Many modes of variability, such as the ENSO index, the Madden-Julian Oscillation index, and the Pacific Decadal Oscillation are often defined by statistical modes. On the other hand, dynamical modes are predicted patterns of variability that a given dynamical system supports. (For example, see the equatorial wave modes presented in Section 3.3.) They may not be present in a given set of observations but the underlying dynamics permit them under the right conditions. Often, a statistical mode of variability may correspond to a dynamical mode (e.g., the ENSO index or the Madden-Julian Oscillation index) but occasionally it does not (e.g., the Pacific Decadal Oscillation).

2.1.1 Empirical Orthogonal Function Analysis

Empirical orthogonal function (EOF) analysis is a technique which accounts for the total variance of a set of random variables using linear combinations of those variables (e.g., *Johnson and Wichern* (2002)). Each linear combination corresponds to a statistically uncorrelated mode of variability. The weights in the combination are referred to as EOF modes and the associated time series are called the principal components. For geophysical data this often results in a small number of EOF modes accounting for most of the variability in the original data set and such modes can often be associated with known phenomena (e.g., the NAO). In fact, principal components from an EOF analysis of selected tropical atmospheric variables are used to define the Wheeler and Hendon MJO index.

Consider a vector of p random variables: $\boldsymbol{x} = [x_1 \ x_2 \ \cdots \ x_p]^{\mathrm{T}}$, where $^{\mathrm{T}}$ denotes transpose. The EOF modes are found by solving the eigenvalue problem

$$\boldsymbol{\Sigma}_{\boldsymbol{xx}}\boldsymbol{e}_i = \lambda_i \boldsymbol{e}_i \quad \text{with} \quad i = 1, 2, \ldots, p \tag{2.1}$$

where $\boldsymbol{\Sigma}_{\boldsymbol{xx}}$ is the covariance matrix of $\boldsymbol{x}$. The $\{\boldsymbol{e}_i | i = 1, 2, \ldots, p\}$ is a set of p orthonormal eigenvectors that each represent an independent mode of variability. The proportion of variance accounted for by the i^{th} mode is given by $\lambda_i / \sum_{j=1}^{p} \lambda_j$ where λ_i is the eigenvalue associated with the i^{th} mode. In this way, the total variance, $\mathrm{tr}\boldsymbol{\Sigma}_{\boldsymbol{xx}}$, is decomposed into p modes of variability. Generally, the modes that account for most of the variability are of primary interest. However, modes that explain essentially no variability (i.e., $\lambda_i \simeq 0$) but have a well defined structure can correspond to time-invariant quantities in $\boldsymbol{x}$ and may be of interest as well.

2.1.2 Frequency Dependent EOF Analysis

Empirical orthogonal function analysis, when generalized to the frequency domain, is known as frequency-dependent EOF analysis (FDEOF; *Wallace and Dickinson*, 1972; *Brillinger*, 1981).

Consider a random process $\{\boldsymbol{x}_t\}$ where $\boldsymbol{x}_t$ is given by $[x_1\ x_2\ \cdots\ x_p]_t^{\mathrm{T}}$. At a particular frequency ω, the FDEOF modes are found by solving the eigenvalue problem

$$\boldsymbol{f}_{\boldsymbol{xx}}(\omega)\boldsymbol{e}_i = \lambda_i \boldsymbol{e}_i \quad \text{with} \quad i = 1, 2, \ldots, p \tag{2.2}$$

where $\boldsymbol{f}_{\boldsymbol{xx}}$ is the cross-spectral matrix of the process (*Priestley*, 1981). As above the $\{\boldsymbol{e}_i | i = 1, 2, \ldots, p\}$ is a set of p orthonormal eigenvectors (i.e., the FDEOF modes) and the proportion of power accounted for by the i^{th} mode is given by $\lambda_i / \sum_{j=1}^{p} \lambda_j$ where λ_i is the eigenvalue for the i^{th} mode. In general the λ_i will be real and non-zero.

The usefulness of this technique over traditional EOF analysis is twofold. First, the cross-spectral matrix, $\boldsymbol{f}_{\boldsymbol{xx}}$, is a function of frequency and so the modes will vary with frequency. This allows one to isolate a particular timescale and examine the modes of variability that are important on that timescale alone. Second, the cross-spectral matrix is complex valued and so the eigenvectors (and thus the modes) may be complex as well which means that the modes can be written in terms of amplitude and phase. Therefore, propagating waves at a particular frequency can be detected with a single mode using FDEOF analysis. Using traditional EOF analysis would require more advanced techniques such as bandpassing the data about the timescale of interest, and using two standing modes in quadrature, to describe such propagating waves.

2.1.3 Dynamical Modal Analysis

Consider the real-valued random $p \times 1$ vector $\boldsymbol{u}_t$ with the i^{th} element corresponding to the ocean state at location (x_i, y_i) and time t. The spectral representation of $\boldsymbol{u}_t$ is given by (*Priestley*, 1981)

$$\boldsymbol{u}_t = \int_{-\pi}^{\pi} e^{i\omega t} d\boldsymbol{u}(\omega), \tag{2.3}$$

where $d\boldsymbol{u}(\omega)$ is a random orthogonal increment process and ω denotes frequency.

Now consider a model for $\boldsymbol{u}_t$ consisting of a set of m dynamical modes each defined at (x_i, y_i) for $i = 1 \ldots p$. The vector $\boldsymbol{u}_t$ is now decomposed into the sum of modal contributions $\hat{\boldsymbol{u}}_t$ and residuals $\boldsymbol{r}_t$ representing noise and other processes not explained by the model as follows:

$$d\boldsymbol{u}(\omega) = d\hat{\boldsymbol{u}}(\omega) + d\boldsymbol{r}(\omega). \tag{2.4}$$

The modal contributions are taken to be a linear combination of the m dynamical modes

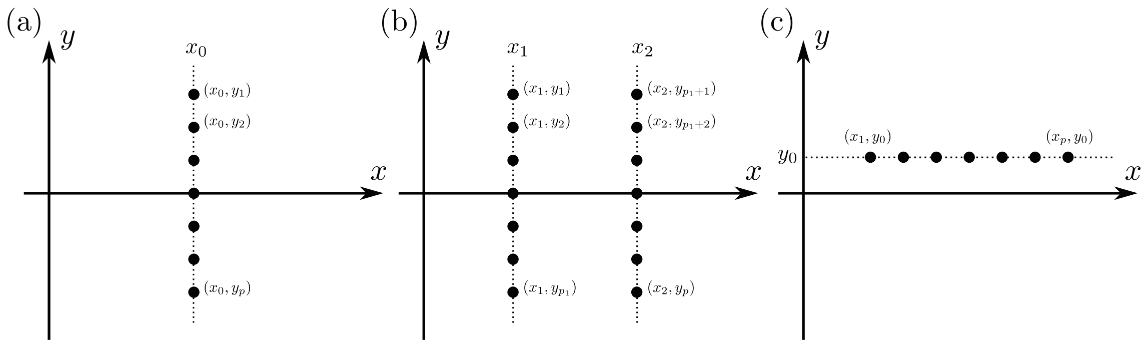

Figure 2.1: Locations of stations for three dynamical modal analysis case studies. Waves propagate in the x-direction.

with amplitudes at time t specified by the $m \times 1$ vector $\boldsymbol{a}_t$. In the frequency domain, the modal contribution $d\hat{\boldsymbol{u}}(\omega)$ is expressed as the product of a $p \times m$ frequency-dependent *dynamical mode matrix* $\boldsymbol{M}(\omega)$ and the $m \times 1$ vector $d\boldsymbol{a}(\omega)$ which is the spectral representation of $\boldsymbol{a}_t$. The model for $\hat{\boldsymbol{u}}_t$ is then taken to be

$$\hat{\boldsymbol{u}}_t = \int_{-\pi}^{\pi} e^{i\omega t} \boldsymbol{M}(\omega) d\boldsymbol{a}(\omega). \tag{2.5}$$

The j^{th} column of $\boldsymbol{M}(\omega)$ represents an individual mode evaluated at locations (x_i, y_i) for $i = 1 \ldots p$ (i.e., the rows of $\boldsymbol{M}$). In order for $\hat{\boldsymbol{u}}_t$ to be real-valued the mode matrix must obey the following restriction: $\boldsymbol{M}(-\omega) = \boldsymbol{M}(\omega)^*$, where * denotes complex conjugate.

Let the cross-spectral matrix of $\boldsymbol{a}_t$ at frequency ω be given by $\boldsymbol{f}_{\boldsymbol{aa}}(\omega)$. It is now straightforward to calculate the modal contributions and residuals. The cross-spectral matrix of the modal contributions is given by

$$\boldsymbol{f}_{\hat{\boldsymbol{u}}\hat{\boldsymbol{u}}}(\omega) = \boldsymbol{M} \boldsymbol{f}_{\boldsymbol{aa}}(\omega) \boldsymbol{M}' \tag{2.6}$$

where $'$ represents conjugate transpose. This technique, referred to as Dynamical Modal Analysis (DMA), will be explored further by considering several simple cases.

Case (a): Consider a line of stations at locations (x_0, y_i) for $i = 1 \ldots p$ (Figure 2.1a) and consider a dynamical model that provides a set of functions $\phi_j(y, \omega)$ for $j = 1 \ldots m$ that define the y-dependence of m modes at a given frequency. For example, if the model represents equatorially trapped oceanic Kelvin waves (see Section 3.3.2) then the $\phi_j(y, \omega)$ functions would be Gaussian in y with a trapping scale that decreases with increasing mode number j. The elements of the mode matrix can be written $M_{ij} = \phi_j(y_i, \omega)$.

Case (b): Consider two lines of stations at locations (x_1, y_i) for $i = 1 \ldots p_1$ and (x_2, y_i) for $i = (p_1 + 1) \ldots p$ (Figure 2.1b). As above, a set of functions $\phi_j(y, \omega)$ describes the y and ω dependence of each mode. Wave propagation can be modelled by assuming $\hat{\boldsymbol{u}}_t$ is made up of propagating wave solutions with dependence in x and t of the form $\exp i(kx + \omega t)$ where wavenumber $k = k(\omega)$. The elements of the mode matrix can be written $M_{ij} = \phi_j(y_i, \omega)e^{ikx_1}$ for $i = 1 \ldots p_1$ and $M_{ij} = \phi_j(y_i, \omega)e^{ikx_2}$ for $i = (p_1 + 1) \ldots p$.

The two lines can be uncoupled by removing the constraint of wave propagation between them. In this case the j^{th} column in the mode matrix is replaced by two columns, j_1 and j_2, doubling the number of columns in $\boldsymbol{M}$. The first column is given by $M_{ij_1} = \phi_j(y_i, \omega)$ for $i = 1 \ldots p_1$ and $M_{ij_1} = 0$ for $i = (p_1 + 1) \ldots p$. The second column is given by $M_{ij_2} = 0$ for $i = 1 \ldots p_1$ and $M_{ij_2} = \phi_j(y_i, \omega)$ for $i = (p_1 + 1) \ldots p$.

Case (c): Consider a line of stations at locations (x_i, y_0) for $i = 1 \ldots p$ (Figure 2.1c). Propagating wave solutions are considered as in the previous case. There is no need for y dependence of the mode shapes and so the $\phi_j(y, \omega)$ functions drop out and the elements of the mode matrix are simply given by $M_{ij} = e^{ik_jx_i}$. The relationship between wavenumber and frequency has been generalized such that it can be different for each mode, e.g., $k_j = k_j(\omega)$. In this case, the j^{th} mode is simply a sine wave of frequency ω that propagates along the line with speed of $\omega/k_j(\omega)$.

Consider the case where $\boldsymbol{f_{uu}}(\omega)$ is known but the modal amplitudes are unknown. Given a mode matrix $\boldsymbol{M}(\omega)$ it is possible to fit these modes to $\boldsymbol{u}_t$. The cross-spectral matrix of the modal amplitudes $\boldsymbol{a}_t$ is estimated following *Haines et al.* (1991):

$$\boldsymbol{f_{aa}}(\omega) = (\boldsymbol{M}'\boldsymbol{M})^{-1}\boldsymbol{M}'\boldsymbol{f_{uu}}(\omega)\boldsymbol{M}(\boldsymbol{M}'\boldsymbol{M})^{-1}, \tag{2.7}$$

which follows from Equations 2.4 and 2.5 assuming the residuals are incoherent with the modal amplitudes and that the matrix $\boldsymbol{M}'\boldsymbol{M}$ can be inverted. Various quantities, such as the proportion of variance in the observations that are accounted for by the modes, follow in a straightforward manner (e.g., *Haines et al.* (1991)). For example, the quality of the fit Q can be quantified by

$$Q = 1 - \frac{||\boldsymbol{f_{\hat{u}\hat{u}}} - \boldsymbol{f_{uu}}||}{||\boldsymbol{f_{uu}}||}, \tag{2.8}$$

where the norm is defined as the absolute value of the root mean square: $||\cdot|| = |\text{RMS}(\cdot)|$.

The numerator of the second term is the RMS error between the fit and the observations and decreases as the fit improves; the denominator of the second term can be interpreted as the RMS error between a null fit (i.e., all zeros) and the observations and remains constant. Therefore, provided the fit explains at least some of the variability in the observations, Q gives a number between 0 and 1 and increases as the quality of fit increases.

It is interesting to note that frequency dependent EOF analysis (Section 2.1.2) is a special case of dynamical modal analysis. The FDEOF eigenvalue problem (Equation 2.2) can be written

$$\boldsymbol{f_{uu}}\boldsymbol{E} = \boldsymbol{E}\boldsymbol{\Lambda} \tag{2.9}$$

where $\boldsymbol{E}$ is a matrix where the i^{th} column represents the eigenvector $\boldsymbol{e}_i$ and $\boldsymbol{\Lambda}$ is a matrix with the eigenvalues $\{\lambda_i\}$ on the diagonal and zeros elsewhere. If a dynamical modal analysis is performed with the mode matrix composed of the FDEOF eigenvectors (i.e., $\boldsymbol{M} = \boldsymbol{E}$) then $\boldsymbol{f_{aa}}(\omega)$ is simply

$$\boldsymbol{f_{aa}}(\omega) = \boldsymbol{\Lambda} \tag{2.10}$$

using the property that the FDEOF eigenvectors are orthogonal (e.g., $\boldsymbol{M'M} = \mathbf{I}$). Therefore, the modal amplitudes are uncorrelated with each and the spectral densities of the modes are given by the FDEOF eigenvalues.

2.2 Relationships Between Sets of Random Variables

The techniques outlined below are concerned with relationships that exist between sets of random variables. Often this type of analysis is concerned with calculating the proportion of variability in one set of random variables that can be predicted by another set of random variables.

2.2.1 Partial Correlation

The squared correlation between two random variables, x and y, is defined by

$$\rho_{xy}^2 = \frac{\sigma_{xy}^2}{\sigma_x^2 \sigma_y^2}, \tag{2.11}$$

where σ_x^2 and σ_y^2 are the variances of x and y, respectively, and σ_{xy} is the covariance between them. Now consider a third random variable, z which may be correlated with both

x and y. The correlation between x and y, after taking into account their mutual linear relationship with z, is given by the squared *partial correlation* (*Priestley*, 1981):

$$\rho_{xy\cdot z}^2 = \frac{\left(\rho_{xy} - \rho_{xz}\rho_{zy}\right)^2}{\left(1 - \rho_{xz}^2\right)\left(1 - \rho_{zy}^2\right)}. \tag{2.12}$$

The partial correlation measures the correlation between x and y after removing the common influence of z. The equivalent metric in the frequency domain is the *partial coherence* (*Priestley*, 1981).

2.2.2 Multiple Coherence

The squared coherence between two scalar random processes, $\{x_t\}$ and $\{y_t\}$, is defined by

$$\kappa_{yx}^2(\omega) = \frac{\left|f_{yx}(\omega)\right|^2}{f_{xx}(\omega) f_{yy}(\omega)}, \tag{2.13}$$

where f_{xx} and f_{yy} are the power spectra of $\{x_t\}$ and $\{y_t\}$, respectively, and f_{yx} is the associated cross-spectrum (*Priestley*, 1981). Note the similarity between the expressions for coherence and correlation (Equation 2.11).

Given the bivariate random process $\{\boldsymbol{x}_t\}$ where $\boldsymbol{x}_t$ is given by $[x_1 \; x_2]_t$ the coherence between $\{y_t\}$ and both components of $\{\boldsymbol{x}_t\}$ can be calculated using the squared *multiple coherence* (*Priestley*, 1981):

$$\kappa_{y\boldsymbol{x}}^2(\omega) = \frac{\boldsymbol{f}_{y\boldsymbol{x}}(\omega)\boldsymbol{f}_{\boldsymbol{x}\boldsymbol{x}}^{-1}(\omega)\boldsymbol{f}_{y\boldsymbol{x}}^*(\omega)}{f_{yy}(\omega)}, \tag{2.14}$$

where

$$\boldsymbol{f}_{y\boldsymbol{x}}(\omega) = \begin{bmatrix} f_{yx_1}(\omega) & f_{yx_2}(\omega) \end{bmatrix} \quad \boldsymbol{f}_{\boldsymbol{x}\boldsymbol{x}}(\omega) = \begin{bmatrix} f_{x_1x_1}(\omega) & f_{x_1x_2}^*(\omega) \\ f_{x_1x_2}(\omega) & f_{x_2x_2}(\omega) \end{bmatrix}. \tag{2.15}$$

Equation 2.14 generalizes for multivariate $\{\boldsymbol{x}_t\}$. The equivalent metric in the time domain is the *coefficient of determination* for a multiple linear regression model.

2.2.3 Frequency Independent Measures of Fit

The squared coherence, $\kappa_{y\boldsymbol{x}}^2$, measures the proportion of spectral density of $\{y_t\}$ that is accounted for by $\{\boldsymbol{x}_t\}$ as a function of frequency. In some situations it may be more useful to know the proportion of variance of $\{y_t\}$ that is accounted for by $\{\boldsymbol{x}_t\}$, independent of frequency. The variance of $\{y_t\}$ is given by the integral of its spectral density

$$\sigma_y^2 = \int_{-\infty}^{\infty} f_{yy}(\omega) d\omega \tag{2.16}$$

and the variance of $\{y_t\}$ that is accounted for (or predicted) by $\{\boldsymbol{x}_t\}$ using a frequency-dependent linear regression model is given by the integral of the product of its spectral density and the squared coherence with $\{\boldsymbol{x}_t\}$ (*Priestley*, 1981):

$$\sigma_{\mathrm{p}}^2 = \int_{-\infty}^{\infty} \kappa_{y\boldsymbol{x}}^2(\omega) f_{yy}(\omega) d\omega, \tag{2.17}$$

where subscript p denotes *predicted*. It is now straightforward to calculate the proportion of variance in $\{y_t\}$ that is accounted for by $\{\boldsymbol{x}_t\}$:

$$\bar{\kappa}_{y\boldsymbol{x}}^2 = \frac{\sigma_{\mathrm{p}}^2}{\sigma_y^2} = \frac{\displaystyle\int_{-\infty}^{\infty} \kappa_{y\boldsymbol{x}}^2(\omega) f_{yy}(\omega) d\omega}{\displaystyle\int_{-\infty}^{\infty} f_{yy}(\omega) d\omega}, \tag{2.18}$$

which is effectively a weighted average of $\kappa_{y\boldsymbol{x}}^2$ with the weights given by f_{yy}. If $\{\boldsymbol{y}_t\}$ is a bivariate process, the equivalent quantity is given by

$$\bar{\kappa}_{\boldsymbol{y}\boldsymbol{x}} = \frac{\sigma_{\mathrm{p}_1}^2 + \sigma_{\mathrm{p}_2}^2}{\sigma_{y_1}^2 + \sigma_{y_2}^2}, \tag{2.19}$$

where $\sigma_{y_i}^2$ is the variance of $\{y_{i,t}\}$ and $\sigma_{\mathrm{p}_i}^2$ is the variance of $\{y_{i,t}\}$ that is predicted by $\{\boldsymbol{x}_t\}$.

If $\{\boldsymbol{x}_t\}$ is a banded time series (such as the MJO index) the calculation of $\kappa_{y\boldsymbol{x}}^2$ is modified by adding a small constant to $\boldsymbol{f}_{\boldsymbol{xx}}$ (effectively the same as adding a small amount of white noise to the original time series). In this way, $\boldsymbol{f}_{\boldsymbol{xx}}$ is now nonzero outside the banded region ensuring that $\kappa_{\boldsymbol{y}\boldsymbol{x}}^2$ goes to zero at frequencies for which there is little to no energy in $\{\boldsymbol{x}_t\}$ (since $\boldsymbol{f}_{\boldsymbol{xx}}$ appears in the denominator of Equation 2.13). This also allows us to integrate over all frequencies rather than arbitrarily choosing a frequency band of interest (i.e., a range of “MJO frequencies”). In practice, this small constant offset is between one and five percent of the maximum value of $\boldsymbol{f}_{\boldsymbol{xx}}$.

2.2.4 *Assessing Statistical Significance*

For some statistics, such as correlation and coherence, theoretical results for calculating statistical significance are available. For other statistics I have used a pragmatic approach. For example, to assess the statistical significance of an estimated value of $\bar{\kappa}^2_{\boldsymbol{yx}}$ I used the following Monte Carlo technique. "Clone" time series of $\{\boldsymbol{x}_t\}$ are generated with the same mean, variance and spectral density but randomized phases. This is achieved by manipulating and inverting its Fourier transform. Using a large number of cloned $\{\boldsymbol{x}_t\}$, the sampling distribution for $\bar{\kappa}^2_{\boldsymbol{yx}}$ can be approximated under the assumption of no relationship between $\{\boldsymbol{x}_t\}$ and $\{\boldsymbol{y}_t\}$. The value of $\bar{\kappa}^2_{\boldsymbol{yx}}$ for which 95% of the distribution falls below it is taken as the 5% significance level and denoted by $\bar{\kappa}^2_{5\%}$. See Appendix A for a worked example using the MJO index and a time series of sea level from San Diego, USA.

2.3 Autoregressive Models

An autoregressive process is a random process for which the state at any given time depends on the state at previous times plus stochastic forcing. Autoregressive models are often used to fit time series in situations when classical regression models provide a poor representation of the underlying dynamics (*Shumway and Stoffer*, 2000). In this section a forced damped harmonic oscillator will be presented as a differential equation in continuous time. It is then shown how this can be expressed as an autoregressive model and generalized to include autoregressive stochastic forcing. This model is used in Chapter 7 as a model for the MJO index.

2.3.1 *Damped Harmonic Oscillator Model in Continuous Time*

The equation for the state x of a stochastically forced, one dimensional damped harmonic oscillator is

$$\ddot{x} + \alpha_1 \dot{x} + \alpha_2 x = F(t), \tag{2.20}$$

where a dot over a variable indicates a derivative with respect to t and $F(t)$ represents a time-dependent forcing function. Traditionally, $\alpha_1 = 2\beta$ and $\alpha_2 = \omega_0^2$ where β represents the damping coefficient and ω_0 is the natural oscillation frequency (e.g., *Marion and Thornton* (1995)). Equivalently, this can be written as a pair of coupled, first order differential equations:

$$\begin{aligned} \frac{dx}{dt} &= \dot{x} \\ \frac{d\dot{x}}{dt} &= -\alpha_1\dot{x} - \alpha_2 x + F(t). \end{aligned} \tag{2.21}$$

The case of interest is for x and $\dot{x}$ oscillating in quadrature with an exponentially decaying amplitude. This is known as the *underdamped* case and exists for $\alpha_1^2 - 4\alpha_2 < 0$.

2.3.2 Damped Harmonic Oscillator Model in Discrete Time

By discretizing time and making the approximation $dx/dt \simeq (x_{t+1} - x_t)/\Delta t$, it can be shown that a stochastically forced damped harmonic oscillator can be represented in discrete time by an order 2 autoregressive, or AR(2), process (*Priestley*, 1981):

$$x_{t+2} + a_1 x_{t+1} + a_2 x_t = f_{t+2},$$

where $\{f_t\}$ is a forcing process. The relationships between the coefficients for the discrete AR(2) process and the continuous model presented above, are

$$\alpha_1 = -\frac{a_1 + 2a_2}{a_2\Delta t} \quad \alpha_2 = \frac{1 + a_1 + a_2}{a_2\Delta t^2} \quad F(t\Delta t) = \frac{f_t}{a_2\Delta t^2},$$

where Δt is the time step of the discrete process. As above for the continuous problem, the univariate AR(2) process can be written as a bivariate AR(1) process:

$$\boldsymbol{x}_{t+1} = \boldsymbol{A}\boldsymbol{x}_t + \boldsymbol{f}_{t+1}, \tag{2.22}$$

where $\boldsymbol{x}_t$ is the bivariate state vector at time t and $\{\boldsymbol{f}_t\}$ is a forcing process at time t. For an underdamped harmonic oscillator the 2×2 transition matrix can be written

$$\boldsymbol{A} = \gamma \begin{bmatrix} \cos\theta & -\sin\theta \\ \sin\theta & \cos\theta \end{bmatrix} \tag{2.23}$$

where $0 < \gamma < 1$ is the damping coefficient and $\theta \neq 0$ is the rotation rate. The rotation rate θ can be expressed in terms of a rotation period P by writing it as $\theta = 2\pi/P$ and γ can be expressed in terms of a decay time scale τ by writing it in the form $\gamma = \exp(-1/\tau)$, i.e., $\tau = -1/\ln\gamma$.

Note that the transition matrix $\boldsymbol{A}$ is normal (i.e., $\boldsymbol{A}^*\boldsymbol{A} = \boldsymbol{A}\boldsymbol{A}^*$). The normality of $\boldsymbol{A}$ implies that perturbations must decay monotonically to zero (*Farrell and Ioannou*, 1996). As an illustration, the length of $\boldsymbol{x}_t$ for the model described above, under unforced conditions, is given by $|\boldsymbol{x}_{t+k}| = \gamma^k|\boldsymbol{x}_t|$. In continuous time this corresponds to an exponential decay: $|\boldsymbol{x}(t)| = |\boldsymbol{x}(0)|\exp(-t/\tau)$. If $\boldsymbol{A}$ were non-normal, the model although asymptotically stable may support the transient growth of perturbations.

2.3.3 Damped Harmonic Oscillator Model With Autoregressive Forcing

If the oscillator is driven by autoregressive stochastic forcing then it can be represented by the following *quadrivariate* stochastically forced AR(1) model:

$$\boldsymbol{x}_{t+1} = \boldsymbol{A}\boldsymbol{x}_t + \boldsymbol{\varepsilon}_{t+1}, \tag{2.24}$$

where $\boldsymbol{x}_t$ is now a 4×1 state vector at time step t, $\boldsymbol{A}$ is a 4×4 transition matrix that carries the state vector forward one time step, and $\boldsymbol{\varepsilon}_t$ is the 4×1 stochastic noise that drives the system away from a state of rest. The first two components of $\boldsymbol{x}_t$ are taken to represent the oscillator (as described in Section 2.3.2) and the last two components are taken to represent the autoregressive forcing. The transition matrix is of the form

$$\boldsymbol{A} = \begin{bmatrix} \boldsymbol{A}_1 & \mathrm{I} \\ \boldsymbol{0} & \boldsymbol{A}_2 \end{bmatrix} \tag{2.25}$$

where I is a 2×2 identity matrix and

$$\boldsymbol{A}_1 = \gamma_1 \begin{bmatrix} \cos\theta & -\sin\theta \\ \sin\theta & \cos\theta \end{bmatrix}, \qquad \boldsymbol{A}_2 = \gamma_2 \begin{bmatrix} 1 & 0 \\ 0 & 1 \end{bmatrix}. \tag{2.26}$$

In the absence of forcing the oscillator rotates through an angle θ over one time step, and its amplitude is scaled by a factor γ_1. For $\theta \neq 0$, $0 < \gamma_1 < 1$, and $\gamma_2 = 0$ this model reduces to the one presented in Section 2.3.2.

The forcing drives the oscillator away from zero and is modeled by Equation 2.25 as a pair of independent AR(1) processes with autoregressive parameter γ_2. The forcing itself

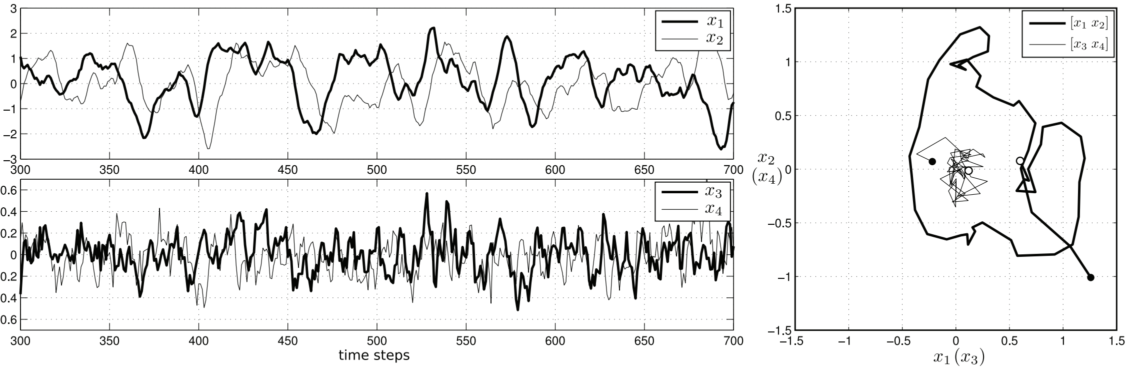

Figure 2.2: Damped harmonic oscillator model in discrete time with autoregressive stochastic forcing. Model parameters are $\tau_1 = 15$, $\tau_2 = 2.5$, and $P = 50$ and the variance of the noise process is $\sigma_\varepsilon^2 = 0.017$. On the left the oscillator components (upper) and the forcing components (lower) of x are plotted for time steps 300 to 700. The first 300 time steps are discarded to avoid transient effects from the initial conditions ($\boldsymbol{x}_0$ =[1,-1,0,0]). On the right, the second oscillator component is plotted against the first oscillator component (thick line) and the second forcing component is plotted against the first forcing component (thin line) for time steps 300 (open circle) to 350 (closed circle).

is driven by an independent white noise process with variance

$$\boldsymbol{\Sigma}_{\boldsymbol{\varepsilon}} = \sigma_\varepsilon^2 \begin{bmatrix} \mathbf{0} & \mathbf{0} \\ \mathbf{0} & \mathrm{I} \end{bmatrix} \tag{2.27}$$

The parameter γ_2 controls the memory of the forcing and it is constrained to be between 0 and 1. It too can be expressed in terms of a decay time scale τ_2 by writing $\gamma_2 = \exp(-1/\tau_2)$.

A realization of $\{\boldsymbol{x}_t\}$ with model parameters $\tau_1 = 15$, $\tau_2 = 2.5$, and $P = 50$ is shown in Figure 2.2. The variance of the noise process is $\sigma_\varepsilon^2 = 0.017$. The oscillator components of $\boldsymbol{x}$ are clearly in quadrature (upper left) and when plotted in phase space (i.e., $\{x_{2,t}\}$ versus $\{x_{1,t}\}$) evidence of counterclockwise rotation and stochastic forcing are clear (right, thick line). By contrast the forcing (third and fourth components of $\boldsymbol{x}$) show very little coherent behaviour in phase space (right, thin lines).

2.3.4 *Statistical Properties of the Damped Harmonic Oscillator Model*

Given the model parameters, it is straightforward to calculate the statistical properties of the damped harmonic oscillator model. First, note that the process is asymptotically stationary to second order with mean zero and covariance matrix $\mathbf{\Sigma}_{\infty}$ that satisfies

$$\mathbf{\Sigma}_{\infty} = \boldsymbol{A}\mathbf{\Sigma}_{\infty}\boldsymbol{A}' + \mathbf{\Sigma}_{\boldsymbol{\varepsilon}}. \tag{2.28}$$

where $'$ denotes transpose. The solution is given explicitly by (e.g., *Harvey* (1991))

$$\mathrm{vec}(\mathbf{\Sigma}_{\infty}) = \left[\mathrm{I} - \boldsymbol{A} \otimes \boldsymbol{A}\right]^{-1} \mathrm{vec}(\mathbf{\Sigma}_{\boldsymbol{\varepsilon}}), \tag{2.29}$$

where vec denotes the vectorization of a matrix by stacking the columns of the matrix on top of one another. The 4×4 cross-spectral density matrix of $\boldsymbol{x_t}$ is given by (*Priestley*, 1981)

$$\boldsymbol{f}_{\boldsymbol{xx}}(\omega) = \left[e^{i\omega}\mathrm{I} - \boldsymbol{A}\right]^{-1} \boldsymbol{f}_{\boldsymbol{\varepsilon\varepsilon}}(\omega) \left[e^{i\omega}\mathrm{I} - \boldsymbol{A}\right]^{*-1}, \tag{2.30}$$

where $*$ denotes the conjugate transpose. If $\{\boldsymbol{\varepsilon}_t\}$ is white noise then $\boldsymbol{f}_{\boldsymbol{\varepsilon\varepsilon}}(\omega)$ is simply $\frac{\sigma_\varepsilon^2}{2\pi}\mathrm{I}$.

For model parameters $P = 50$, $\tau_1 = 15$, $\tau_2 = 2.5$ and noise variance of $\sigma_\varepsilon^2 = 0.017$ the spectral properties of the model (Figure 2.3) demonstrate that the power of the oscillator is confined within a narrow band about the natural oscillation frequency ($2\pi/50$). It is also clear that the oscillator components of $\boldsymbol{x}$ are highly coherent with each other and are in quadrature ($\pi/2$ phase shift).

It is also straightforward to calculate the EOF and FDEOF modes: the eigenvalue problems given by Equations 2.1 and 2.2 using the covariance matrix given by Equation 2.29 and the cross-spectral matrix given by Equation 2.30 are solved. The first two EOF modes each account for 49% of the total variance and the last two account for 1% of the variance each. The eigenvectors for the first two modes are dominated by the first and second components, respectively. This implies that 98% of the variance in $\{\boldsymbol{x}_t\}$ can be accounted for by the first two EOF modes and these two modes roughly correspond to $\{x_{1,t}\}$ and $\{x_{2,t}\}$. Note that the variances of the first two components of $\{\boldsymbol{x}_t\}$ are greater than the last two components and therefore get a higher weighting in the EOF analysis. Note that the results may change for other model parameter choices.

When FDEOF analysis is performed at the central oscillation frequency of $\omega_0 = 2\pi/P$ the first mode alone accounts for 94% of the variability and consists primarily of $\{x_{1,t}\}$ and $\{x_{2,t}\}$ with equal amplitude and a $\pi/2$ phase shift between them as expected. Clearly, the FDEOF analysis is more useful in this case as most of the variability is reduced to a single, oscillating mode. However, if ω_0 is chosen so that it is far from the central

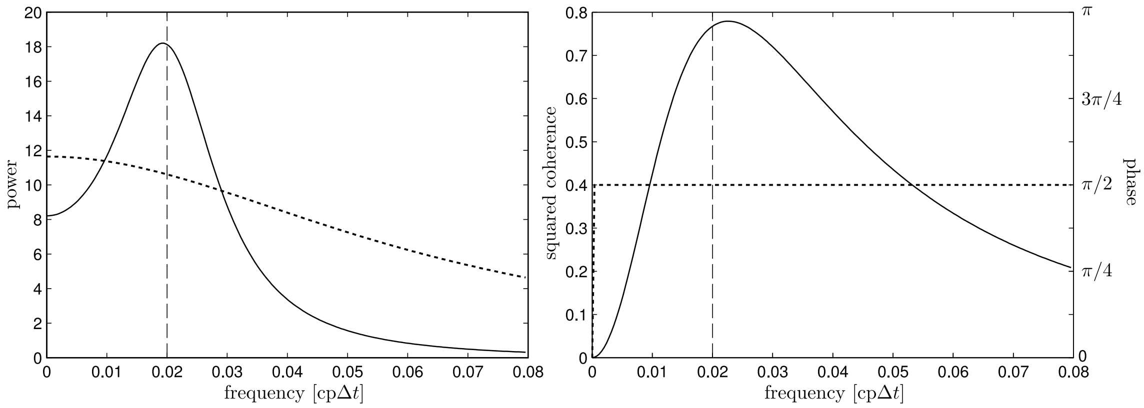

Figure 2.3: Spectral properties of the damped harmonic oscillator model. Model parameters are $\tau_1 = 15$, $\tau_2 = 2.5$, and $P = 50$ and the variance of the noise process is $\sigma_\varepsilon^2 = 0.017$. On the left the power spectral densities of the first oscillator component (solid line) and the first forcing component (dashed line, scaled by a factor of 75) of $\boldsymbol{x}$ are plotted as a function of frequency. On the right, the coherence (solid line) and phase (dashed line) between the two oscillator components of $\boldsymbol{x}$. The dashed vertical lines show the natural oscillation frequency $(2\pi/P)$.

oscillation frequency the partitioning of FDEOF modes becomes less clear as the dynamics are no longer dominated by the resonant oscillation. For example, for $\omega_0 = 0.25 \times 2\pi/P$ or $\omega_0 = 4 \times 2\pi/P$ the first mode still represents an oscillation of $\{x_{1,t}\}$ and $\{x_{2,t}\}$ in quadrature; however, the first mode accounts for only 68% of the variability and the second mode, for which the influence of the stochastic forcing is much stronger, accounts for about 30% of the variability.

CHAPTER 3

OCEAN DYNAMICS AND MODELS

The ocean dynamical theory and related numerical models used in this thesis are outlined below. The equations of motion for an incompressible and inviscid fluid and the separation of solutions into normal modes are presented in Sections 3.1 and 3.2, respectively. The dynamics of tropical ocean waves are presented in Section 3.3. Two numerical models, the Princeton Ocean Model and the Nucleus for European Modelling of the Ocean, are described in Section 3.4 along with the fully nonlinear and viscous equations upon which they are based.

3.1 Equations of Motion

The equations governing an incompressible and inviscid fluid observed with respect to a rotating system of coordinates are (Appendix B)

$$\begin{aligned}
\frac{\partial u}{\partial t} + u\frac{\partial u}{\partial x} + v\frac{\partial u}{\partial y} + w\frac{\partial u}{\partial z} - fv &= -\frac{1}{\rho_0}\frac{\partial p_{\mathrm{P}}}{\partial x} && (3.1)\\
\frac{\partial v}{\partial t} + u\frac{\partial v}{\partial x} + v\frac{\partial v}{\partial y} + w\frac{\partial v}{\partial z} + fu &= -\frac{1}{\rho_0}\frac{\partial p_{\mathrm{P}}}{\partial y} && (3.2)\\
\frac{\partial p}{\partial z} &= -g\rho && (3.3)\\
\frac{\partial u}{\partial x} + \frac{\partial v}{\partial y} + \frac{\partial w}{\partial z} &= 0, && (3.4)
\end{aligned}$$

where $u(x, y, z, t)$, $v(x, y, z, t)$, $w(x, y, z, t)$ are the fluid velocities in the x, y, and z directions respectively, $f(y)$ is the Coriolis parameter, $\rho(x, y, z, t)$ is the fluid density,

$\rho_0(z)$ is the equilibrium fluid density, $p(x, y, z, t)$ is the fluid pressure, $p_{\mathrm{p}}(x, y, z, t)$ is the perturbation fluid pressure, and g is gravitational acceleration. These equations are formulated under the hydrostatic approximation, the Boussinesq approximation, and assuming that horizontal scales of motion are much larger than vertical scales of motion (see Appendix B for more details). Equations 3.1 and 3.2 are known as the *momentum equations*, Equation 3.3 as the *hydrostatic equation*, and Equation 3.4 as the *continuity equation*.

3.2 Vertical Normal Modes

Following *Gill* (1982), solutions to Equations 3.1–3.4 for a continuously stratified fluid, i.e., $\rho_0 = \rho_0(z)$, with a flat bottom can be expressed as a sum of solutions for uniform fluids of various depths. The variability in the vertical is separated from the variability in the horizontal and the solutions are assumed to take the following forms:

$$[u(x,y,z,t), v(x,y,z,t)] = \frac{1}{g\rho(z)} \sum_{m=0}^{\infty} \hat{p}_m(z)[\tilde{u}_m(x,y,t), \tilde{v}_m(x,y,t)] \qquad (3.5)$$

$$w(x,y,z,t) = \sum_{m=0}^{\infty} \hat{h}_m(z)\tilde{w}_m(x,y,t) \qquad (3.6)$$

$$p_{\mathrm{p}}(x,y,z,t) = \sum_{m=0}^{\infty} \hat{p}_m(z)\tilde{\eta}_m(x,y,t) \qquad (3.7)$$

$$h(x,y,z,t) = \sum_{m=0}^{\infty} \hat{h}_m(z)\tilde{\eta}_m(x,y,t) \qquad (3.8)$$

where $h(x, y, z, t)$ represents the vertical displacement of a fluid particle, $\hat{h}_m(z)$ and $\hat{p}_m(z)$ are vertical structure functions, $\tilde{u}_m(x, y, t)$, $\tilde{v}_m(x, y, t)$, $\tilde{w}_m(x, y, t)$ and $\tilde{\eta}_m(x, y, t)$ are solutions in the horizontal.

The vertical structure functions $\hat{h}_m(z)$ and $\hat{p}_m(z)$ are solutions to the pair of Sturm-Liouville equations

$$\frac{d^2\hat{h}_m}{dz^2} + \frac{N^2}{c_m^2}\hat{h}_m = 0 \qquad (3.9)$$

$$\frac{d}{dz}\left(\frac{1}{N^2}\frac{d\hat{p}_m}{dz}\right) + \frac{1}{c_m^2}\hat{p}_m = 0 \qquad (3.10)$$

where $N^2(z)$ is the *buoyancy frequency* defined by

$$N^2 = -\frac{g}{\rho_0}\frac{d\rho_0}{dz}. \tag{3.11}$$

Given a fluid of constant depth and an appropriate set of boundary conditions, Equations 3.9–3.10 yield an infinite sequence of eigenvalues c_m and corresponding eigenfunctions $\hat{h}_m(z)$ and $\hat{p}_m(z)$ for $m = 0, 1, \ldots, \infty$. The eigenfunctions correspond to vertical *normal modes* with the barotropic mode given by $m = 0$ and baroclinic modes by $m \geq 1$.

The solutions in the horizontal $(\tilde{u}_m, \tilde{v}_m, \tilde{\eta}_m)$ are solutions to the *shallow water equations* (Appendix B):

$$\begin{aligned}
\frac{\partial \tilde{u}_m}{\partial t} + \tilde{u}_m\frac{\partial \tilde{u}_m}{\partial x} + \tilde{v}_m\frac{\partial \tilde{u}_m}{\partial y} + \tilde{w}_m\frac{\partial \tilde{u}_m}{\partial z} - f\tilde{v}_m &= -g\frac{\partial \tilde{\eta}_m}{\partial x} && (3.12)\\
\frac{\partial \tilde{v}_m}{\partial t} + \tilde{u}_m\frac{\partial \tilde{v}_m}{\partial x} + \tilde{v}_m\frac{\partial \tilde{v}_m}{\partial y} + \tilde{w}_m\frac{\partial \tilde{v}_m}{\partial z} + f\tilde{u}_m &= -g\frac{\partial \tilde{\eta}_m}{\partial y} && (3.13)\\
\frac{\partial \tilde{\eta}_m}{\partial t} + H_m\left(\frac{\partial \tilde{u}_m}{\partial x} + \frac{\partial \tilde{v}_m}{\partial y}\right) &= 0 && (3.14)
\end{aligned}$$

for a homogeneous fluid with uniform depth H_m, known as the *equivalent depth*, defined by the eigenvalues: $H_m = c_m^2/g$. In addition, the vertical velocity is given by surface boundary condition: $\tilde{w}_m = \partial\tilde{\eta}_m/\partial t$.

3.3 Equatorial Waves

Ocean dynamics predicts several wave types that are trapped about the Equator. The properties of these waves are summarized below.

3.3.1 *Equatorial β-plane*

The Coriolis parameter $f(y)$ varies sinusoidally with latitude. At low latitudes, the equatorial beta plane approximation can be made:

$$f = \beta y \;\text{ where }\; \beta = 2.3 \times 10^{-11}\ \mathrm{m}^{-1}\mathrm{s}^{-1}.$$

In addition, the height of the free surface will be expressed as geopotential height, $\phi = g\eta$, and the linearized shallow water equations, dropping the tildes and subscript m, reduce to

$$\begin{aligned} \frac{\partial u}{\partial t} - \beta y v &= -\frac{\partial \phi}{\partial x} & (3.15) \\ \frac{\partial v}{\partial t} + \beta y u &= -\frac{\partial \phi}{\partial y} & (3.16) \\ \frac{\partial \phi}{\partial t} + c^2 \left(\frac{\partial u}{\partial x} + \frac{\partial v}{\partial y} \right) &= 0, & (3.17) \end{aligned}$$

where $c^2 = gH$ and H is the water depth. It is convenient to non-dimensionalize the equations of motion using a time scale $\sqrt{1/c\beta}$ and a length scale $\sqrt{c/\beta}$, leading to the governing equations

$$\begin{aligned} \frac{\partial u'}{\partial t'} - y'v' &= -\frac{\partial \phi'}{\partial x'} & (3.18) \\ \frac{\partial v'}{\partial t'} + y'u' &= -\frac{\partial \phi'}{\partial y'} & (3.19) \\ \frac{\partial \phi'}{\partial t'} + \frac{\partial u'}{\partial x'} + \frac{\partial v'}{\partial y'} &= 0 & (3.20) \end{aligned}$$

where $'$ denotes a non-dimensionalized variable. These equations predict several distinct types of equatorially trapped ocean waves as detailed below.

3.3.2 Equatorially Trapped Kelvin Waves

Consider the case of no meridional motion, i.e., $v = 0$ and $\partial v/\partial t = 0$. Upon dropping the primes, Equations 3.18–3.20 reduce to

$$\begin{aligned} \frac{\partial u}{\partial t} &= -\frac{\partial \phi}{\partial x} & (3.21) \\ yu &= -\frac{\partial \phi}{\partial y} & (3.22) \\ \frac{\partial \phi}{\partial t} + \frac{\partial u}{\partial x} &= 0. & (3.23) \end{aligned}$$

These equations lead to second order linear wave equations in the x and t dimensions with the structure in the y direction governed by Equation 3.22. The solution is known as an *equatorially trapped Kelvin wave* (*Gill*, 1982) with

$$u = \exp\left(-\frac{y^2}{2}\right) F(x-t) \tag{3.24}$$

$$\phi = \exp\left(-\frac{y^2}{2}\right) F(x-t) \tag{3.25}$$

where $F(x)$ is an arbitrary function. This solution represents an eastward propagating wave, $F(x-t)$, trapped near the equator with a meridional decay scale of $\sqrt{c/2\beta}$ (in dimensional units), also known as the *equatorial radius of deformation*. If sinusoidal wave motion is considered, e.g., $F(x-t) \sim \exp i(kx+\omega t)$, the following Kelvin wave dispersion relationship can be derived[1]:

$$\omega = -k. \tag{3.26}$$

Wavenumber and frequency are linearly related and therefore Kelvin waves are non-dispersive (Figure 3.1). Wave speeds are typically $c \sim 200$ m/s for barotropic waves and $c \sim 0.5-3$ m/s for baroclinic waves (*Gill*, 1982) leading to trapping scales of about 2000 km for the barotropic mode and 100–250 km for the baroclinic modes.

3.3.3 Equatorially Trapped Rossby, Gravity, and Yanai Waves

There are three types of equatorially trapped waves that exist in addition to Kelvin waves. If meridional motion is allowed, Equations 3.18–3.20 (again dropping the primes) can be combined to yield wave equations for each variable such as the following for v (*Gill*, 1982):

$$\frac{\partial}{\partial t}\left(\frac{\partial^2 v}{\partial t^2} + y^2 v - \frac{\partial^2 v}{\partial x^2} - \frac{\partial^2 v}{\partial y^2}\right) - \frac{\partial v}{\partial x} = 0. \tag{3.27}$$

---

[1] In order to be consistent with the formulation of frequency-domain statistics presented in Chapter 2, I have chosen a wave solution of the form $\exp i(kx+\omega t)$. Given a positive frequency, positive wavenumbers represent westward phase speeds and negative wavenumbers represent eastward phase speeds. Therefore, there will be sign differences between the expressions found here and those found in sources such as *LeBlond and Mysak* (1978), *Gill* (1982), or *Pedlosky* (1987) which assume a wave solution of the form $\exp i(kx-\omega t)$. However, this difference does not affect the dynamical properties of the waves that will be discussed.

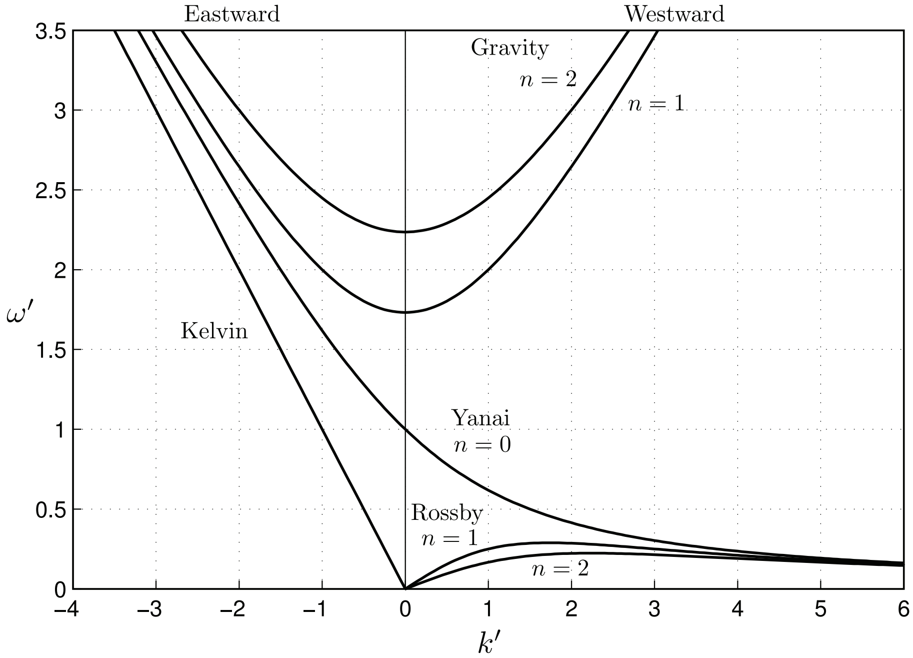

Figure 3.1: Dispersion curves for waves on an equatorial β-plane. Waves have westward phase velocities for $k' > 0$ and eastward phase velocities for $k' < 0$. Waves have westward group velocity for $\partial\omega'/\partial k' > 0$ and a eastward group velocity for $\partial\omega'/\partial k' < 0$. Note that ω' and k' are in nondimensional units (see Section 3.3.1 for time and length scales).

If wave solutions of the form $[u, v, \phi] = [U, V, \Phi] \exp i(kx + \omega t)$ are considered then the following solutions are obtained (*Matsuno*, 1966):

$$U_n = \left[\frac{1}{2}(\omega - k)\mathrm{H}_{n+1}(y) + n(\omega + k)\mathrm{H}_{n-1}(y)\right] G(y) \tag{3.28}$$

$$V_n = i(\omega^2 - k^2)\mathrm{H}_n(y)G(y) \tag{3.29}$$

$$\Phi_n = \left[\frac{1}{2}(\omega - k)\mathrm{H}_{n+1}(y) - n(\omega + k)\mathrm{H}_{n-1}(y)\right] G(y), \tag{3.30}$$

where $G(y) = \exp(-y^2/2)$, H_n is a Hermite polynomial of order n, and n is a non-negative integer which will be referred to as the *meridional mode number*. These solutions form a discrete set of waves with a meridional structure trapped about the equator and strong dependence on n (Figure 3.2). Furthermore, these waves satisfy the following dispersion relation (*Matsuno*, 1966)

$$\omega^2 - k^2 + \frac{k}{\omega} = 2n + 1. \tag{3.31}$$

The three wave types that are governed by Equations 3.28–3.31 are outlined below.

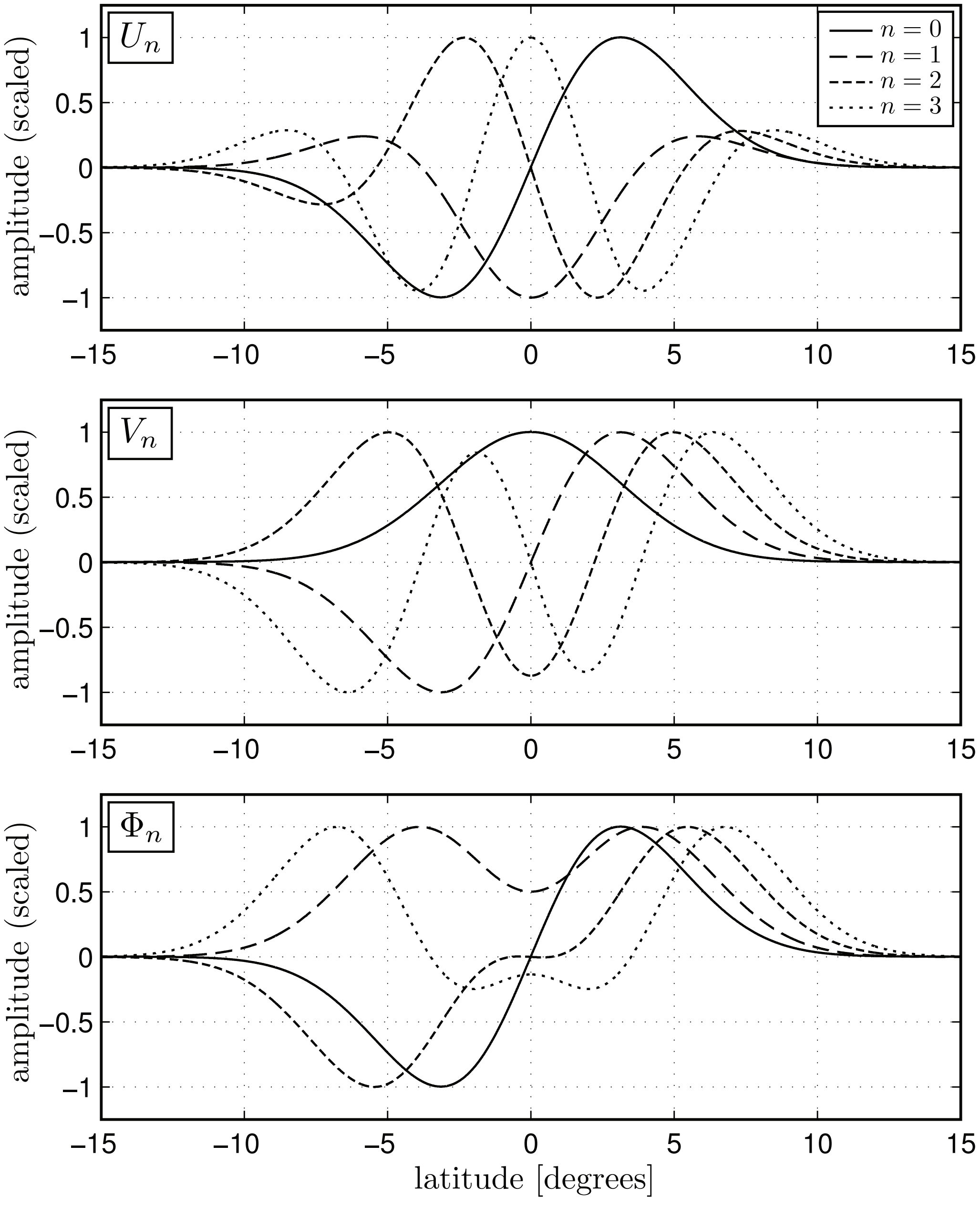

Figure 3.2: Meridional structure of equatorially trapped waves. The latitudinal dependence of the zonal velocity (top), meridional velocity (middle), and geopotential height (bottom) associated with equatorially trapped waves (Equations 3.28–3.30) are shown for $n = 0$ (solid line), $n = 1$ (long-dashed line), $n = 2$ (short-dashed line), and $n = 3$ (dotted line). The calculations have been performed assuming a wave speed of $c_m = 2.8$ m/s. Yanai waves are represented by the $n = 0$ solution; Rossby and Gravity waves are represented by the $n \geq 1$ solutions.

Rossby Waves: For $n \geq 1$ and $\omega^2 \ll 1$ the dispersion relation simplifies to

$$\omega = \frac{k}{k^2 + 2n + 1}. \tag{3.32}$$

Waves that satisfy this relationship are known as equatorially trapped *Rossby waves* or *planetary waves*. This relationship is plotted in Figure 3.1. Rossby waves propagate with a westward phase velocity and can be further subdivided into two categories: (i) long Rossby waves ($k << 1$) carry energy westward and are nearly non-dispersive as the dispersion relationship simplifies to $\omega = -k/(2n+1)$, and (ii) short Rossby waves ($k >> 1$) carry energy eastward and have a much slower phase speed than long Rossby waves.

Gravity Waves: For $n \geq 1$ and $k/\omega \ll 1$ the dispersion relation simplifies to

$$\omega^2 \simeq 2n + 1 + k^2. \tag{3.33}$$

Waves that satisfy this relationship are known as *gravity waves*. Gravity waves can propagate eastward or westward depending on the sign of k (Figure 3.1). Note the distinct frequency gap between Rossby waves and Gravity waves.

Yanai Waves: For $n = 0$ the expressions for U_n, V_n, and Φ_n reduce to (*Matsuno*, 1966)

$$\begin{aligned} U_0 &= 2y \exp\left(-\frac{y^2}{2}\right) && (3.34) \\ V_0 &= 2i(\omega + k) \exp\left(-\frac{y^2}{2}\right) && (3.35) \\ \Phi_0 &= 2y \exp\left(-\frac{y^2}{2}\right) && (3.36) \end{aligned}$$

and the dispersion relationship simplifies to

$$\omega + k - \frac{1}{\omega} = 0. \tag{3.37}$$

These waves are known as *Yanai waves* and can propagate eastward or westward depending on the sign of k but energy always propagates to the east. For large positive k they behave like Rossby waves and for large negative k they behave like gravity waves (Figure 3.1). For this reason they are also known as *mixed Rossby-gravity waves* or *mixed planetary-gravity waves*. At small $|k|$, they, along with Kelvin waves, can exist with frequencies between

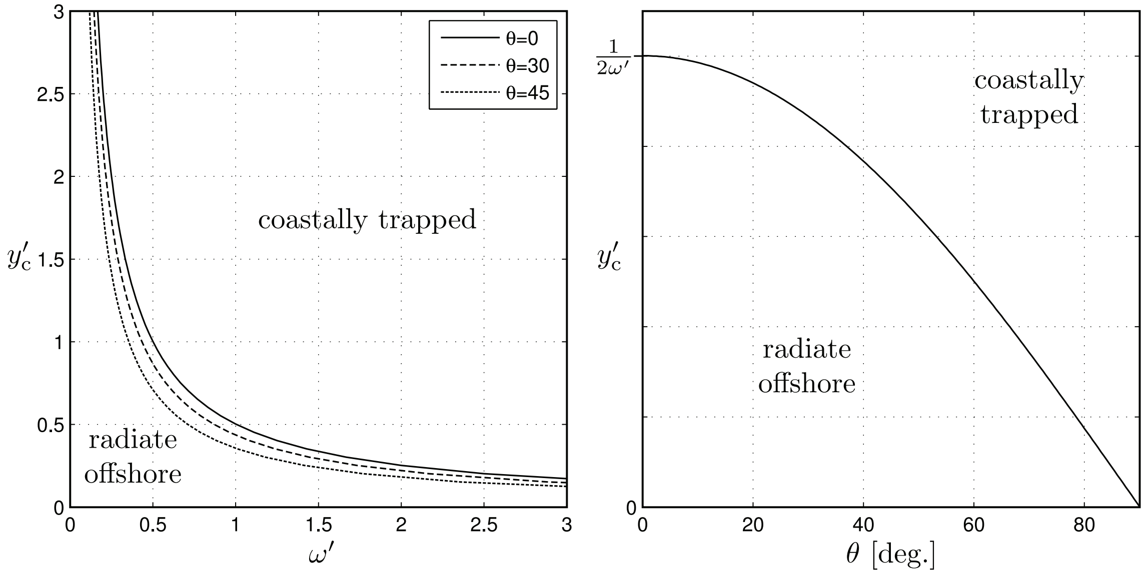

Figure 3.3: Relationship between critical latitude (y_c), frequency (ω), coastline angle (θ), and the behaviour of waves near ocean boundaries. The lines separate the regions of (y, ω) and (y, θ) space which lead to coastally trapped solutions or solutions which radiate offshore. Note that y and ω are in nondimensional units (see Section 3.3.1 for length and time scales).

Rossby waves and Gravity waves.

3.3.4 Reflection and Transmission at an Eastern Boundary

Waves near an eastern boundary can either propagate away from the boundary or remain trapped near the coastline. Near a boundary with angle θ relative to a meridian, a critical latitude y_c can be defined (*Grimshaw and Allen* (1988), *Clarke and Shi* (1991), Appendix C):

$$y_c = \frac{\cos\theta}{2\omega} \tag{3.38}$$

such that waves at frequency ω radiate away from the boundary for latitudes equatorward of y_c and remain trapped to the coastline for latitudes poleward of y_c. The boundary between these solutions, in (y, ω) and (y, θ) space, is illustrated in Figure 3.3. Note that this expression is given in nondimensional units.

In addition, coastline angle plays a significant role in determining the critical latitude. Due to conservation of potential vorticity, the north-south displacement of a fluid particle determines the change in relative vorticity which in turn is responsible for the propagation of Rossby waves (*Gill*, 1982). At latitudes above the critical latitude, the same north-south displacement is not able to produce a change in relative vorticity large enough to become dynamically significant and thus Rossby waves are not radiated away from the boundary (*Clarke and Shi*, 1991). For alongshore wave motions at a given frequency, this north-south displacement is reduced for non-meridional coastlines and thus the critical latitude is more equatorward for more angled coastlines (Figure 3.3).

3.4 Numerical Models

Two general circulation models, which include friction and dissipation as well as evolution equations for temperature and salinity, are used in this thesis and they are described in the following two sections.

3.4.1 Princeton Ocean Model (POM)

The Princeton Ocean Model (POM) was developed in the late 1970s and has since become one of the most well-known ocean models available today (*Blumberg and Mellor*, 1987). POM is simple to use and is applied extensively to simulate regional ocean circulation in coastal areas.

POM is a σ-coordinate model so that the vertical coordinate is scaled by the water column depth (bathymetry plus free surface height), $\sigma = (z - \eta)/(H + \eta)$, so that the vertical coordinate varies between -1 at the bottom and 0 at the surface. This implies that there is a fixed number of vertical σ-levels regardless of the water depth (Figure 3.4, left panel). Figure 3.5 shows how the model variables are laid out on the model grid in the horizontal and vertical. The horizontal arrangement corresponds to an Arakawa C-grid.

The model separates the calculation of the three-dimensional circulation (internal mode) from the calculation of the two-dimensional, depth-independent circulation (external mode). The internal mode integrates discretized versions of the equations of motion (see Section 3.1) as well as additional tracer equations for temperature, salinity, and turbulence kinetic energy. The external mode integrates discretized versions of the shallow water equations (see Appendix B). In both cases additional terms for friction and surface forcing (i.e., surface wind stress) are included. Vertical mixing coefficients are provided by the Mellor-Yamada turbulence closure model (e.g., *Mellor and Yamada* (1982)) and horizontal mixing is calculated using the Smagorinsky parameterization (*Smagorinsky*, 1993).

The model equations are integrated in time using a leap-frog scheme. The time steps

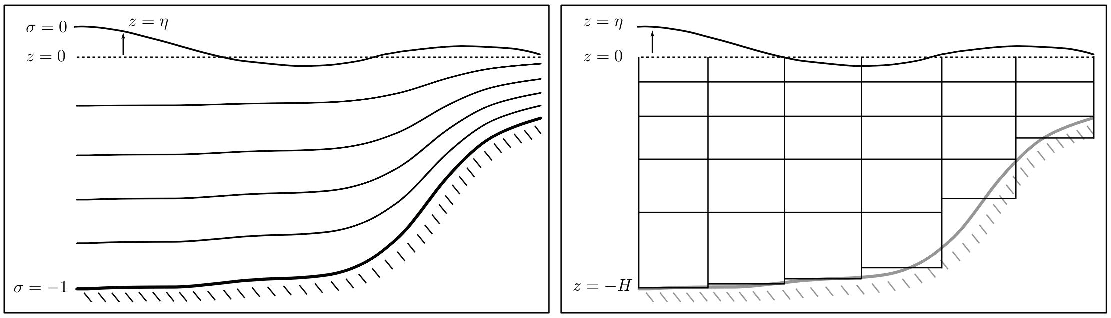

Figure 3.4: Vertical coordinates used in general circulation models: σ-levels (left) and z-levels (right).

for the integration of the discretized equations are subject to the Courant-Friedrichs-Levy (CFL) computational stability condition which is generally much more restrictive for the external mode than for the internal mode (e.g., the time step for the internal mode can be $\sim$10 times larger than the time step for the external mode). Therefore, the external mode undergoes many time steps and only interacts with the internal mode occasionally, to which it provides updates of sea surface height and depth averaged velocities.

3.4.2 Nucleus for European Modelling of the Ocean (NEMO)

The Nucleus for European Modelling of the Ocean (NEMO) is a complete ocean modelling framework (*Madec*, 2008). It includes engines for the dynamics and thermodynamics of the ocean (OPA), the dynamics and thermodynamics of sea-ice (LIM), and biogeochemistry (TOP). It is most usually employed to model the dynamics of the deep ocean, often globally.

The OPA component of NEMO is a complex numerical ocean circulation model. It supports multiple vertical coordinate discretizations but it has been configured here to use z-level coordinates (Figure 3.4, right panel). It follows that the discretization of the vertical coordinate is homogeneous throughout the whole model domain and the number of vertical levels will depend on the ocean depth. In addition, the model allows for *partial steps* so that the thickness of the lowest vertical level is modified based on the depth specified by the input bathymetry. The arrangement of variables on the model grid in the horizontal and vertical is shown in Figure 3.5.

The model simulates the full three-dimensional ocean state. The modeled equations include the horizontal momentum equations (Equations 3.1–3.2), the hydrostatic equation

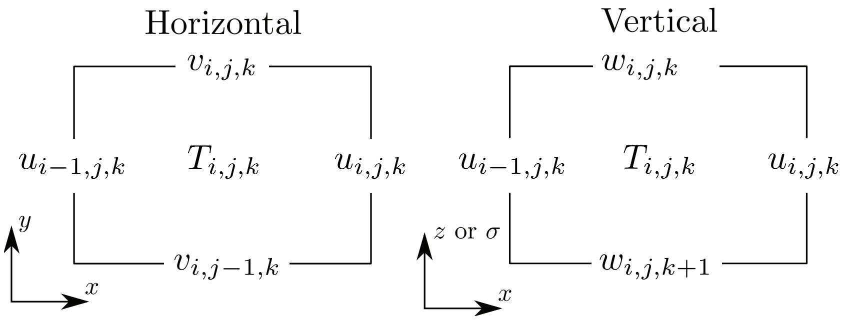

Figure 3.5: Arrangement of ocean variables on model grids (Arakawa C-grid). The left panel shows arrangement in the horizontal and the right panel shows the arrangement in the vertical. Sea surface height is collocated with temperature T at the topmost level.

(Equation 3.3), the continuity equation (Equation 3.4), tracer equations for temperature and salinity, and the thermodynamic equation of state $\rho = \rho(T, S, p)$. The momentum and thermodynamic tracer equations contain surface forcing terms and parameterizations for small scale physics. Vertical mixing is parameterized using a total kinetic energy turbulence closure scheme (*Bougeault and Lacarrere*, 1989; *Gaspar et al.*, 1990; *Madec et al.*, 1998). Details of the parameterization of horizontal diffusion and momentum mixing, including coefficient values, are given in Chapter 6 when the model configuration is described.

The model equations are integrated using a three-level time-stepping scheme:

$$X_{t+\Delta t} = X_{t-\Delta t} + 2\Delta t \mathrm{RHS}^{(X)}_{t-\Delta t,t,t+\Delta t} \tag{3.39}$$

where X stands for u, v, temperature or salinity, RHS$^{(X)}$ is the right-hand side of the corresponding evolution equation, and Δt is the time step. The terms that compose RHS are evaluated at different time steps depending on the physics with which it is associated (*Madec*, 2008).

The model is forced at the surface by zonal and meridional wind, specific humidity, air temperature, precipitation (both solid and liquid), and radiation (both longwave and shortwave). The wind, specific humidity, and air temperature are assumed to be measured at 10 m above the sea surface. The model uses a linear free surface formulation that assumes its height variations are small compared to thickness of the levels and therefore level thicknesses are assumed to be constant in time.

CHAPTER 4

RESPONSE OF THE GLOBAL OCEAN TO THE MADDEN-JULIAN OSCILLATION

4.1 Introduction

Although the strongest effects of the MJO are experienced in the tropics, the MJO does affect atmospheric and oceanic conditions on a global scale. There have been observations of large-scale intraseasonal sea level variability in the extratropics (South Atlantic Ocean, South Indian Ocean, and North Pacific Ocean) which were well correlated with wind stress curl (*Fu*, 2003). This sea level variability was found to be consistent with a basic barotropic vorticity model forced by the global wind field but connections to the MJO were never explored. *Enfield* (1987) used tide gauge data to study intraseasonal oscillations along the Pacific coast of the Americas and *Spillane et al.* (1987) speculated on remote forcing by equatorially trapped waves generated by the MJO. They attributed significant variability to coastally trapped waves that were not obviously forced by local meteorology and were coherent with eastward propagating equatorially trapped waves with periods of about 50 days. This area has continued to be an active area of research (e.g., *Clarke and Ahmed* (1999)).

One goal of the present chapter is to expand on these previous works by including global altimeter observations of sea level. Most studies have focussed on the Pacific Ocean but a few works discuss intraseasonal variability in the Indian Ocean (e.g., *Moore and McCreary*

(1990); *Han et al.* (2001); *Sengupta et al.* (2001); *Iskandar et al.* (2005)). The relevant aspects of these papers are discussed later.

The theory governing the coastal response to low-frequency equatorially trapped Kelvin waves incident upon an eastern boundary includes subtleties worthy of note. There exists a critical latitude, equatorward of which the incident energy is reflected back into the basin as Rossby waves; poleward of this latitude the incident energy is transmitted poleward as propagating coastal trapped waves (e.g., *Grimshaw and Allen* (1988); *Clarke and Shi* (1991); *Clarke* (1992) and Section 3.3.4). For perfectly meridional eastern boundaries, this critical latitude is identical to the turning point associated with Rossby waves in the open ocean (*Cane and Sarachik*, 1981). Furthermore, using the curved coastline metrics of (*Clarke*, 1977), it can be shown that for non-meridional eastern boundaries the critical latitude depends on the orientation of the coastline (e.g., *Clarke and Shi* (1991) and Equation 3.38). This dependence is such that the critical latitude is closer to the equator for more inclined coastlines leading to decreased leakage of Rossby waves and increased flux of energy associated with coastal trapped waves.

The understanding of the dynamics of the MJO at present comes primarily from observations rather than physical principles or models, both of which perform poorly at consistently explaining and predicting the genesis and evolution of the MJO, its interaction with the extratropical atmosphere and coupling with the ocean. Thus at the present time there remains an important role for empirical studies which use statistical techniques to explore the relationship between the MJO and atmospheric and ocean variables.

This chapter focuses on the relationship between the MJO and observed sea level defined on a global grid. Sea level was chosen as the ocean variable of interest for several reasons. First, with the advent of altimeter measurements, it has been continuously mapped on a global scale since 1992 (see *Fu et al.* (1994) and *Cazenave et al.* (2008)). Second, it is a fundamental variable of interest in its own right and also a variable that can be used to infer, for example, changes in quantities like surface geostrophic flow, heat content and wave propagation. Sea level appears in the momentum equations as a gradient term and is thus a natural integrator of ocean dynamics.

In this chapter global sea level is related to the MJO using a scalar metric based on the coherence between the MJO and global sea level averaged across the MJO band. The global perspective allows us to identify regions of the ocean with a particularly strong connection with the MJO. Three such regions are identified: the equatorial Pacific and coastal Americas, the Gulf of Carpentaria and the northeastern Indian Ocean. In a set of regional analyses, frequency dependent statistical techniques are used to isolate and describe the sea level variability in the MJO band and then the results are explained using simple physical principles and concepts (e.g., wind set-up, wave propagation, local and remote forcing).

The chapter is structured as follows. The data are presented in Section 4.2 and the statistical methods used to explore connections between sea level and the MJO, and relationships within the sea level dataset itself, are described in Section 4.3. In Section 4.4 the global connection between the MJO and sea level variability is described followed by regional analyses in Section 4.5. In the last section, modelling experiments are discussed as a means of examining and confirming some of the speculations raised here.

4.2 Data

The Wheeler and Hendon MJO index and global observations of sea level and surface wind are described in this section. Records of observed sea level from tide gauges along the Pacific coast of the Americas are also described.

4.2.1 The Madden-Julian Oscillation

Daily values of Wheeler and Hendon's bivariate MJO index were obtained from the Government of Australia Bureau of Meteorology for the period 1 January 1974 to 31 December 2007[1]. Most of the energy of the MJO has periods between 30 and 90 days, making it a quasi-periodic phenomenon. This frequency band will be referred to as the MJO band. The MJO index is based on the first two principal components from an empirical orthogonal function analysis of tropical outgoing longwave radiation and zonal winds after removing seasonal and interannual signals (*Wheeler and Hendon*, 2004). The two indices describe a propagating phenomenon and are approximately in quadrature.

4.2.2 Global Observations of Sea Level

Global fields of satellite-based altimeter measurements of isostatically adjusted sea level anomalies were obtained from Aviso[2]. Weekly data are available on a 1/4° resolution

---

[1] `http://www.bom.gov.au/bmrc/clfor/cfstaff/matw/maproom/RMM/index.htm`

[2] `http://www.aviso.oceanobs.com/en/home/index.html`

grid for the period 14 October 1992 to 12 May 2007. Because the memory requirements of the regional analyses performed in Section 4.5 scale as the square of the number of locations, the data were further processed by spatially averaging to produce a dataset with a resolution of 1° (each 4 by 4 block of adjacent points were averaged with equal weights) for these analyses. For both the 1/4° and 1° datasets, time series of anomalies for each spatial grid point were generated by filtering the data using a third order, highpass Butterworth filter with a cutoff period of 120 days. The anomalies are denoted η'_{a}. Note that η'_{a} has had all interannual variability as well as the annual cycle and its first harmonic removed by the filter.

4.2.3 Coastal Observations of Sea Level

Measurements of coastal sea level by tide gauges were used to supplement the satellite-based observations. The altimeter does not resolve the coastal sea level well within about 25 km of the coast. Given this limitation, the tide gauge data complement well the observations made by the altimeter. Daily time series were obtained for thirteen tide gauges along the coast of the Americas (seven south and six north of the equator, for more details see Section 4.5.1) from the University of Hawai‘i Sea Level Center[3]. Tides have been removed by the University of Hawai‘i Sea Level Center. Weekly means were generated from this dataset, in order to match the time step of the altimeter data, for the period 23 December 1998 to 14 October 2002. (Gaps of missing data shorter than 20 days were interpolated.) Measurements of sea level pressure, obtained from the NCEP/NCAR Reanalysis[4] and interpolated to the locations of the tide gauges, were used to remove the inverse barometer effect. The tide gauge data were then highpass filtered as above. The highpass filtered and isostatically adjusted coastal sea level anomalies are denoted by η'_{c}.

4.2.4 Global Observations of Surface Wind

Global fields of zonal and meridional surface (10 m) winds were obtained from the NCEP/DOE Reanalysis 2 (*Kanamitsu et al.*, 2002). Daily fields of global data on a T62 grid were available from 1979 to 2008 inclusive. In order to facilitate cross-spectral analysis with η'_{a} the wind data were output as weekly averages and anomalies were generated by highpass filtering as above.

---

[3] `http://uhslc.soest.hawaii.edu/`

[4] `http://www.cdc.noaa.gov/cdc/data.ncep.reanalysis.html`

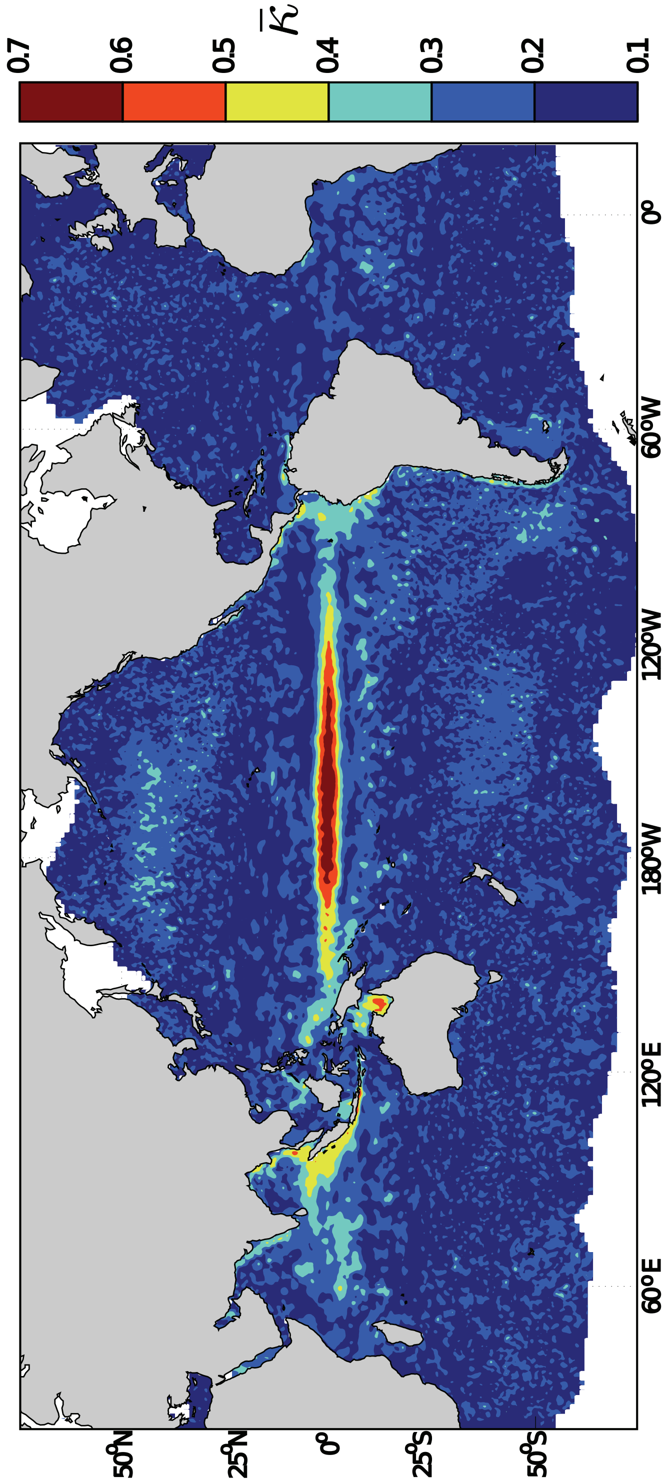

Figure 4.1: Global map of the proportion of global sea level variability related to the MJO. Filled contours show $\bar{\kappa}$, the proportion of the standard deviation of η'_{a} accounted for by the MJO. The 5% significance level is $\bar{\kappa}_{5\%} \sim 0.3$. Regional blowups of this map are shown in Figure 4.4 (west coast of the Americas), Figure 5.5 (Gulf of Carpentaria), and Figure 6.4 (northeastern Indian Ocean).

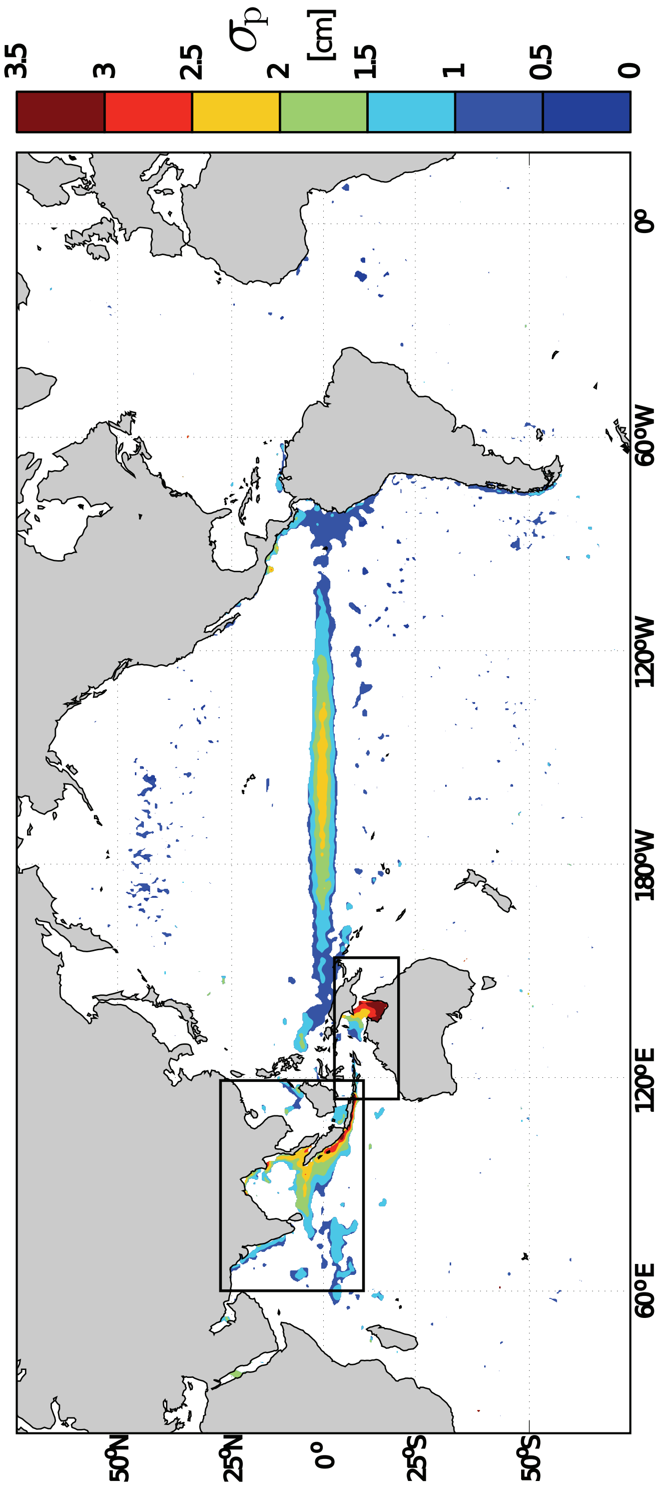

Figure 4.2: Global map of the amount of global sea level variability related to the MJO. Filled contours show σ_p, the magnitude of the standard deviation of η'_a accounted for by the MJO. The quantity σ_p is only shown for regions where $\bar{\kappa} > \bar{\kappa}_{5\%}$. The boxes show the study regions examined in Sections 4.5.2 and 4.5.3.

4.3 Statistical Methods

Two different statistical methods are used to analyze the sea level observations. The first method relates the sea level to the MJO and the second method looks at relationships within the sea level data set. The advantage of the first method is that it uses the MJO index as a surrogate forcing term thus allowing us to explore links between the response (sea level at a specific grid point) and the forcing (MJO). A drawback of using a single index to characterize the MJO is that it has no information on the spatial variability of the MJO. In order to assess the spatial dependence of intraseasonal sea level variability associated with the MJO the above technique is supplemented by looking for modes of variability within the sea level dataset in the MJO band.

4.3.1 Relationships Between Sea Level and the MJO

Given a time series of interest, such as η'_{a} at a particular grid point, how can its relationship with the MJO be quantified? It is possible to explore the relationship between η'_{a} and the MJO by compositing based on phase and strength of the MJO (*e.g.*, *Hall et al.* (2001); *Wheeler and Hendon* (2004); *Vecchi and Bond* (2004)). One of the strengths of such an approach is that it allows nonlinear relationships to be resolved. However, compositing of sea level with the MJO index (not shown) has indicated that the assumption of a linear relationship between these variables is reasonable and so traditional time series techniques (*e.g.*, spectral analysis, regression) are used in this study to explore the relationship between sea level and the MJO.

A simple metric was developed to quantify the strength of the relationship between sea level variability and the Madden-Julian Oscillation. It represents the ratio of the variance in η'_{a} predicted by the MJO (σ^2_{p}) to the total observed variance in η'_{a} (σ^2_{o}):

$$\bar{\kappa}^2 = \frac{\sigma^2_{\mathrm{p}}}{\sigma^2_{\mathrm{o}}} = \frac{\int \kappa^2(\omega) f(\omega) d\omega}{\int f(\omega) d\omega}, \tag{4.1}$$

where κ^2 is the multiple coherence squared between η'_{a} and the bivariate MJO index and f is the power spectrum of η'_{a}. The total observed variance is defined as the integral over f and the predicted variance is the integral over the product of f and κ^2. This statistic is discussed in Section 2.2.3.

The $\bar{\kappa}^2$ statistic reduces the coherency spectra to a scalar value at each spatial point and has the additional useful property that it lies between zero and unity. Similar to coherence, a value of zero implies no relationship (no sea level variance is predicted by the MJO) and a value of unity implies a perfect linear relationship (all the variance is predicted by the MJO). This metric is more general than a correlation because it allows linear relationships to be found between broad-banded time series even when they are in quadrature (in which case the correlation would be zero).

From the practical standpoint of prediction a large $\bar{\kappa}$ is not useful unless the predicted response is significant as well. Thus the quantity σ_p, which is the standard deviation of η'_a predicted by the MJO, is used to assess practical significance. Regions where both quantities are large have a significant implied connection with the MJO. The statistical significance of $\bar{\kappa}$ is assessed using a Monte Carlo method to generate a sample distribution of $\bar{\kappa}$ under the assumption of no relationship with the MJO (see Section 2.2.4 and Appendix A).

4.3.2 Modes of Sea Level Variability in the MJO Band

Relationships within a spatially distributed dataset can be assessed using frequency dependent empirical orthogonal function (FDEOF) analysis (*e.g.*, *Wallace and Dickinson* (1972); *Brillinger* (2001); Section 2.1.2). This technique allows us to determine the presence of propagating or standing waves within a narrow band of frequencies. This analysis yields a set of complex, frequency-dependent modes which specify the spatial patterns of magnitude and phase relationships within each mode.

4.4 Global Response of Sea Level to the MJO

The global maps of $\bar{\kappa}$ and σ_p for η'_a are shown in Figures 4.1 and 4.2. The ocean shows a statistically significant response of sea level to the MJO across the Equatorial Pacific ($\bar{\kappa} \sim 0.4 - 0.7$), an intermediate response along coastlines ($\bar{\kappa} \sim 0.3 - 0.5$) and a weaker but large scale response in the central North and South Pacific ($\bar{\kappa} < 0.3$). One of the most notable features is that a much higher fraction of the coastal response is explained by the MJO along the western coastlines than along the eastern coastlines of each landmass (most obvious along the coasts of Sumatra and the Malay Peninsula). This coastal response is strongest along the Maritime Continent ($\bar{\kappa} \sim 0.5$), followed by the Americas ($\bar{\kappa} \sim 0.3 - 0.5$) and weakest along the coast of west Africa ($\bar{\kappa} < 0.3$). This is consistent with the understanding of the MJO as an eastward propagating phenomenon which originates, and is strongest, in the vicinity of the Indian Ocean.

The map of σ_p (Figure 4.2) is masked according to statistical significance of $\bar{\kappa}$. From this map several major regions with large $\bar{\kappa}$ and σ_p can be identified. First, there is a band along the Equatorial Pacific. This region has been treated in detail by *Zhang et al.* (2009). A second region is identified in the northeastern Indian Ocean and includes a complex array of features including coastal responses along Sumatra, the Bay of Bengal and the west coast of the Indian subcontinent as well strong signals in the central part of the ocean. A third region covers the Gulf of Carpentaria and the nearby Arafura and Timor Seas, between Australia and New Guinea. Finally, a fourth region is the Pacific coast of the Americas, especially near Central America and tropical South America but also extending to the extratropics along the coast of Chile. As noted above, the altimeter does not resolve the signal near the coast very well in the extratropics. However, the coastal Americas form a continuous waveguide based on the strong tropical signal, the strong signal near Chile, and the work of previous authors (*Enfield*, 1987; *Spillane et al.*, 1987; *Clarke and Ahmed*, 1999).

Coherence of sea level with the MJO at the selected regions is quantified in Figure 4.3. The Equatorial Pacific and coastal Americas are combined into one region. For the Equatorial Pacific coastal Americas region both η'_a and η'_c are used; for the Gulf of Carpenta and northeastern Indian Ocean only η'_a is used. The η'_c series were recorded at the coastal tide gauge locations shown in Figure 4.4 (the exact locations, along with information on time span and completeness, are given in Table 4.1). Each region shows a peak at a period of about 75 days which suggests that the same large-scale atmospheric forcing may be responsible for driving the variability observed in each region.

4.5 Regional Responses of Sea Level to the MJO

The following subsections describe the sea level variability in the three regions mentioned in Section 4.4 and explain it in terms of simple physical processes.

4.5.1 The Equatorial Pacific and Coastal American Waveguides

Figure 4.4 shows a map of $\bar{\kappa}$ focusing on the eastern equatorial Pacific and the coastal Americas between 50°N and 50°S. There are indications that the sea level response reaches into the extratropics (with decaying magnitude and zonal extent in the poleward direction).

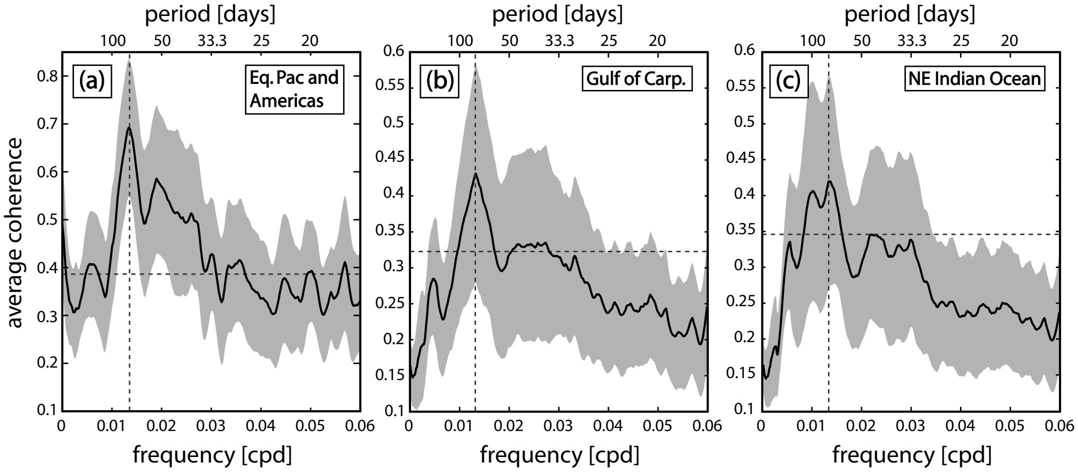

Figure 4.3: Coherence between the MJO and sea level for three regions. The continuous line is the coherence between regional sea level time series and the MJO index averaged over the following regions: (a) the Pacific-Americas waveguide, (b) the Gulf of Carpentaria, and (c) Northeastern Indian Ocean (the latter two regions are defined by the boxes in Figure 4.2). For each region there is clear maximum at about a period of 75 days (shown by a vertical dashed line) which is used as the frequency for the subsequent FDEOF analysis. The grey band indicates the standard deviation of coherence values within a region. The dashed line shows the 5% significance level based on an individual calculation of coherence. "cpd" denotes cycles per day.

Name	Latitude	Longitude	% Complete
San Francisco	37°48'N	122°28'W	100
Monterey	36°36'N	121°53'W	99.3
Los Angeles	33°43'N	118°16'W	100
San Diego	32°42'N	117°10'W	99.8
Acajutla	13°35'N	89°50'W	99.2
Armuelles	6°16'N	82°52'W	99.9
La Libertad	2°12'S	80°55'W	99.4
Lobos	5°56'S	80°43'W	99.6
Callau	12°3'S	77°9'W	99.7
Arica	18°28'S	70°20'W	99.9
Antofagasta	23°39'S	70°24'W	94.6
Caldera	27°4'S	70°50'W	99.5
Valparaiso	33°2'S	71°38'W	98.4

Table 4.1: Details on the tide gauge records. The completeness percentage is over the common period from 23 December 1998 to 14 October 2002.

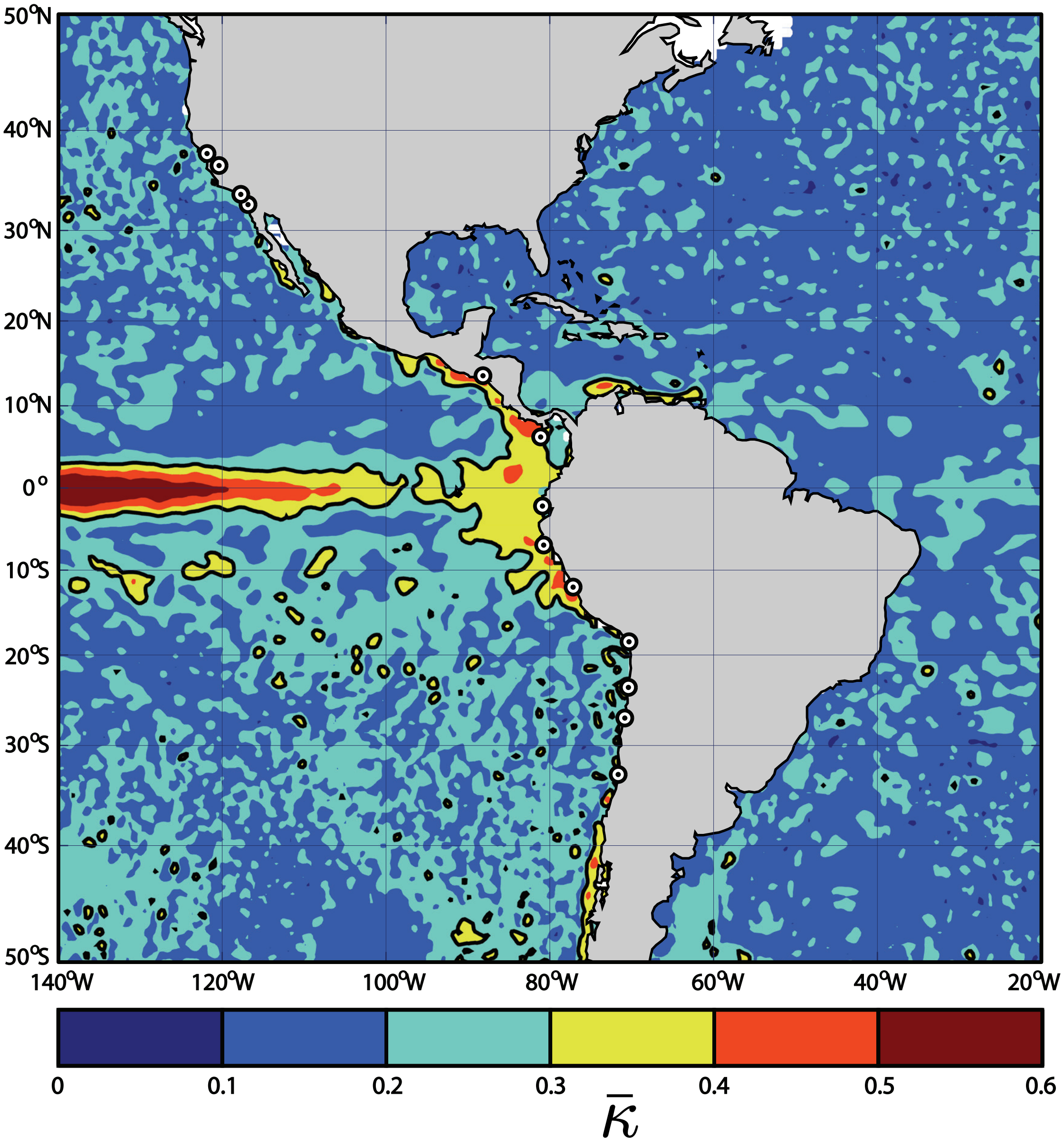

Figure 4.4: Proportion of sea level variability measured by altimeters accounted for by the MJO near the Americas (a regional blowup of Figure 4.1) . $\bar{\kappa}$ represents the fraction of standard deviation of η'_{a} predicted by the MJO. The 5% significance level (see Section 2.2.4) is $\bar{\kappa}_{5\%} \sim 0.3$ and is denoted by the black contour. The dots show the locations of the coastal tide gauges providing records of η'_{c} (see Table 4.1 for detail on each tide gauge).

A possible physical explanation is that the atmospheric component of the MJO generates equatorially trapped waves in the western Pacific which propagate eastward along the equator before reaching the coastal boundary at which point the energy is reflected as Rossby waves at low latitudes and transferred to poleward propagating coastally trapped waves at higher latitudes (*Spillane et al.*, 1987; *Clarke and Ahmed*, 1999). For the Americas on intraseasonal timescales, this critical latitude occurs between 8.5° and 11° from the equator (calculated following *Clarke and Shi* (1991), see Section 3.3.4). These latitudes are consistent with the region of significant seaward extend of $\bar{\kappa}$ in the tropics off the coast of the Americas. Also, the poleward reduction in seaward extent is consistent with internal Rossby radius of deformation which decreases poleward and defines the length scale for coastal trapping.

A FDEOF analysis was performed on η'_{a} and η'_{c} to test the theory that the coastal response is related to waves travelling along the equator and coastlines. The η'_{a} series were recorded at 25 equally spaced points along the equator from 155°E to 85°W, and 44 near coastal points along the coast of the Americas from 45°S to 44°N (equally spaced in latitude). Note that the tide gauge data were made into weekly averages and that the time span η'_{a} was shortened to match that of η'_{c} (23 December 1998 to 14 October 2002). The time series were also scaled so that the total variance of the equatorial set is equal to the total variance of the coastal set. This ensures that both the equatorial signal and the coastal signal are weighted equally in the statistical analysis.

The proportion of spectral density accounted for by the first twenty FDEOF modes is shown in Figure 4.5. This analysis was performed at a frequency corresponding to a period of about 75 days which is the location of the peak in coherence between sea level and the MJO (Figure 4.3a). The first mode accounts for approximately two-thirds of the total spectral density (defined as the trace of the cross-spectral matrix) and the higher order modes add less than 10% each.

Figure 4.6 shows the first mode from the FDEOF analysis. The upper panel shows the magnitude of this mode (absolute value of the elements of $\boldsymbol{e}_i$, see Section 2.1.2) and the lower panel shows the time delay of the mode (derived from the phase of the elements of $\boldsymbol{e}_i$) as functions of "distance" along the waveguides (i.e., the equatorial waveguide and the coastal waveguide). Distance was calculated along two paths: both run along the equator but split into north and south paths at the coastal boundary. This division into two paths is

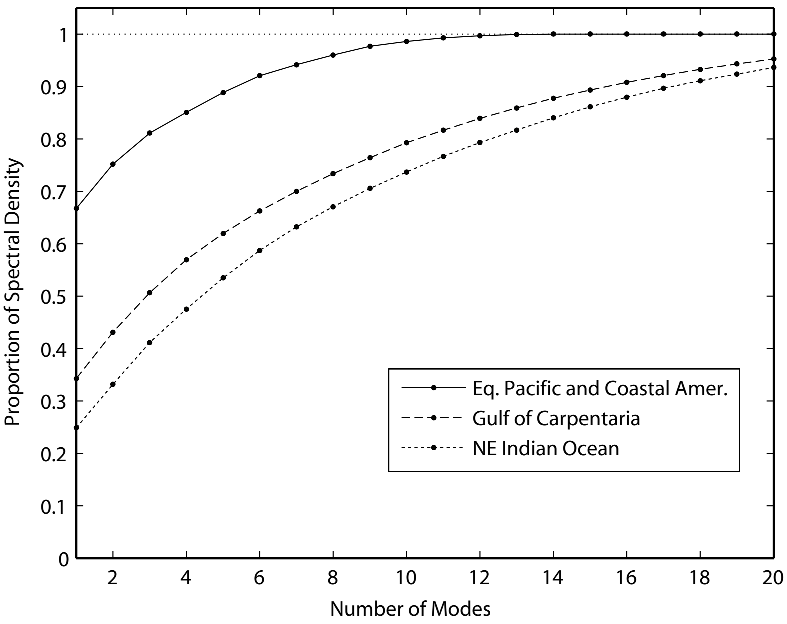

Figure 4.5: Total spectral density of sea level accounted for by the FDEOF as a function of the number of FDEOF modes included. The vertical axis is the fraction of the spectral density at a 75 day period accounted for by the FDEOF modes and the horizontal axis represents the number of modes included.

performed under the assumption that some energy will travel north and some will travel south once the equatorially trapped energy reaches the coastal boundary thus splitting the energy along two paths. The time delay was calculated from the phase of the eigenvector elements and the timescale of 75 days (the most westerly station is assumed to be $t = 0$).

The time delays shown in Figure 4.6 are consistent with a response propagating eastwards along the equator which excites coastally trapped waves that move poleward along the coast of the Americas. From the linear regression of phase lag on distance the equatorial wave is estimated to have a speed of 2.6 ± 0.1 ms^{-1} which is consistent with the first baroclinic mode of equatorially trapped oceanic Kelvin waves (*Gill* (1982); *Hendon et al.* (1998); *Zhang et al.* (2009), see Section 3.3.2). The coastal waves have speeds of 5.6 ± 2.8 ms^{-1} (northern hemisphere) and 3.3 ± 0.6 ms^{-1} (southern hemisphere). Error bounds were determined from the distribution of linear fit parameters based on 300 fits using bootstrap resampling (300 was sufficiently large to give stable results upon repetition).

The speeds found here are similar to those found by *Brink* (1982) who developed a semi-theoretical model for free, coastally trapped long waves (with periods from a few days up to 20 days). The estimated wave speed along the coast of South America is also consistent with the speed obtained from the model developed in *Clarke and Ahmed* (1999). The amplitude increases slightly with distance eastward along the equator. According to theory, the sea level amplitude of the coastal trapped wave should increase as $\sqrt{|f|}$ due to flux conservation (*Clarke*, 1992), substantially less so if the effects of topography and friction are included *Clarke and Ahmed* (1999). However, along the coastal boundaries the amplitude has too much scatter to make a definitive conclusion as to the trend. As discussed previously, outside the tropics the sea level signals within a Rossby radius from the coast are not well resolved by the altimeter measurements. This may explain the large amount of scatter in the mid- and high latitude altimeter points in the delay of the mode (Figure 4.6). It may be possible to obtain a more accurate measure of wave speed by omitting the altimeter data at higher latitudes but the small number of points would make the sample size too small to give much confidence in the results.

Intraseasonal coastal trapped waves along the coast of the Americas were studied by *Spillane et al.* (1987). They examined relationships between time series of sea level height from coastal tide gauges. *Spillane et al.* (1987) found a coherent wave with a period between 47 and 58 days travelling poleward from the equator to 55°N and 15°S. Over the range 10°N to 40°N the wave has a nearly constant speed of $\sim$1.7 ms^{-1} which is slower that the speed estimated here (although the wave has a different timescale). A follow-up study examined possible forcing in the equatorial Pacific ocean (*Enfield*, 1987) and found that there is a coherent wave that travels along the equatorial Pacific and the coast of the Americas. They concluded that the forcing occurred remotely in the western Pacific. The analysis performed here expands on the work of *Enfield* (1987) and *Spillane et al.* (1987) by including satellite-based measurements of sea level in addition to tide gauges and by making a statistical connection with the MJO which is treated as a surrogate for forcing.

4.5.2 Gulf of Carpentaria

In order to explain the high values of $\bar{\kappa}$ in the Gulf of Carpentaria, the FDEOF technique is applied to sea level measured from altimeters within a region surrounding northern Australia (see box in Figure 4.2). The period of the FDEOF analysis is 75 days (see Figure 4.3b).

The first mode accounts for 34% of the total spectral density (see Figure 4.5). Maps showing the cyclic evolution of the first mode are given in Figure 4.7. This mode describes

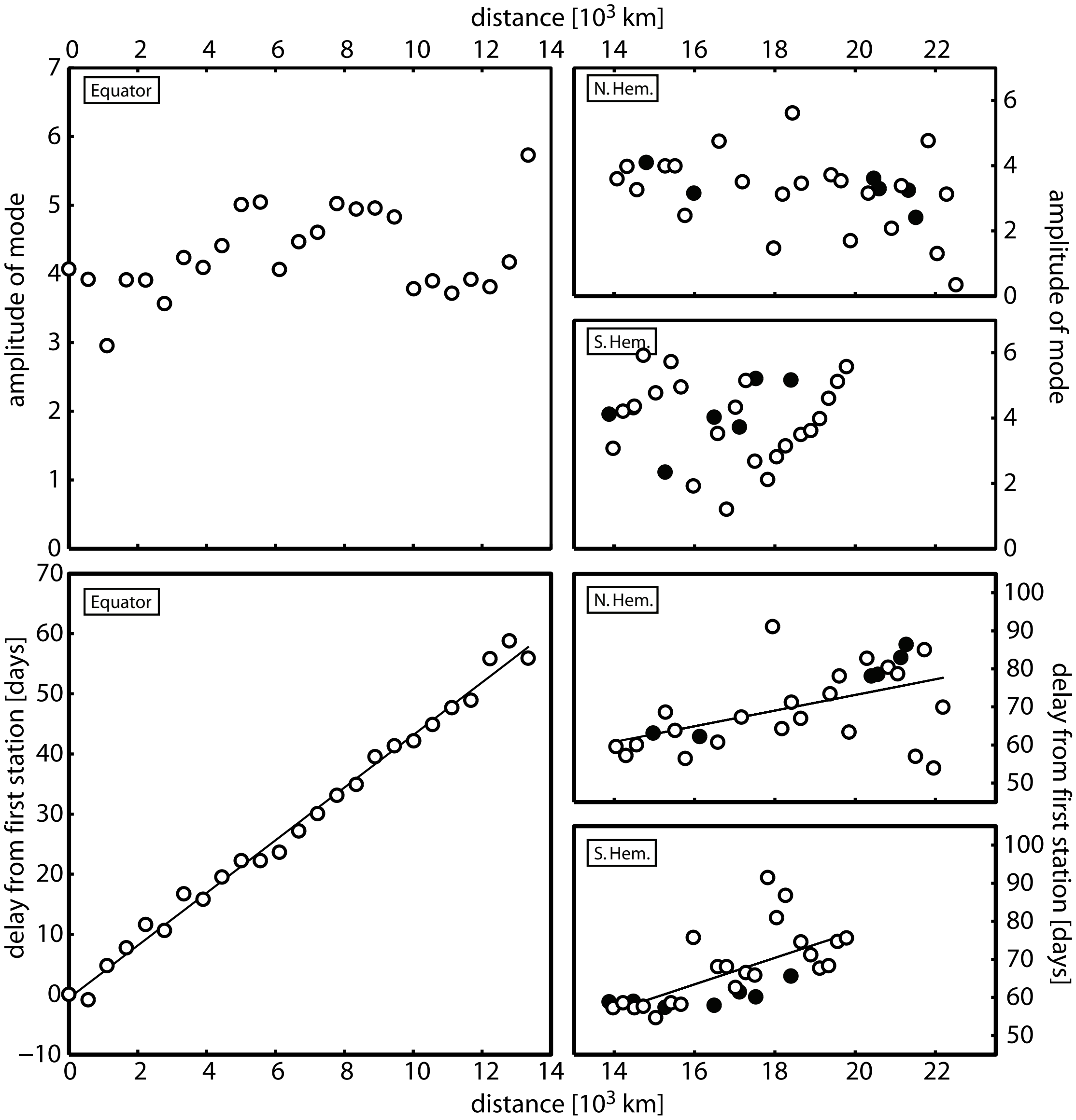

Figure 4.6: The first mode of the FDEOF analysis of sea level from the Pacific-Americas waveguide at a period of 75 days. The magnitude of response is shown in upper panels and time delay from first station in lower panels. Open circles represent satellite data and filled circles represent tide gauge data. The equator, northern hemisphere coast and southern hemisphere coast are split for visual clarity. The lines on the lower panels represent linear regressions with slopes representing wave speeds of 2.6 ± 0.1 ms^{-1} (equator), 5.6 ± 2.8 ms^{-1} (N. Hemisphere) and 3.3 ± 0.6 ms^{-1} (S. Hemisphere).

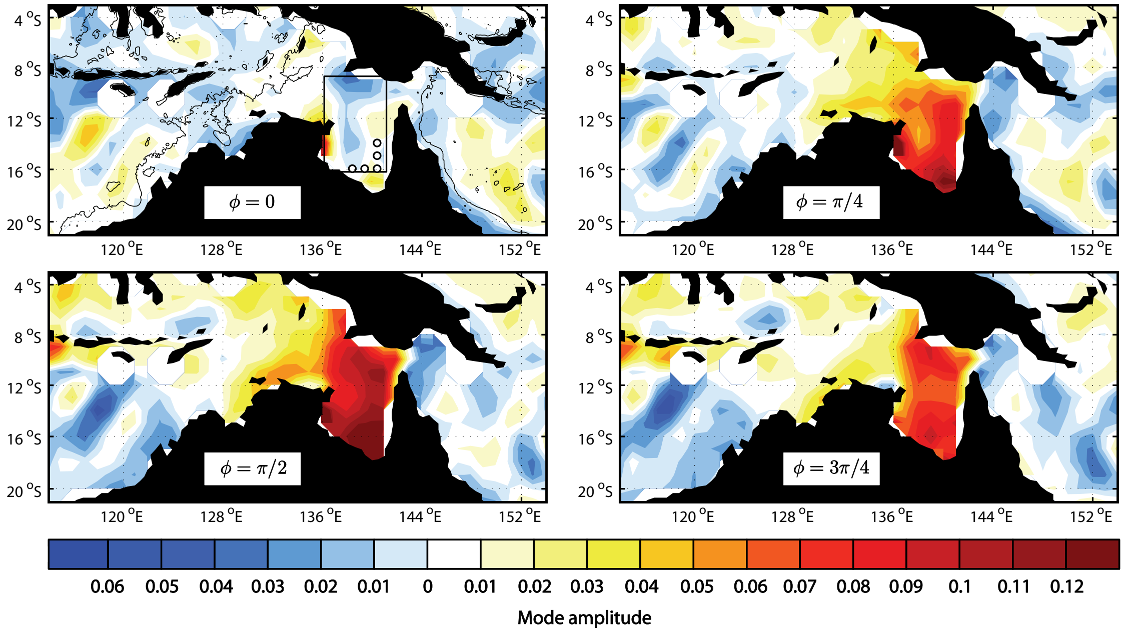

Figure 4.7: Maps of the first FDEOF mode in the Gulf of Carpentaria region for one half of its cycle (in $\pi/4$ radian steps). The complete cycle can be constructed by repeating these snapshots with positive and negative values switched. The mode is dominated by a standing wave in the Gulf of Carpentaria as well as smaller amplitude travelling waves to the east and west of Australia. Note that given the period of the mode is 75 days, the above sequence has a time range of 32.5 days. In order to show the shallow waters of the Gulf of Carpentaria and the Arafura and Timor Seas a thin black line representing the 100 m bathymetric contour is shown in the first panel. The box shows the region for the wind field (8.75°S to 16.25°S and 136.25°E to 141.5°E) and the circles show the locations of sea level time series used in the set-up analysis ([16°S,138.5°E], [16°S,139.5°E], [16°S,140.5°E], [15°S,140.5°E] and [14°S,140.5°E]).

a standing wave in the relatively shallow Gulf of Carpentaria and nearby Arafura and Timor Seas to the west (see the first panel of Figure 4.7). Weaker progressive waves are also evident in the deeper water off the northwestern and northeastern Australian coasts.

The standing wave may be due to the effect of wind set-up over the shallow waters noted above. To explore this possibility the sea level variability at the head of the Gulf of Carpentaria is examined. Sea level at the head of the Gulf (the southeastern end), η_{H}, is taken as the average of the five points whose locations are depicted in the first panel of Figure 4.7. A plot of this time series over a 6-year time period is shown in Figure 4.8. The upper panel shows η_{H}. Variations on the order of 60 cm, including a strong seasonal cycle, are observed. The middle panel shows the same data after removing the seasonal

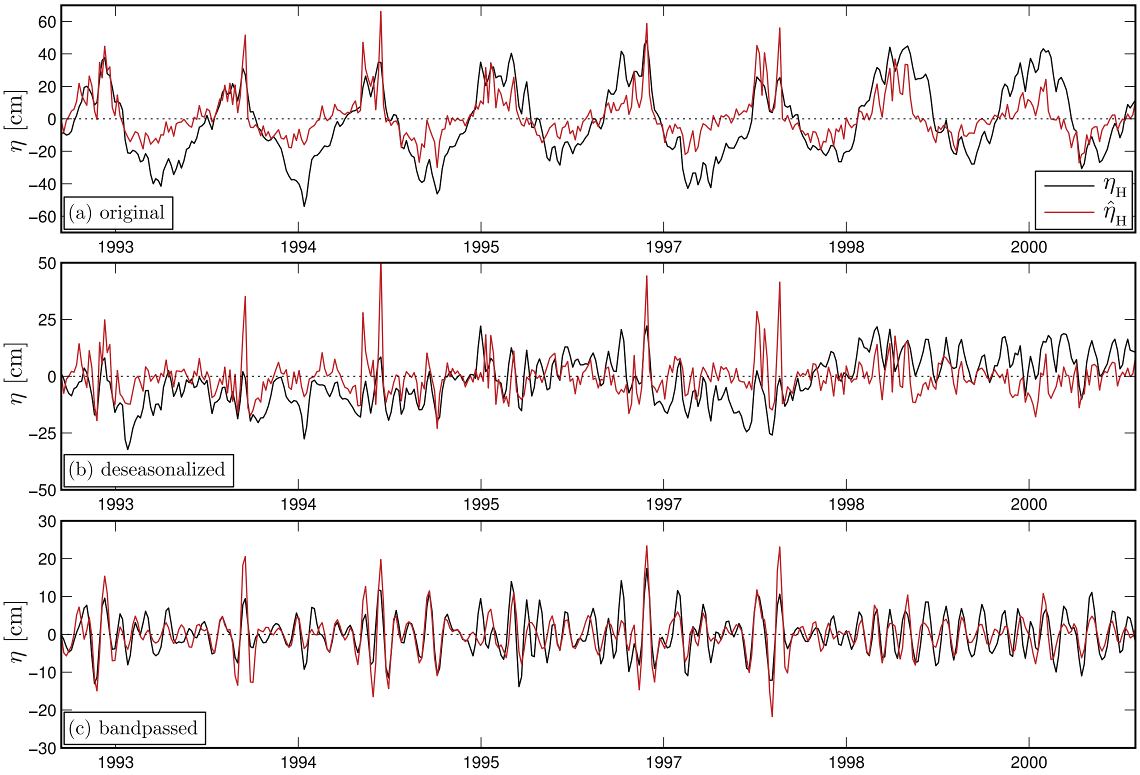

Figure 4.8: Sea level and local wind set-up in the Gulf of Carpentaria. The sea level anomaly at the head of the Gulf of Carpentaria, $\eta_{\rm H}(t)$, and the set-up due to wind, $\hat{\eta}_{\rm H}(t)$, are both shown over a 6-year period. The upper panel (a) shows the sea level at the head of the Gulf $\eta_{\rm H}(t)$ and sea level from the set-up calculation using wind stress $\hat{\eta}_{\rm H}(t)$. The middle panel (b) shows the deseasonalized $\eta_{\rm H}(t)$ and $\hat{\eta}_{\rm H}(t)$, and the lower panel (c) shows the bandpassed (30-90 days) $\eta_{\rm H}(t)$ and $\hat{\eta}_{\rm H}(t)$. There is good agreement particularly in the timing and sign of the predicted set-up response.

cycle (annual and semiannual cycles were removed by harmonic regression). Much of the remaining variability is concentrated in the MJO band which is emphasized in the 30-90 day bandpassed series shown in the lower panel.

The prediction of the sea level anomaly at the head of the Gulf of Carpentaria due to wind set-up, $\hat{\eta}_{\rm H}$, was calculated as follows. Assuming constant density and depth, and steady state, the linearized momentum equations representing the ocean response to wind forcing leads to a balance of surface wind stress, τ, and the pressure gradient along the Gulf (which is taken to be northwest-southeast, based on the shape of the standing mode in Figure 4.7 and the local shape of the coastline). The head of the Gulf is chosen to be in the southeast corner (see Figure 4.7, panel 1) and length is defined to be L = 1000 km.

This value is somewhat subjective and open to uncertainty. The averaging period for the sea level is one week and this is much longer than the time estimated to reach a steady state ($\sim$1 day). It follows that set-up theory can be applied independently at each point in time to predict the sea level response to wind stress. Assuming the sea level change at the "mouth" is zero, this leads to the following expression for the sea surface height at the head:

$$\hat{\eta}_{\mathrm{H}} = \frac{L\tau}{\rho g H}, \tag{4.2}$$

where g is gravitational acceleration (9.8 ms^{-2}), ρ is the density of seawater (taken to be 1024 kg/m^3) and H is the water depth (36 m, based on ETOPO2 bathymetry data[5]). The along-gulf wind component, w, was calculated from the average of all northwesterly winds in the box shown in the first panel of Figure 4.7. The wind stress was calculated using $\tau = \rho_{\mathrm{a}} c_{\mathrm{d}}(a) a w$, where ρ_{a} is the density of air (taken to be 1.2 kg/m^3), $c_{\mathrm{d}}(a)$ is the wind-dependent air-sea drag coefficient and a is a modification of the wind speed to account for the contribution to the stress from variability lost by taking a weekly average of the daily winds (see *Thompson et al.* (1983) for details on the calculation of a).

The predicted sea level set-up, $\hat{\eta}_{\mathrm{H}}$, is plotted in the upper panel of Figure 4.8 along with the aforementioned time series of η_{H}. The middle and lower panels show the observed sea level and set-up after removing the seasonal cycle and applying a 30-90 day bandpass filter, respectively. It is clear that wind set-up explains most of the seasonal cycle as well as several large events in the original data; it is particularly powerful at predicting the bandpassed sea level variability. Quantitatively, the zero-lag crosscorrelation between the bandpassed sea level and set-up is 0.70. However, the model overestimates the observed sea level significantly (the minimum RMS difference between η_{H} and $\hat{\eta}_{\mathrm{H}}$ is found for $0.64\hat{\eta}_{\mathrm{H}}$). At a period of 75 days the coherence between the bandpassed η_{H} and $\hat{\eta}_{\mathrm{H}}$ (effectively the wind stress) is 0.81 (between 0.5 and 0.85 across the entire MJO band with a 5% significance level of 0.28). Sea level set-up therefore explains a large portion of sea level variability at the head of the Gulf and is especially relevant on MJO timescales.

Note the multiple coherence between the northwesterly wind stress and the MJO index is 0.68 at a period of 75 days (between 0.4 and 0.7 across the entire MJO band with a 5% statistical significance level of 0.25). From this result it is concluded that the intraseasonal

---

[5] `http://www.gfdl.noaa.gov/products/vis/data/datasets/etopo2_topography.html`

sea level variability in the Gulf of Carpentaria region is mainly due to the MJO through its influence on local sea level set-up. Note that the reanalysis, which is a numerical model simulation of the atmosphere, provides the MJO-related wind component despite the MJO not being well resolved by numerical models (see Section 1.4). This is most likely due to the reanalysis being constrained by numerous observations of MJO-related winds and simply providing dynamically-smoothed atmospheric fields. As will become clear in Chapter 7, if the observations are too sparse in space and time the model will not be able to accurately simulate the MJO.

The influence of the Madden-Julian Oscillation on sea level and circulation in the Gulf of Carpentaria, as well as a discussion of its predictability, will be explored in more detail in Chapter 5.

4.5.3 Northeastern Indian Ocean

The FDEOF technique was applied to a region in the northeastern Indian Ocean bounded by the box shown in Figure 4.2. As above, the 1° resolution η'_{a} data were used and the frequency, corresponding to a period of 75 days, was chosen based on the peak in average coherence between sea level and the MJO for this region (see Figure 4.3c). The first mode accounts for 25% of the total spectral density at 75 days (see Figure 4.5) and its time variation is visualized in Figure 4.9.

This mode represents a mixed set of dynamics. It is clear from Figure 4.9 that there are relatively fast waves travelling eastward along the equator which reach the western coast of Sumatra. This energy is then reflected back into the basin at low latitudes as Rossby waves or carried poleward at higher latitudes by coastal trapped waves moving along two paths: south along the coasts of Sumatra and Java and north along the coasts of Sumatra and the Bay of Bengal. This phenomenon is similar to that observed in the Pacific Ocean (see Section 4.5.1) and consistent with observations of coastally trapped waves in the southern hemisphere along the coasts of Sumatra and Java (*Clarke and Liu*, 1993; *Iskandar et al.*, 2005). The Rossby waves are most prominent in the northern hemisphere, forming near the northern tip of Sumatra and propagating along 5.5°N. For a coastline angle of 45° (approximately the coastline angle of Sumatra) and a period of 75 days, the critical latitude is $\sim$ 9°N which is poleward of the northern tip of Sumatra. Therefore, these Rossby waves are permissible and are consistent with observations by *Chelton et al.* (2003). The observed asymmetry (i.e., that the Rossby wave signal is stronger north of

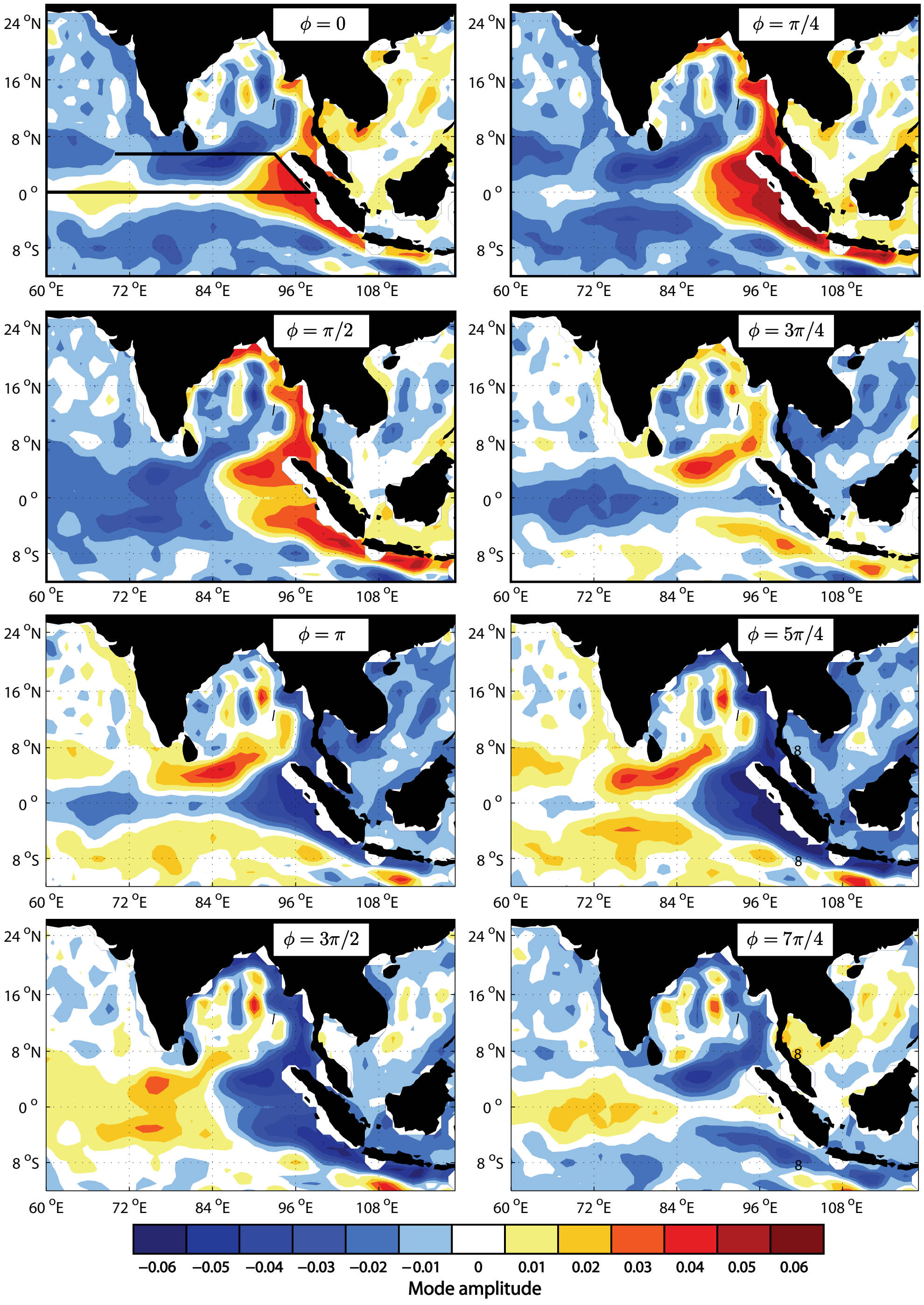

Figure 4.9: Maps of the first FDEOF mode in the northeastern Indian Ocean region for one full cycle (in $\pi/4$ radian steps). The mode shows an equatorially trapped wave reaching the western coast of Sumatra and exciting westward propagating waves around 5.5°N and 5.5°S. There are also indications of coastal trapped waves in the Bay of Bengal. A full cycle is completed in 75 days.

the equator than south of the equator) may be due to the shapes of the specific meridional modes that are excited (see Section 3.3.3).

In order to illustrate this propagation pattern a modified Hovmöller diagram has been generated of η'_{a} showing the continuous propagation of signals and westward reflection in the tropical Indian Ocean. The horizontal axis of the Hovmöller diagram represents the path of a wave in three sections: (i) eastward along the equator from 50°E (near Africa) to 99°E (Sumatra), (ii) northwestwards along the coast of Sumatra from the equator to 5°N, and (iii) westward along 5.5°N from 94°E to 70°E (this path is shown in the first panel of Figure 4.9). Part of the Hovmöller diagram for a subset of the full time period is shown in Figure 4.10.

There is continuity between the eastward-propagating signals along the equator and those which propagate westward along 5.5°N (Figure 4.10). The eastward-propagating component in the first portion of the figure is consistent with a first mode baroclinic Kelvin wave. In order to illustrate this, a line corresponding to a wave speed of 2.8 ms^{-1} (speed of the first baroclinic mode for equatorial oceanic Kelvin waves in this region (*Chelton et al.*, 1998)) is shown. As noted above, the westward-propagating component appears to be the result of Rossby waves forming off the coast of Sumatra and travelling along 5.5°N. Lines are added to Figure 4.10 demonstrating the predicted speeds of the first two baroclinic Rossby wave modes (0.93 m/s and 0.47 m/s, respectively).

These observations are consistent with *Chelton et al.* (2003) who discuss an observed maximum in the westward propagating Rossby wave signal near 5.5°N and phase speeds between 0.5 ms^{-1} and 1 ms^{-1}. *Chelton et al.* (2003) also state that theoretically these waves should be associated with identical waves travelling westward along 5.5°S but also note that observations usually identify the waves in the southern hemisphere (if they are identified at all) as having much smaller amplitude. The results found in *Chelton et al.* (2003) are consistent with these observations in which a slight indication of these waves developing in the southern hemisphere is seen but they do not propagate far into the ocean interior.

A possible explanation is as follows. The more meridional a coastline, the more poleward is the critical latitude which delineates the change between reflected Rossby waves and coastally trapped waves. The tropical eastern boundary of the Indian Ocean is more meridional in the northern hemisphere (Sumatra and Myanmar) than in the southern

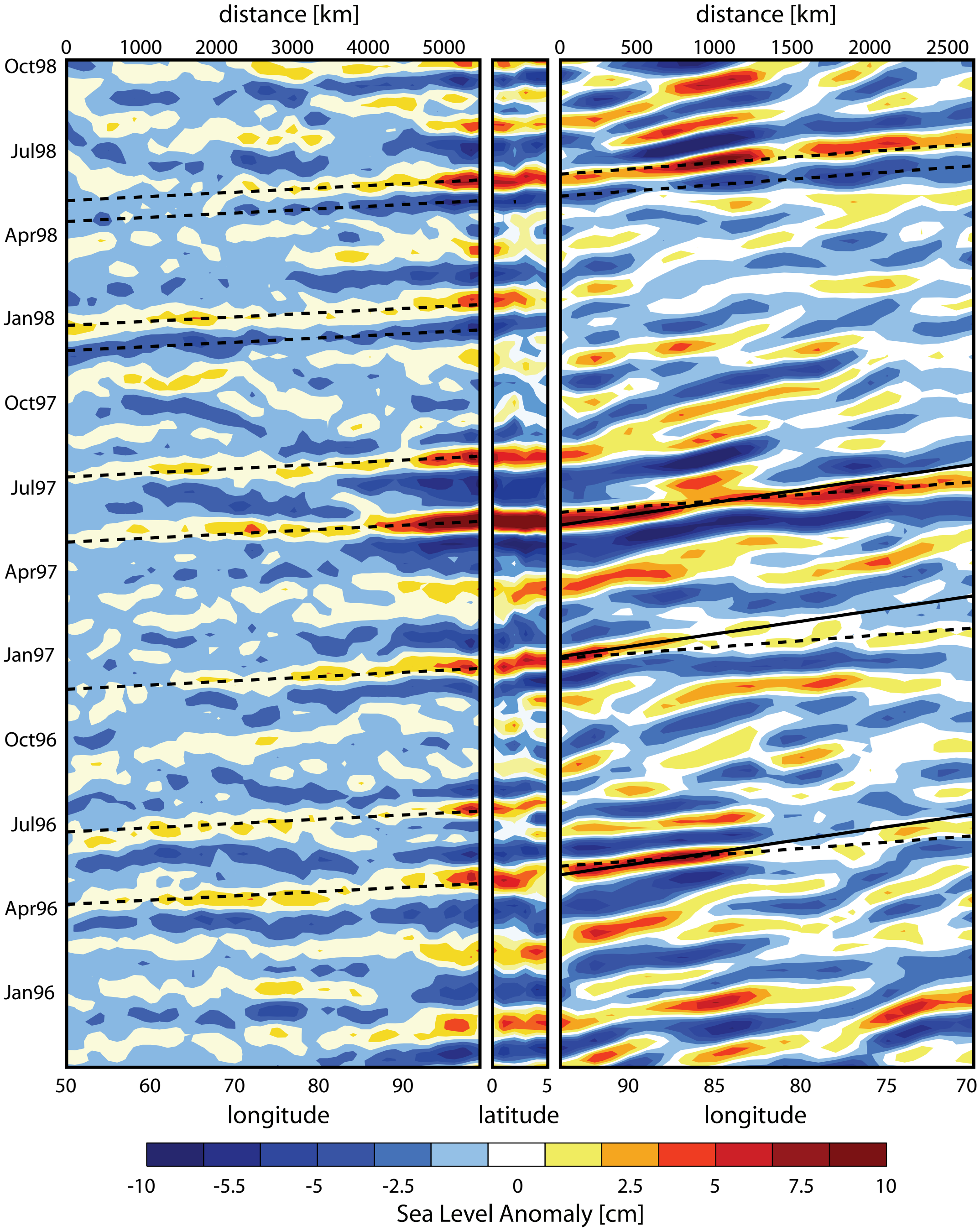

Figure 4.10: Modified Hovmöller diagram for η'_a for the period from October 1995 to October 1998. The horizontal axis is split into three regions: (i) eastward along the equator, (ii) northwestward along the coast of Sumatra, and (iii) westward along 5.5°N. The propagation of signals along the equator, and reflection from the eastern boundary, are evident. The lines represent wave speeds of 2.8 ms^{-1} in the first section representing the first mode baroclinic Kelvin wave and 0.933 ms^{-1} and 0.467 ms^{-1} in the third section (solid and dashed, respectively) representing the first two Rossby wave modes.

hemisphere (Sumatra and Java) and so the critical latitude will be more poleward in the north than in the south. This will result in more energy radiated into the basin as Rossby waves in the north. It should also be noted that the westward propagating waves do not travel west of about 72°E which could be due to the presence of the Maldives Island chain which lies off the southwest coast of India near this longitude and is oriented in the north-south direction.

The strength and generation of equatorially trapped Kelvin waves are known to be influenced by zonal wind stress along the surface of the equatorial Ocean. It is also known that the MJO is strongly correlated with zonal wind in this region (*Madden and Julian*, 1972; *Zhang et al.*, 2009). Many equatorial events evident in Figure 4.10 occur at times that correspond with large MJO events. Generally the best correspondence between MJO and sea level events occurs during late Boreal spring and summer (approximately from May through to August). One particularly notable example of this is the summer of 1997. The westward propagating waves along 5.5°N may be a combination of remote and local forcing. Figure 4.10 shows that they are often partly based on signals originating in the equatorial region and so are partially forced remotely by wind generated waves in the equatorial Indian Ocean. Note that the westward propagating waves exhibit characteristics such as multiple wave speeds and amplification or decay along their paths that cannot be attributed solely to such remote forcing. A more detailed modelling study of this region is pursued in Chapter 6 in order to determine the dominant waveforms along with their forcing and decay.

4.6 Summary and Discussion

Using satellite-based measurements of sea level it is shown that the Madden-Julian Oscillation can have a significant effect on sea surface height. Using traditional statistics a simple scalar statistic is developed that measures the strength of the connection between the MJO and sea level variability in a given frequency band and at a fixed location. The connection between sea level and the MJO on a global scale was mapped for the first time using this statistic.

The global maps were used to identify regions which have a strong connection between sea level and the MJO by considering both statistical significance (the magnitude of the coherence) and practical significance (the magnitude of the predicted sea level response).

The most significant regions include the equatorial Pacific Ocean and the west coast of the Americas (combined into one region), the shallow seas off the north coast of Australia (including the Gulf of Carpentaria and the Arafura and Timor Seas), and the northeastern Indian Ocean. These regions were examined individually in order to determine the dominant physical processes relevant for variability on MJO timescales.

The equatorial Pacific and coastal Americas act as a continuous waveguide linking both equatorially and coastally trapped waves. Signals are forced by zonal surface winds in the western Pacific which then propagate east along the equator as Kelvin waves. Once they strike the American coast they excite coastally trapped waves which propagate poleward and are detected as far as 37°N and 33°S. The sea level variability north of Australia consists of a standing wave in the Gulf of Carpentaria and nearby shallow seas. Further investigation shows that most of the variability is due to sea level set-up driven by local onshore winds associated with the MJO. Finally, the northeastern Indian Ocean exhibits a complex variety of different behaviours. It is speculated that equatorially trapped Kelvin waves, generated by surface wind forcing (as in the equatorial Pacific), excite signals along the coasts of Sumatra that propagate poleward as coastal trapped waves and into the basin as Rossby waves that travel westward along 5.5°N.

The present study relies on a combination of statistical analysis and dynamical reasoning (*e.g.*, sea level set-up due to wind based on linear theory as well as considerations of local and remote forcing). There are, however, some important questions to be answered. Does the wind-driven sea level set-up in the Gulf of Carpentaria act as a generator of Rossby waves in the adjacent deep ocean as suggested by the small amplitude waves observed off the west coast of Australia? Is the fact that westward Rossby waves in the northeastern Indian Ocean are predominantly radiated along 5.5°N related to bathymetry or coastal geography? In order to shed light on some of these questions, and confirm the physical explanations given earlier, more complex modeling studies are presented in Chapter 5 (Gulf of Carpentaria) and Chapter 6 (northeastern Indian Ocean) that include realistic bathymetry, forcing and stratification.

CHAPTER 5

THE GULF OF CARPENTARIA: LOCAL RESPONSE TO THE MJO AND REMOTE FORCING FROM THE PACIFIC OCEAN

5.1 Introduction

It was shown in Chapter 4 that sea level from the Gulf of Carpentaria has a significant correlation with the MJO. In this chapter I examine the effect of the Madden-Julian Oscillation on sea level in the Gulf of Carpentaria and expand the analysis to include circulation variability. This is done using a regional ocean model that is validated through comparison with coastal tide gauge observations.

There have been few studies on sea level variability in the Gulf of Carpentaria. *Church and Forbes* (1983) examined the barotropic tidal circulation in the Gulf and *Forbes and Church* (1983) observed a strong seasonal cycle in sea level, with maximum variability in the southeast corner of the Gulf, and showed it was related to surface wind, atmospheric pressure and steric density effects. The observed sea level range at Karumba (140°49′E,17°29′S) is 75 cm which is speculated to be partly due to local effects and partly due to the influence of nearby seas (*Forbes and Church*, 1983). A similar pattern to what was presented in Chapter 4 was observed by *Tregoning et al.* (2008), except on annual time scales, and compared estimates of sea level from GRACE to those from a wind- and

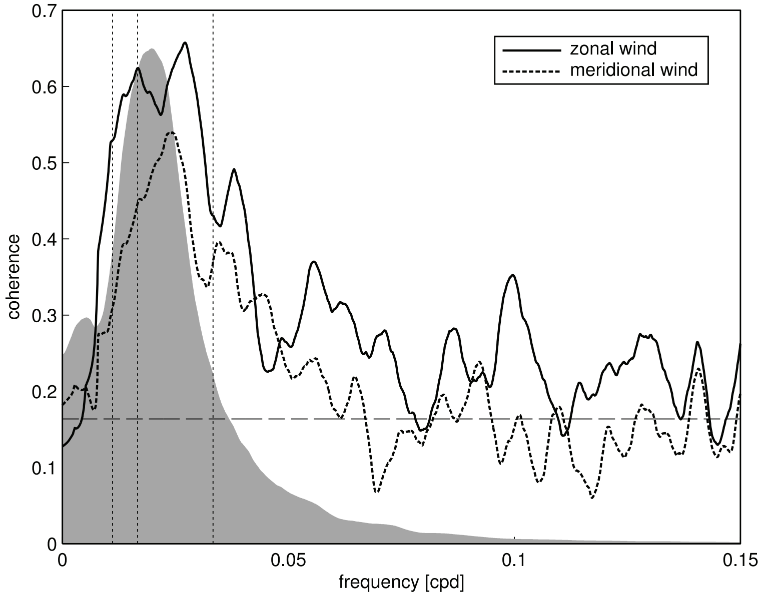

Figure 5.1: Power spectrum of the MJO and its relationship to wind over the Gulf of Carpentaria. The two lines show the coherence between the MJO and zonal (solid) and meridional (dashed) surface wind averaged over the box shown in Figure 5.3. The horizontal dashed line indicates the 5% significance level and vertical lines indicate periods of 30, 60 and 90 days. The grey shaded region shows the shape of the power spectrum of the MJO index (the spectra of the two individual components have been summed).

pressure-driven barotropic model and measurements from a local tide gauge. The role of the MJO was not discussed in the above studies.

Exploring the coastal expressions of the Madden-Julian Oscillation as well as lower frequency variability such as ENSO in the Gulf of Carpentaria is interesting from a scientific perspective. From a more applied perspective it is important to note that the Gulf is an important fishing area and understanding how environmental changes can affect these fisheries is potentially important from a resource management perspective. It has already been shown that ENSO affects Rock Lobster populations off the northwest coast of Australia through changes in sea level and circulation (*Pearce and Phillips*, 1988) and wind variability has been shown to affect the banana prawn fishery in the northern Gulf of Carpentaria (*Vance et al.*, 1985).

This chapter is organized as follows. The observations and a preliminary statistical analysis are presented in Section 5.2 and Section 5.3, respectively. The ocean model is described in Section 5.4 and in Section 5.5 it is used to better understand the dynamics in the Gulf of Carpentaria and the role of the Madden-Julian Oscillation. In Section 5.6, the low frequency residual signal (i.e., that component not predicted by the model) is related to remote forcing from the Pacific and Indian Oceans via the Indonesian Throughflow region. A summary of the results and implications of this study, as well as a discussion of future work, are presented in Section 5.7.

5.2 Observations of Sea Level, the MJO, and Surface Wind

Observations of the MJO, sea level, and the wind data which are used to validate and force the coastal model are presented here as a prelude to the more complete modeling study described in Section 5.4. The altimeter-based observations of sea level, which were used in Chapter 4, are supplemented with coastal observations from tide gauges.

5.2.1 The Madden-Julian Oscillation Index

The MJO is characterized using the bivariate index of *Wheeler and Hendon* (2004). Daily values from 1/1/1979 to 30/1/2010 were obtained from the Government of Australia Bureau of Meteorology[1]. The power spectrum of the MJO index is shown in Figure 5.1.

5.2.2 Sea Level from Altimeters

Global fields of satellite-based altimeter measurements of sea level anomalies were obtained from Aviso[2]. The data were isostatically adjusted for local pressure effects and corrected for tides by Aviso. Weekly data from a 1/4° resolution grid for the period 14/10/1992 to 22/7/2009 are analyzed, after the annual cycle and its first two harmonics were removed from each grid point time series using least squares.

5.2.3 Sea Level from Tide Gauges

Hourly time series of sea level were obtained from three tide gauge locations (Figure 5.3) around the Gulf of Carpentaria for the period 14/11/1979 to 30/1/2010. The data for Groote Eylandt were obtained from the Australian Baseline Sea Level Monitoring Project[3] and those for Karumba and Weipa were obtained from Maritime Safety Queensland,

---

[1] `http://www.bom.gov.au/bmrc/clfor/cfstaff/matw/maproom/RMM/index.htm`

[2] `http://www.aviso.oceanobs.com/en/home/index.html`

[3] `http://www.bom.gov.au/oceanography/projects/abslmp/data/index.shtml`

Tide Gauge	Latitude (S)	Longitude (E)	Start	End	% Complete
Groote Eylandt	13°50′	136°30′	2/9/93	31/8/09	99
Karumba (1)	17°29′	140°49′	15/11/79	12/3/91	96
Karumba (2)	17°29′	140°49′	14/10/93	31/12/09	98
Weipa (1)	12°40′	141°52′	2/6/84	3/9/91	95
Weipa (2)	12°40′	141°52′	6/9/91	31/12/09	99

Table 5.1: Details of the tide gauge records. The Karumba and Weipa records were split into two segments because there was a large gap in the middle of the record that was too long to fill by standard interpolation.

Queensland Government, Australia. See Table 5.1 for details. The records were de-tided using the analysis package of *Pawlowicz et al.* (2002) using 68 tidal constituents and averaged to daily values using a simple Doodson X0 filter (*Doodson*, 1928). The inverse barometer effect was removed using daily sea level pressures from the NCEP/NCAR Reanalysis 1 (*Kalnay et al.*, 1996) defined on a 2.5° grid. The annual cycle and its first two harmonics were removed using least squares prior to analysis. The daily mean tidal residual of coastal sea level is denoted by η_o. Sample plots of the time series are shown in Figure 5.2.

5.2.4 Surface Wind

Six-hourly fields of surface (10 m) winds were obtained from the NCEP/DOE Reanalysis 2 (*Kanamitsu et al.*, 2002) for the period 1/1/1979 to 31/12/2009. The data are defined on a global T62 Gaussian grid with an approximate resolution of 2°. The wind fields were mapped onto the ocean model grid (Section 5.4) using two-dimensional bicubic interpolation and stresses were subsequently calculated using the air-sea drag coefficient of *Large and Pond* (1981). This drag formula ignores the stability of the atmosphere lying over the ocean surface. This is not a major concern because *McBride and Frank* (1999) have shown that the atmospheric stratification over the Gulf of Carpentaria is weak. The Gulf-mean wind is defined as the average over the area shown by the box in Figure 5.3 (data over both land and ocean are included).

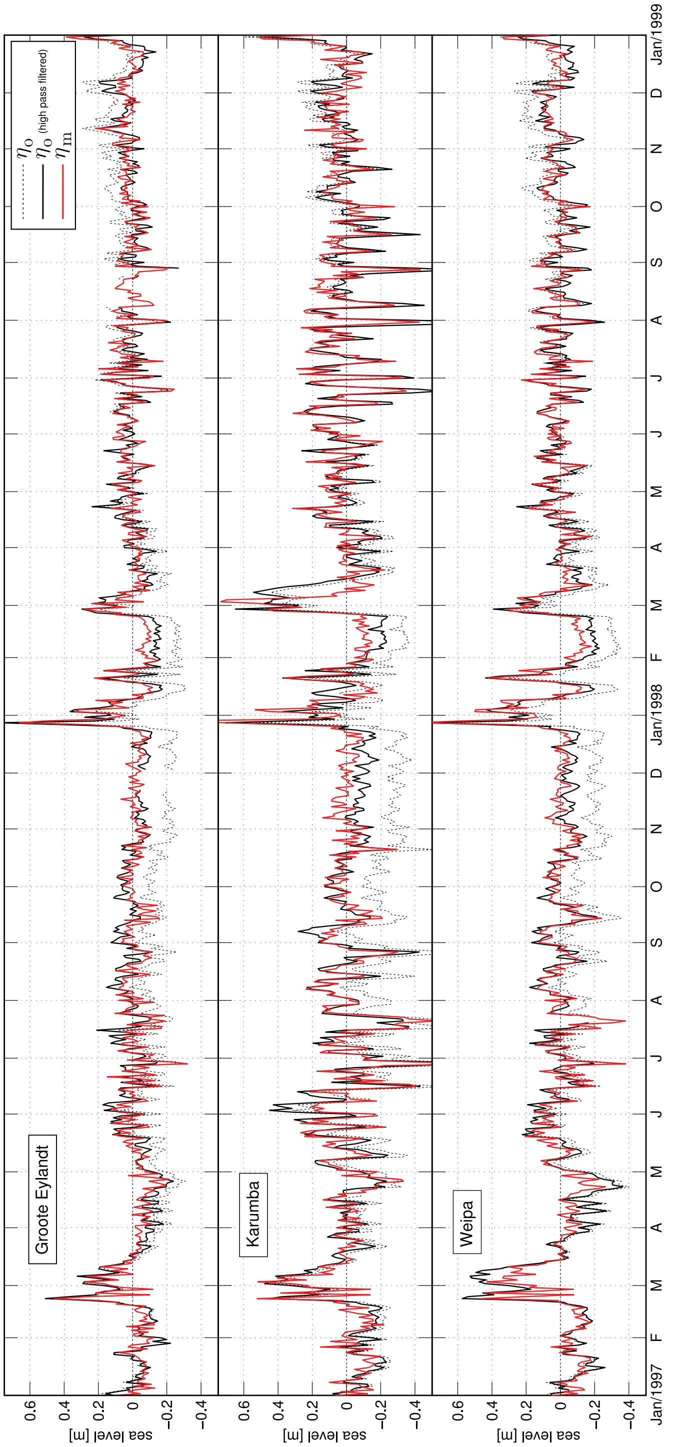

Figure 5.2: Observed and predicted sea level for a typical two-year period. The dashed line shows the observed sea level (η_o) and the red line shows the corresponding model prediction (η_m). The solid line shows the observed sea level after high-pass filtering with a cutoff period of 1/2 year.

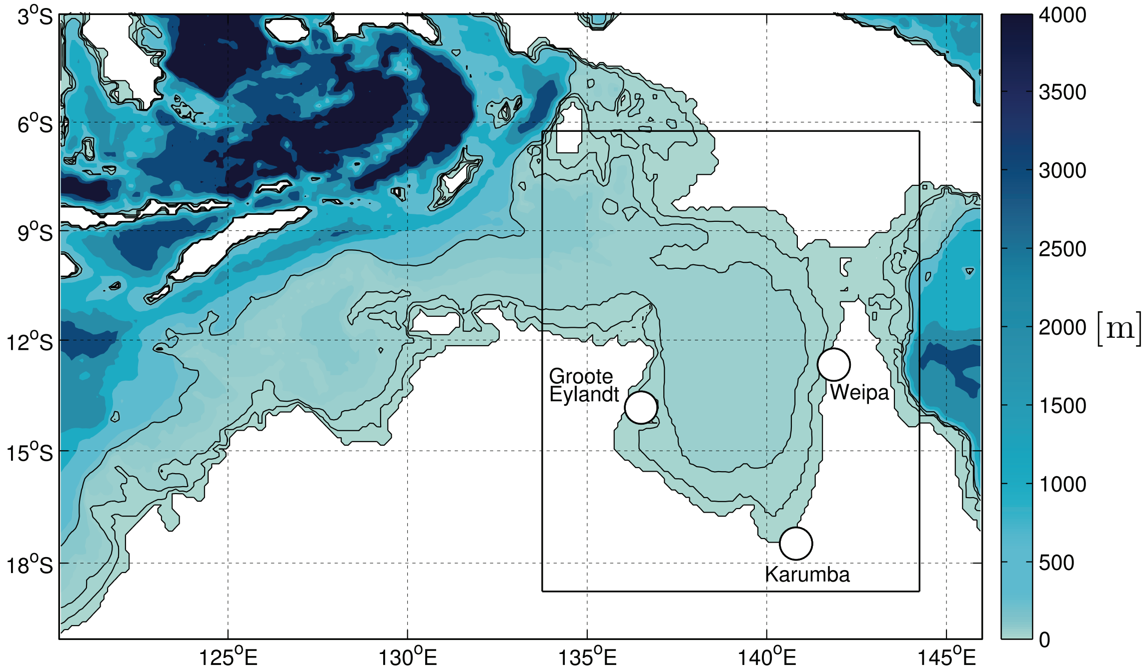

Figure 5.3: The model domain and bathymetry. Black lines show the 25 m, 50 m, and 200 m depth contours. The three white circles show the locations of the tide gauges. The box shows the area used to form the Gulf-mean wind and sea level (see Sections 5.3 and 5.5).

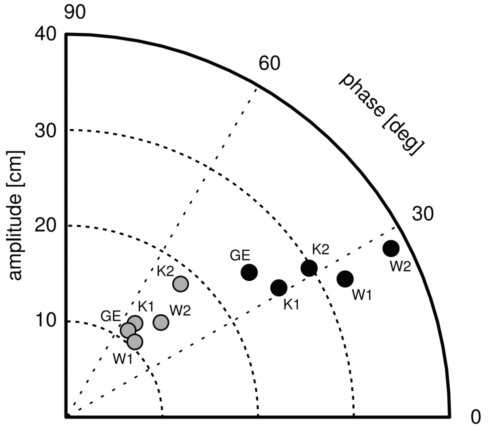

Figure 5.4: Annual cycle of observed sea level. Black circles show the amplitude and phase for the annual cycle at each station (calculated by harmonic regression). Grey circles show the residual after removing the predicted annual cycle from the observations. Note that phases of 30, 60 and 90 degrees roughly correspond to the end of January, February and March, respectively. Stations are coded GE (Groote Eylandt), K1/K2 (Karumba, first and second segments), and W1/W2 (Weipa, first and second segments).

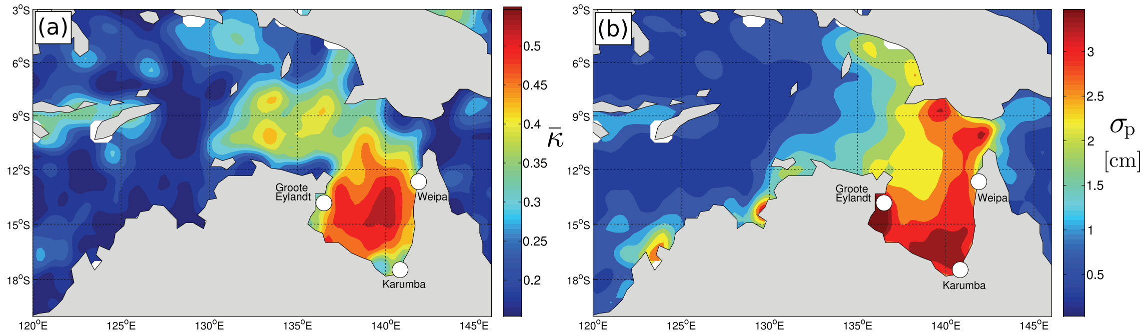

Figure 5.5: Maps of the amount of Gulf of Carpentaria sea level variability related to the MJO (regional subset of Figure 4.1). The left panel (a) shows $\bar{\kappa}$, the proportion of the standard deviation of altimeter-derived sea level accounted for by the MJO. The right panel (b) shows σ_p, the magnitude of the standard deviation of altimeter-derived sea level accounted for by the MJO. Sea level has had variability on time scales longer than 120 days filtered out.

5.3 Intraseasonal Variability in Observed Sea Level and Surface Wind

The annual cycle of η_o was estimated for each tide gauge location by harmonic regression. Phases are similar across all stations, with sea level peaking in late January and February (Figure 5.4), consistent with *Forbes and Church* (1983). It was shown in Chapter 4 that the MJO was found to account for over 50% of the standard deviation of sea level in the Gulf after filtering out seasonal and interannual variability (Figure 5.5). It was speculated that the underlying principal cause of this statistical relationship was set-up by local surface winds that are strongly linked to the MJO. *Tregoning et al.* (2008) also examined the effect of wind on sea level set-up in the Gulf of Carpentaria but did not relate the wind forcing to the MJO. Furthermore, the coherence between the MJO and η_o is statistically significant across the MJO band (see Figure 5.6).

The wind direction over the Gulf of Carpentaria is strongly linked to both the local trade winds and the Australian-Indonesian monsoon. The background flow in this region is dominated by the southeasterly trade winds which peak in July. During Austral Summer the Australian-Indonesian monsoon causes the mean flow to be predominantly northwesterly (see (*Forbes and Church*, 1983) and histogram in Figure 5.7).

The coherence as a function of frequency (Figure 5.1) was calculated to examine the relationship between the MJO index and Gulf-mean wind. In general, the coherence peaks for both wind components for periods between 30 and 60 days. Zonal wind has the highest coherence with the MJO (between 0.5 and 0.7 across the intraseasonal band).

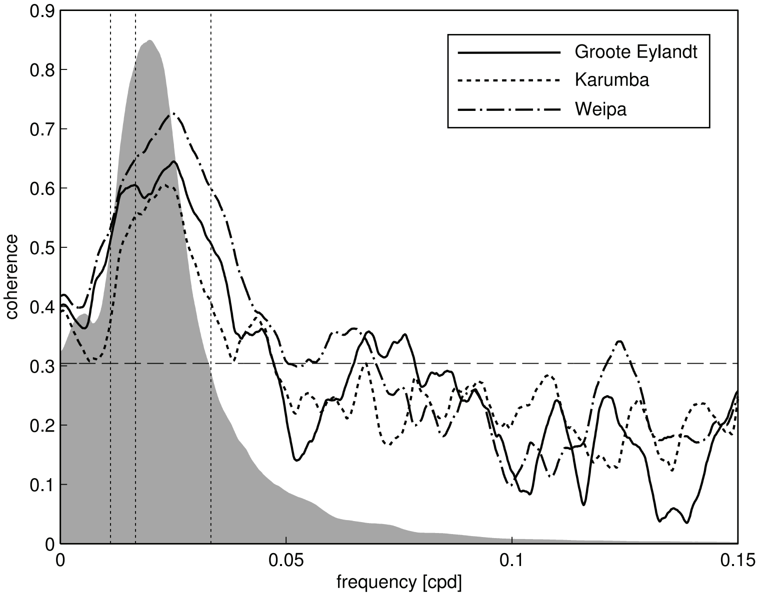

Figure 5.6: Power spectrum of the MJO and coherence between the MJO and observations of coastal sea level from the Gulf of Carpentaria. Same format as Figure 5.1.

Directional dependence was explored by looking at the average intraseasonal coherence (periods between 30 and 90 days) between the MJO and wind projected onto an axis. The coherence was then plotted as a function of axis direction (Figure 5.7). The intraseasonal coherence peaks for westerly to northwesterly winds (or easterly to southeasterly). As noted above, the prevailing winds in the region are northwesterly/southeasterly. It will be shown in Section 5.5.1 that the Gulf responds most strongly to wind in this direction. Therefore, it is anticipated that the MJO will provide a strong contribution to intraseasonal wind-driven variability of sea level and circulation in this region.

Another way of exploring the dependence of wind and sea level on the MJO is by compositing based on its phase. The MJO phases are defined following *Wheeler and Hendon* (2004): phases 2/3 represent an active MJO over the Indian Ocean, 4/5 over the Maritime Continent, 6/7 over the Western Pacific, and 8/1 over the Western Hemisphere and Africa. Composites of zonal wind (not shown) show the passage of a convergence region at the surface associated with the movement of active MJO-related convection over the Maritime Continent (e.g., *Zhang* (2005)). This leads to anomalous easterlies over the Maritime Continent at the equator when the convective centre is over the Indian Ocean (phases 1-3) and anomalous westerlies when it is over the Pacific Ocean (phases 6-7).

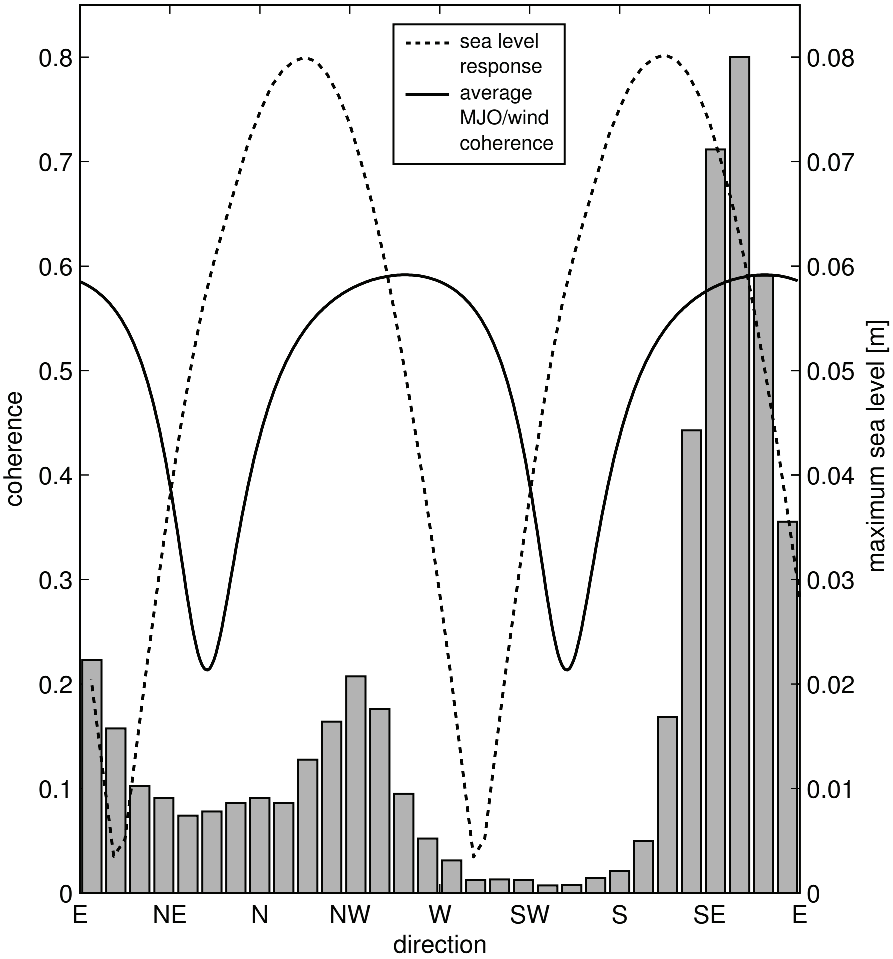

Figure 5.7: Wind statistics over the Gulf of Carpentaria as a function of wind direction. The grey boxes form a histogram of daily wind directions of the Gulf-mean wind. The solid line shows the coherence (averaged over intraseasonal frequencies) between the Gulf-mean wind, projected onto an axis at the direction given, and the MJO. The dashed line shows the magnitude of the steady state response of Gulf-mean sea level as a function of wind direction as predicted by the ocean model.

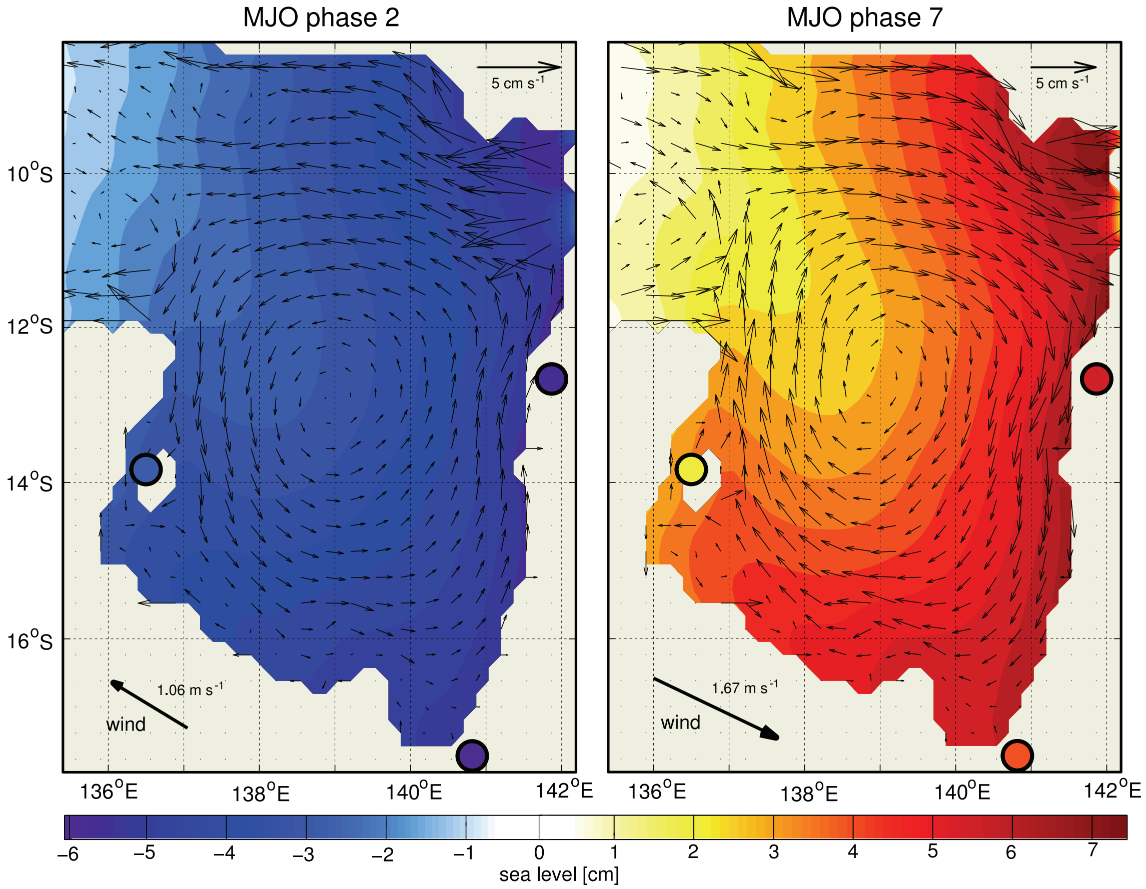

Figure 5.8: Composites of sea level, wind, and surface current anomalies associated with phase 2 (left) and phase 7 (right) of the MJO (for MJO amplitudes exceeding 1). The thick black arrows in the lower left corner of each panel are the composites of the Gulf-wide wind. The filled contours and filled circles show the composites of η_{m} and η_{o}, respectively. The black arrows show composite of predicted currents with reference speed shown in the upper right of each panel.

The Gulf of Carpentaria, just south of the Maritime Continent, experiences anomalous northwesterlies during phases 6-7 with set-up of coastal sea level evident at all three tide gauges and anomalous southeasterlies during phases 1-3 with set-down at all three stations (illustrated for phases 2 and 7 in Figure 5.8).

To explore the seasonal variation of the spectral properties of the wind and the MJO spectra are calculated using 180 day subsets of the Gulf-mean wind time series with succesive blocks shifted by one day. The seasonal cycle of spectral density was then calculated by averaging across years for January 1, January 2, etc. The seasonal variation of the northwesterly wind spectrum (Figure 5.9, left panel) shows that the energy is

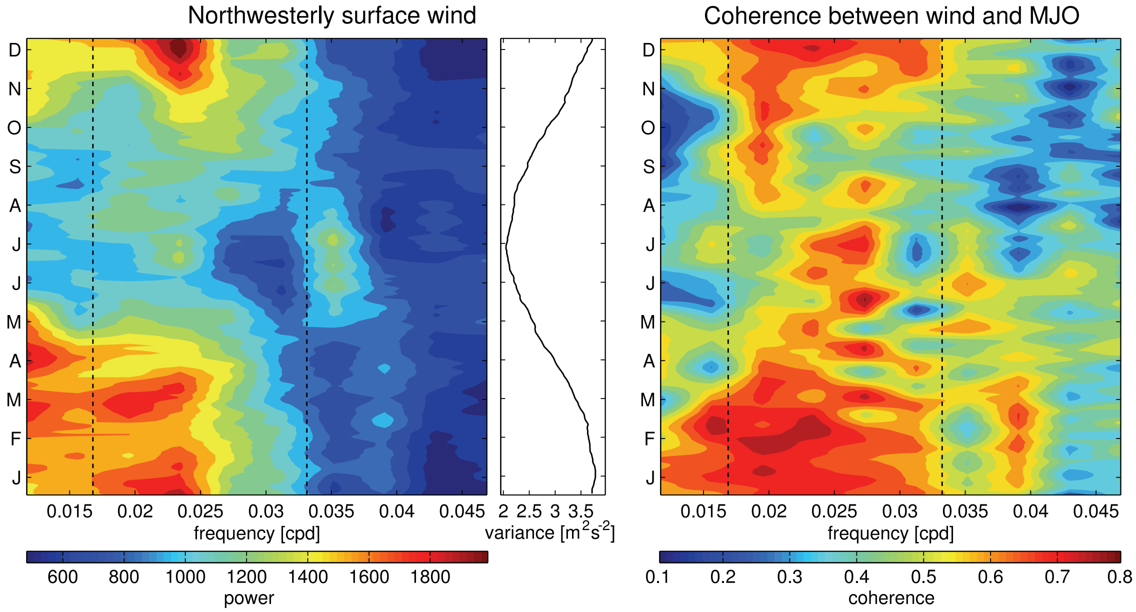

Figure 5.9: Seasonal variation of the spectral properties of the Gulf-mean wind. Left panel: the seasonal cycle of the spectral density of northwesterly wind across the intraseasonal band. To emphasize the seasonal changes in spectral shape, the spectrum for a given time of year has been normalized by the corresponding variance (see centre panel). Right panel: the seasonal cycle of the coherence between northwesterly wind and the MJO across the intraseasonal band. The vertical lines indicate periods of 30 and 60 days.

relatively high at periods between 30 and 60 days during Austral Summer which coincides with the Australian-Indonesian monsoon. This time of year also corresponds to relatively high coherence between the wind and the MJO (Figure 5.9, right panel) consistent with previous work (*Salby and Hendon*, 1994; *Zhang and Dong*, 2004; *Bellenger and Duvel*, 2007). The seasonal cycle in the spectral density of η_o shows the same cycle as the wind (compare the left-hand panels of Figure 5.10 with Figure 5.9).

In Section 5.5 I check if the ocean model can reproduce these seasonal variations in the spectral properties of sea level and the relationship between sea level and the MJO.

5.4 Numerical Model

The Princeton Ocean Model (POM, e.g. *Blumberg and Mellor* (1987) and Section 3.4.1) was used to dynamically simulate the Gulf of Carpentaria, the adjacent shallow Arafura and Timor Seas, and the deep waters to the northeast and northwest of Australia (see

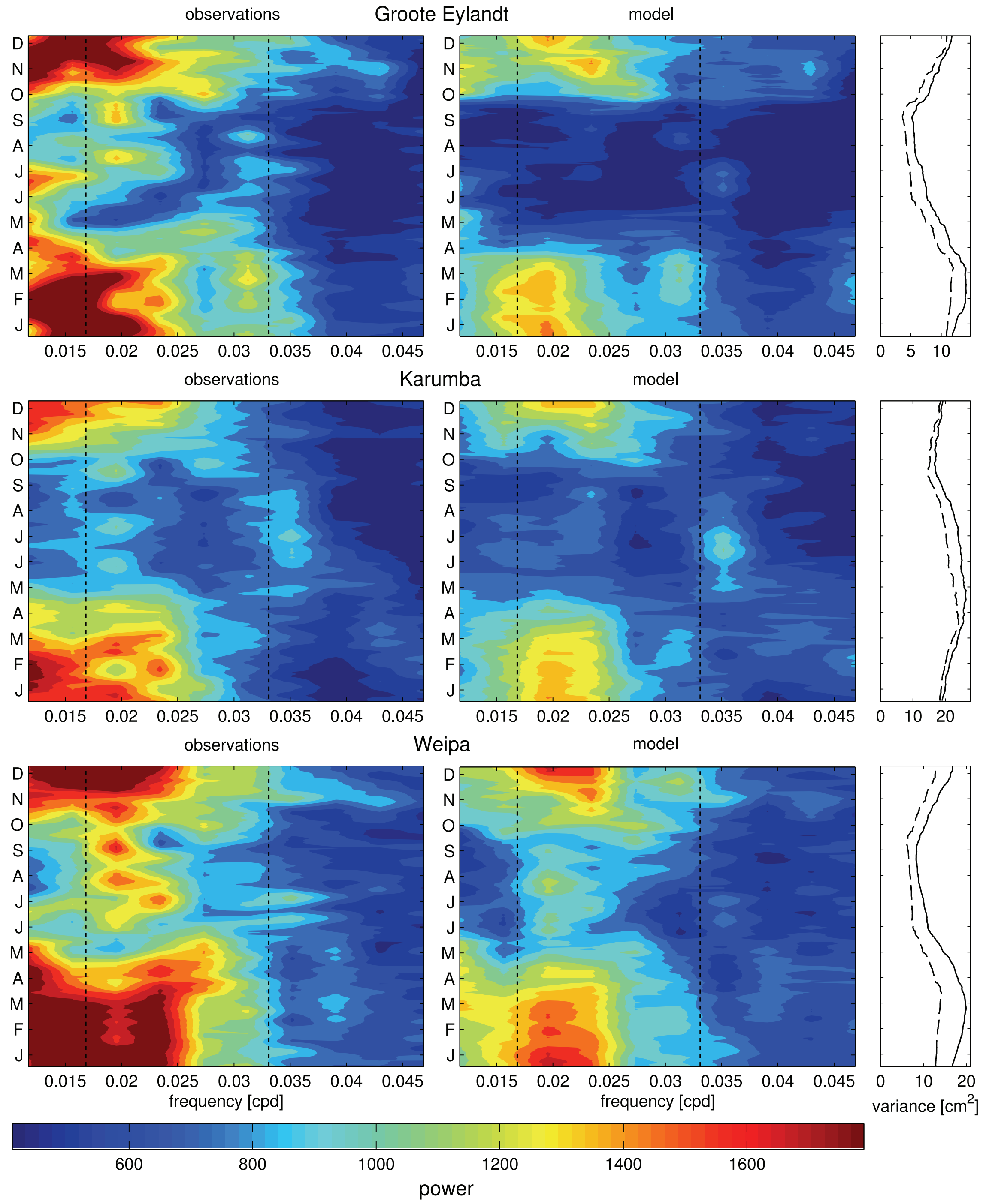

Figure 5.10: Seasonal variation of the spectral density of observed and predicted sea level. Left panels correspond to observations and middle panels to predictions. The spectra have been normalized by the variances shown in the right panels (solid: observations, dashed: predictions). Otherwise same format as Figure 5.9.

Figure 5.3 for model domain). The model grid is defined with a spatial resolution of 1/6° (103 points meridionally and 157 points zonally for a total of 16171 grid points). The bathymetry (Figure 5.3) was interpolated to the model grid from the 1/10° Australian Bathymetry and Topography Grid [David Griffin, CSIRO, personal communication]. The model is forced by surface stress derived from six-hour reanalysis surface winds (Section 5.2.4) linearly interpolated to the model time step (see below). Note that the model is not forced by variations in atmospheric pressure.

The model was run barotropically to simulate sea level and the depth averaged flow. The bottom stress was formulated in terms of depth averaged flow $\boldsymbol{U}$ and was of the form $c_{\mathrm{d}}\boldsymbol{U}|\boldsymbol{U}|$ where $c_{\mathrm{d}} = 2.5 \times 10^{-3}$. The time step for the barotropic calculations was 12 s, satisfying the CFL condition for stability. The coastal boundary condition was no normal flow and no slip; radiation conditions were applied at the open boundaries to allow transients generated within the domain to escape with minimal reflection. The initial condition was a state of rest and a flat sea surface. The model was run for 31 years (forced by the reanalysis wind field) and sea level and current fields were output daily (sufficient for this study because the variability of interest occurs on intraseasonal timescales).

5.5 Comparison of Observed and Predicted Sea Level

The predicted sea level and circulation in the Gulf of Carpentaria for the period 1/1/1979 to 31/12/2009 were used to explore the forcing mechanisms that link intraseasonal variability in sea level and circulation to the Madden-Julian Oscillation. After evaluating the effect of natural resonances of the model, the model predictions are compared to observations at the three tide gauge locations.

5.5.1 Dynamical Response of the Gulf to Wind Forcing

The possibility of a natural resonance with frequencies within the MJO band, such as an internal seiche, must be ruled out in order to link sea level variability in the Gulf with the MJO. To quantify the resonance characteristics of the model, it was forced for 700 days by periodic along-gulf winds (northwesterly direction with an amplitude of 7.1 ms^{-1}). Individual runs were performed for forcing periods between 2 and 150 days. For each run, the amplitude of the Gulf-mean sea level was calculated and plotted against frequency (not shown). Over intraseasonal timescales the gain is flat, consistent with *Pariwono et al.*

(1986) who estimated the resonant period of the Gulf of Carpentaria to be about 26 hours. Therefore, the model is not resonant at intraseasonal frequencies.

The sensitivity of sea level to the direction of surface wind was also examined. The model was forced for 1 year by a steady, uniform wind of 5 ms^{-1}. Simulations were run independently for 64 discrete wind directions. For each run, the steady state response of the Gulf-mean sea level was averaged over days 201 through 365 and stored. The largest sea level response was found for northerly to northwesterly winds for set-up and the opposite directions for set-down (dashed line, Figure 5.7), consistent with the discussion in Section 5.3.

5.5.2 Seasonality and Intraseasonal Variability in Observed and Predicted Sea Level

Predicted seasonal cycles (estimated by harmonic regression) are of smaller amplitude (10 to 20 cm) than the observed seasonal cycles. However, the ocean model does not include steric effects which are present in the observations. *Forbes and Church* (1983) calculated the seasonal cycle of steric sea level anomalies to have an amplitude of 9.4 cm at Karumba which the ocean model is consistent with. The residual seasonal cycle, calculated by subtracting the predicted annual cycle from the observed annual cycle, is similar across all stations (Figure 5.4). This is consistent with steric changes in the adjacent deep water which peak near the end of the southern hemisphere warming cycle.

The model predictions of sea level at the three tide gauge locations were then deseasonalized by removing the annual cycle and its first two harmonics using least squares (henceforth denoted by η_{m}). After deseasonalization, observed and predicted sea levels agree quite well in terms of amplitude and correlation (Figure 5.2 and Table 5.2). On intraseasonal timescales the agreement between η_{o} and η_{m} is particularly high with coherence above 0.80 for Groote Eylandt and Weipa, and above 0.7 for Karumba. From Table 5.2, the RMS of the prediction errors are generally less than 8 cm (except at Karumba which are as high as $\sim$12.5 cm). It should be noted that the predicted sea level represents all of the wind-forced intraseasonal variability, i.e., the predicted sea level includes both MJO and non-MJO related components. The MJO component of the observed and predicted sea level variability is discussed in Section 5.5.3.

It was encouraging to find that the model captures well the observed seasonal cycle of intraseasonal variability (right-hand panels of Figure 5.10) except at very low intraseasonal

Name	σ_o	σ_m	$\sigma_\mathrm{o\text{-}m}$	ρ_om
Groote Eylandt	9.38	8.65	6.24	0.763
Karumba (1)	13.18	13.27	12.38	0.562
Karumba (2)	15.86	14.13	10.98	0.737
Weipa (1)	10.86	9.63	7.45	0.741
Weipa (2)	11.70	10.27	6.41	0.837

Table 5.2: Comparison of observed and predicted sea level. Standard deviation of η_o and η_m (σ_o and σ_m, respectively), the standard deviation of their difference ($\sigma_\mathrm{o\text{-}m}$), and correlation ($\rho_\mathrm{om}$) are shown. Note η_o and η_m were highpass-filtered with a cutoff period of 1/2 year prior to the calculation of these statistics. Standard deviations are in cm.

frequencies (<0.015 cpd). Interestingly, the seasonally-stratified coherences between η_o and η_m (not shown) are above 0.9 (0.8 for Karumba) during Austral Summer but drop to about 0.75 during Austral Winter when the connection with the MJO through surface wind forcing is weak. I conclude that the model captures the wind-driven intraseasonal component of sea level variability in the Gulf of Carpentaria.

5.5.3 *Influence of the MJO on Circulation and Sea Level*

The composites of model predicted sea level and depth-averaged current anomalies were calculated as a function of MJO phase. The composites for phases 2 and 7 (Figure 5.8) illustrate that the wind during these phases is consistent with sea level set-up and set-down, respectively. The phase 7 (2) composite of depth averaged currents exhibits a cyclonic (anticyclonic) gyre centred in the Gulf of Carpentaria and strong eastward (westward) flow through the Torres Strait. As the MJO performs a cycle, the composites pass through a quiescent state (phase 8), followed by the set-down pattern (phase 1-3), and then another quiescent state (phase 4-5), before returning to the set-up pattern (phases 6-7).

A time series that represents set-up and set-down favorable conditions was generated by projecting the bivariate MJO index onto the phase 3 / phase 7 axis. By definition, positive values occur during phase 7 and negative values during phase 3. From Figure 5.11 it can be seen that strong set-up and set-down events often occur when the MJO is of extreme amplitude during phases 7 and 3, respectively. It is also clear from this figure that this connection is particularly strong during Austral Summer.

The predicted sea level does not reproduce well the observed variability on timescales longer than 120 days (Figure 5.2). The physical origin of this low frequency signal is discussed in the folowing section.

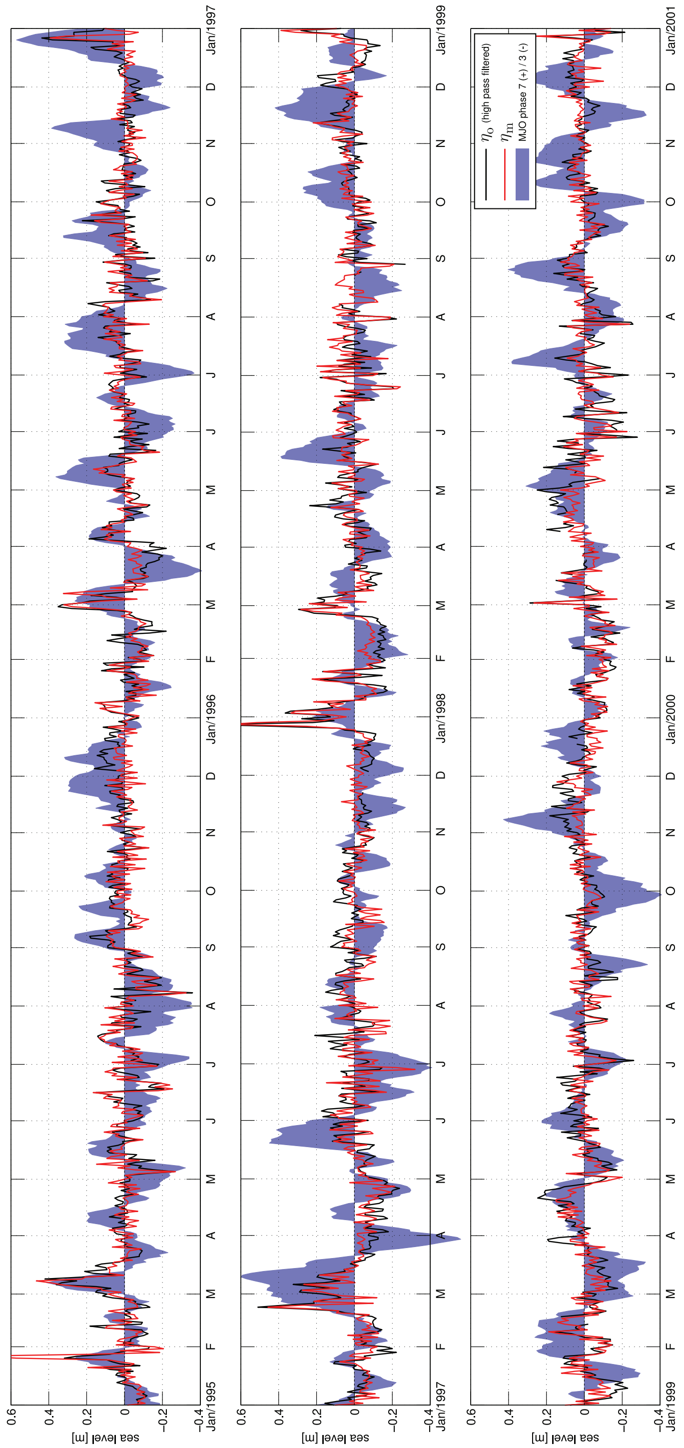

Figure 5.11: Observed and predicted sea level at Groote Eylandt over a typical six-year period. Solid black line: η_o after high-pass filtering with a cutoff period of 1/2 year. Red line: η_m. Blue filled curve: the MJO index, projected onto the phase 7 / phase 3 axis (positive values correspond to phase 7 and negative values to phase 3).

5.6 Cause of Low-Frequency Sea Level Variability

Now the sea level variability that is unexplained by the model is examined. A residual time series $\eta_{\mathrm{o-m}}$ was generated by removing the model predictions from the observed coastal sea level. Removing η_{m} from η_{o} effectively removes the high-frequency local wind effect leaving a low frequency residual that is very similar at each tide gauge location (correlations above 0.7). To obtain a single regional signal, the three $\eta_{\mathrm{o-m}}$ series were averaged into one (henceforth denoted by $\bar{\eta}_{\mathrm{o-m}}$). The variations of $\bar{\eta}_{\mathrm{o-m}}$ are on the order of 10–20 cm (Figure 5.12, upper panel).

What is the cause of variability of $\bar{\eta}_{\mathrm{o-m}}$? It is not present in the surface wind forcing and so it is likely due to variations in the deeper waters along the open boundaries of the model domain. Figure 5.12 compares $\bar{\eta}_{\mathrm{o-m}}$ and altimeter-observed sea level from a point at the shelf edge (denoted by η_{sh}, see caption for exact location). The close agreement between $\bar{\eta}_{\mathrm{o-m}}$ and η_{sh} leads us to hypothesize that the unexplained low frequency variability is driven by larger scale sea level changes in the deeper water, seaward of the Gulf of Carpentaria.

What is the cause of the variability of η_{sh}? Equatorial Kelvin waves can be excited by surface winds blowing over the Indian Ocean which then propagate eastward across the basin. Once they reach the eastern boundary they can be channeled towards the Indonesian Throughflow region as coastal trapped waves travelling along the western coast of the Indonesian Archipelago. Similarly, westward propagating Rossby waves from the tropical Pacific can drive variability in the throughflow region upon reaching the western ocean boundary (*Spall and Pedlosky*, 2005). This raises the question of which ocean basin is the primary source of the variability of η_{sh}. *Clarke and Liu* (1994) predicted that signals originating in the Indian Ocean would travel no further than the Lombok Strait. They also predicted, and showed with sea level observations along the northwestern Australian coast, that Pacific Ocean signals can penetrate the Indonesian Throughflow region and propagate along the western Australian coast. It is therefore not surprising that interannual sea level changes along the western boundaries of the Indonesian Archipelago and western Australia are in phase and highly correlated with sea level in the western Pacific (*Clarke*, 1991). Other studies have supported the view that a significant part of the variability of Australian coastal sea level originates in the Pacific Ocean (*Pariwono et al.*, 1986; *Potemra*, 2001; *Wijffels and Meyers*, 2004). It has been shown that a positive ENSO phase is associated

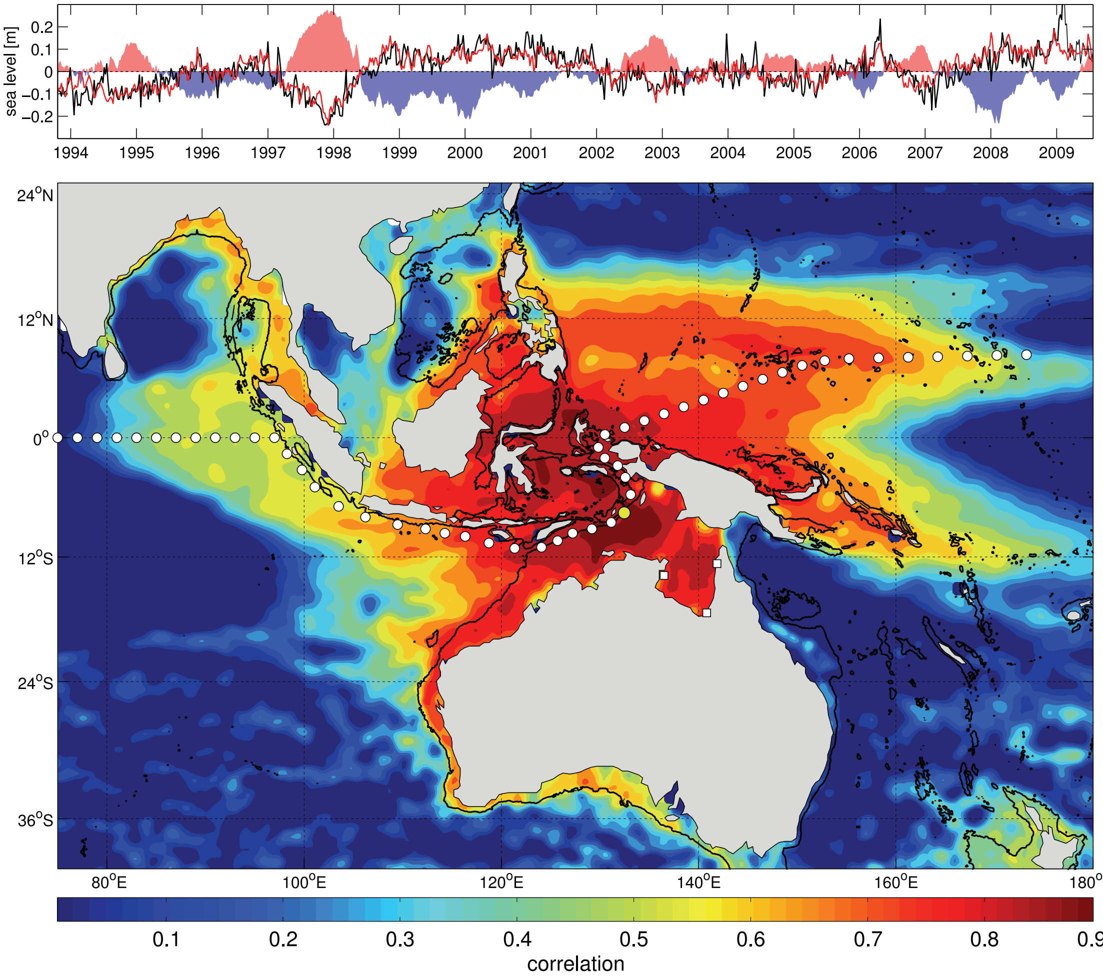

Figure 5.12: Time series and correlations of low frequency sea level. Top panel: $\bar{\eta}_{\mathrm{o-m}}$ is shown in black and η_{sh}, sea level from [132.45°E, 7.60°S] (yellow circle, bottom panel), is shown in red. The Niño 3.4 index, I_{EN}, is shown by the blue and red filled curve. Bottom panel: correlation between altimeter-measured sea level, low-pass filtered with a cutoff period of 1/2 year, and $\bar{\eta}_{\mathrm{o-m}}$. The black line is the 1000 m depth contour. Open circles are positions from which altimeter records were extracted for the Hovmöller diagrams in Figure 5.14.

with a drop in sea level in the waters surrounding Indonesia (*Nerem et al.*, 1999). This drop is consistent with a quasi-steady response to low frequency wind forcing in the Pacific which is in turn related to ENSO (*Clarke*, 2008). I have used three approaches to explore the origin of the low frequency variability in the Gulf of Carpentaria as detailed below.

5.6.1 Correlations of Sea Level with Climatalogical Indices

The Niño 3.4 Index, I_{EN}, was used as a measure of Pacific Ocean variability and the Dipole Mode Index (*Saji et al.*, 1999), I_{DMI}, was used as a measure of Indian Ocean variability[4]. For periods longer than one year, $\bar{\eta}_{\mathrm{o-m}}$ is coherent with I_{EN} and I_{DMI} at about 0.8 and 0.4 respectively (both significant at the 5% level). This could lead one to conclude that both oceans contribute significantly to the variability of $\bar{\eta}_{\mathrm{o-m}}$. However, these two indices are not independent (*Saji and Yamagata*, 2003; *Yuan and Li*, 2008) and partial coherence was used to remove the effect of one index on the coherence between $\bar{\eta}_{\mathrm{o-m}}$ and the other index (see Section 2.2.1). The partial coherence between $\bar{\eta}_{\mathrm{o-m}}$ and I_{EN}, allowing for I_{DMI}, is about 0.7 for periods exceeding one year (see Figure 5.12 for time series); the corresponding partial coherence between $\bar{\eta}_{\mathrm{o-m}}$ and I_{DMI}, allowing for the effect of I_{EN}, is not significant at the 5% level. This simple and exploratory analysis leads us to speculate that $\bar{\eta}_{\mathrm{o-m}}$ is forced primarily by large scale, ENSO-related variability in the Pacific Ocean rather than in the Indian Ocean.

5.6.2 Regional Sea Level Correlations

Correlations between $\bar{\eta}_{\mathrm{o-m}}$ and sea level from altimeters were calculated on a 1/4° grid and contoured (Figure 5.12). The patterns formed by the high correlations (above 0.4) suggest connections between the Indian and Pacific Oceans and the Gulf of Carpentaria. In the Indian Ocean there is a tongue of high correlation extending from the eastern equatorial boundary which encompasses Sumatra as well as extending poleward both north, around the Bay of Bengal, and south, along the Indonesian Archipelago. In the Pacific Ocean there are two extended tongues of high correlation in the tropics, north and south of the equator. Finally, there is a long narrow tongue hugging the coast of Australia that links Tasmania back to Indian and Pacific Oceans.

To identify the source regions for the variability in the Gulf of Carpentaria the correlation between sea level on the 1/4° grid with sea level at various potential source locations was

---

[4] Both were obtained from `http://ioc-goos-oopc.org/state_of_the_ocean/all/`

mapped. By examining the associated time lags (not shown) in the high correlation regions it is concluded that there are in fact only two potential sources for the variability: the equatorial Indian Ocean and the northern tongue of high correlation in the tropical Pacific Ocean (see upper panels of Figure 5.13). Noting the high correlation in the Gulf one might conclude that both oceans are important drivers of variability in this region. However, as noted above, variability in the Indian and Pacific Oceans are not independent and so partial correlations were calculated as before to quantify the effect of each basin separately (see lower panels of Figure 5.13). The maps of partial correlation clearly show that the variability originating in the Indian Ocean does not propagate past the Lombok Strait, consistent with the work of *Clarke and Liu* (1994). On the other hand, variability from the Pacific Ocean can reach the Gulf of Carpentaria, and can continue to propagate west and south around the coast of Australia.

The partial correlation map for the Pacific Ocean source region (and the corresponding lag map, not shown) are consistent with equatorial Rossby waves propagating westward across the basin and entering the Indonesian Throughflow region. The partial correlation and lag maps for the Indian Ocean source region are consistent with equatorially trapped Kelvin waves travelling eastward and then poleward as coastally trapped waves towards the Indonesian Throughflow region. These interpretations are consistent with the discussion and references given above.

5.6.3 Hovmöller Diagrams

In order to better understand how the two ocean basins influence low frequency sea level in the Gulf of Carpentaria Hovmöller diagrams were generated along the two pathways identified in the previous section. (The advantage of Hovmöller diagrams is that they allow the identification of individual events as well as explicitly show lags as these events propagate.) Both pathways originate in the interior of their respective oceans and terminate at the location of η_{sh} on the northwestern Australian shelf edge. Other potential pathways through the Indonesian Throughflow (such as the channel between Borneo and Sulawesi and exiting through the Lombok strait) were identified but were not explored further in this study. The chosen pathways are shown by white circles in Figure 5.12 and time series of sea level from the positions were low-pass filtered with a cutoff period of 1/2 year prior to plotting. The time axis of the Hovmöller diagram runs from 1994 to 2009.

The Hovmöller diagram for the Indian Ocean (Figure 5.14, left) shows that signals

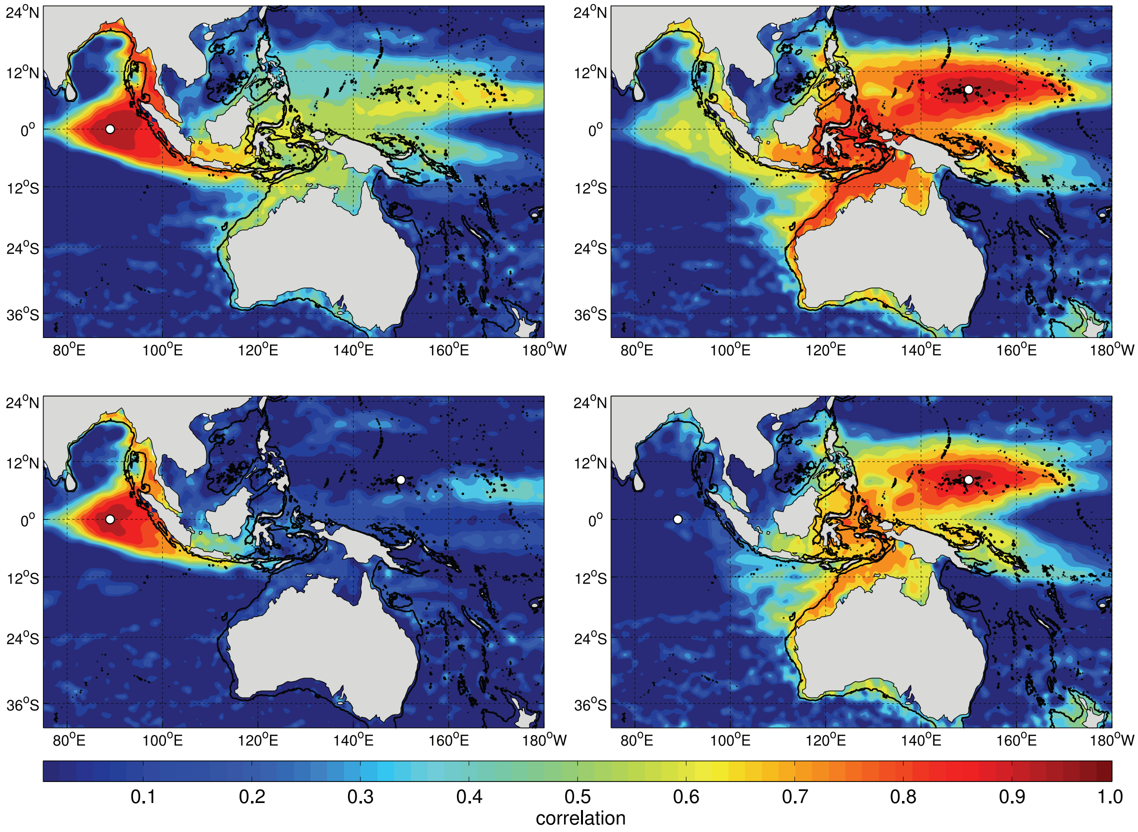

Figure 5.13: Connections between the Indian and Pacific Oceans and the Gulf of Carpentaria. Upper panels: correlation between gridded altimeter sea levels and sea level at [0°N, 89°E] in the Indian Ocean source region (top left) and [8.25°N, 150°E] in the Pacific Ocean source region (top right). Lower panels: partial correlations allowing for the effect of the other source region. Locations of sources are indicated by white dots. The thin black line is the 1000 m depth contour.

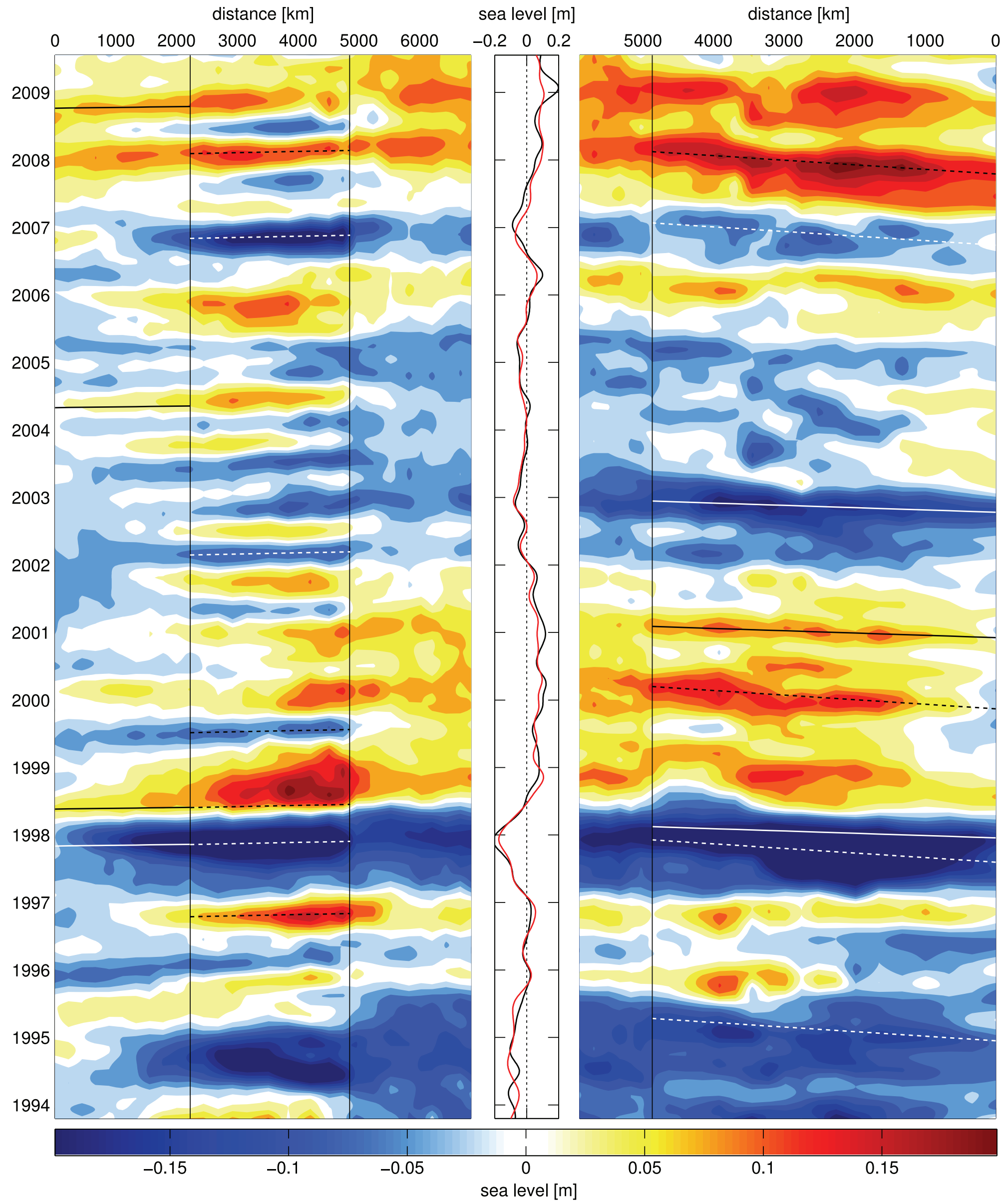

Figure 5.14: Propagation of signals along pathways originating in the Indian Ocean and the Pacific Ocean and terminating at the location of $\eta_{\rm sh}$. The pathways are shown in Figure 5.12. Left panel: Hovmöller diagram for the Indian Ocean pathway. The vertical line at a distance of ∼2000 km indicates where the equator meets Sumatra; the second line approximates the location of Lombok Strait. Sloped lines show equatorial Kelvin wave speeds (2.8 ms^{-1}, solid line) and coastal trapped wave speeds (1.78 ms^{-1}, dashed line). Right panel: similar format as left panel but for the Pacific Ocean pathway. The vertical line marks the entrance to the Indonesian Archipelago. Sloped lines show the speeds of first and second mode equatorial Rossby waves (0.93 ms^{-1} and 0.47 ms^{-1}). Centre panel: $\bar{\eta}_{\rm o-m}$ (black) and $\eta_{\rm sh}$ (red), low-pass filtered with a cutoff period of 1/2 year. Note that the innermost time series in each Hovmöller diagram also corresponds to $\eta_{\rm sh}$.

from the equatorial Indian Ocean are channeled along the coast of Indonesia but are severely attenuated when crossing the Lombok Strait as predicted by *Clarke and Liu* (1994). Signals travelling along the equator propagate at the expected speed of first baroclinic mode equatorial Kelvin waves (2.8 ms^{-1}, *Chelton et al.* (1998)). The speed of propagation along the Indonesian coast agrees well with previous estimates (1.78 ms^{-1} for coastal South America, *Spillane et al.* (1987); *Arief and Murray* (1996)).

The Hovmöller diagram for the Pacific Ocean (Figure 5.14, right) shows signals originating in this basin propagate westward and then through the Indonesian Archipelago and along the Australian shelf break where they force sea level in the shallow Timor and Arafura Seas and the Gulf of Carpentaria. Evidence of these signals can often be seen propogating past the location of η_{sh} and continuing along the Australian shelf edge (i.e., the large event in 1994/1995). These westward propagating signals travel at wave speeds which agree with the first and second mode equatorial Rossby wave speeds (0.93 ms^{-1} and 0.47 ms^{-1}, *Chelton et al.* (2003)).

Overall the correlations with indices, regional sea level correlations, and Hovmöller diagrams are consistent with the conclusion that the low frequency variability in the Gulf of Carpentaria is dominated by energy originating in the Pacific Ocean rather than the Indian Ocean.

5.7 Summary and Discussion

A barotropic circulation model has been used to show that sea level variability in the shallow waters of the Gulf of Carpentaria is dominated by simple wind set-up. The same model was also used to map out the associated depth-averaged flow and thus supplement and extend the study presented in Chapter 4 based on simple dynamical balances.

A reconstruction of sea level and circulation variability driven by observed winds for the period 1979-2009 showed that the model could reproduce many of the features present in three long observed sea level records from the Gulf. The timing and amplitude of the seasonal cycles were consistent with the observations once the effects of density were taken into account. After deseasonalization, the amplitudes of the predictions were similar to those of the observations; correlations between observed and predicted sea level at tide gauge locations were typically above 0.8 on intraseasonal timescales. Furthermore, the predictions capture the seasonal cycle of the spectral properties of the observations.

The along-Gulf wind is strongly correlated with the Madden-Julian Oscillation. As the centre of convection propagates from the Indian to the Pacific Ocean, low level wind anomalies dominate the wind variability over the Gulf. Thus changes in sea level and circulation in the Gulf are associated with a larger scale atmospheric mode of intraseasonal variability. Sea level changes of up to 7 cm can occur along the coast and fluid speeds of 3–5 cm/s, with corresponging particle excursions of 20–35 km, can occur in the interior of the Gulf during significant MJO events. This has implications for predictability of sea level and circulation in the Gulf; if the initiation and evolution of the MJO can be reliably predicted, which can be done out to 2 to 3 weeks (see Sections 1.3 and 7.5), then this information will lead to better forecast skill for sea level and circulation variability in the Gulf of Carpentaria on intraseasonal timescales.

Subtracting the predictions of sea level from the coastal observations leaves a large scale low frequency signal unexplained by the model. The weak spatial gradients and long time scale of this residual mode of variability imply that it will not be associated with significant changes in circulation. To identify the cause of this residual low frequency signal three statistical approaches have been used. First, it is shown that the large scale signal was correlated with two indices describing Indian Ocean Dipole variability and ENSO variability. However, a more detailed analysis based on partial coherence and correlation suggested the signal was driven by mainly ENSO-related signals originating in the Pacific Ocean.

The second approach involved calculating correlations amongst coastal sea level and gridded sea level measurements from satellite-based altimeters. Several possible pathways were identified based on high correlations between the coastal and altimeter observations. Two possible source regions for the variability in the Gulf have been identified by examining lagged correlations: the Indian Ocean and the Pacific Ocean. Using partial correlations, sea level variations originating in the Pacific were shown to pass through the Indonesian Archipelago, unlike those originating in the Indian Ocean. The correlations between sea level in the Gulf and Indian Ocean are non-causal (i.e., due to correlations between the forcings of the two ocean basins such as wind stress).

Finally, Hovmöller diagrams aligned with the pathways connecting the Indian Ocean, the seaward edge of the Gulf of Carpentaria, and the Pacific Ocean have been constructed. These diagrams confirm the Pacific is the origin of low frequency sea level variability along the northwestern Australian shelf edge and thus the Gulf of Carpentaria. They also confirm that the Lombok Strait is a barrier to the propagation of signals from the Indian Ocean. It is also shown that the low frequency signal in the Gulf is strongly correlated with El Niño. Knowledge of the future state of El Niño, which can be predicted with 6-24 months lead time (*Chen et al.*, 2004; *Jin et al.*, 2008), can therefore be used to predict potential large scale changes in the Gulf on long time scales.

The study undertaken in this chapter confirms the connection between the MJO and ocean variability in the Gulf of Carpentaria that was noted in Chapter 4. The next chapter undertakes a similar exploration of the connection between the MJO and variability in the northeast Indian Ocean.

CHAPTER 6

THE NORTHEASTERN INDIAN OCEAN: LOCAL AND REMOTE RESPONSE TO THE MJO

6.1 Introduction

The connection between the MJO and sea level in the northeastern Indian Ocean that was noted in Chapter 4 will be explored in more detail in this chapter. There have been several notable studies on intraseasonal variability in the tropical Indian Ocean. *Luyten and Roemmich* (1982) discovered a spectral peak near 50 days in 200 m zonal flow measured by moored current meters in the equatorial Indian Ocean [47–63°E]. Similarly, *Reppin et al.* (1999) found a 40–60 day spectral peak in near surface currents further east [80°30'E,0°45'S–5°N] and *Webster et al.* (2002) found a near-50 day oscillation of zonal surface current at 90°E.

Zonal wind is highly coherent with zonal currents in the central equatorial Indian Ocean down to 100 m depth for periods between 30 and 60 days (*McPhaden*, 1982). Using a 4-1/2 layer model, *Han et al.* (2001) found that 40–60 days surface current variability were forced primarily by zonal winds associated with the MJO. In addition, with a numerical model forced by realistic winds, *Han* (2005) found a preferential excitement of lower order baroclinic Rossby and Kelvin waves with a possible resonant excitation of second baroclinic mode waves on intraseasonal time scales.

A large scale pattern of variability matching what was presented in Chapter 4 was recently mapped by *Vialard et al.* (2009). They observed intraseasonal fluctuations in alongshore current off the west coast of India and were able to predict this variability from altimeter-derived sea level. The local sea level changes were then traced back to this coherent basin-scale pattern in the 70–90 day band. They claim that zonal surface winds drive equatorially trapped Kelvin waves which then excite a coastal response upon reaching the eastern boundary. This response is partly radiated back into the basin (along 5°N and 5°S) as Rossby waves and partly sent around the Bay of Bengal as coastal trapped waves. Later, a reversal in the wind pattern reinforces these dynamics. *Webber et al.* (2010) observed the same pattern described above and claim that the westward propagating signals, with phase speeds of 0.7 m/s, are meridional mode 1 baroclinic Rossby waves and that these waves are locally forced as they propagate. These Rossby waves were also noted by *Girishkumar et al.* (2011) who examined the intraseasonal variability in the barrier layer thickness (the difference between the mixed layer depth and the isothermal layer depth, i.e., the depth where T is 0.8°C less than SST) at [8°N,90°E]. They found that intraseasonal variability in the barrier layer thickness is mainly controlled by the vertical movement of the isothermal layer depth. In the southern Bay of Bengal they attribute this variability to the westward propagating intraseasonal Rossby waves and claim that they are remotely forced by intraseasonal surface winds in the equatorial Indian Ocean.

In the Pacific Ocean, energy that is remotely forced by the MJO is radiated away from the forcing region. Conversely, in the Indian Ocean, MJO-excited energy can return to the forcing region by way of reflected Rossby waves and coastally trapped waves propagating around the Bay of Bengal. Therefore, the Indian Ocean response has the potential for feedback with the MJO itself. *Webber et al.* (2010) speculate that these westward Rossby waves, once they reach the western Indian Ocean, may help trigger the next MJO event due to associated SST anomalies.

It was shown in Chapter 4 (see also *Oliver and Thompson* (2010)) that sea level in the northeastern Indian Ocean has a statistically significant and dynamically complex relationship with the MJO. In this chapter, several important questions related to the effect of MJO-related surface forcing on the northeastern Indian Ocean are addressed. What is the depth-dependence of this response? Can the variability be described by known dynamical modes, i.e., equatorially trapped waves? Finally, what is the physical cause of this variability and does the MJO provide some predictability in the system?

Tide Gauge	Latitude	Longitude	Start	End	% Complete
Gan, Maldives	0°41′S	73°9′E	12/7/1991	8/3/2009	99
Colombo, Sri Lanka	6°57′N	79°51′E	16/7/1989	26/8/1992	94
Sabang, Indonesia	5°50′’N	95°20′E	21/12/2005	21/4/2008	100

Table 6.1: Details on the tide gauge records. See Figure 6.1 for locations.

The basin scale pattern in the northeastern Indian Ocean described above will be generated by a general circulation model forced by realistic winds. The general circulation model is validated by comparison with altimeter-derived measurements of sea level, coastal tide gauge observations and ADCP-measured currents. Then the effect of MJO-related surface forcing will be examined in the three-dimensional ocean state in order to characterize the response of the ocean at depth and detect equatorially trapped waves based on dynamical theory. Finally, the physical cause of the observed variability will be determined with a series of process studies.

This chapter is organized as follows. The observations and a preliminary statistical analysis are presented in Sections 6.2 and 6.3. The model is described in Section 6.4. The model results are validated against observations and the dynamics examined in Section 6.5. The source of the variability and its predictability are discussed in Section 6.6. A summary of the results, and a discussion of future work, are found in Section 6.7.

6.2 Observations of Sea Level, Currents, MJO Index, and Surface Wind

Observations of the MJO index, sea level, ocean currents, and atmospheric forcing are presented here. The altimeter-based observations of sea level, which were used in Chapter 4, have been supplemented with coastal observations from tide gauges and ADCP profiles of ocean currents. The observations of sea level and currents are used to validate the global general circulation model that is forced by reanalyzed atmospheric fields.

6.2.1 The Madden-Julian Oscillation Index

The MJO is characterized using the bivariate index of *Wheeler and Hendon* (2004). Daily values from 1/1/1979 to 30/12/2006 were obtained from the Government of Australia

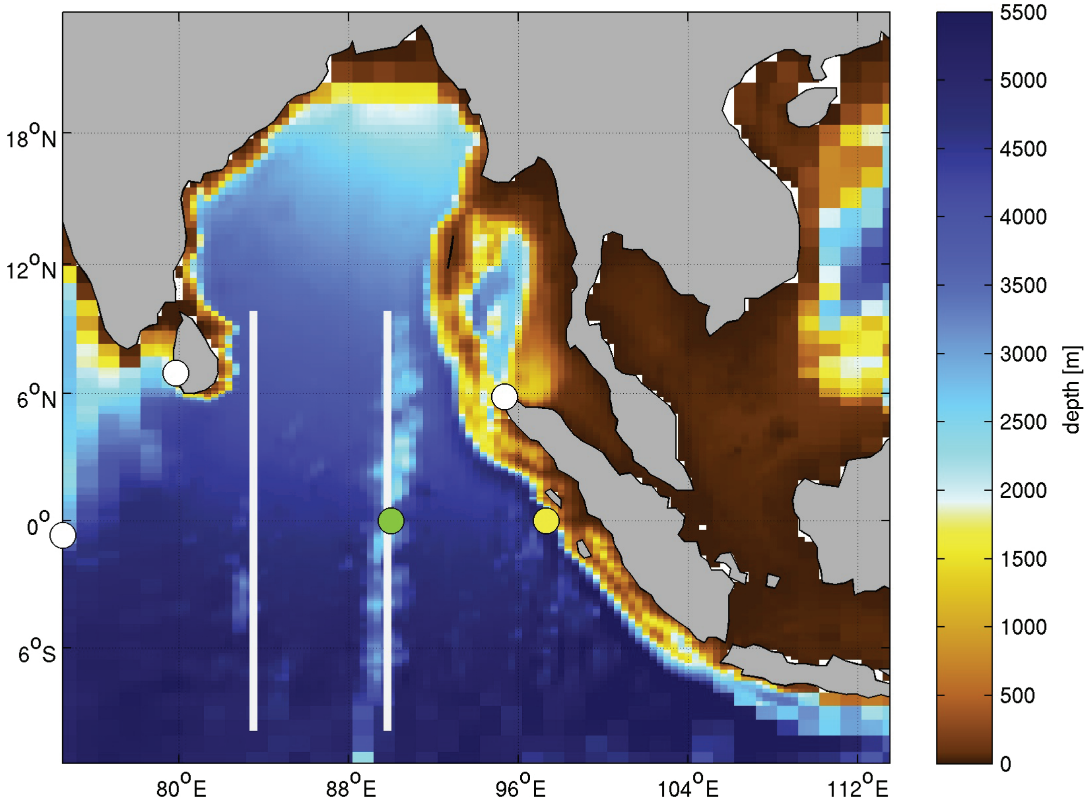

Figure 6.1: The domain and bathymetry of the high resolution submodel which is nested within the global model. The grid size in the meridional direction varies from 1/9° at the equator to 1/3° near the northern boundary; the grid size in the zonal direction is everywhere 1/3°. The blocky bathymetry around the edges are the connection points at which the depth is defined by the coarse bathymetry. The vertical lines indicate the meridional sections along which the depth-dependent flow is analyzed in Section 6.5.3. The three white circles show the locations of the tide gauges. The Gan tide gauge (left-most white circle) is actually located 150 km further west than indicated, which is outside the domain of the high resolution nest. The green circle indicates the location of the RAMA ADCP data. The yellow circle indicates the location used for an illustration of predictability in the final section.

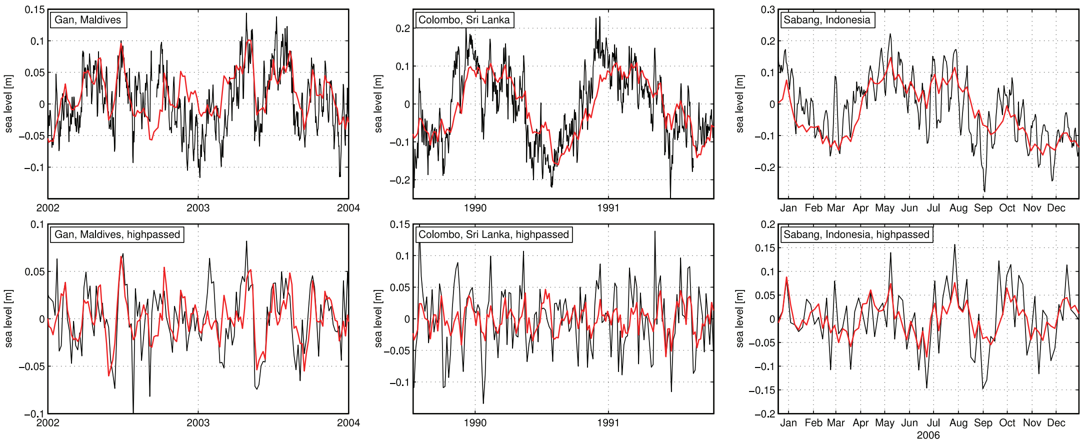

Figure 6.2: Observed and predicted sea level at three locations in the northeastern Indian Ocean. The observed sea level, after removing the mean, linear trend, and inverse barometer effect, is shown in the upper panels (black lines) for Gan, Maldives (left), Colombo, Sri Lanka (middle), and Sabang, Indonesia (right). The observed sea level, after filtering out variability on time scales longer than 120 days and then interpolating to the model output step, is shown in the lower panels (black lines). The red lines show the corresponding model predictions of isostatically adjusted sea level from the FULL run. The predicted sea level for Gan was taken from the coarse resolution global model; the predicted sea level for Colombo and Sabang were taken from the high resolution nest.

Bureau of Meteorology[1].

6.2.2 *Sea Level from Altimeters*

Global fields of weekly altimeter measurements of sea level were obtained from Aviso[2] on a 1/4° resolution grid for the period 14/10/1992 to 22/7/2009. Aviso has removed the seven-year mean, adjusted the data for the inverse barometer effect and corrected for tides. The annual cycle and its first two harmonics were removed by linear regression.

6.2.3 *Sea Level from Tide Gauges*

Hourly time series of sea level were obtained from three tide gauge locations around the northeastern Indian Ocean from the Hawai'i Sea Level Center. (See Figure 6.1 for locations and Table 6.1 for details such as time period covered and completeness.) The records were de-tided using the analysis package of *Pawlowicz et al.* (2002) using 68 tidal constituents and then averaged to daily values. The inverse barometer effect was removed

---

[1] `http://www.bom.gov.au/bmrc/clfor/cfstaff/matw/maproom/RMM/index.htm`

[2] `http://www.aviso.oceanobs.com/en/home/index.html`

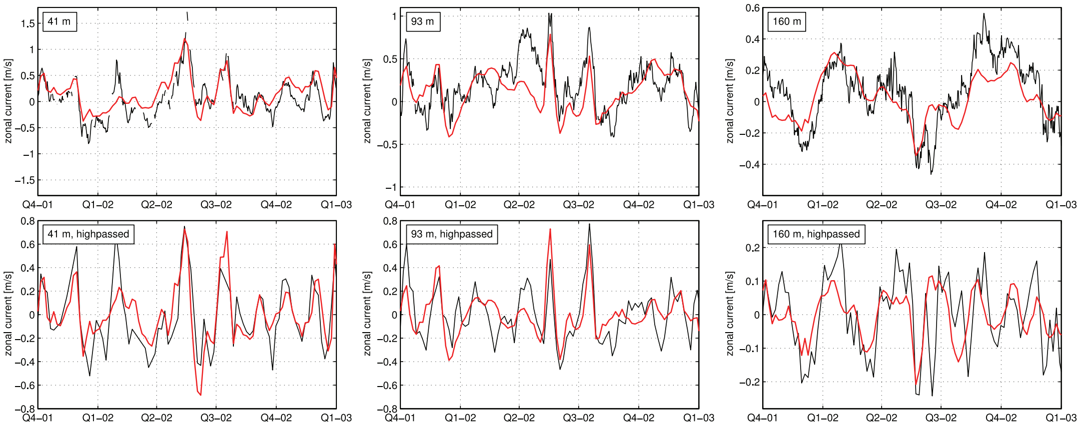

Figure 6.3: Observed and predicted zonal current at [0°N,90°E] and depths of 41 m, 93 m, and 160 m. The observed current, after removing the mean and linear trend, is shown in the upper panels (black lines). The observed current, after filtering out variability on time scales longer than 120 days and then interpolated to the model output step, is shown in the lower panels (black lines). The observed current has been linearly interpolated to model depths of 41 m (left), 93 m (middle), and 160 m (right). The red lines show the corresponding model predictions from the FULL run. For all depths the predicted currents were taken from the high resolution nest. The location of the ADCP profiles is shown by the green dot in Figure 6.1.

using daily sea level pressures from the NCEP/NCAR Reanalysis 2 (*Kanamitsu et al.*, 2002) defined on a 2.5° grid. Sample plots of the time series are shown in Figure 6.2.

6.2.4 Zonal and Meridional Currents from ADCPs

Daily time series of ADCP-measured zonal and meridional currents at [90°E,0°N] (green dot, Figure 6.1) were were obtained from the RAMA array which is part of the Tropical Atmosphere Ocean (TAO) project[3] for 18/11/2000 to 29/11/2006. This location was chosen over other RAMA locations after considering data length, completeness, and colocation with model output used in later analyses. Currents were obtained for depths between 40 m and 180 m at 10 m intervals. Sample plots of the time series are shown in Figure 6.3.

6.2.5 Atmospheric Forcing Fields

Global fields of 10 m zonal and meridional wind, 10 m air temperature, 10 m specific humidity, shortwave and longwave radiation, and liquid (rain) and solid (snow) precipitation were obtained from the Common Ocean-ice Reference Experiment version 2 (COREv2)

---

[3] `http://www.pmel.noaa.gov/tao/index.shtml`

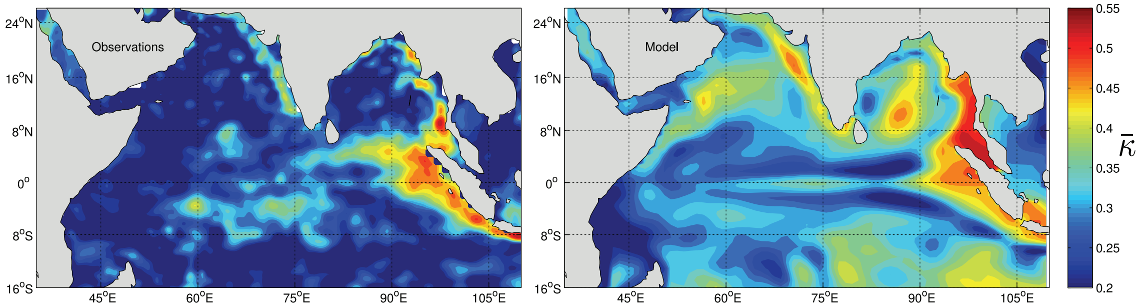

Figure 6.4: Maps of the amount of tropical Indian Ocean sea level variability related to the MJO. The left panel shows $\bar{\kappa}$, the proportion of the standard deviation accounted for by the MJO, for altimeter-derived sea level (regional subset of Figure 4.1). The right panel shows $\bar{\kappa}$ for the predicted sea level from the global model (FULL run). Observed and predicted sea level have had variability on time scales longer than 120 days filtered out prior to analysis.

reanalysis[4]. COREv2 is generated by combining and correcting a variety of reanalyses and data sources (*Large and Yeager*, 2009) and was used because it was prepared especially for use as forcing in ocean modelling experiments. The data are defined on a global T62 Gaussian grid with an approximate resolution of 2° and with sample rates of monthly (for precipitation), daily (for longwave and shortwave radiation), and 6-hourly (for wind, temperature, and humidity). Both climatological forcing (Corrected Normal Year Forcing, or CNYF) and realistic forcing over the period 1979 to 2006 (Corrected Inter-Annual Forcing, or CIAF) were obtained.

6.3 Intraseasonal Variability of Observed Sea Level, Currents and Atmospheric Variables

It was shown in Chapter 4 that the MJO can account for up to 50% of the standard deviation of altimeter-derived sea level after filtering out variability on time scales longer than 120 days (e.g., Figure 6.4, left panel). Additionally, there is significant intraseasonal variability in observed tide gauge records of sea level (Figure 6.2, lower panels) and ADCP records of zonal current (Figure 6.3, lower panels). The MJO index accounts for a significant amount of sea level variability in tide gauge records especially at Colombo and Sabang (~ 0.5, see Table 6.2). In addition, the MJO index accounts for a significant amount of zonal

---

[4] `http://data1.gfdl.noaa.gov/nomads/forms/mom4/COREv2.html`

Sea Level Station	ρ	Observed $\bar{\kappa}$	Predicted $\bar{\kappa}$
Gan, Maldives	0.52	0.25	0.34
Colombo, Sri Lanka	0.50	0.46	0.51
Sabang, Indonesia	0.66	0.64	0.69

Zonal Current Depth (m)	ρ	Observed $\bar{\kappa}$	Predicted $\bar{\kappa}$
41	0.74	0.50	0.46
52	0.74	0.48	0.46
64	0.73	0.47	0.43
77	0.71	0.47	0.42
93	0.66	0.41	0.42
112	0.56	0.35	0.41
134	0.56	0.31	0.41
160	0.56	0.33	0.41

Meridional Current Depth (m)	ρ	Observed $\bar{\kappa}$	Predicted $\bar{\kappa}$
41	0.48	0.30	0.35
52	0.52	0.30	0.35
64	0.51	0.30	0.34
77	0.48	0.29	0.32
93	0.45	0.25	0.32
112	0.46	0.31	0.31
134	0.39	0.30	0.32
160	0.36	0.31	0.31

Table 6.2: Correlations between observed and predicted (FULL run) sea level, zonal current and meridional current and their relationship to the MJO. The correlations between observed (tide gauges, ADCP) and predicted series are denoted by ρ. The proportions of standard deviation accounted for by the MJO index are denoted by $\bar{\kappa}$. Observed and predicted sea level and currents have had variability on time scales longer than 120 days filtered out prior to analysis. The predicted sea level for Gan was taken from the coarse resolution global model; the predicted sea level for Colombo and Sabang were taken from the high resolution nested model. The predicted currents for all depths were taken from the high resolution nested model.

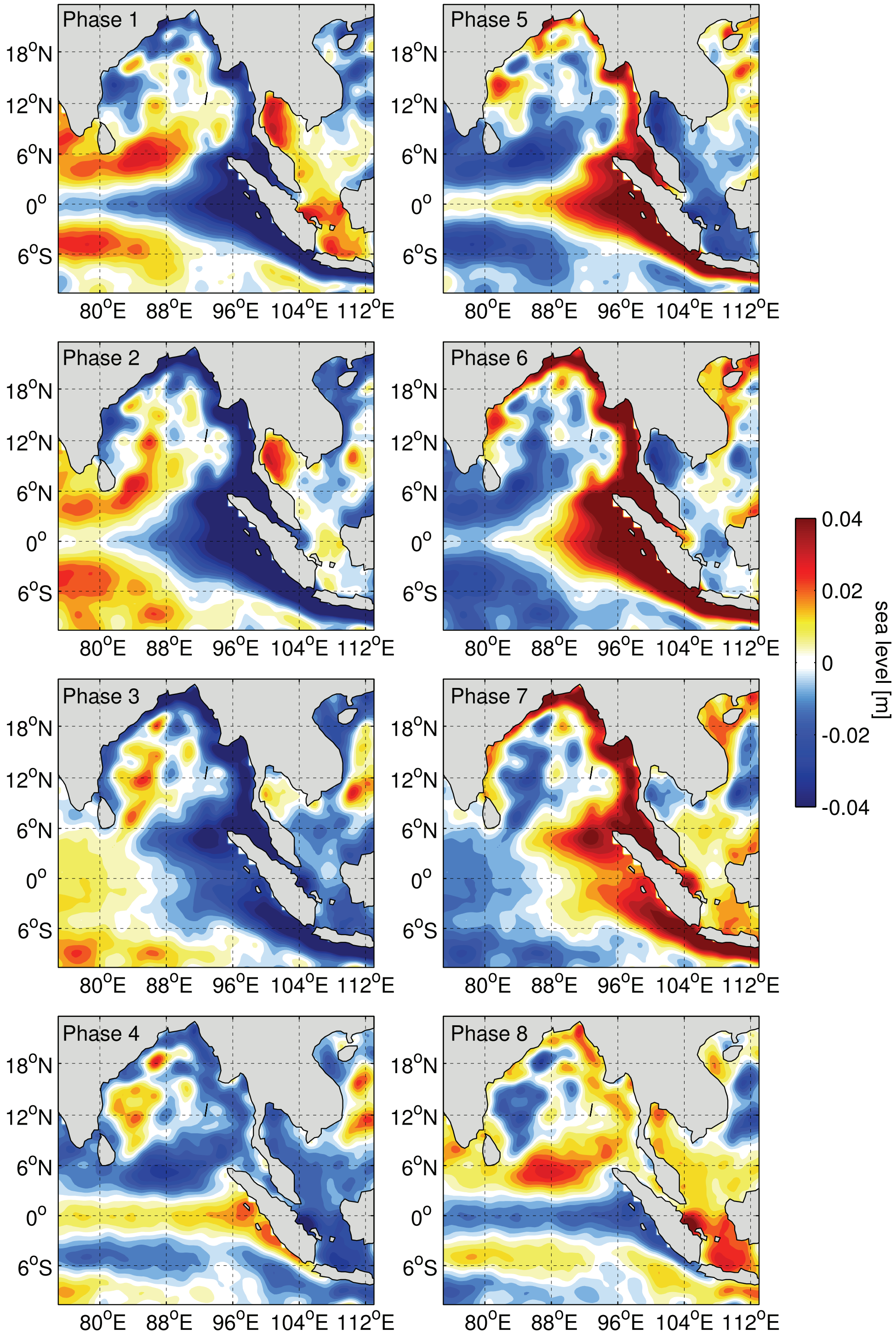

Figure 6.5: The MJO response of observed sea level for the eight MJO phases. The annual cycle and its first two harmonics were removed from the sea level by linear regression prior to analysis.

current variability, especially at shallower depths (~ 0.5), but accounts for less variability in meridional current (< 0.3).

Sea level observed by altimeters at each location were regressed onto the two components of the MJO index using the linear model

$$\eta_t = \beta_0 + \beta_1 I_{1,t} + \beta_2 I_{2,t} + \epsilon_t, \tag{6.1}$$

where η_t is sea level at time t, $I_{1,t}$ and $I_{2,t}$ are the first and second components of the MJO index respectively, $\{\beta_i | i = 0, 1, 2\}$ are the regression coefficients, and ϵ_t is an error term corresponding to measurement error and effects not included in the model[5]. The estimated regression coefficients, $\hat{\beta}_1$ and $\hat{\beta}_2$, were calculated by least squares and the "MJO-reconstructed" sea level is given by

$$\eta_t^{\mathrm{MJO}} = \hat{\beta}_1 I_{1,t} + \hat{\beta}_2 I_{2,t}. \tag{6.2}$$

For all variables, both from observations and model predictions, the "MJO-reconstructed" variable is calculated using Equation 6.2 and the *Wheeler and Hendon* (2004) MJO index for $I_{1,t}$ and $I_{2,t}$. The "MJO response" of sea level is calculated using a sinusoidal MJO oscillation of amplitude a, i.e., [$I_{1,t}$,$I_{2,t}$] = [$a\cos\phi$,$a\sin\phi$] where $\phi = -7\pi/8, -5\pi/8 \ldots 7\pi/8$ (corresponding to the MJO phases 1,2. . .8). An amplitude of $a = 2$ was chosen in order to examine the response to a moderate/strong MJO cycle. For all variables, both from observations and model predictions, the "MJO response" is given by Equation 6.2 using a sinusoidal MJO index at the eight phases listed above.

The MJO response of observed sea level (Figure 6.5) illustrates the basin-scale pattern that was described in Chapter 4. A sea level depression propagates eastward along the equator from phase 8 to phase 2 at which point it causes sea level to fall at the coast of Sumatra. This coastal signal propagates poleward around the Bay of Bengal and along southern Sumatra and Java during phases 1 through 4. Additionally, an off-equatorial signal is reflected off of the eastern boundary and can be seen propagating westward along 5.5°N as far as Sri Lanka for phases 3 to 6. At phase 4 this pattern is repeated with opposite sign starting with a positive sea level anomaly propagating eastward along the equator.

---

[5] This simple model is appropriate if the response time of sea level to surface forcing is short compared to the period of the MJO. If this criterion is satisfied then maps of β_1 and β_2 can be interpreted as "response patterns" of sea level to the MJO.

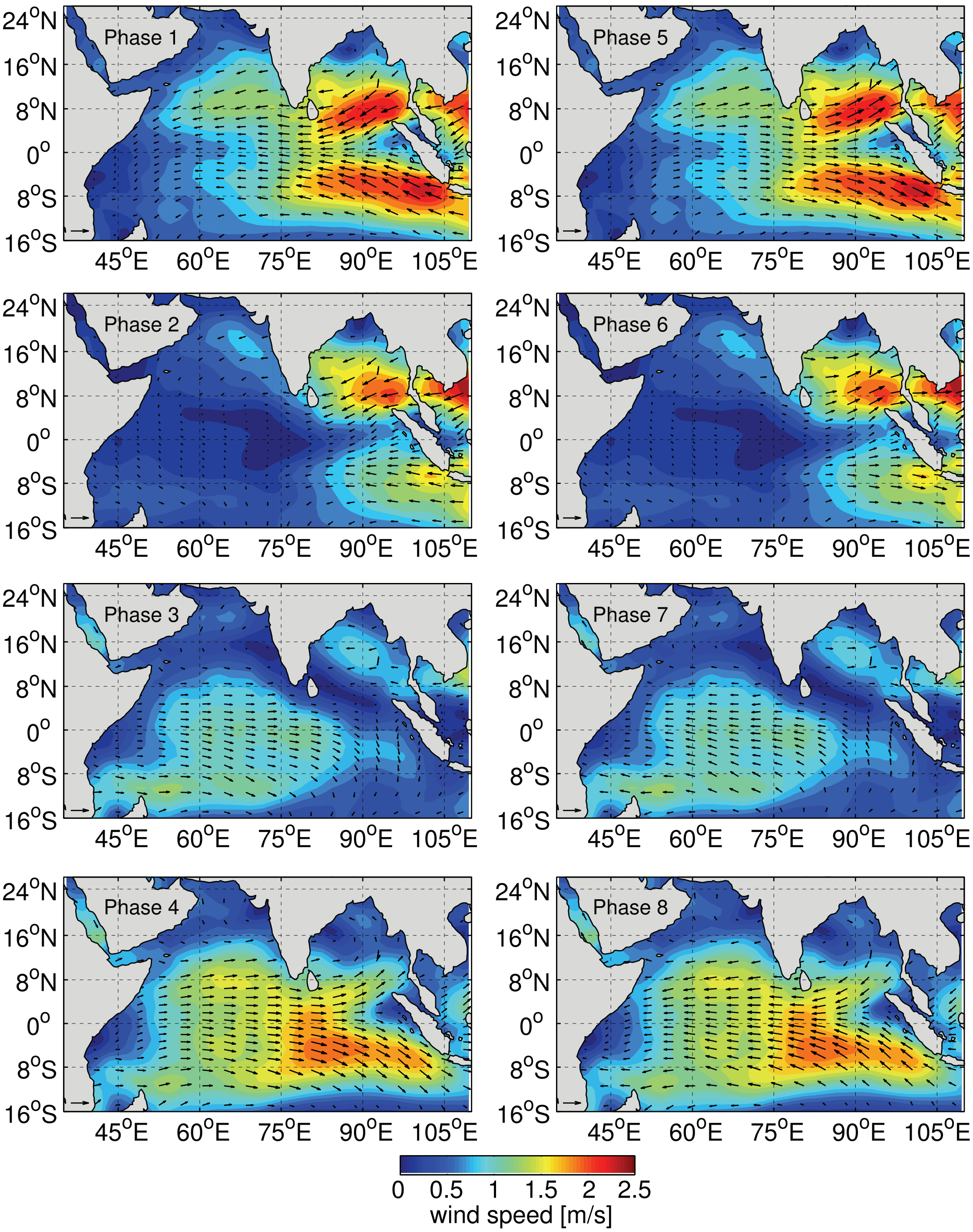

Figure 6.6: The MJO response of 10 m wind for the eight MJO phases. The arrows show wind direction with arrow length proportional to speed; the coloured contours show wind speed. The arrow in the lower left corner indicates a wind speed of 1 m s^{-1}. The annual cycle and its first two harmonics were removed from the wind by linear regression prior to analysis.

The influence of the MJO on atmospheric forcing was examined by regressing zonal and meridional wind onto the MJO index as above. The MJO response of wind propagates eastward over the tropical Indian Ocean as the MJO cycles through its phases (Figure 6.6). Zonal wind is strongest along the equator during phases 4 and 8. These phases correspond to when the sea level signal is excited along the equator. The signal is also strong off the equator (3–12°N and S) in phases 4 to 6 and 8 to 2. The two off-equatorial regions of strong wind may be due to seasonality, i.e., the zonal wind is strong just north of the Equator in Boreal Summer and just south of the Equator in Boreal Winter (e.g., *Wheeler and Hendon* (2004)). The phases at which the wind is strongest off the equator correspond to when the sea level signal is propagating westward along 5.5°N and 5.5°S. The observed timing suggests that the observed sea level pattern may be driven by a combination of local and remote forcing. Air temperature is strongest in the southeastern and northwestern Indian ocean with predominantly eastward propagation over the equatorial Indian Ocean (not shown); specific humidity is strong in a large swath of the Indian ocean stretching from the northwest to the southeast and propagates eastward and southward (not shown).

A global circulation model, described in the next section, with a high resolution nested submodel in the northeastern Indian Ocean is used to examine the role surface forcing plays in exciting the complex sea level pattern described above, and also provide complete three-dimensional fields of ocean variables so that the influence of the MJO can be examined below the surface. A series of sensitivity studies is then performed to determine the physical cause of the observed variability.

6.4 Numerical Model

The Nucleus for European Modelling of the Ocean (NEMO, e.g. *Madec* (2008) and Section 3.4.2) was used to dynamically simulate the global ocean. In the horizontal the model is defined on a tripolar ORCA1 grid with one pole in Antarctic, a second in Canada, and a third in Siberia. The grid has a nominal resolution of 1° but is refined meridionally in the tropics and reaches a minimum of 1/3° near the equator. The grid spacing reduces near the poles but this is only relevant for the ocean around the Canadian Arctic Archipelago where the grid size reaches a minimum of 25 km.

The model bathymetry has been derived from version 9 of the *Smith and Sandwell*

(1997) global dataset at 1-min resolution[6] and interpolated to the model grid. The model has a maximum of 46 z-levels in the vertical with partial cells at the bottom. The model uses a linear free surface formulation. Level thickness increases from 6 m at the surface to a maximum of almost 250 m for the bottom-most level. The maximum depth is 5720 m.

A grid with a resolution increased by a factor of three in both directions was created using the AGRIF adaptive mesh refinement tool[7] in the northeastern Indian Ocean. The boundaries of the high-resolution nest are 73.5°E, 111.5°E, 12.2°S and 21.4°N. The bathymetry for the nest region was interpolated from a high resolution (ORCA025) grid and smoothed (Figure 6.1). A connection zone lies around the inner edge of the nest for which the depth is defined by the coarse bathymetry. The nesting is performed two-way so that the coarse model supplies the boundary conditions to the nest and the nest feeds information back to the coarse model.

The model is integrated using a filtered, three-level time-stepping scheme (see Equation 3.39 and associated text). The time step for the calculations was 3600 s (1 hour) thereby satisfying the CFL condition for stability. The coastal boundary conditions for velocity were no normal flow and no-slip; for other variables it was no flux into the coast. Horizontal tracer diffusion is parameterized using a Laplacian scheme along isopycnals. Horizontal momentum mixing is parameterized using a Laplacian scheme along horizontal planes. The horizontal mixing coefficients are proportional to the size of the horizontal grids. The maximum values of horizontal mixing coefficients are $K_{\mathrm{h}} = 1000$ m s^{-1} for diffusivity and $A_{\mathrm{h}} = 10000$ m^2 s^{-1} for viscosity.

The model is forced by 10 m surface wind, 10 m surface air temperature, 10 m specific humidity, longwave and shortwave radiation, and liquid and solid precipitation interpolated to the model time step and grid. Note that the model is not forced by variations in atmospheric pressure. The model calculates surface fluxes from bulk formulae using the atmospheric forcing and the predicted ocean state.

The model was spun-up for 10 years using the CNYF of COREv2 representing the climatology, i.e., the climatological forcing was repeated each year for 10 years. The FULL run was continued from the end of the climatology spin-up of the model and was forced using the CIAF of COREv2 for 28 years covering the period 1979 to 2006 (see Table 6.3). Sea surface height and three-dimensional fields of velocity, temperature, and

---

[6] `http://topex.ucsd.edu/marine_topo/mar_topo.html`

[7] `http://www-ljk.imag.fr/MOISE/AGRIF/index.html`

Name	Start	End	Length (yrs)	Notes
CLIM	-	-	10	Climatological forcing
FULL	1 Jan 1979	31 Dec 2006	28	Realistic forcing
HEAT	1 Jan 1979	31 Dec 1986	8	Climatological momentum flux
MJO1	1 Jan 1979	31 Dec 1986	8	Remote MJO forcing
MJO2	1 Jan 1979	31 Dec 1986	8	Local and remote MJO forcing

Table 6.3: Details of model runs including name, start date, end date, duration, and forcing fields. The FULL, HEAT, MJO1, and MJO2 runs were continued from the end of the 10-year CLIM run.

salinity, were output every 5 days (sufficient for my purposes because my interest is in variability on intraseasonal timescales).

6.5 Validation and Analysis of the FULL Run

In this section the model output is validated by comparing it to observed sea level and currents of the FULL run. Then the analysis is extended to the complete three-dimensional ocean state by exploring how the predicted flow fields vary with MJO forcing. Finally, dynamical wave modes are fit to the model output in an attempt to explain the MJO-related component of the three-dimensional flow.

6.5.1 Validation of Predicted Sea Level and Currents

Predicted sea surface height at the tide gauge locations listed in Table 6.1 are shown in Figure 6.2 (red lines). The model is able to capture the seasonal cycle, the 1997/1998 El Niño event (not shown), and the intraseasonal variability. The correlations between tide gauge records and predictions, after filtering out variability on time scales longer than 120 days, is 0.50–0.66 indicating that the model is predicting observed sea level reasonably well. Predicted zonal currents at [90°E,0°N] and three depths are shown in Figure 6.3 (red lines). The model is able to capture the observed currents and their intraseasonal variability. The correlations between observed and predicted zonal current, after filtering out variability on time scales longer than 120 days, is 0.56–0.74 (highest for measurements closest to the surface). The correlations are much lower for meridional currents. In addition, the proportion of variability which is accounted for by the MJO is consistent between observed and predicted records of sea level and zonal and meridional currents and decreases with depth.

The MJO accounts for $\sim$50% of the standard deviation of predicted sea level in the northeastern Indian Ocean (Figure 6.4, right panel). The pattern, especially along the equator and eastern boundary, is similar to the pattern formed from observed sea level (Figure 6.4, left panel). However, there are regions where the MJO accounts for a significant amount of the variability, especially in the open ocean, which is not reflected in the observations. The model also fails to capture the full amplitude of the westward propagating signal along 5.5°N.

The variability in the FULL run which is coherent with the MJO was examined using the same technique used for the observations. The MJO response was calculated by first regressing the predicted fields onto the MJO index and then using a sinusoidal MJO index at the eight standard phases. The MJO response of modelled sea level matches reasonably well with observations in terms of amplitude and very well in terms of timing (Figure 6.7, contours).

6.5.2 Response of the Ocean to the MJO

In the previous section it was shown that the ocean model reproduces well the variability of observed sea level from altimeters and tide gauges and currents from ADCP profiles. These tide gauges and ADCP profiles are very sparsely distributed in space. The analysis is now extended to include the complete three-dimensional circulation predicted by the model.

The MJO response of sea level is shown for the eight MJO phases in Figure 6.7 (colour shading). The relationship between the predicted sea level and the MJO matches well with the observed relationship (compare with Figure 6.5). The fact that the MJO response of sea level is well captured by the model and that the $\bar{\kappa}$ map for predicted sea level (Figure 6.4) does not match as closely to observations may be indicative of poor representation of the total sea level variability (i.e., MJO and non-MJO related components combined) by the model (see Equation 2.18 for the relationship between $\bar{\kappa}$, total sea level variability, and MJO-related sea level variability).

The MJO response of near-surface (3 m) circulation is shown in Figure 6.7 (arrows). The circulation is dominated by (i) zonal flow at the equator, strongest in phases when the surface wind forcing is also strong and in the same direction, and (ii) alongshore flow following the propagation of sea level along the coast of Indonesia and the Bay of Bengal.

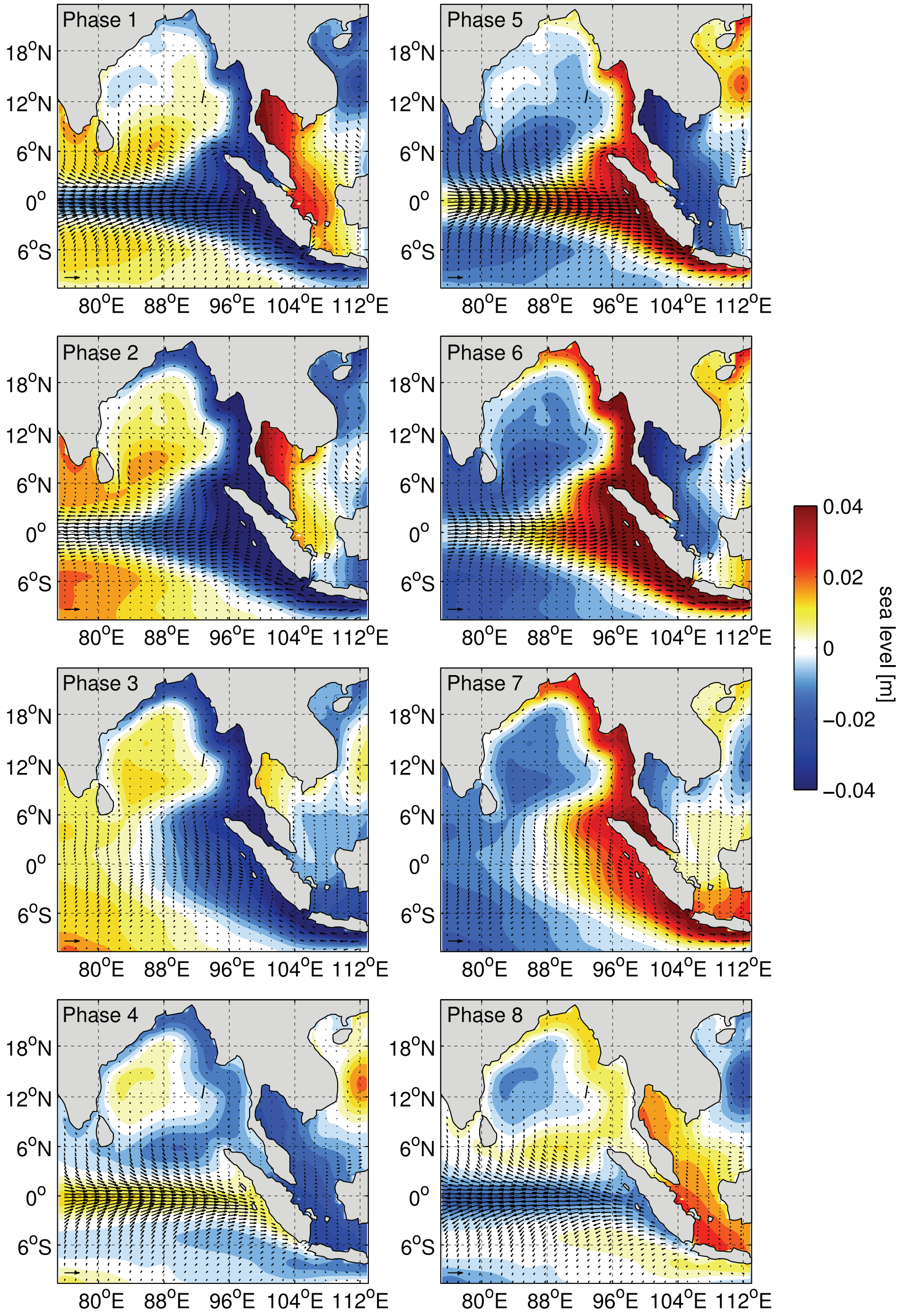

Figure 6.7: The MJO response of modelled sea level and horizontal velocity from the FULL run at 3 m depth for the eight MJO phases. The filled contours show sea level. The arrows show horizontal circulation; the arrow in the lower left corner indicates a current speed of 0.1 m s^{-1}. The annual cycle and its first two harmonics have been removed by linear regression prior to analysis.

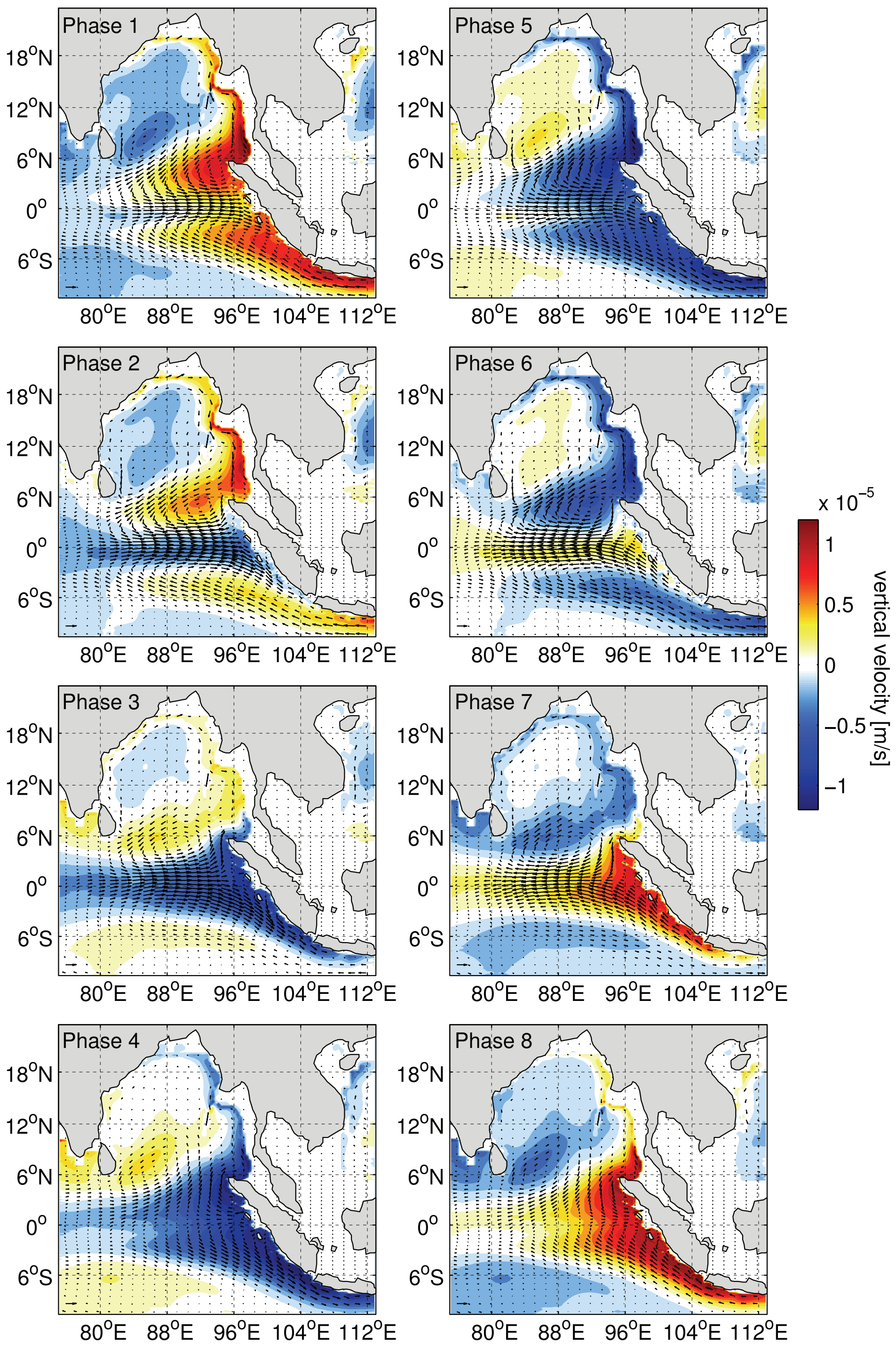

Figure 6.8: The MJO response of modelled vertical and horizontal velocity from the FULL run at 200 m for the eight MJO phases. Format identical to Figure 6.7 except that filled contours show vertical velocity. The arrow in the lower left corner indicates a current speed of 0.01 m s^{-1}. The annual cycle and its first two harmonics have been removed by linear regression prior to analysis.

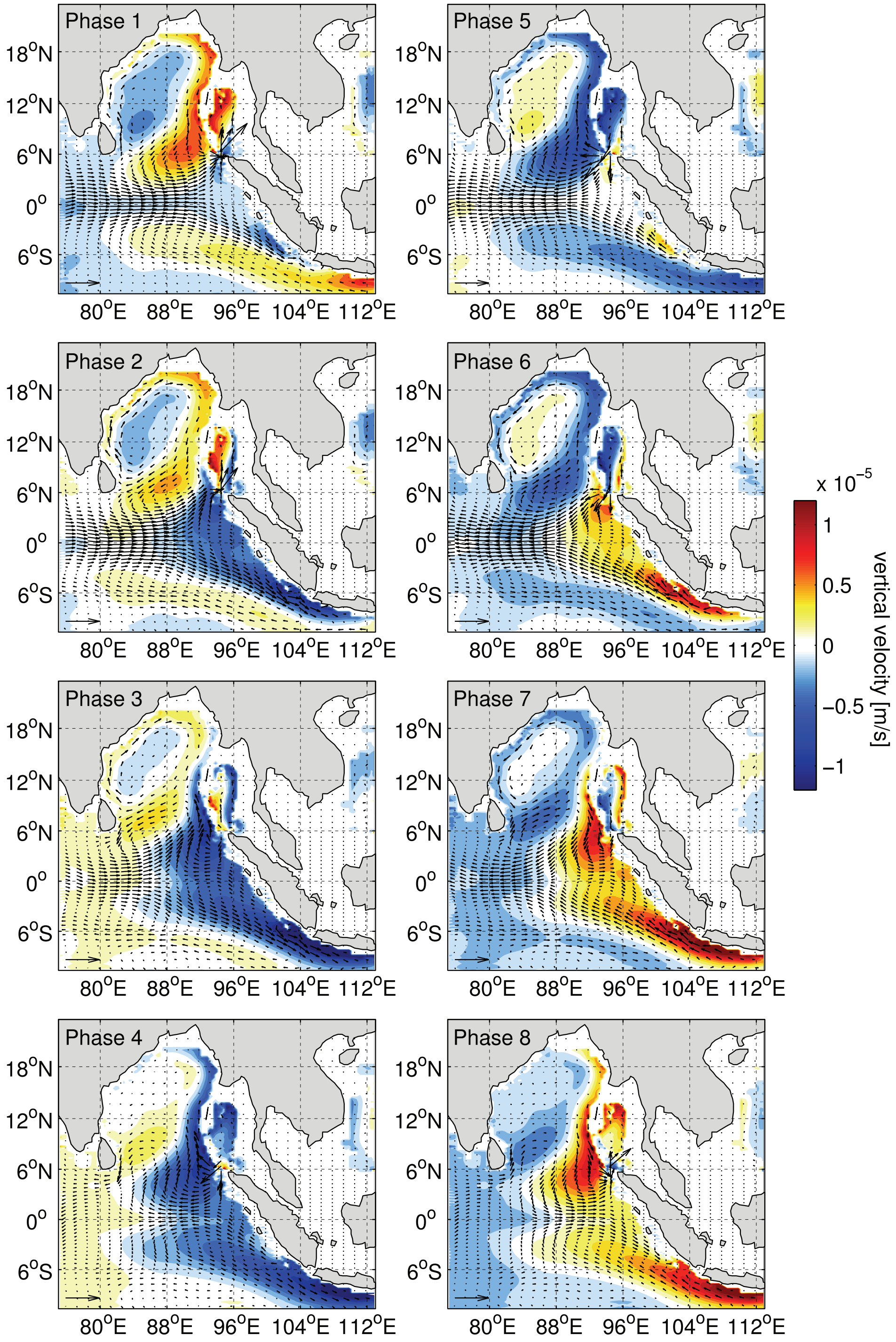

Figure 6.9: The MJO response of modelled vertical and horizontal velocity from the FULL run at 1000 m depth for the eight MJO phases. Format identical to Figure 6.8. The arrow in the lower left corner indicates a current speed of 0.01 m s^{-1}. The annual cycle and its first two harmonics have been removed by linear regression prior to analysis.

There is very little near-surface circulation signature of the westward propagating waves along 5.5°N.

The MJO response of horizontal and vertical velocity at 200 m and 1000 m depth are shown in Figures 6.8 and 6.9. The eastward propagating equatorial waves and the poleward propagating coastally trapped waves that are clear at the surface are well represented in all three fields at 200 m and 1000 m depths. Also evident are cyclonic and anticyclonic circulation cells about regions of downwelling and upwelling. These correspond to the westward propagating waves with wavelengths on the order of 2000–3000 km observed in sea level along 5.5°N. Typical velocities are 1–2.5 m s^{-1} in the horizontal and 10^{-5} m s^{-1} in the vertical; the vertical velocities lead to a vertical excursion of $\sim$10 m assuming an MJO period of 50 days. These signatures appear earlier at greater depths. These results support the idea of Kelvin and Rossby waves propagating along the equatorial waveguide which is tested against dynamical theory in the following subsection.

6.5.3 Physical Interpretation in Terms of Dynamical Wave Modes

The previous section provided evidence for the existence of equatorially trapped waves. In this section dynamical wave modes are fit to the model output to obtain a better physical understanding of their origin and evolution.

Sea level was subsampled to 25 latitude locations along each section. The cross-spectral matrix for MJO-reconstructed sea level from the FULL run along two North-South sections (at 83.5°E and 90°E, between 10°S and 10°N, thick lines in Figure 6.1) was calculated over 58 non-overlapping 175-day segments and then averaged across all segments. The analysis is carried out at a frequency corresponding to a period of 58.3 days (within the 40–60 day time scale range of the MJO, but on the slower end to be consistent with Chapter 4).

The sea level variability along these sections, calculated from the auto- and cross-spectra, supports the equatorial wave propagation interpretation given above (Figure 6.10, top row). For both sections, eastward propagating sea level variability is significant on the equator and westward propagating sea level variability is significant off the equator (4–8°N and S). Propagation speeds are calculated from the phase spectra between points of equal latitude on the two meridional sections, i.e., the time lag between sea level along the two lines at each latitude. The propagation speeds (1.68 m/s eastward on the equator and 0.39–1.13 m/s westward over the range 4–8°N) are within the ranges of the first three baroclinic mode (m =1,2,3) equatorially-trapped Kelvin waves and the first three baroclinic mode, first

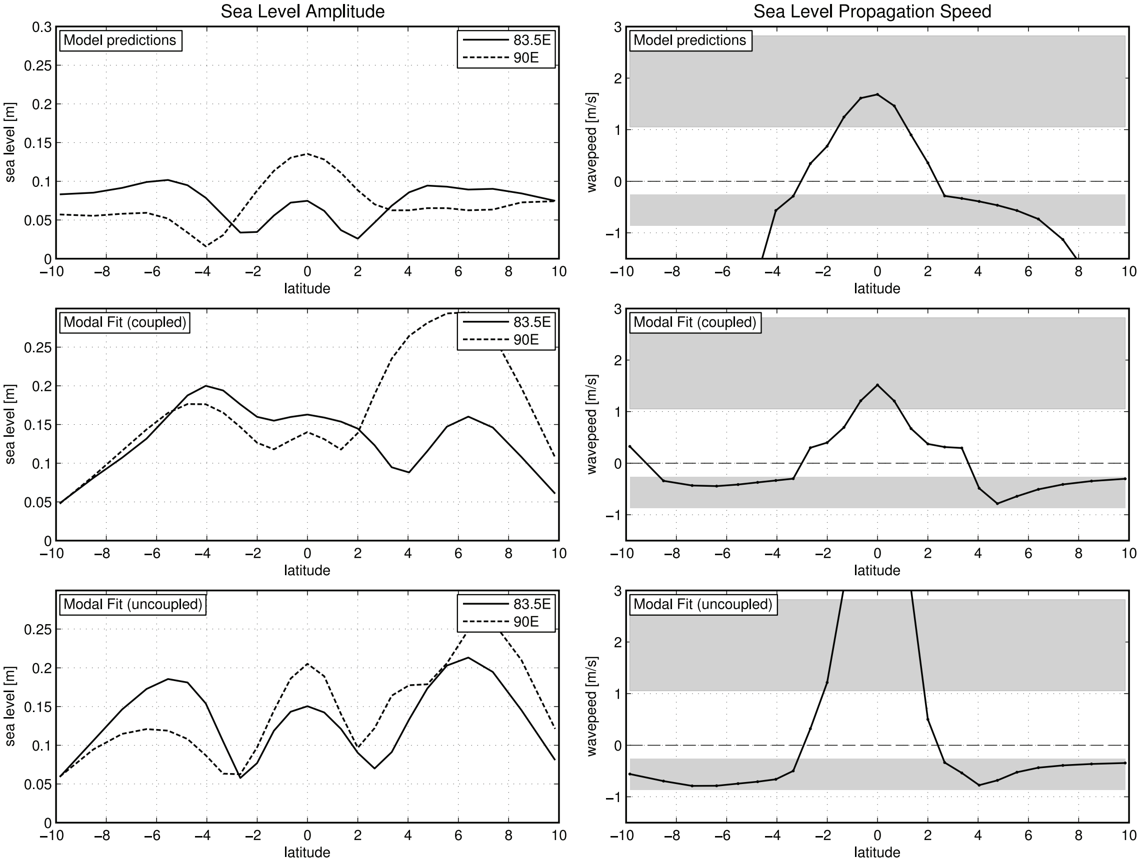

Figure 6.10: Sea level variability and phase propagation speeds for the FULL run and dynamical modal fits along 83.5°E and 90°E. Top row: the left panel shows the square root of the spectral density of the MJO-reconstructed sea level from the ocean model (at a period of 58.3 days) along 83.5°E (solid line) and 90°E (dashed line). The right panel shows the speed of sea level propagation, calculated from the cross-spectra (i.e., time lag) between the two sections at each at each latitude. Positive velocities are eastward, negative velocities are westward. Middle and bottom row: same format as the top row except for the dynamical modal fits using coupled sections (middle) and uncoupled sections (bottom, see text for discussion). The shaded regions show the range of Kelvin and Rossby wave speeds for the first 3 baroclinic wave modes (m =1,2,3) and the first meridional wave mode ($n = 1$).

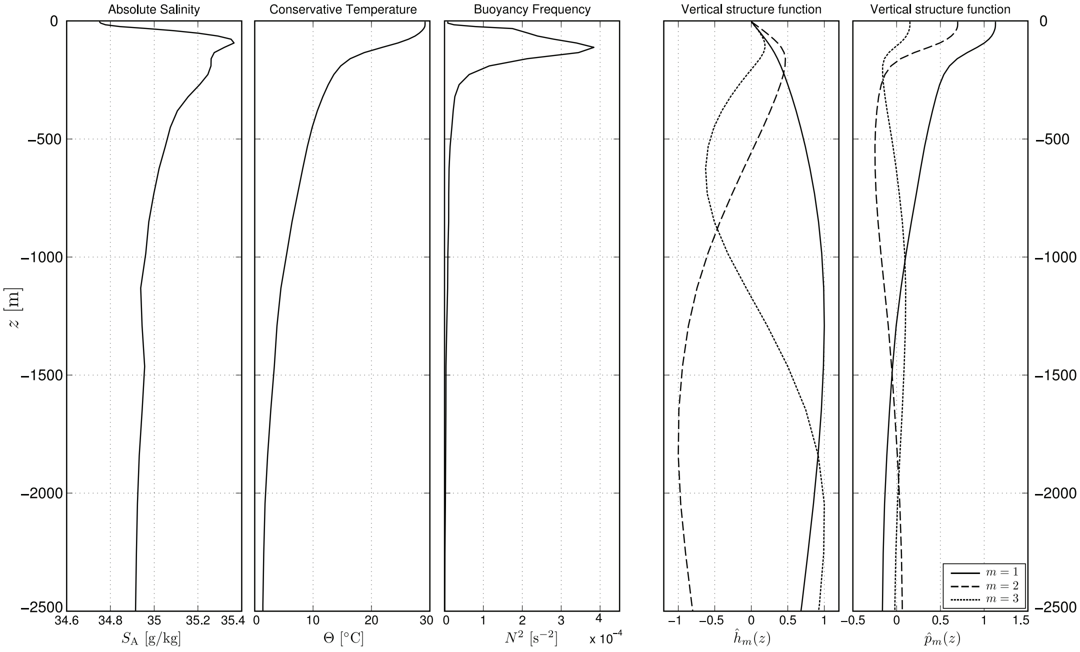

Figure 6.11: Vertical profiles of absolute salinity S_A, conservative temperature Θ, buoyancy frequency N^2, and the vertical structure functions $\hat{h}_m(z)$ and $\hat{p}_m(z)$ at 83.5°E and 90°E. The vertical structure functions are shown for the first three baroclinic modes ($m = 1, 2, 3$).

meridional mode (m =1,2,3, $n = 1$) equatorially-trapped Rossby waves (shaded regions). Additionally, sea level along 90°E propagates poleward, travelling from the equator to 5.5°N in 16.8 days.

To determine the existence of dynamical modes wave types have been identified with the Dynamical Modal Analysis (DMA) fitting technique (see Section 2.1.3) which expresses the fields as a linear combination of modes. The dynamical modes used are free waves on an equatorial β-plane linearized about a state of rest (see Section 3.3). These modes were fit to the three dimensional fields from the FULL run. The solution was decomposed into normal modes (see Section 3.2) and taken to be a linear combination of baroclinic mode equatorially trapped Rossby, Kelvin, and Yanai waves. The vertical structure functions, $\hat{h}_m(z)$ and $\hat{p}_m(z)$, and baroclinic wave speeds c_m are needed in order to calculate the dynamical wave forms. They obey the following equations:

$$\frac{d^2\hat{h}_m}{dz^2} + \frac{N^2}{c_m^2}\hat{h}_m = 0 \qquad (6.3)$$

$$\frac{d}{dz}\left(\frac{1}{N^2}\frac{d\hat{p}_m}{dz}\right) + \frac{1}{c_m^2}\hat{p}_m = 0, \qquad (6.4)$$

m	0	1	2	3
c_m [m/s]	198	2.82	1.73	1.05

Table 6.4: The wave speeds c_m calculated from the density profile shown in Figure 6.11. The barotropic mode is denoted by $m = 0$; the baroclinic modes are denoted by $m \geq 1$.

where $N^2(z)$ is the buoyancy frequency defined by

$$N^2 = -\frac{g}{\rho}\frac{d\rho}{dz}, \tag{6.5}$$

$g = 9.8$ m/s^2 is gravitational acceleration and $\rho = \rho(z)$ is the fluid density profile. Density profiles and buoyancy frequency were calculated from the average model temperature and salinity along these two meridional sections using the Gibbs SeaWater (GSW) Oceanographic Toolbox [8] (Figure 6.11, left panels). These profiles were then used to calculate the vertical structure functions, evaluated at the model z-levels (Figure 6.11, right panels), by solving Equations 6.3–6.4 numerically. This eigenvalue/eigenvector calculation was performed using the code written by J. Klinck and available on the Woods Hole SEA-MAT site[9]. It was performed assuming a constant depth equal to the average depth of the two sections (4029 m). The barotropic and first three baroclinic wave speeds are shown in Table 6.4. The first baroclinic mode wave speed of 2.82 m/s is consistent with *Chelton et al.* (1998) for the region being considered. The dynamical mode shapes in the horizontal were calculated using the functional forms given in Section 3.3.

Equatorially trapped wave modes were estimated by fitting the dynamical mode shapes to the model output along 83.5°E and 90°E using DMA. This technique is used for the case of wave propagation between two meridional sections (e.g., case (b) in Section 2.1.3). The model fields consist of the MJO-reconstructed sea level and zonal, meridional, and vertical velocity at depths down to 2000 m (30 vertical levels) and subsampled meridionally to 25 latitude points. Each field has been area weighted and then normalized to have unit total variance. Velocities below the minimum depth of the two sections were discarded ($\sim$2500 m along the Ninetyeast Ridge); in addition, velocities between 2000 m and 2500 m were also discarded as enhanced bottom flow over this ridge may contaminate the data.

Equatorially trapped Kelvin, Rossby, and Yanai waves for $m = 1, 2 \ldots 10$ and $n =$

---

[8] `http://www.teos-10.org/`

[9] `http://woodshole.er.usgs.gov/operations/sea-mat/`

m	1	2	3	4	5	6	7	8	9	10
Kelvin	0.01	0.07	0.02	-	-	-	-	-	-	-
Yanai	-	-	-	-	-	-	-	-	-	-
Rossby (1)	0.02	0.18	0.04							
Rossby (2)	0.01	0.03								
Rossby (3)	0.01									
Rossby (4)	-									

Table 6.5: Quality of fit Q for individual dynamical wave modes. Each wave type corresponds to a given row and each baroclinic mode m corresponds to a column. The numbers in parentheses for the Rossby wave modes indicate the meridional mode number n. The dashes indicate modes with $Q < 0.01$ (to two decimal places precision); the blank cells indicate the Rossby wave modes that are not permitted at a period of 58.3 days (see text).

$1, 2 \ldots 10$ were considered for a total of 120 possible mode shapes. In fact, there are only 27 possible mode shapes since many of the Rossby wave modes are not permitted at a period of 58.3 days, i.e., the Rossby wave dispersion curves for many of the modes are not defined for this oscillation period (see Figure 3.1). Barotropic waves have been ignored because their meridional trapping scale (∼2000 km) is on the order of the meridional extent of the sections and thus it would be difficult to distinguish different barotropic wave modes from each other and from variations in the meridional-mean ocean state. The meridional trapping scales of the baroclinic modes are ∼100–250 km.

The fit of individual wave modes was quantified by fitting with that mode only. The quality of fit Q, which lies between zero and one as defined by Equation 2.8, is highest for the $m = 2$ Kelvin wave and for the $m = 2$, $n = 1$ Rossby wave (see Table 6.5 for a summary of individual mode fits). Yanai waves do not fit the model variability well at all. Allowing for all 37 wave modes together leads to a quality of fit of $Q = 0.41$.

The sea level signal associated with the fit indicates a strong signal at the equator with significant amplitude off the equator (3–8°N and S) as well (Figure 6.10, middle row). At 90°E the off-equatorial sea level amplitude is stronger in the Northern Hemisphere than in the Southern Hemisphere; conversely, at 83.5°E the off-equatorial sea level amplitude is stronger in the Southern Hemisphere than in the Northern Hemisphere.

The propagation pattern of the dynamical mode fit is consistent with the interpretation given above: sea level at the equator propagates with an eastward wave speed of 1.52 m/s (Figure 6.10, middle row), then sea level signal along 90°E propagates from the equator in a poleward direction taking 13.9 days to reach to 5.5°N (not shown), finally sea level between 4°N–8°N propagates with westward wave speeds of 0.42–0.78 m/s (Figure 6.10, middle row).

There is mismatch between the fitted modes and the numerical model variability especially in the meridional amplitude structure (Figure 6.10). The modal fit lacks a clear separation between the equatorial and off-equatorial signal and is too large in general. My interpretation of the poor fit is that the DMA method is limited in two ways:

Limitation 1: Local Forcing The dynamical modes represent free waves. If the variability is locally forced, there is no reason why the forced response should project down onto a small number of free modes. In an attempt to allow for a more local, forced response, the modal amplitudes were uncoupled between the lines (see Section 2.1.3, case (b)). This allows each mode to have a different amplitude response at each section and the modes are no longer constrained to propagate between sections at the theoretical wave speed. The quality of fit for uncoupled wave modes is $Q = 0.56$ indicating that uncoupled wave modes fit the variability better than coupled wave modes ($Q = 0.41$). This is to be expected because the DMA has been given more degrees of freedom. It is encouraging to note that the propagation speeds between 4°N–8°N (0.39–0.77 m/s, Figure 6.10, bottom row) are consistent with the numerical model but the propagation speed at the equator is now much too large (4.63 m/s). There is a clearer separation of amplitude between the equatorial signal and the off-equatorial signal consistent with the FULL run. However, sea level amplitudes are still too large in general.

Limitation 2: Background State The dynamical wave modes are calculated from a β-plane linearized about a state of rest which is an approximation unlikely to hold in the real ocean. Therefore, it is likely that an inappropriate set of modes is being fit to the model output. *Chelton et al.* (2003) calculated the meridional structure of Rossby modes on an equatorial β-plane linearized about the observed background flow of the Equatorial Pacific Ocean. They suggested that asymmetric meridional shears in the mean equatorial current system alter the potential vorticity gradient which is in turn responsible for the observed asymmetries in free Rossby wave modes (see also *Perez et al.* (2005)). *Durland et al.* (2011) confirmed this and showed that the modification of the wave modes is strongly dependent on how the background potential vorticity gradient projects down onto each mode. The zonal currents along 83.5°E and 90°E from the FULL run are significantly different from zero and strongly seasonal (not shown) leading to modifications of the Rossby wave mode shapes. A superposition of members of an inappropriate set of modes will nonetheless be able to explain some of the variability. Therefore, the fit can be improved by providing the correct set of dynamical modes.

6.6 Physical Causes of Variability

Kelvin and Rossby waves were suggested in the previous section to play an important role in the MJO-related variability of the northeastern Indian Ocean. However, the interpretation is difficult due to a possible mix of local and remote forcing and a non-zero background state. This section will perform a series of process studies in order to gain insight into the physical cause of the MJO-related variability. First, the roles of momentum and buoyancy flux were examined. Second, the relative importance of local and remote forcing due to surface winds was examined.

6.6.1 Momentum Versus Buoyancy Forcing

The importance of momentum versus buoyancy forcing was examined with a process study. This process study was a model run, hereafter referred to as the HEAT run (see Table 6.3), identical to the FULL run with the exception that wind stress was calculated using the climatological (CNYF) 10 m wind velocities instead of using the realistic (CIAF) wind. Effectively, this is like turning off the wind stress on intraseasonal time scales where the MJO plays a role; on intraseasonal time scales the ocean variability will be driven primarily by buoyancy flux. The HEAT run was performed for 8 years covering the period 1979 to 1986.

The amplitude and phase of the MJO-response of sea level[10] for the HEAT run (Figure 6.12, second row of panels) exhibits a similar pattern to the FULL run (Figure 6.12, top row of panels) however the amplitude of the sea level response is significantly reduced with only a hint of the pattern seen in the FULL run. The phase propagation is preserved which is not surprising given the weak variations that are excited must still propagate along the same waveguides. However, the much reduced amplitude indicates that the role of wind stress is of primary importance in generating the waves described above.

---

[10] The amplitude of the MJO response is given by $a\sqrt{\hat{\beta}_1^2 + \hat{\beta}_2^2}$ and the phase is given by $\arctan(\hat{\beta}_2/\hat{\beta}_1)$ (see Equation 6.2).

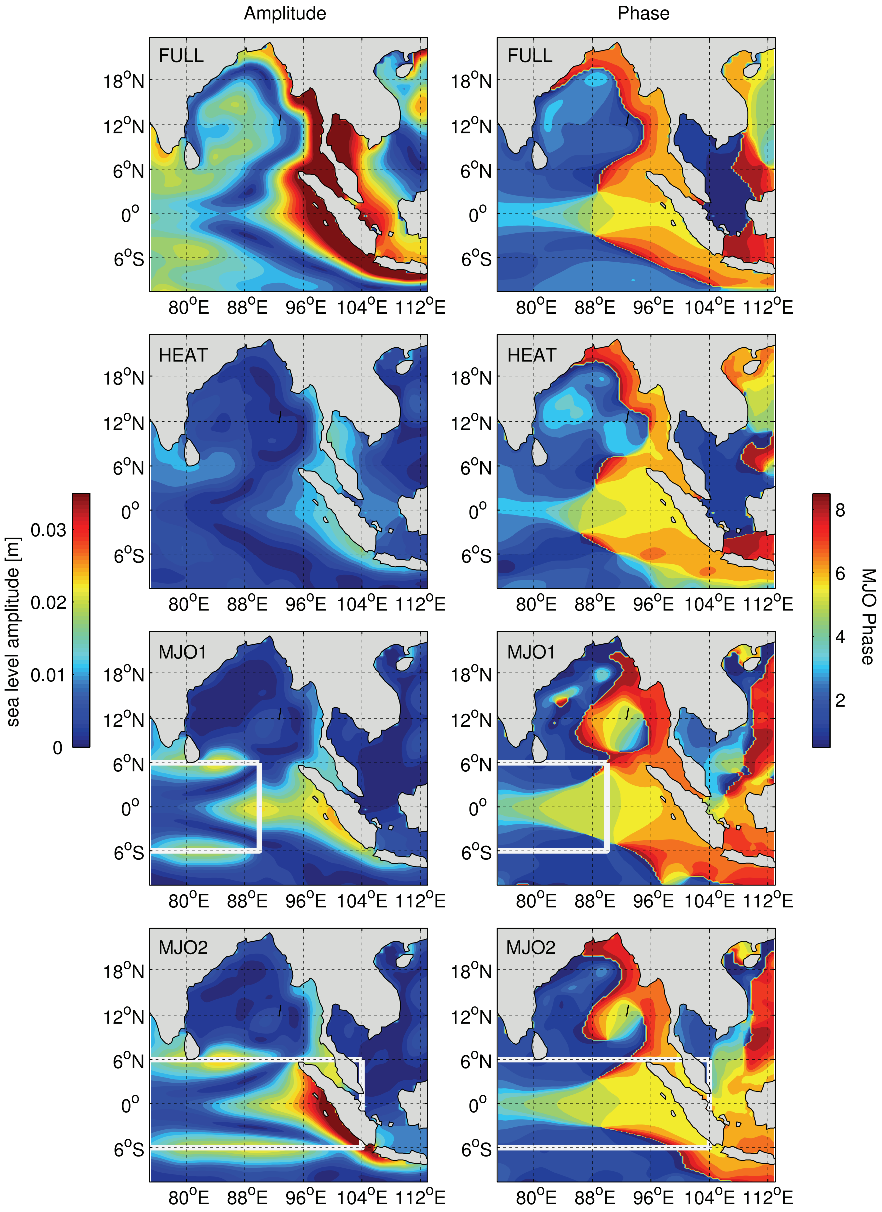

Figure 6.12: MJO response of sea level for various model runs. Amplitude (left) and phase (right) of MJO response of sea level for the FULL run (first row), the HEAT run (second row), the MJO1 run (third row), and the MJO2 run (fourth row). The left side colorbar is for amplitude; the right side colorbar is for phase. The white boxes show the geographic extent of the weighting functions used to restrict the MJO-reconstructed forcing in the MJO1 and MJO2 runs. All calculations have been performed over the same time period (1/1/1979–31/12/1986). Sea level has had the annual cycle and its first two harmonics removed by linear regression prior to analysis.

6.6.2 Role of Local and Remote Forcing by the MJO

The role of local and remote forcing by MJO-related atmospheric processes was examined with a pair of process studies in which the atmospheric forcing fields have been spatially restricted. Consider 10 m zonal wind forcing u_{ijt} at location (i, j) and time t which is due to a sum of climatology u^{c}_{ijt} and MJO-reconstructed wind u^{MJO}_{ijt}. In addition, the MJO-reconstructed wind forcing is localized in space by a weighting function w_{ij} with a range between 0 and 1:

$$u_{ijt} = u^{\mathrm{c}}_{ijt} + w_{ij} u^{\mathrm{MJO}}_{ijt}. \tag{6.6}$$

The MJO-reconstructed wind u^{MJO}_{ijt} is calculated using an equation of the form given by Equation 6.2.

Two process studies have been run with 10 m zonal and meridional wind, 10 m temperature, 10 m humidity, and longwave and shortwave radiation of the form given above. Solid and liquid precipitation, which are specified monthly and thus too coarse to resolve variability on intraseasonal time scales, are represented by climatological forcing only.

The first process study (MJO1) used a weighting function which is unity within the box defined by 50°E, 90°E, 6°S, and 6°N and zero elsewhere. This weighting function was chosen so that the ocean is forced “upstream” with regards to the equatorial waveguide, i.e., this process study represents a purely remotely forced run. The second process study (MJO2) extends the eastern edge of this box to 104°E in order to examine the role of mixed local and remote forcing. The edges of the boxes (shown in Figure 6.12) are defined by hyperbolic tangent functions, with a 1 degree length scale, in order to ensure a smooth transition between 0 and 1. See Table 6.3 for details on the model runs.

The pattern exhibited by the MJO response of sea level from the FULL run is also evident in both the MJO1 and MJO2 runs (Figure 6.12, third and fourth rows of panels). The signal is strong along the equator, the coast of Sumatra, and around the Bay of Bengal indicating that remotely forced equatorial Kelvin waves propagate freely and then excite a coastal response. Therefore, remote forcing is important for setting up the observed pattern. However, the MJO2 run has a stronger response than the MJO1 run. For the MJO1 run, the amplification of the equatorial signal towards the coast is strongly reduced east of 90°E (i.e., outside of the MJO-forced region). For the MJO2 run, where the MJO-forced region extends further eastward, the amplification of the equatorial signal continues right up to the eastern boundary indicating that local forcing is also important in generating both the coastal response and the equatorial signal just offshore. Westward propagating Rossby waves are present around 5–6°N and 5–6°S but appear to be locally forced: their eastward extent is controlled by the extent of the MJO-forcing region and in the MJO1 run do not appear to be reflected from the coast but are generated in the open ocean. Therefore, the complex pattern that the MJO excites in the northeastern Indian Ocean is driven by a combination of local and remote forcing. Additionally, the MJO-related forcing is constrained to lie over Indian Ocean domains only and so forcing from the Pacific does not appear to be a factor.

6.7 Summary and Discussion

A three-dimensional general circulation model with a high resolution nested submodel in the northeastern Indian Ocean, in addition to dynamical mode fitting and several process studies, showed that intraseasonal variability in that region is driven by a combination of local and remote forcing by wind stress over the Indian Ocean. This model was used to predict both sea level and the associated depth-dependent flow and extend the study presented in Chapter 4 that relied only on observed sea level from altimeters.

A reconstruction of sea level and three-dimensional circulation variability driven by reanalyzed atmospheric fields of surface wind, air temperature, humidity, radiation and precipitation for the period 1979-2006 showed that the model could reproduce many of the features present in three observed sea level records from around the region and for ADCP profiles of zonal and meridional flow. The amplitude and timing of the predicted sea level signature, with respect to the MJO, were broadly consistent with observations from altimeter-derived measurements of sea level as well as from tide gauges and ADCP measurements. The model underestimated the amplitude of the reflected Rossby waves. This may be caused by an overly smoothed bathymetry allowing energy to propagate around the northern tip of Sumatra as coastally trapped waves instead of being scattered by steep bathymetry gradients and reflected back into the interior of the basin. A series of carefully designed sensitivity studies in which the bathymetry is modified could shed light on this problem but it is beyond the scope of the present study.

Once the predictions were validated against observations the analysis was extended to include the full three-dimensional circulation. The near-surface circulation is dominated by horizontal flow associated with waves along the equator and the poleward propagating waves along the coast. However, at depth there is a three-dimensional circulation pattern associated with the surface signal. This pattern includes the equatorial and coastal signature mentioned above as well as cyclonic and anticyclonic circulation about downwelling and upwelling events that are due to the westward propagating off-equatorial waves.

Dynamical modes for equatorially trapped baroclinic waves were fit to the model output in order to better understand the underlying dynamics. Second baroclinic mode Kelvin waves and second baroclinic mode, first meridional mode Rossby waves were detected with phase relationships consistent with observations: eastward propagation along the equator followed by westward propagation off the equator. However, the mode shapes used are not appropriate as a non-zero background flow will alter the equatorially trapped wave modes. The results also suggest that a combination of local and remote forcing may play a role. The limitations of the technique can be overcome by providing dynamical modes that accurately represent the response, within a realistic background state, due to local and remote forcing. However, this is beyond the scope of the study presented here.

The physical cause of the variability was explained in three process studies. First, it was determined that realistic momentum flux is necessary for the generation of the observed sea level pattern presented in Chapter 4; buoyancy flux is of secondary importance. Second, a pair of process studies in which the geographic extent of MJO-related surface forcing was limited spatially lead to the conclusions that (i) the MJO is largely responsible for the observed sea level pattern, (ii) both local and remote forcing play a significant role, and (iii) the source of the forcing lies over the Indian Ocean and not over the Pacific Ocean.

The above analysis points to the possibility of some predictability in the northeastern Indian Ocean due to the MJO. The timing of sea level variability and depth-dependent circulation with respect to the MJO cycle can be read off directly from Figures 6.7–6.9. If the initiation and evolution of the MJO can be reliably predicted, which can be done out to 2–3 weeks (see Sections 1.3 and 7.5), then this information will lead to better forecast skill not only for sea level and circulation variability in the region but may help to predict major upwelling events and their impact on local fisheries. As an illustration, predicted sea level and sea level from altimeter-derived measurements at [97.3°E,0°N] near the coast of Sumatra (Figure 6.1, yellow circle) are plotted in Figure 6.13 (top panel) along with the MJO index projected onto the phase at which sea level at this location has the strongest response (MJO phase 6/2). Many large sea level events are well-timed with corresponding

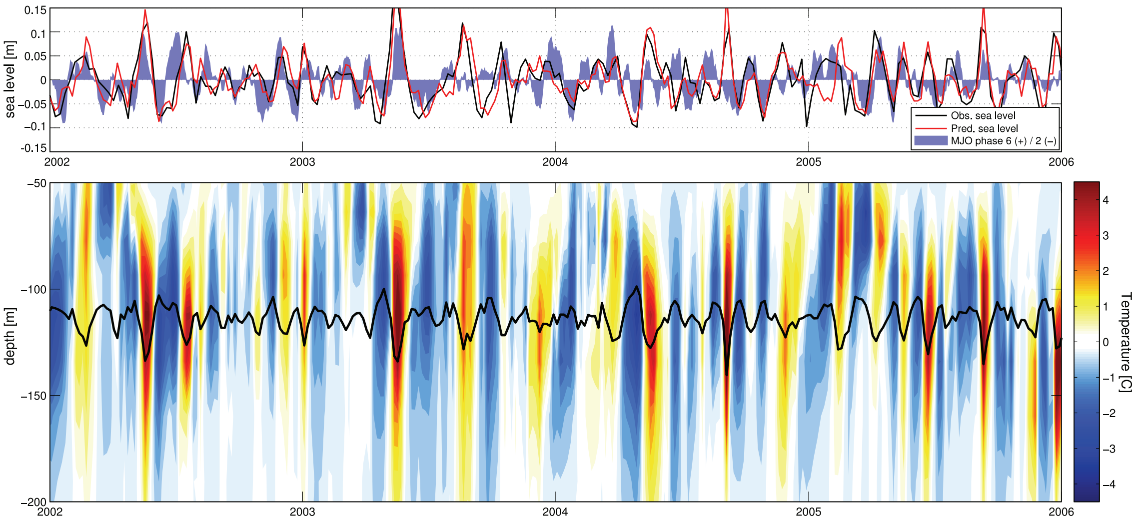

Figure 6.13: Relationship between the MJO index and sea level, upwelling, and temperature at [97.3°E,0°N] (yellow circle, Figure6.1). Top panel: observed sea level (black line) and predicted sea level from the FULL run (red line) are shown along with the the MJO index (shaded area) which has been projected onto the phase 6/2 axis. Bottom panel: predicted temperature from the FULL run between 50 m and 200 m is shown as filled contours along with the depth of the 1025 g/kg isopycnal (black line). Sea level, isopycnal depth, and temperature have had variability on time scales longer than 120 days filtered out prior to analysis.

MJO events.

Upwelling and downwelling due to the baroclinic waves associated with these sea level events modulate temperature down to a depth of 200 m according to the ocean model (Figure 6.13, bottom panel). For example, at 120 m the temperature varies by as much as ±4°C during strong MJO events. This location is just on the edge of the shelf break near the coast of Sumatra and such upwelling/downwelling events will undoubtedly modulate the nutrient levels in nearby coastal waters. Predictable changes in temperature and nutrient levels may lead to significant changes in biological productivity and fishery yields.

CHAPTER 7

HISTORICAL RECONSTRUCTION OF THE MADDEN-JULIAN OSCILLATION AND AN EXAMINATION OF ITS PREDICTABILITY

7.1 Introduction

The Madden-Julian Oscillation (MJO) is the dominant mode of intraseasonal variability of the tropical atmosphere. The original studies on what would later become known as the MJO identified a “40–50 day oscillation” in sea level pressure and upper and lower level zonal wind in the tropics (*Madden and Julian*, 1971, 1972). Since then, the MJO has been quantified in many different ways. For example, *Shinoda et al.* (1998) used EOF analyses of tropical outgoing longwave radiation (OLR) and *Jones et al.* (2004) used EOF analyses of global OLR and zonal wind at low and high levels. Filtering of OLR over a select band of MJO wavenumbers and frequencies has also been used to characterize the MJO (*Wheeler and Kiladis*, 1999; *Wheeler and Weickmann*, 2001). The index presented by *Wheeler and Hendon* (2004), henceforth WH04, is now widely used to quantify the MJO. It is based on the first two principal components of filtered tropical fields of OLR and zonal wind at heights of 200 hPa and 850 hPa.

The Wheeler and Hendon index, henceforth $\boldsymbol{I}_t^{\mathrm{WH}}$, is not defined for the pre-satellite era (i.e., before June 1974). As noted above, sea level pressure has a strong relationship with the MJO (*Donald et al.*, 2006) and observations have been made by land- and ship-borne sensors for centuries. This raises the possibility of reconstructing the Wheeler and Hendon MJO index to cover the pre-satellite era. Such a reconstruction would be useful in quantifying the long time scale (i.e., decadal) variability of the MJO and connections with other phenomena (e.g., ENSO) and environmental variables (e.g., San Diego sea level). Additionally, a long reconstruction could be useful for examining the role of the MJO in oceanic records which do not overlap with the WH04 index (e.g., decomissioned tide gauges). *Pohl and Matthews* (2007) generated an MJO index from 1950 to 2005 using an EOF analysis of upper- and lower-level zonal winds from NCEP reanalysis fields. In addition, *Jones and Carvalho* (2009) inferred the intensity of MJO activity over the period 1880 to 2008 using a simple Markov-chain model forced with monthly SST but did not provide an MJO index of the same form as the Wheeler and Hendon index.

In this chapter, the MJO index has been reconstructed over the period 1905 to 2008 by using air pressure time series from a long reanalysis (*Compo et al.*, 2011) as inputs to a multivariate regression model. The selection of the pressure series was based on (i) the strength of their relationship with the MJO, (ii) the decorrelation length scales of the pressure variability, and (iii) the quality of the reanalysis pressures. The reconstructed MJO index, $\boldsymbol{I}_t^{\mathrm{OT}}$, is shown to have similar temporal and spectral properties to $\boldsymbol{I}_t^{\mathrm{WH}}$ including measures of predictability based on a stochastically forced, damped harmonic oscillator model. The low frequency variability of $\boldsymbol{I}_t^{\mathrm{OT}}$ is validated through comparison with independent environmental variables including its relationship with precipitation, temperature, and sea level.

Only pressure was chosen to be included in the regression model. It could be argued that including zonal wind at upper and lower levels could provide better model results. Surface pressure was chosen for two reasons. First, to the extent that the relationship between surface pressure and wind is linear, adding winds will have no impact on the performance of the regression model. Second, the use of wind data, especially upper level winds, would introduce additional errors due to the assimilation of only sparse surface-based observations by the reanalysis.

The outline of this chapter is as follows. The data are described in Section 7.2. The regression model used to estimate the MJO is presented in Section 7.3 and the internal variability of the reconstructed index, including connections with several independent environmental variables, is examined in Section 7.4. The predictability of the MJO is examined in Section 7.5 using a stochastically forced, damped harmonic oscillator model. Conclusions and discussion are provided in the final section.

7.2 Data and Preliminary Analysis

The Wheeler and Hendon index, and the surface pressure reanalysis used for its historical reconstruction, are described in this section. Long records of observed Australia precipitation and air temperature, California sea level, and surface pressure from a group of stations clustered around Jakarta are also described. These long time series are used to assess the reliability of the low frequency variability of the reconstructed index over the last century.

7.2.1 The Madden-Julian Oscillation Index, $\boldsymbol{I}_t^{WH}$

Daily values of the bivarate index $\boldsymbol{I}_t^{\mathrm{WH}}$ were obtained from the Government of Australia Bureau of Meteorology for the period 1979 to 2008 inclusive (this is henceforth referred to as the WH04 period). Due to a gap in the instrumental record for part of 1978, the MJO index prior to 1979 was not used in order to have a continuous time series. The two components of the index have most of their energy at periods between about 30 and 90 days. Some variability does exist at higher frequencies; it is believed to be due to the signature of Kelvin waves and Equatorial Rossby waves in the wind and OLR fields used to generate $\boldsymbol{I}_t^{\mathrm{WH}}$ (*Roundy et al.*, 2009). Given that the goal is to reconstruct the MJO index from surface pressure measurements which may not contain these higher-frequency components, the MJO index has been low-pass filtered with a cut-off period of 10 days.

7.2.2 Global Surface Pressure

Daily fields of surface pressure were obtained from the 20th Century Reanalysis Project (20CR) for the period 1871 to 2008 inclusive (*Compo et al.*, 2011). The reanalysis was carried out on a global grid with a resolution of 2° and based on assimilating surface pressure observations, monthly sea surface temperatures, and sea ice distribution using an ensemble Kalman smoother. The ensembles have 58 members with the ensemble mean pressure at grid point (i,j) and time t given by p_{ijt} (with zonal and meridional indices ranging from $i = 1 \ldots 180$ and $j = 1 \ldots 91$, respectively). The reanalysis also supplies the standard deviation of the 56 member ensemble, Δp_{ijt}. For reasons related to data scarcity

Location	Variable	Latitude	Longitude	Start	End	%
Booby Is., Aus	precip.	10°37′S	141°55′E	1/8/1908	8/7/2001	96.3
Darwin P.O., Aus	T_{max}	12°28′S	130°50′E	1/1/1885	31/1/1942	99.7
Darwin Airp., Aus	T_{max}	12°25′S	130°53′E	1/1/1941	2/10/2010	99.0
San Diego, USA	sea level	32°43′N	117°10′W	21/1/1906	31/12/2008	97.6
Kemayoran, Ind	pressure	6°9′S	106°51′E	30/4/1949	30/3/1987	60.0
Jakarta, Ind	pressure	6°11′S	106°49′E	30/5/1905	31/1/2008	42.5
Serang, Ind	pressure	6°7′S	106°8′E	23/9/1975	31/12/2006	70.9
Kalijati, Ind	pressure	6°33′S	107°40′E	7/6/1951	26/11/1999	35.3

Table 7.1: The long meteorological and oceanographic records used for validation of the reconstructed MJO index. The Australian records were obtained from the Australian Bureau of Meteorology, the USA record from the Hawai'i Sea Level Center, and the Indonesian records from the International Surface Pressure Database (*Yin et al.*, 2008). The numbers in the final column indicate the completeness of the time series. The four pressure records were averaged into a single series. The same was done for the two temperature records (although each was scaled to have the same variance before averaging).

which will be investigated in more detail later, the analysis has been restricted to the period 1905 to 2008.

Seasonal and interannual variability of the p_{ijt} series was removed following the procedure outlined in WH04. Specifically, the annual cycle and its first two harmonics were removed using least squares and the time mean of the previous 120 days was also removed. Following the recommendation of *Gottschalck et al.* (2010), the only difference between the method applied here for removing low-frequency variability and that presented in WH04 is that the linear contribution of El Niño / La Niña was not removed. The pressure series were also low pass filtered with a cutoff period of 10 days. The processed pressures are henceforth denoted by p^{a}_{ijt}.

7.2.3 Observed Records of Precipitation, Air Temperature, Sea Level, and Surface Pressure

Observations of three environmental variables that were believed to be strongly related to the MJO have been included in the study. The station locations were chosen based in part on an understanding of the physics governing the connections to the MJO and in part on data availability. Pressure records from a cluster of land stations near Jakarta are used to assess the reliability of the pressure reanalysis. Details of the long environmental records are summarized in Table 7.1 and discussed below.

Two time series of daily air temperature were obtained for Darwin (Northern Territory, Australia). The temperature records were averaged over the shared period into a single series. An hourly time series of sea level measured by the tide gauge in San Diego (California, USA) was obtained and the inverse barometer effect was removed using the daily 20th Century Reanalysis mean sea level pressure interpolated to the location of the tide gauge. The adjusted sea level was de-tided using a simple Doodson X0 filter (*Doodson*, 1928), detrended, and subsampled to daily values. A daily time series of precipitation was obtained for Booby Island (Queensland, Australia). The time series was first transformed into a binary times series with 1 indicating rainfall and 0 otherwise. This binary series was then filtered with a running 7-day sum to give the number of rainy days per week centred on each day.

Time series of surface pressure were obtained from four stations within 1 degree of Jakarta (Indonesia). The time series are irregular with sample rates of daily, twice-daily, or four-times daily. The time series contained many outliers that were removed by setting all points more than 3 standard deviations from the mean to a missing value. Each pressure time series was then averaged to daily means. The annual cycle and its first two harmonics were removed using least squares, and interannual and high-frequency signals were removed using the same procedure applied to the p_{ijt} series. The pressure records were averaged into a single series.

7.3 Reconstructing the MJO

The MJO index has been reconstructed over 1905–2008 by performing a multivariate linear regression of $\boldsymbol{I}_t^{\mathrm{WH}}$ onto m predictors using the following model:

$$\boldsymbol{I}_t = \boldsymbol{\beta}\,\boldsymbol{p}_t + \boldsymbol{\epsilon}_t, \tag{7.1}$$

where $\boldsymbol{I}_t$ is the observed bivariate index (a column vector of length two), $\boldsymbol{\beta}$ is a 2xm matrix of regression coefficients, $\boldsymbol{p}_t$ is a mx1 vector of predictors at time t, and $\boldsymbol{\epsilon}_t$ is an error term corresponding to measurement error and effects not included in the model. The estimated regression coefficients ($\hat{\boldsymbol{\beta}}$) were based on a least squares fitting of the model to the Wheeler and Hendon index; the MJO index was reconstructed from 1905 to 2008 using $\boldsymbol{I}_t^{\mathrm{OT}} = \hat{\boldsymbol{\beta}}\,\boldsymbol{p}_t$.

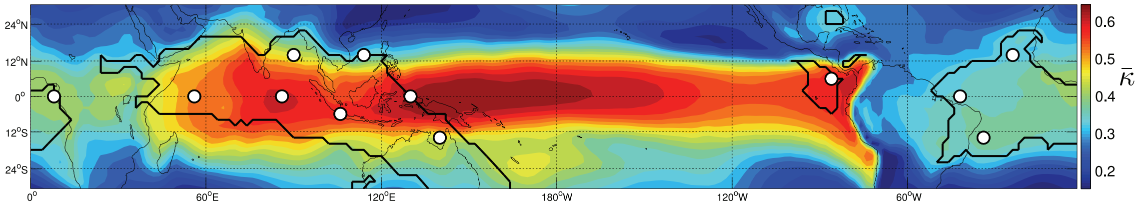

Figure 7.1: Relationship between the MJO index and surface pressure. $\bar{\kappa}_{ij}$ represents the fraction of the total standard deviation of $\boldsymbol{I}_t^{\mathrm{WH}}$ that can be statistically accounted for by surface pressure (p^{a}_{ijt}) for the period 1979 to 2008. It is calculated using a frequency dependent regression (see text and Section 2.2.3 for details). White circles show the locations of predictors used in the regression model and the thick black line defines the exclusion area discussed in Section 7.3.

The MJO is a propagating phenomenon and so including lagged pressures as predictors in the regression model would reduce the mean square error. However, allowing for lags of up to 20 days or more would lead to an overly complex regression with too many predictors and an overfit model. The approach used here is based on the observation that the two components of $\boldsymbol{I}_t^{\mathrm{WH}}$ are quasiperiodic and in quadrature so the Hilbert transform of one component is well correlated with the other component. (The correlations for $\boldsymbol{I}_t^{\mathrm{WH}}$ exceeds 0.7 at zero lag.) Thus, instead of adding lagged variables, the Hilbert transform has been included in the set of predictors. This provides sine- and cosine-like time series for each pressure series which gives freedom to the regression to choose a linear combination in order to achieve the best lag-relationship with $\boldsymbol{I}_t^{\mathrm{WH}}$. This doubles the number of predictors but it does improve significantly the skill of the regression model (see below). The Hilbert transform is calculated in the frequency domain using the algorithm provided by *Oppenheim et al.* (1989).

7.3.1 Location of Pressures Chosen for Inclusion in the Regression Model

Much of the tropics exhibits a strong relationship between surface pressure and the MJO index (Figure 7.1). To limit the number of predictors in the regression model, and thus avoid overfitting, the strength of the linear relation of the candidate predictor and the MJO and the quality of the hindcast pressure have been taken into account (see Appendix D). These considerations led to a restriction of available locations from which predictors could be chosen (Figure 7.1, thick black line). Twelve locations were then chosen (Figure 7.1, white circles) with preference given to regions with a stronger relationship with $\boldsymbol{I}_t^{\mathrm{WH}}$ and higher data quality while also taking into account meridional and zonal decorrelation

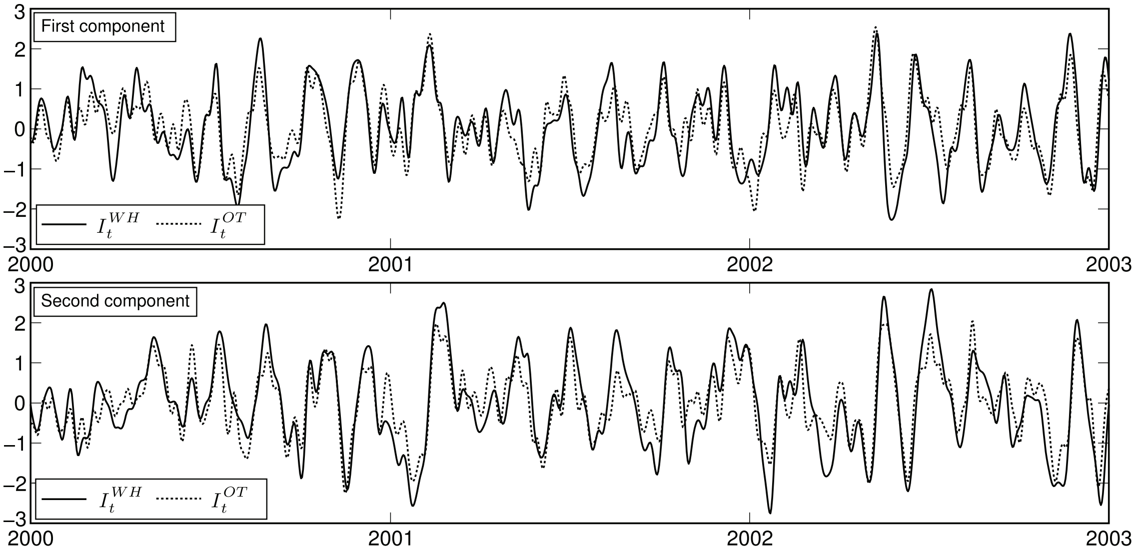

Figure 7.2: Comparison of $\boldsymbol{I}_t^{\mathrm{WH}}$ and $\boldsymbol{I}_t^{\mathrm{OT}}$ over the period 2000 to 2002. The first component of the indices is shown in the top panel and the second component in the bottom panel.

lengthscales. Details are given in Appendix D. Pressures from these twelve locations (and their corresponding Hilbert transforms) form the set of predictors for the regression model (thus $m = 12 \times 2 = 24$).

7.3.2 The Reconstructed Historical Index

The regression of $\boldsymbol{I}_t^{\mathrm{WH}}$ onto the 24 predictors for 1979–2008 can account for 69% of the total variance of $\boldsymbol{I}_t^{\mathrm{WH}}$ (i.e., the sum of the variances of its two components). It follows that the predicted index will underestimate $\boldsymbol{I}_t^{\mathrm{WH}}$ by a factor of about $\sqrt{0.69}$, i.e., 0.83. Note there remains a certain degree of collinearity amongst the predictors despite the precautions taken to choose them. Therefore, the magnitude of the regression coefficients do not by themselves indicate the importance of an individual predictor.

To reconstruct the MJO index from 1905 to 2008 the regression coefficients estimated by fitting the model over the WH04 period were used. Plots of $\boldsymbol{I}_t^{\mathrm{WH}}$ and $\boldsymbol{I}_t^{\mathrm{OT}}$ over a common three year period (Figure 7.2) show the new index predicts well the timing of $\boldsymbol{I}_t^{\mathrm{WH}}$ although the amplitude is slightly underestimated for the reasons given above. Plots of $\boldsymbol{I}_t^{\mathrm{OT}}$ for 2000-2002 and 1920-1922 (Figure 7.3) show the qualitative behaviour of the reconstructed index is consistent over these two, widely separated periods. (These periods were chosen because they both exhibit strong MJO events but similar behaviour is found for other periods.)

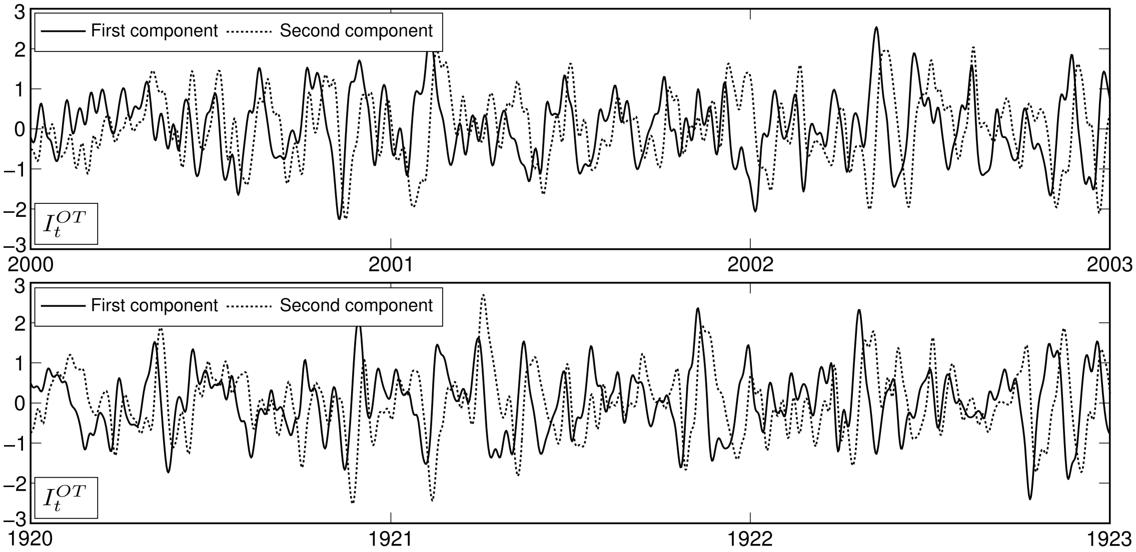

Figure 7.3: Comparison of the two components of $\boldsymbol{I}_t^{\mathrm{OT}}$ for 2000 to 2002 (top) and 1920 to 1922 (bottom).

The power spectra of $\boldsymbol{I}_t^{\mathrm{WH}}$, $\boldsymbol{I}_t^{\mathrm{OT}}$ over 1979–2008, and $\boldsymbol{I}_t^{\mathrm{OT}}$ over the 1905–1978 period have the same shape (Figure 7.4) but the power of $\boldsymbol{I}_t^{\mathrm{OT}}$ is lower by a factor of about 0.69 (as expected). The reconstructed index is highly coherent and in phase with $\boldsymbol{I}_t^{\mathrm{WH}}$ over their common period. In addition, the two components of $\boldsymbol{I}_t^{\mathrm{OT}}$ are highly coherent over the MJO band (30–90 days) and the phase relationship indicates that the two components are in quadrature as expected.

At each latitude two-dimensional frequency-wavenumber spectra of p_{ijt} (after removing the annual cycle and its first three harmonics) have been calculated over 96-day segments. These spectra were then averaged over all segments, and summed over 16°S–16°N, following *Wheeler and Kiladis* (1999) in order to generate a frequency-wavenumber diagram for tropical surface pressure (Figure 7.5, upper panel).

This diagram indicates variability on time- and space-scales that is partially consistent with classical equatorial wave theory. The dispersion curves for equatorially trapped Kelvin waves (equivalent depths of 25 m and 70 m), and equatorially trapped Rossby waves (equivalent depths of 12 m, 30 m, and 10 km) are shown as solid lines. The shallow equivalent depths are consistent with moist convectively coupled waves (*Wheeler and Kiladis*, 1999; *Wheeler et al.*, 2000) and the 10 km equivalent depth represents the gravest Rossby wave mode permitted in the atmosphere (*Diky and Golitsyn*, 1968; *Kasahara*,

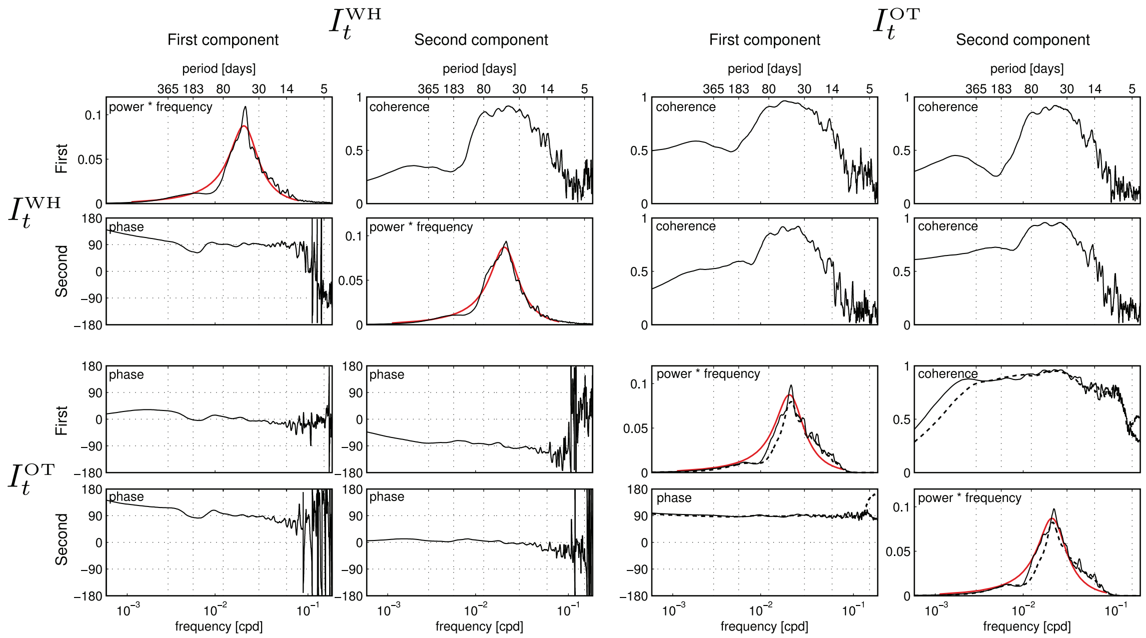

Figure 7.4: Cross-spectral analysis of $\boldsymbol{I}_t^{\mathrm{WH}}$ and $\boldsymbol{I}_t^{\mathrm{OT}}$. The power spectral densities lie along the diagonal panels (scaled by 0.69 for $\boldsymbol{I}_t^{\mathrm{WH}}$) and the coherence and phase spectra on the off-diagonal panels. Solid lines indicate that the spectra was calculated from data over the 1979 to 2008 period and dashed lines indicate that it was performed from data over the 1905 to 1979 period. The spectral density for the autoregressive model (with $\tau_1 = 15$ days, $\tau_2 = 2.5$ days, and $P = 50$ days) are shown as red lines in the diagonal panels.

1976). Variability with zero wavenumber is present indicating variability in the zonal mean pressure on a variety of time scales. There also seems to be eastward propagating variability present on intraseasonal time scales where we would expect to find the signature of the MJO. However, this signal is buried within variability associated with Kelvin waves and the zonal mean.

To demonstrate that the reconstructed index captures the eastward-propagating, intraseasonal surface pressure signal associated with the MJO, the $\boldsymbol{I}_t^{\mathrm{OT}}$-reconstructed pressure was generated by projecting surface pressure onto $\boldsymbol{I}_t^{\mathrm{OT}}$ by linear regression. Its frequency-wavenumber diagram (Figure 7.5, lower panel) indicates the dominance of intraseasonal, zonal wavenumber 1, eastward propagating pressure variability, consistent with the observed dynamics of the MJO. These results do not vary significantly with choice of period (i.e., 1905–2008, 1905–1978, 1979–2008). Additionally, two Hovmöller diagrams for the $\boldsymbol{I}_t^{\mathrm{OT}}$-reconstructed pressure indicate that the eastward-propagating signature of the MJO is strongly present in surface pressure in the modern and historical periods (Figure 7.6).

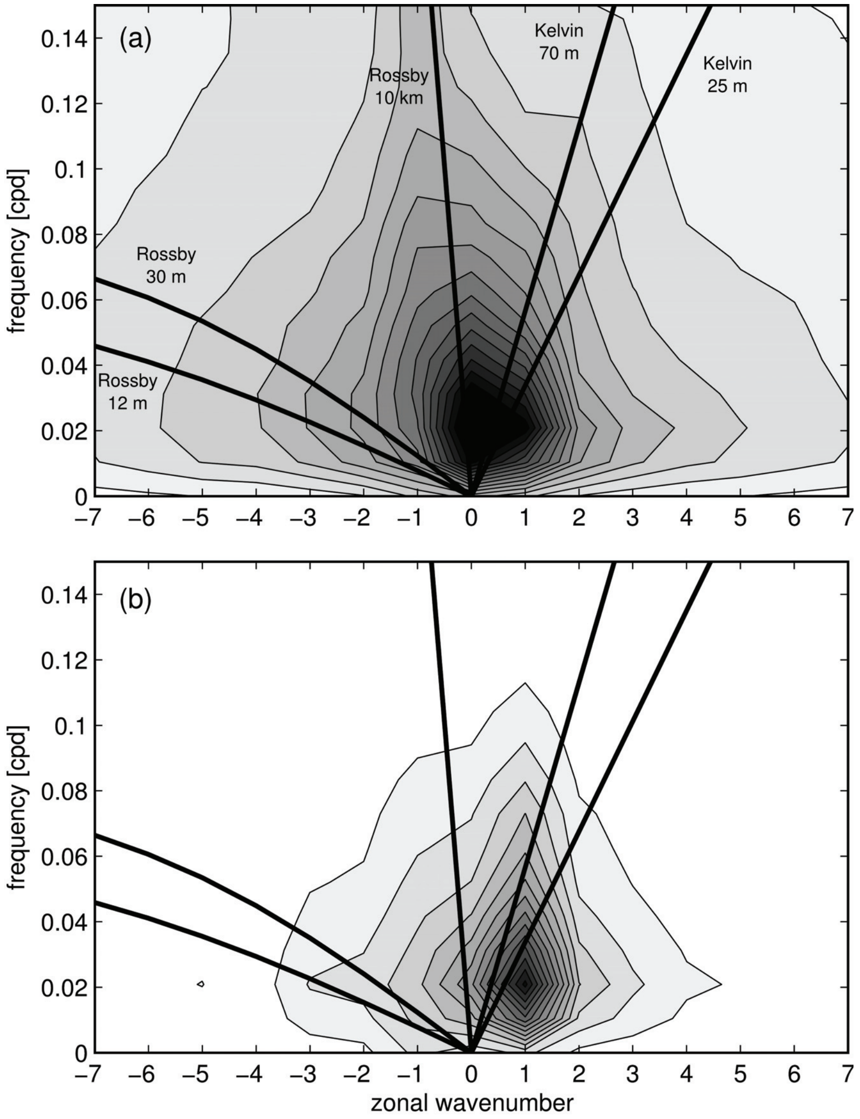

Figure 7.5: Frequency-wavenumber spectra of tropical (16°S–16°N) surface pressure. Spectra are shown for (a) the raw pressure field (p_{ijt}, with the annual cycle and first three harmonics removed) and (b) the $\boldsymbol{I}_t^{\mathrm{OT}}$-reconstructed pressure (see text for details). In both cases the analysis was performed over the 1905 to 2008 period. This diagram was generated by following the same calculation for OLR performed by *Wheeler and Kiladis* (1999). Lines represent the dispersion curves for equatorially trapped Kelvin waves (equivalent depths of 25 m and 70 m) and equatorially trapped Rossby waves (equivalent depths of 12 m, 30 m, and 10 km).

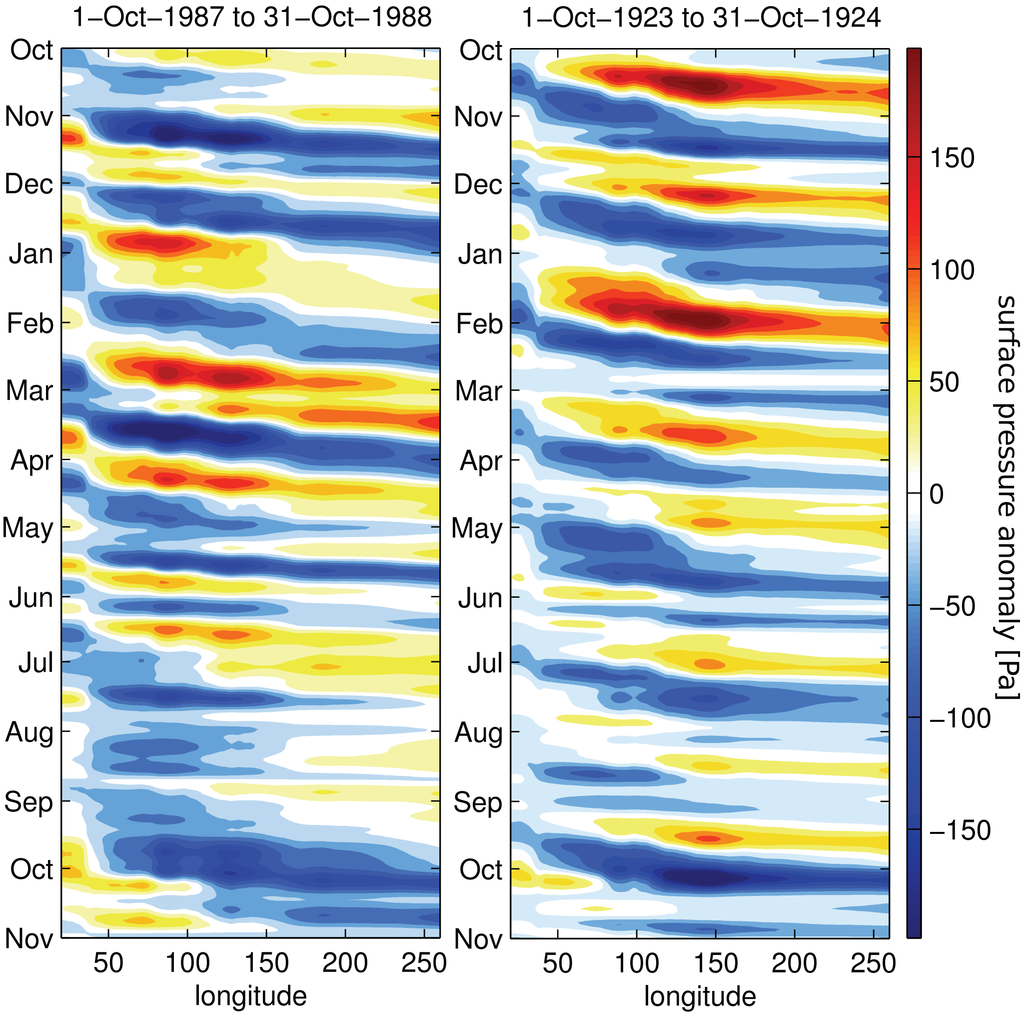

Figure 7.6: Hovmöller diagram of $\boldsymbol{I}_t^{\mathrm{OT}}$-reconstructed tropical (16°S–16°N) surface pressure for 1 Oct 1987 to 31 Oct 1988 (left) and 1 Oct 1923 to 31 Oct 1924 (right). Note that time is increasing downwards.

The three-year running variance of $\boldsymbol{I}_t^{\mathrm{OT}}$ and $\boldsymbol{I}_t^{\mathrm{WH}}$ (Figure 7.7, upper panel) agree well over the WH04 period after allowing for the attenuation factor mentioned above. Using $\boldsymbol{I}_t^{\mathrm{OT}}$ it is possible to calculate low-frequency changes in the variance of the MJO over most of the last century. Changes in variance of almost a factor of two were found on time scales of decades and longer (thin line, top panel of Figure 7.7), along with a weak linear trend. The fact that the MJO seems more variable after the mid-1970s is consistent with *Pohl and Matthews* (2007) and *Jones and Carvalho* (2009).

The three-year running power spectra of $\boldsymbol{I}_t^{\mathrm{OT}}$ and $\boldsymbol{I}_t^{\mathrm{WH}}$ (Figure 7.7, middle and lower panels) again show good agreement over the WH04 period. Much of the variability in the spectral density of $\boldsymbol{I}_t^{\mathrm{OT}}$ is associated with changes in the overall power levels. This is confirmed by a principal component analysis of the running spectra of $\boldsymbol{I}_t^{\mathrm{OT}}$ over the 1905–2008 period which shows that most (59%) of the variability in the spectra can be accounted for by a time-varying modulation of a fixed spectral shape. (The time varying amplitude agrees well with the running variance as expected). More interestingly, the second principal component accounts for an additional 24% of the variability in spectral shape and effectively shifts power with periods of 30 to 50 days to periods longer than 100 days. The effect of this second mode of spectral variation is evident in the extended low frequency tails of spectral energy of $\boldsymbol{I}_t^{\mathrm{OT}}$ at certain times (e.g., 1915–1921, 1995–2001, middle panel of Figure 7.7). It is encouraging to find that a similar analysis of $\boldsymbol{I}_t^{\mathrm{WH}}$, and $\boldsymbol{I}_t^{\mathrm{OT}}$ over the pre-WH04 period, gave essentially the same results, i.e., over 80% of the variability in spectral shape could be accounted for by the two modes described above.

The next section explores the reality of the low-frequency variations of $\boldsymbol{I}_t^{\mathrm{OT}}$ over the pre-WH04 period.

7.4 Validity of Reconstructed Low Frequency Variability

To assess the reliability of $\boldsymbol{I}_t^{\mathrm{OT}}$ before 1979 two distinct approaches based on analysis of independent environmental observations have been used. First, each environmental variable (Table 7.1) is regressed onto $\boldsymbol{I}_t^{\mathrm{OT}}$ and $\boldsymbol{I}_t^{\mathrm{WH}}$ and the stability of the regression coefficients is examined. Second, $\boldsymbol{I}_t^{\mathrm{WH}}$ is reconstructed for Boreal Winter (DJF) using a regression model driven by the independent set of environmental variables and changes in variance and spectral shape are compared to corresponding values based on $\boldsymbol{I}_t^{\mathrm{OT}}$.

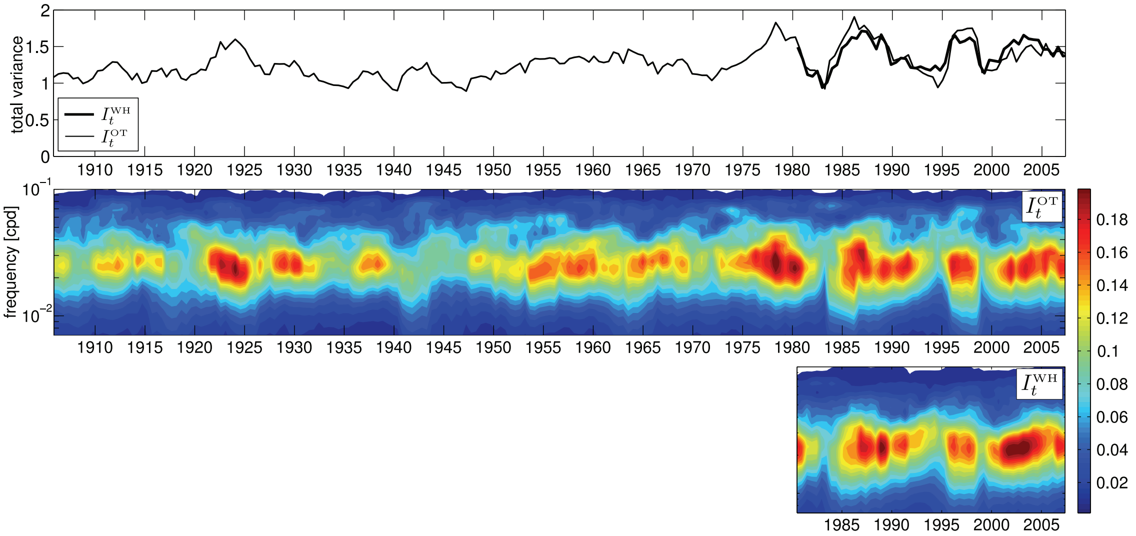

Figure 7.7: Variance and spectral content of $\boldsymbol{I}_t^{\mathrm{OT}}$ over most of the last century. Running 3-year variances are shown in the upper panel ($\boldsymbol{I}_t^{\mathrm{WH}}$ has been scaled by 0.69). Running 3-year spectral density of $\boldsymbol{I}_t^{\mathrm{OT}}$ is shown in the middle panel and $\boldsymbol{I}_t^{\mathrm{WH}}$ in the lower panel. The spectra of the two components of each index have been summed in order to generate these figures.

7.4.1 Stability of the Relationship Between the MJO and Environmental Variables

The validity of the low-frequency variability of the reconstructed index is first tested by examining the stability of its relationship with independent observations of precipitation, air temperature, and sea level (Table 7.1). Each of the three environmental variables was regressed onto the two components of $\boldsymbol{I}_t^{\mathrm{WH}}$ and then the two components of $\boldsymbol{I}_t^{\mathrm{OT}}$. The regression was performed over different periods thereby allowing a comparison of the two indices over their common period, and also an examination of the long term stability of the regression coefficients. The motivations for choosing each environmental variable are described below followed by the results.

Precipitation has been demonstrated to have a strong relationship with the MJO in a band across northern Australia during DJF (*Wheeler and Hendon*, 2004; *Wheeler et al.*, 2009; *Risbey et al.*, 2009). Previous studies have found a higher probability of extreme rainfall during MJO phases 5 and 6 and speculated that this is due to a modulation of the monsoon by the MJO. *Hidayat and Kizu* (2009) also found that the MJO strongly modulates DJF precipitation over the Indonesian Archipelago. The stability of this connection is examined

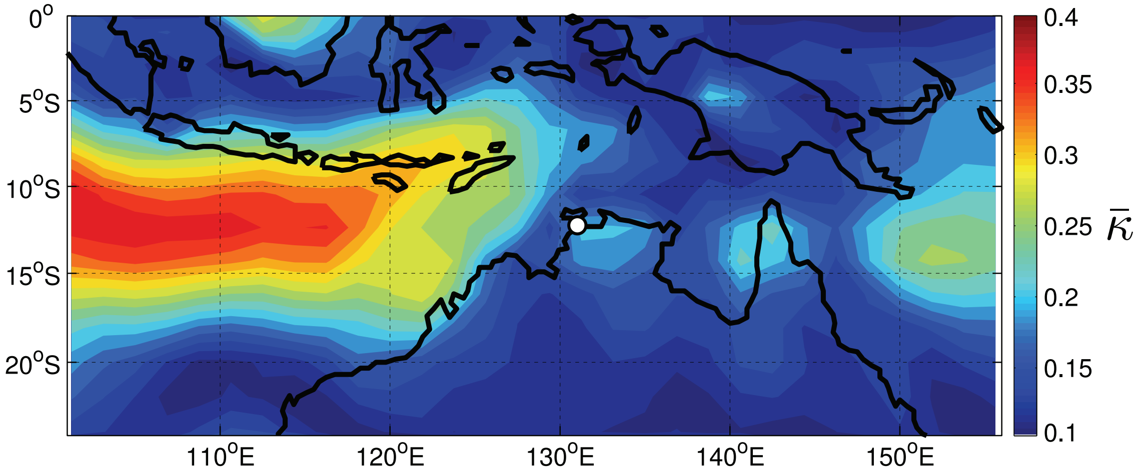

Figure 7.8: Relationship of Australian DJF surface air temperature to $\boldsymbol{I}_t^{\mathrm{WH}}$. Filled contours show the proportion of standard deviation of DJF surface air temperature that is accounted for by $\boldsymbol{I}_t^{\mathrm{WH}}$ (see Section 2.2.3 for details on this calculation). The white circle shows the location of Darwin, Australia.

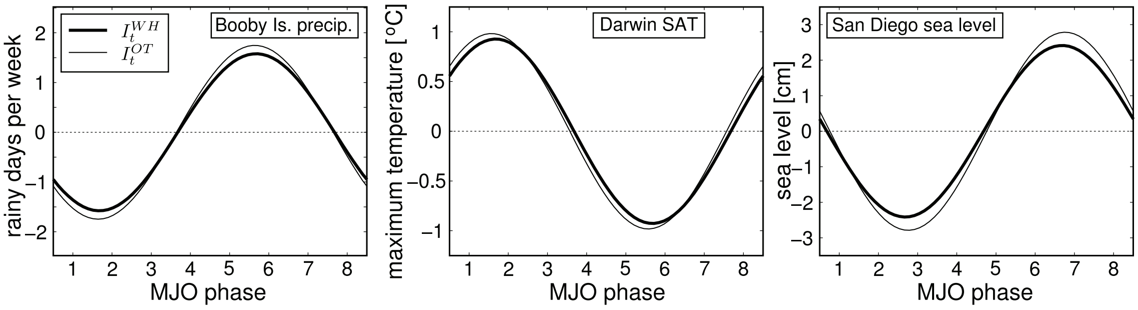

Figure 7.9: Relationship between the MJO and three independent environmental variables. The response of each variable to an MJO cycle of amplitude 2 based on a linear regression onto $\boldsymbol{I}_t^{\mathrm{WH}}$ (thick lines) and $\boldsymbol{I}_t^{\mathrm{OT}}$ (thin lines): precipitation at Booby Island, Australia (left), surface air temperature at Darwin, Australia (centre), and sea level at San Diego, USA (right) based on a regression over the 1979–2008 period.

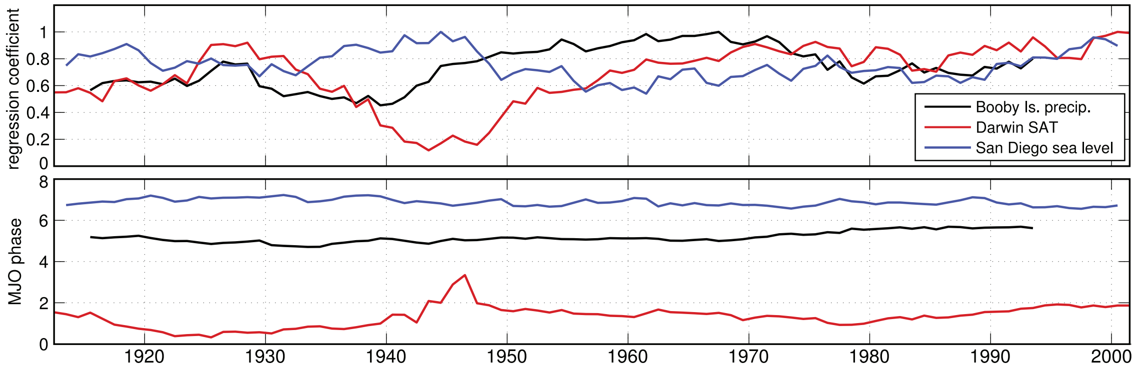

Figure 7.10: Stability of the regression of the three environmental variables onto the reconstructed index. The amplitude of the regression coefficients (upper panel, scaled to have a maximum of 1) and phase at maximum response (lower panel, shown as MJO phase) for precipitation at Booby Island (Australia, black), surface air temperature at Darwin (Australia, red), and sea level at San Diego (USA, blue).

over much of the last century using a record of DJF precipitation from Booby Island in northeastern Australia.

Surface air temperature (SAT) was statistically related to the MJO and visualized with global maps of $\bar{\kappa}$ (not shown) using the technique developed in Chapter 4. It was found that SAT from northwestern Australia had a significant relationship with the MJO. Specifically, it was found that SAT in this region undergoes a seasonally dependent modulation such that $\boldsymbol{I}_t^{\mathrm{WH}}$ accounts for almost 40% of the standard deviation of DJF surface air temperature[1] between Southeast Asia and northwestern Australia (Figure 7.8). A simple explanation for this statistical relationship is that the mean DJF surface air temperature over the interior of the Australian landmass is up to 4°C warmer than the neighbouring Indian Ocean[2]. Low-level wind anomalies associated with the MJO advect relatively warm continental air past northwestern Australia during MJO phases 1-3, and westerly anomalies have the opposite effect during MJO phases 5-7. Given the above statistical analysis and physical interpretation, as well as considerations of record length, Darwin surface air temperature was chosen as the second environmental variable.

Sea level along the Pacific coast of North and South America is known to be influenced by coastal trapped waves that are remotely forced in the equatorial Pacific (*Spillane et al.*,

---

[1] NCEP/DOE Reanalysis 2 gridded daily surface air temperature (*Kanamitsu et al.*, 2002)

[2] NOAA/ESRL Physical Sciences Division, Boulder Colorado from their Web site at `http://www.esrl.noaa.gov/psd/`

1987; *Enfield*, 1987). Zonal surface wind over the equatorial Pacific is strongly related to the MJO during Boreal Autumn/Winter (*Kessler et al.*, 1995) and equatorially trapped Kelvin waves generated by this wind will take approximately 80 days to travel along the equator and up the coast of North America to affect coastal Southern California (*Oliver and Thompson*, 2010). A long record of sea level from San Diego (USA) from September to December (SOND) and lagged 80 days is used as the third environmental variable. Details on the location, record length, and completeness are available in Table 7.1.

As mentioned above, each of the three environmental variables was regressed onto the two components of $\boldsymbol{I}_t^{\mathrm{WH}}$ and then the two components of $\boldsymbol{I}_t^{\mathrm{OT}}$ over different time periods. Let the regression coefficients for the first and second components of the MJO index be β_1 and β_2 respectively. The response of the three environmental variables to an idealized MJO oscillation has been estimated by forcing each fitted regression model with a sinusoidally varying MJO of the form [$a\cos\phi$,$a\sin\phi$] where $\phi = -7\pi/8, -5\pi/8 \ldots 7\pi/8$ (corresponding to the MJO phases 1,2. . .8). This corresponds to a cycle of amplitude a (a circle of radius a in MJO space). An amplitude of $a = 2$ was chosen in order to examine the response to a moderate/strong MJO cycle. It follows that the amplitude of the response is $a\sqrt{\beta_1^2 + \beta_2^2}$ and the phase of the response is $\arctan\left(\beta_2/\beta_1\right)$. This is analogous to calculating composites of the environmental variable based on MJO phase except that we are assuming a linear relationship.

The predicted responses of precipitation, surface air temperature and sea level to the idealized MJO forcing is consistent between $\boldsymbol{I}_t^{\mathrm{WH}}$ and $\boldsymbol{I}_t^{\mathrm{OT}}$ for all three variables (Figure 7.9). By carrying out the regressions using a 15-year sliding window the temporal stability of the relationship between the MJO and the three environmental variables could be examined (Figure 7.10). Average correlation over the 1905 to 2008 period was around 0.41 for the precipitation record, 0.29 for the temperature record, and 0.27 for the sea level record and were very stable for the precipitation and sea level records but more variable for the temperature record. The drop in amplitude, and change in phase of the regression coefficients, for temperature in the mid-1940s coincide with the drop in correlation below 0.1. Despite this, it was found that changes in the phase of the predicted response were remarkably stable over the 1905 to 2008 period. This stability points to the realism of $\boldsymbol{I}_t^{\mathrm{OT}}$ over the last century.

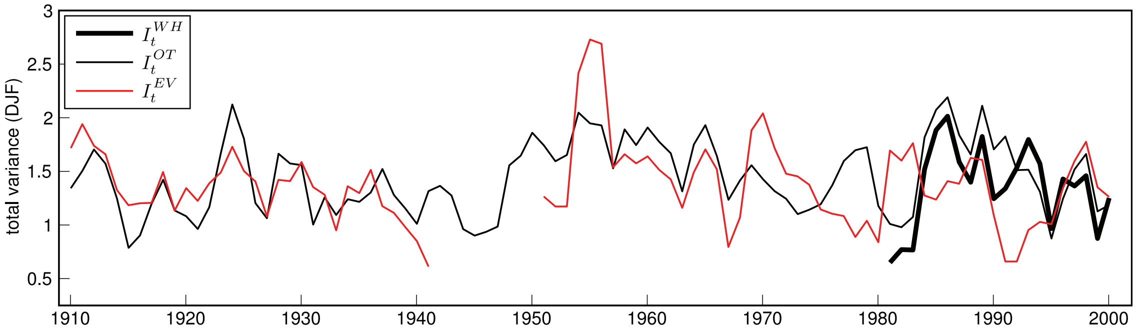

Figure 7.11: Running three-year variance of $\boldsymbol{I}_t^{\mathrm{WH}}$, $\boldsymbol{I}_t^{\mathrm{OT}}$, and $\boldsymbol{I}_t^{\mathrm{EV}}$ for December to January inclusive. Note that $\boldsymbol{I}_t^{\mathrm{EV}}$ and $\boldsymbol{I}_t^{\mathrm{WH}}$ have been scaled to have the same variance as $\boldsymbol{I}_t^{\mathrm{OT}}$.

7.4.2 Reconstructing MJO Variability from Long Land-Based Records

An independent estimate of MJO variability over most of the last century was made by fitting the regression model presented in Section 7.3 to $\boldsymbol{I}_t^{\mathrm{WH}}$ using the four observed environmental variables presented in Section 7.2.3, and their Hilbert transforms, as predictors (thus $m = 4 \times 2 = 8$). The regression model was first fit to $\boldsymbol{I}_t^{\mathrm{WH}}$ over the WH04 period. The analysis was restricted to DJF because this is the time of year when the connection between the MJO and most of the predictors is strongest (see Section 7.4.1). The regression model was then used to predict MJO variability from 1905 to 2008 from the long environmental records.

The calculation of the Hilbert transforms of the environmental variables was complicated by gaps in the records (see Table 7.1). Short gaps in the precipitation, temperature, and sea level were filled by linear interpolation prior to calculating the Hilbert transform. The long stretches of missing values in the composite pressure record were set to zero before calculating the Hilbert transform and then reset to missing after the transformation.

The regression of $\boldsymbol{I}_t^{\mathrm{WH}}$ onto the environmental variables accounts for 39% of the total variance of $\boldsymbol{I}_t^{\mathrm{WH}}$. As expected, the skill of this new index, $\boldsymbol{I}_t^{\mathrm{EV}}$, does not fit $\boldsymbol{I}_t^{\mathrm{WH}}$ as well as the pressure based regression model. It can, however, be used to assess the realism of the low-frequency changes in variance of $\boldsymbol{I}_t^{\mathrm{OT}}$ over the last century.

The three-year running DJF variance of $\boldsymbol{I}_t^{\mathrm{EV}}$ exhibits many of the peaks and troughs evident in the corresponding changes of $\boldsymbol{I}_t^{\mathrm{OT}}$ (Figure 7.11. The correlation of the three-year running DJF variances is 0.57 over the pre-WH04 period. Furthermore, the $\boldsymbol{I}_t^{\mathrm{OT}}$ and $\boldsymbol{I}_t^{\mathrm{EV}}$ running variances exhibit similar linear trends causing increases of 7% and 5%

respectively over the full record. Overall the comparison of $\boldsymbol{I}_t^{\mathrm{EV}}$ and $\boldsymbol{I}_t^{\mathrm{OT}}$ suggests that the main features of the low-frequency variability evident in $\boldsymbol{I}_t^{\mathrm{OT}}$ are real.

7.5 Predictability of the MJO Index

The predictability of the MJO is now examined in order to assess the reliability of the reconstructed index. In the first subsection three straightforward empirical measures of predictability are introduced and estimated for both $\boldsymbol{I}_t^{\mathrm{WH}}$ and $\boldsymbol{I}_t^{\mathrm{OT}}$. In the second subsection a simple, physically-based model is used to interpret the empirical measures and also gain new insights into the predictability of the MJO.

7.5.1 Empirical Measures of Predictability

Consider a scatter plot of a time-varying MJO index with the first component on the x_1-axis and the second component on the x_2-axis. This set of realized states can be considered as an approximation of the probability density function of the true state of the MJO at some time t_0 given no other information (e.g., *Ristic et al.* (2004)). This distribution will be referred to as the prior distribution (with zero mean and a variance of $\sigma^2_{\mathrm{prior}}$). Suppose that a bivariate observation of the standardized MJO, $\boldsymbol{y}_{\mathrm{obs}}$, becomes available at time t_0. It is assumed that $\boldsymbol{y}_{\mathrm{obs}}$ is subject to a normally distributed, zero mean observation error with covariance $\sigma^2_{\mathrm{obs}}\mathrm{I}$. To update the prior distribution to take into account this new information a Bayesian approach has been taken. The posterior distribution is approximated by sampling, with replacement, from the set of observed points in the above scatter plot using weights that are proportional to the likelihood function, i.e., $\exp(-|\boldsymbol{y}_{\mathrm{obs}} - \boldsymbol{x}|^2/2\sigma^2_{\mathrm{obs}})$ where x denotes the true state of the MJO at time t_0. As $\sigma^2_{\mathrm{obs}} \rightarrow 0$ the posterior distribution will reduce in spread and become centred more closely on $\boldsymbol{y}_{\mathrm{obs}}$; as $\sigma^2_{\mathrm{obs}} \rightarrow \infty$ the posterior will revert back to the prior distribution.

It is straightforward to approximate the posterior distribution of the true state of the MJO at a future time $t_0 + k$ by simply tracking the observed evolution of each point in the posterior sample by following the original MJO time series. This procedure is illustrated in Figure 7.12 for k increasing from zero to 35 days. (The two components of the MJO index have been scaled by their respective sample standard deviations.) The thin lines in each panel are a representative selection of observed trajectories of the MJO with the initial positions at time t_0 reflecting the posterior distribution. In all of these panels the observation is $\boldsymbol{y}_{\text{obs}} = (\sqrt{2}, -\sqrt{2})$ and the observation error variance is taken to be $\sigma^2_{\text{obs}} = 0.07$. It is clear from Figure 7.12 that the ensemble undergoes a counterclockwise rotation, the amplitude of the ensemble mean (thick line) decreases, and the ensemble spread (shaded area) increases through time. It can also be seen that the position of the ensemble members relative to their sample mean at time t_0 is lost with increasing time. For example, if an ensemble member is to the left of the ensemble mean at t_0, then the probability of the member remaining to the left of the mean decreases as k increases.

Based on the above discussion of the evolution of the posterior distribution three empirical measures of predictability are proposed: the rate of decay of the posterior mean towards zero, the increase of the variance, and the decrease of the correlation between the MJO state at time t_0 and $t_0 + k$. Let $\boldsymbol{\mu}_{t_0+k}$ denote the mean of the posterior distribution at time $t_0 + k$. The first measure of predictability is taken to be the time required for $|\boldsymbol{\mu}_{t_0+k}|/|\boldsymbol{\mu}_{t_0}|$ to drop below a specified critical value (henceforth τ_μ). Let $\sigma^2_{t_0+k}$ denote the total variance of the posterior distribution at time $t_0 + k$. The second measure of predictability is the time required for $\sigma^2_{t_0+k}/\sigma^2_{\text{prior}}$ to exceed a specified critical value (henceforth τ_{σ^2}). Let ρ_{t_0,t_0+k} denote the proportion of standard deviation of the MJO at time $t_0 + k$ that can be accounted for by the MJO at time t_0 according to the evolved posterior distribution. The final measure of predictability is the time for ρ_{t_0,t_0+k} to fall below a specified critical value (henceforth τ_ρ).

The measures of predictability based on the mean and the variance are similar to those developed using information theory (e.g., *Schneider and Griffies* (1999); *Kleeman* (2002)). These two quantities measure the predictability of the system by comparing the current state of an MJO event ensemble to either the initial condition (i.e., $|\boldsymbol{\mu}_{t_0+k}|/|\boldsymbol{\mu}_{t_0}|$) or the equilibrium distribution (i.e., $\sigma^2_{t_0+k}/\sigma^2_{\text{prior}}$). On the other hand, the correlation ρ_{t_0,t_0+k} is a fundamentally different measure of predictability. This measure can be thought of as measuring the loss of information due to "mixing" that occurs within an ensemble.

To compare $\boldsymbol{I}^{\text{WH}}_t$ and $\boldsymbol{I}^{\text{OT}}_t$ over different periods their corresponding predictability measures have been calculated. There have been suggestions that the time scale for the loss of predictability of a given MJO event depends on the time at which the event is initially defined (*Lin et al.*, 2008; *Kim et al.*, 2009; *Kang and Kim*, 2010). An additional set of experiments has been performed with $|\boldsymbol{y}_{\text{obs}}|$ equal to 1.5 and the phase angle of $\boldsymbol{y}_{\text{obs}}$ taking on eight values centred on each of the MJO phases. For these additional runs the

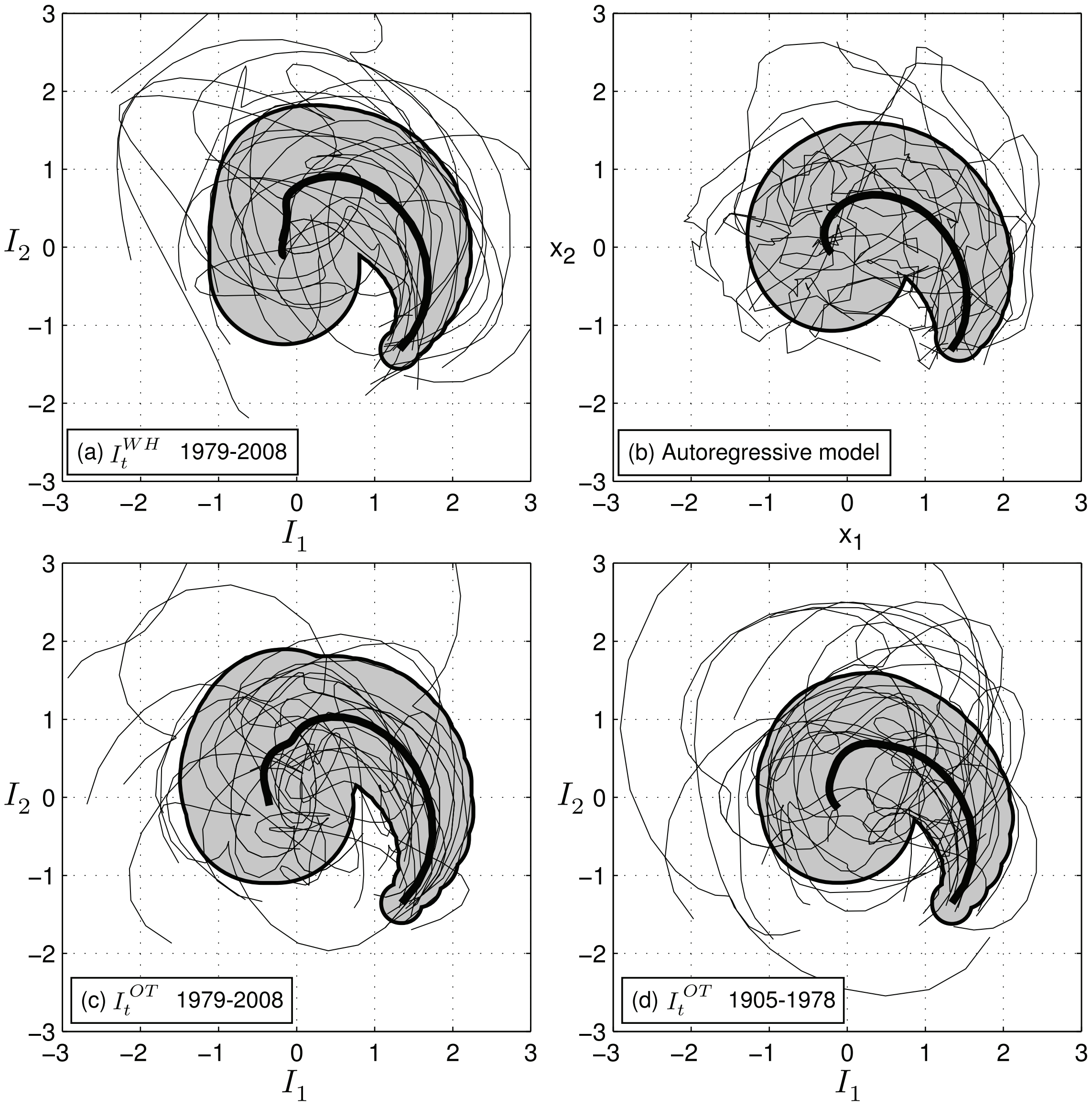

Figure 7.12: Evolution of the MJO in phase space given an imperfectly observed initial condition. The statistical properties of a 4000-member ensemble with $\boldsymbol{y}_{\text{obs}} = (\sqrt{2}, -\sqrt{2})$ and $\sigma^2_{obs} = 0.07$ are shown over the following 35 days for (a) $\boldsymbol{I}_t^{\text{WH}}$, (c) $\boldsymbol{I}_t^{\text{OT}}$ (1979-2008), and (d) $\boldsymbol{I}_t^{\text{OT}}$ (1905-1978). Trajectories calculated using the autoregressive model are shown in panel (b) for 35 time steps. (Model parameters are $\tau_1 = 15$ days, $\tau_2 = 2.5$ days, and $P = 50$ days.) For clarity, only 20 representative trajectories are shown. The thick black line shows the mean of the full ensemble and shaded region shows the standard deviation of the full ensemble about this mean. Note that each index component has been scaled by its standard deviation.

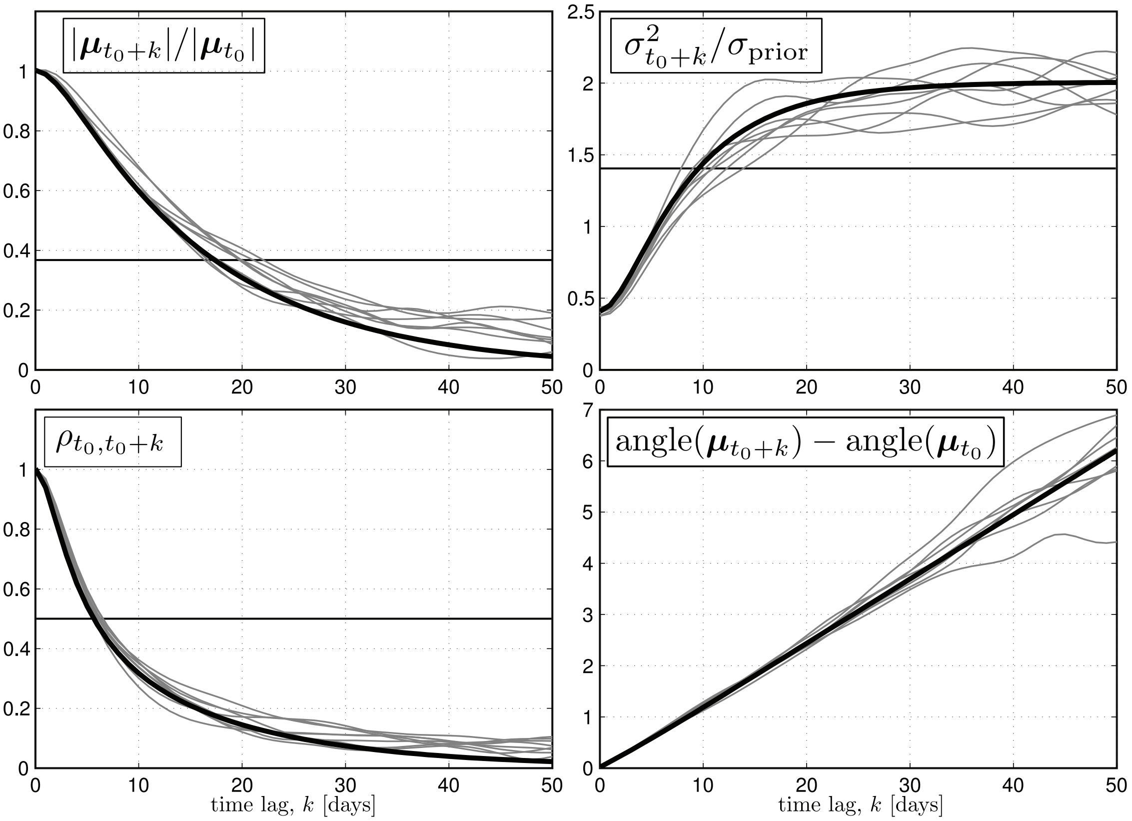

Figure 7.13: Predictability measures for the Wheeler and Hendon MJO index and damped harmonic oscillator model. Decay of the mean (top left), increase of variance (top right), decrease of correlation (bottom left), and increase in angular position (bottom right) are shown. Results are shown for initial ensembles of $\boldsymbol{I}_t^{\text{WH}}$ within each of the eight MJO phases (thin lines), i.e., ensembles are initialized for $\boldsymbol{y}_{\text{obs}}$ in each of the eight MJO phases. Corresponding measures calculated using the damped harmonic oscillator model ($\tau_1 = 15$ days, $\tau_2 = 2.5$ days, and $P = 50$ days) are shown by the thick lines. Critical values used to calculate predictability times scales are e-folding for the mean and the variance and 0.5 for the correlation (shown as horizontal lines). The e-folding critical value for the mean is simply e^{-1} and for the variance it is $\sigma^2_{t_0} + e^{-1}(\sigma^2_{\text{prior}} - \sigma^2_{t_0})$. In order to reproduce the "kinks" visible in the mean, variance and correlation over the first ∼5 days it was necessary to include autoregressive forcing and to properly specify the initial condition.

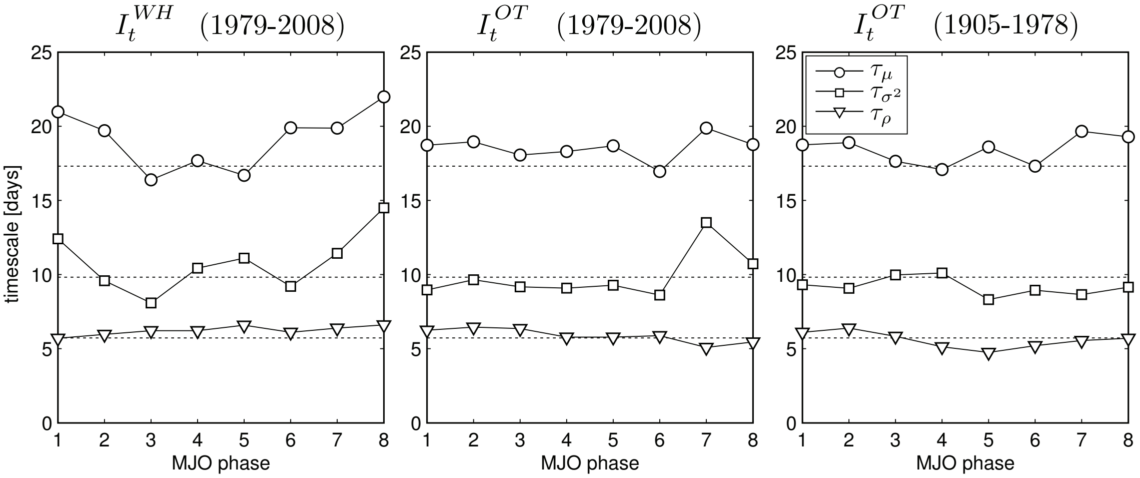

Figure 7.14: Time scales for loss of predictability of a canonical MJO event. The e-folding times for the mean (circles), variance (squares), and lag at which the correlation drops to 0.5 (triangles) as a function of MJO phase for $\boldsymbol{I}_t^{\mathrm{WH}}$ (left), $\boldsymbol{I}_t^{\mathrm{OT}}$ over the 1978–2008 period (middle), and $\boldsymbol{I}_t^{\mathrm{WH}}$ over the 1905–1978 period (right). The dashed lines represent predictions from the damped harmonic oscillator model using $\tau_1 = 15$ days, $\tau_2 = 2.5$ days, and $P = 50$ days.

observation error was kept fixed at 0.25. All of the results are discussed below.

The variation of the three predictability measures ($|\boldsymbol{\mu}_{t_0+k}|/|\boldsymbol{\mu}_{t_0}|$, $\sigma^2_{t_0+k}/\sigma^2_{\mathrm{prior}}$ and ρ_{t_0,t_0+k}) are plotted as a function of k for $\boldsymbol{I}_t^{\mathrm{WH}}$ in Figure 7.13. For all three measures there is a short period (2 to 3 days) over which the initial values persist followed by a slower relaxation to their asymptotic values (the mean and correlation decay to zero and the variance increases towards 2 which is the total variance of the normalized MJO series). The critical values are also shown in this figure; once they are defined it is straightforward to read off τ_μ, τ_{σ^2}, and τ_ρ.

The time scales for loss of predictability are shown in Figure 7.14. The most important feature of Figure 7.14 is that the predictability scales are consistent amongst $\boldsymbol{I}_t^{\mathrm{WH}}$ and $\boldsymbol{I}_t^{\mathrm{OT}}$ over the WH04 period, and $\boldsymbol{I}_t^{\mathrm{OT}}$ over the pre-WH04 period. Overall, the predictability scales for $\boldsymbol{I}_t^{\mathrm{WH}}$ and $\boldsymbol{I}_t^{\mathrm{OT}}$ are independent of phase (Figure 7.14). However, there does appear to be phase dependence of τ_μ for $\boldsymbol{I}_t^{\mathrm{WH}}$ that is not reproduced by $\boldsymbol{I}_t^{\mathrm{OT}}$.

The time evolution of the angular position of the mean is approximately linear especially in the early part of each event (bottom right of Figure 7.13). The slope of the phase line versus time leads to an estimate of the period of the MJO. It is found that the period is stable with respect to MJO phase and is between 48 and 54 days for $\boldsymbol{I}_t^{\mathrm{WH}}$ and $\boldsymbol{I}_t^{\mathrm{OT}}$ over their shared period. Over the pre-WH04 period it was estimated to be about 4 days shorter. Note that τ_μ, τ_σ, and τ_ρ are smaller than the MJO period indicating that an average event lifetime is short compared to the dominant oscillation time scale.

Note that the three predictability measures are all different: the time scale depends on the chosen statistic. I found typical time scales of 18 days for the mean, 10 days for the variance, and 5 days for the correlation. These results are not sensitive to changes in $|\boldsymbol{y}_{\text{obs}}|$ and σ^2_{obs} (tested by doubling and halving the values given above). The dependence of τ_ρ on the observation error is discussed in Section 7.6. The fact that the correlation time scale is short compared to the other properties indicates that, for time scales more than a few days, there is no useful information in the initial position of an ensemble member relative to the initial ensemble mean and the best prediction is simply given by the mean and variance alone.

It should be noted that the choice of critical values upon which the predictability time scales are defined is somewhat arbitrary. It is possible to choose critical values leading to the same time scale for all three predictability measures. For example, τ_ρ could be made equal to $\tau_\mu = 18$ days by choosing a critical value of approximately 0.17. However, if we consider the practical predictability of this system, a correlation of 0.17 is very low and therefore does not properly represent the time scale for loss of correlation. I am confident that the choices made here, though somewhat arbitrary, give a useful picture of the complex relationships amongst the predictability measures for this system.

7.5.2 Predictability and the Damped Harmonic Oscillator

The evolution of the posterior distribution described above (i.e., rotation and decay in MJO space) is reminiscent of the behaviour of a forced, damped harmonic oscillator (e.g., *Marion and Thornton* (1995)). In this subsection a forced, damped harmonic oscillator model is developed in order to explain the different values of the three predictability measures. Similar empirical models have been used in the examination of ENSO predictability (e.g., *Penland* (1996), *Kleeman* (2008), *Newman et al.* (2009)).

Consider the autoregressive model of a damped harmonic oscillator, with autocorrelated stochastic forcing, presented in Section 2.3.3:

$$\boldsymbol{x}_{t+1} = \boldsymbol{A}\boldsymbol{x}_t + \boldsymbol{\varepsilon}_{t+1}, \tag{7.2}$$

where $\boldsymbol{x}_t$ is a 4×1 state vector at time step t, $\boldsymbol{A}$ is a 4×4 transition matrix that carries the state vector forward one time step, and $\boldsymbol{\varepsilon}_t$ is a stochastic forcing process. The state of the oscillator is defined by the first two elements of the state vector (analogous to the position and velocity of a one dimensional oscillator); the last two elements define the autocorrelated stochastic forcing that drives the oscillator away from a state of rest. The transition matrix depends on three model parameters (γ_1, γ_2, θ) and they are expressed in terms of time scales: $\theta = 2\pi/P$, $\gamma_1 = \exp(-1/\tau_1)$, and $\gamma_2 = \exp(-1/\tau_2)$.

If the mean and variance of $\boldsymbol{x}_{t_0}$ are $\boldsymbol{\mu}_{t_0}$ and $\boldsymbol{\Sigma}_{t_0,t_0}$ respectively, then the mean and variance of $\boldsymbol{x}_{t_0+k}$ are given by

$$\boldsymbol{\mu}_{t_0+k} = \boldsymbol{A}^k \boldsymbol{\mu}_{t_0} \tag{7.3}$$

and

$$\boldsymbol{\Sigma}_{t_0+k,t_0+k} = \boldsymbol{A}^k \boldsymbol{\Sigma}_{t_0,t_0} \boldsymbol{A}'^k + \sum_{j=0}^{k-1} \boldsymbol{A}^j \boldsymbol{\Sigma}_{\boldsymbol{\varepsilon}} \boldsymbol{A}'^j \tag{7.4}$$

respectively, and the covariance between $\boldsymbol{x}_{t_0}$ and $\boldsymbol{x}_{t_0+k}$ is given by

$$\boldsymbol{\Sigma}_{t_0+k,t_0} = \boldsymbol{A}^k \boldsymbol{\Sigma}_{t_0,t_0}. \tag{7.5}$$

The squared correlation, calculated as the proportion of variance of the oscillator state at $t_0 + k$ that can be accounted for by the initial state, is given by

$$\rho_k^2 = \frac{\mathrm{tr}(\boldsymbol{\Sigma}_{t_0+k,t_0} \boldsymbol{\Sigma}_{t_0,t_0}^{-1} \boldsymbol{\Sigma}_{t_0,t_0+k})}{\mathrm{tr}(\boldsymbol{\Sigma}_{t_0+k,t_0+k})}, \tag{7.6}$$

where the trace refers only to the first two components of $\boldsymbol{x}_t$.

The variance of the white noise process, σ_ϵ^2, is chosen to make the steady state variance of the oscillator components of $\boldsymbol{x}_t$ each unity. The model and its covariance structure are now defined by the three model parameters: P, τ_1, and τ_2. Given an initial distribution (i.e., posterior distribution, see Appendix E) of $\boldsymbol{x}_t$ at t_0 the evolution of its mean, variance, and correlation is followed through time and three predictability time scales defined in Section 7.5.1 can be calculated.

The damped harmonic oscillator model depends on 3 parameters. The physical interpretation of the three parameters is straightforward: P is the period of the dominant oscillation; τ_1 is the decay scale of the oscillation; τ_2 is the decay scale of the forcing. Once they are defined it is straightforward to calculate the three predictability time scales defined above. It is encouraging to find that the time scales calculated from the oscillator model with a single choice of parameters ($P = 50$ days, $\tau_1 = 15$ days, and $\tau_2 = 2.5$ days[3]) are remarkably similar to the empirical measures (thick line, Figure 7.13 and dashed line, Figure 7.14). It is also encouraging to find that the same set of parameters predicts a spectral density of the MJO that agrees well with the spectral shape of $\boldsymbol{I}_t^{\mathrm{WH}}$ and $\boldsymbol{I}_t^{\mathrm{OT}}$ (diagonal panels of Figure 7.4).

Sample trajectories from the model are shown in Figure 7.12 (upper right panel). Note that the model trajectories do not reproduce the behaviour of many of the trajectories of $\boldsymbol{I}_t^{\mathrm{WH}}$ and $\boldsymbol{I}_t^{\mathrm{OT}}$ which appear to move away from the origin before decaying. The normality of the damped, harmonic oscillator transition matrix $\boldsymbol{A}_1$ leads to a monotonic decrease in $\boldsymbol{\mu}_t$ (see Section 2.3.2). If this normality was not assumed in the original model then it may be possible to better represent this initial increase of perturbations present in the observed MJO trajectories.

7.6 Summary and Discussion

Using long records of surface pressure from the Twentieth Century Reanalysis Project (*Compo et al.*, 2011) and a simple regression model, the Madden-Julian Oscillation index of Wheeler and Hendon has been reconstructed over the period 1905 to 2008. Wheeler and Hendon generated their index using tropical fields of OLR and zonal wind. Surface pressure was chosen because of the availability of observations over much of the last century and the long recognized connection of pressure to the MJO (*Madden and Julian*, 1971, 1972).

The number of pressure predictors was limited by taking into account (i) the strength of their relationship with the MJO, (ii) decorrelation lengthscales of pressure, and (iii) the quality of the reanalysis. Twelve pressure predictors, and their Hilbert transforms, were chosen to reconstruct the MJO. A seasonally dependent model was also considered but it was found that its impact on the skill of the regression was negligible. This is not surprising considering that the algorithm used by Wheeler and Hendon did not seasonally

---

[3] These values were determined by comparing statistical properties of the predictions and observations by eye. Given the observed covariance matrices $\boldsymbol{\Sigma}_{t_0,t_0}$ and $\boldsymbol{\Sigma}_{t_0+k,t_0}$ then the matrix $\boldsymbol{A}$ (and thus P, τ_1, and τ_2) could have been determined using Equation 7.5. However, this method assumes the model is correct. Given that the model is very simple I have instead opted for a more holistic approach in fitting the model to the observations.

stratify their input data.

The reconstructed index accounts for 69% of the variance of Wheeler and Hendon's index, has a similar spectral shape and lead-lag relationship between components, and captures the low frequency changes in variance over the shared period (1979–2008). The reconstructed index was validated for the pre-1979 period using a set of independent environmental variables. The environmental variables were also used independently to reconstruct the index as well as to examine the stability of their connection to the MJO. It was found that (i) the low frequency changes in MJO variance over 1905–2008 were reproduced by this independent reconstruction, (ii) a slight increase in MJO variability from 1905 to 2008 was present in both the reconstruction and the new independent estimate, and (iii) the timing of the connection between the MJO and the aforementioned environmental variables is stable over the 1905–2008 period. These results give us confidence in the low-frequency behaviour of the MJO reconstruction.

The reconstruction was also tested by examining time scales for the loss of predictability based on the decay of the mean (τ_μ), increase in the variance (τ_{σ^2}), and loss of the correlation (τ_ρ) of an ensemble of MJO events centred on a prescribed initial state. It was found that the time scales for the measures were quite different: $\tau_\mu \simeq 18$ days, $\tau_{\sigma^2} \simeq 10$ days, and $\tau_\rho \simeq 5$ days. These results applied to both the Wheeler and Hendon index and the reconstructed index. For the Wheeler and Hendon index, some dependence of τ_μ on the phase of the MJO was observed: greater predictability was found for events initialized in phases 1, 2, 6, 7, and 8. This phase dependence was not reproduced by the historical reconstruction.

The loss of predictability measured by the correlation (τ_ρ) is strongly dependent on the observation error variance (σ^2_{obs}). More specifically, τ_ρ increases with σ^2_{obs}. When σ^2_{obs} is large, the initial ensemble fills a relatively large part of MJO space and an individual ensemble member will retain its position relative to the mean for a longer period of time than when σ^2_{obs} is small. Therefore, the size of σ^2_{obs} will determine the time scale over which a prediction of individual ensemble members relative to the mean is useful. Beyond this time scale there is only value in forecasting the mean and variance.

The complex behaviour of the three predictability measures, and their dependence on the observation error variance, can all be explained in terms of a simple damped harmonic oscillator model specified by three parameters. The damped harmonic oscillator model fits the original and reconstructed indices well with a single set of parameters: $P = 50$ days, $\tau_1 = 15$ days, and $\tau_2 = 2.5$ days. Note, the ratio $\tau_2/\tau_1 = 0.17$ is much less than one and this indicates that the memory of the atmospheric forcing is much shorter than the lifetime of the MJO. More interestingly, the ratio $\tau_1/P = 0.3$ is also less than one and thus the lifetime of an MJO event is predicted to be much shorter than its period, suggesting that the MJO can be thought of as a sequence of pulse-like events rather than a quasiperiodic oscillation.

The predictability time scale based on the mean (τ_μ) is consistent with previous estimates. *Waliser* (2005) suggested that this time scale is between 20 to 30 days. Other studies have estimated the time scale to be 2 weeks using a coupled ocean-atmosphere circulation model (*Vitart et al.*, 2007), 15 days using autoregressive models (*Lo and Hendon*, 2000; *Maharaj and Wheeler*, 2005), and 15 days using a multivariate lag-regression model *Jiang et al.* (2008).

There are great variations in the density of surface pressure observations over the 1905–2008 period and this led to the exclusion of many potential predictors from the regression model. Indeed, a more accurate reconstruction could have been developed over a more recent period, 1950-2008 for example, by including predictors that have been excluded here (e.g., predictors from the Western Pacific or other variables such as zonal wind). It is recognized that there is an inevitable degree of subjectivity in the selection of predictors. However, given the large number of sensitivity studies that have been performed, a slightly different set of predictors that respect the restrictions outlined in this chapter would yield very similar results for the present study period.

CHAPTER 8

SUMMARY AND DISCUSSION

A wide selection of techniques, including statistical analysis of observations, ocean modelling, and dynamical analysis have been used to explore the influence of the Madden-Julian Oscillation on ocean variability and its predictability. A summary of this thesis will be presented below followed by a general discussion.

8.1 Summary

Satellite altimetry was used in Chapter 4 to show that the Madden-Julian Oscillation (MJO) has three main regions of influence on global sea level[1]. A novel statistical measure, $\bar{\kappa}$ which exploits the quasi-periodic nature of the MJO, was used to generate maps of the proportion of sea level variability accounted for by the MJO. The three regions identified with significant connections were: (i) the equatorial Pacific and Coastal Americas, (ii) the Gulf of Carpentaria, and (iii) the northeastern Indian Ocean. In each region it was found that sea level variability was coherent with the MJO index at a period of about 75 days.

For each of the three regions the variability associated with the MJO was characterized using a frequency dependent EOF analysis centred on a period of 75 days and the resulting pattern was explained in terms of simple physical processes. In the Pacific, the 75 day mode consists of equatorially trapped waves propagating eastward across the Pacific with a wave speed of 2.6 m s^{-1}, consistent with a first baroclinic mode equatorially trapped Kelvin wave. Upon reaching the eastern boundary these waves excite poleward propagating

---

[1] A version of this chapter has been published as *Oliver, E. and K. Thompson, The Madden-Julian Oscillation and sea level: Local and remote forcing, Journal of Geophysical Research, 115, C01003, 2010.*

waves along the coast of the Americas with wave speeds of 5.6 m s^{-1} (northward) and 3.3 m s^{-1} (southward). The 75 day FDOEF mode in the Gulf of Carpentaria showed a standing wave over the entire Gulf. A simple dynamical balance showed that most of this variability can be accounted for by sea level set-up due to surface wind over the Gulf which is itself strongly related to the MJO. In the northeastern Indian Ocean, the 75 day mode indicated a complex pattern with signatures of eastward propagating waves along the equator, poleward propagating waves near the coast, westward propagating waves just off the equator. It was speculated that these waves were baroclinic equatorially trapped Kelvin waves, Rossby waves and coastal trapped waves. It was also noted that sea level in each region is either locally forced (Gulf of Carpentaria), remotely forced (equatorial Pacific and coastal Americas), or possibly a combination of the two (northeastern Indian Ocean).

The connection between the MJO and sea level in the Gulf of Carpentaria was examined in more detail in Chapter 5[2]. Sea level from three local tide gauges and surface wind over the Gulf were shown to be coherent with the MJO on intraseasonal time scales. In addition, the wind was most coherent with the MJO when oriented such that it would produce a strong sea level set-up in the Gulf.

A general circulation model was used to reconstruct sea level and depth-averaged circulation in the Gulf for the 1979–2009 period which was validated using the observed tide gauge records. The model predictions were able to capture the observed seasonal cycle and were strongly coherent with observations on intraseasonal time scales. In this manner it was confirmed that the sea level response is simple wind-driven set-up and it was also shown that this connection is seasonally dependent with the strongest response during the Australian-Indonesian monsoon in Austral Summer. The sea level and associated circulation has a predictable pattern given the strength and phase of the MJO: coastal sea level can vary by as much as ±6 cm and velocities can reach 5 m s^{-1} over an MJO cycle with the strongest response for phase 2 (set-down) and phase 7 (set-up) along with an associated anticyclonic and cyclonic circulation in the Gulf. In addition, the low-frequency sea level variations not captured by the model were shown to be related to propagation of ENSO-related variability in the Pacific through the Indonesian Throughflow and along the Australian shelf edge.

---

[2] A version of this chapter has been published as *Oliver, E. and K. Thompson, Sea level and circulation variability of the Gulf of Carpentaria: Influence of the Madden-Julian Oscillation and the adjacent deep ocean, Journal of Geophysical Research, 116, C02019, 2011.*

The connection between the MJO and sea level in the northeast Indian Ocean was examined in more detail in Chapter 6[3]. Sea level from altimeters and tide gauges, subsurface currents from ADCP profiles, and reanalyzed surface wind forcing were shown to have a strong relationship to the MJO in the northeastern Indian Ocean. Additionally, the MJO-related pattern of surface wind forcing was shown to be well-suited to generate equatorially trapped waves.

A general circulation model was used to reconstruct the sea level and three-dimensional circulation in the northeastern Indian Ocean for the 1979–2006 period. By comparison with observed sea level from tide gauges and altimeters, and observed subsurface currents from ADCP profiles, it was shown that the model reproduced well the observed connection with the MJO. The model provided predictions of the complete three-dimensional circulation which were then examined to map the MJO-expression at depth. Significant horizontal circulation and vertical upwelling anomalies were found down to a depth of 1000 m along the equator corresponding to the eastward propagating equatorially trapped Kelvin waves and along the coast of Sumatra, Java and the Bay of Bengal corresponding to the coastally trapped waves. Additionally, cyclonic and anticyclonic circulation cells about regions of upwelling and downwelling were found off the equator corresponding to the westward propagating Rossby waves.

Dynamical Modal Analysis (DMA) was used, along with dynamical equatorial wave modes, to identify the observed waves as primarily second baroclinic mode Kelvin waves and second baroclinic mode, first meridional mode Rossby waves. The limitations of DMA, due to specification of incorrect dynamical modes, were discussed in Chapter 6. A set of process studies were used to show that wind stress is the dominant forcing mechanism for setting up the observed MJO-related sea level pattern in the northeastern Indian Ocean. It was also found that both local and remote MJO-related wind forcing play significant roles in driving the variability.

The connection of the observed variability to the MJO leads to predictability in the system. For example, upwelling and downwelling events off the coast of Sumatra can lead to temperature changes of ±4°C with the strongest responses in phase 6 (downwelling) and phase 2 (upwelling). These upwelling and downwelling events will no doubt also contribute to variability in nutrients and, in turn, biological productivity.

---

[3] A manuscript version of this chapter is in preparation.

Low-frequency variability of the MJO and possible interactions between the MJO and other climate phenomena could be examined if a long record of MJO variability was available. The Wheeler and Hendon (WHO4) MJO index was reconstructed in Chapter 7 over the period 1905 to 2008 using atmospheric surface pressure from a global historical reanalysis[4]. The choice of pressure predictors was restricted by taking into account the strength of the connection with the MJO, the quality of the reanalysis, and the spatial decorrelation lengthscales of surface pressure. These predictors were then used as inputs to a multivariate linear regression model to predict the WHO4 index over the 1979–2008 period. The reconstruction captures the temporal and spectral properties of the WH04 index over this period and was also shown to capture the eastward propagating, intraseasonal, zonal wavenumber 1 signal in surface pressure which is associated with the MJO. The index was then hindcast back to 1905. Over the historical period the reconstructed index was validated using observations of independent environmental variables. First, an independent reconstruction was generated using sea level, sea level pressure, surface air temperature, and precipitation records directly from measurement stations as predictors. Although not as good of a fit to the WH04 index it nevertheless captured much of the interdecadal and multidecadal variability observed in the reconstructed index. Second, the long reconstruction was used to predict the records of sea level, surface air temperature, and precipitation. The timings of these predictions with respect to MJO phase were shown to be stable over the last century. The low-frequency behaviour of the MJO can be examined now that a long MJO index exists.

Finally, the statistical behaviour of a canonical MJO event was examined and three measures of predictability were developed to further validate the historical reconstruction as well as gain insight into the predictability of the MJO. From these three measures, time scales were calculated for the loss of predictability in the mean, the variance, and within-ensemble correlation. The results were largely consistent between the historical reconstruction and the WH04 index with time scales of 18 days for the mean, 10 days for variance, and 5 days for correlation. In addition, it was noted that a canonical MJO event behaves like a forced damped harmonic oscillator. To test this, an autoregressive model of a damped harmonic oscillator with autoregressive stochastic forcing was developed and the predicted time scales were found to match well with the WH04 and historical

---

[4] A manuscript version of this chapter has been submitted to the *Journal of Climate* under the title *A Reconstruction of MJO Variability from 1905 to 2008* and is currently under revision.

reconstruction. This model depends on three parameters which may give insight into the fundamental characteristics of the MJO. For example, the oscillation period is much longer than the damping time scale indicating that an MJO event behaves more like a quickly decaying pulse than an oscillation.

8.2 Discussion and Future Work

The dynamical understanding of modes of variability in the ocean and atmosphere, and the coupling between variability in these two media, are of primary importance in our ability to reliably predict weather and climate. The MJO provides predictability on timescales that bridge the gap between the traditional ranges of weather and climate. The dynamical understanding of some of its connections to the ocean may help provide predictability on these timescales for the regions identified in this thesis. This understanding was obtained by various techniques including analysis of observations, the use of statistical techniques, the application of dynamical theory, and the use of numerical general circulation models. Each of these techniques possesses its own advantages and and disadvantages.

The analysis of observations is most important amongst the techniques. Observations are needed to establish the reality of a given phenomenon and its known properties. However, observations are limited by data scarcity: what observations we do possess are distributed unevenly across time and space. Observing systems are also limited by technology: we cannot observe the ocean at all depths, latitudes, and longitudes simultaneously every day.

Statistical techniques allow simple patterns to be extracted from complex data sets. For example, the MJO index is calculated from an EOF analysis of tropical atmospheric data. However, statistical models are limited by data quality and data scarcity as was noted in the historical reconstruction study undertaken in Chapter 7. Statistical techniques can be very technical and the patterns detected are often difficult to interpret physically. Finally, the assumption of linearity, which has been virtually ubiquitous in this thesis, may not always hold.

Dynamical models can provide useful predictions based on simple physics. The governing process are rooted in fundamental balances (e.g., conservation of energy, conservation of momentum, etc.) and as such can be interpreted physically and used to gain insight into the governing dynamics. However, these dynamical concepts are often based on unsupportable assumptions (e.g., no forcing, flat bottom, inviscid fluid motion, etc) which break down when applied to the real ocean.

Numerical general circulation models can predict the ocean state in a way which fills in the gaps left by missing observations and does not rely on restrictive assumptions that simple models must. Additionally, numerical models allow specific dynamical processes to be examined through sensitivity studies by changing certain aspects of the model (e.g., bathymetry, forcing fields, etc.). However, due to inaccurate forcing, inappropriate boundary conditions, or poor parameterizations of subgrid-scale processes, among other things, these models are often incomplete and do not capture the observed variability properly.

The dynamics involved in weather and climate phenomena, such as those presented in this thesis, are best examined by using the combined strengths of the tools described above. The weaknesses of certain approaches (i.e., the scarcity of observations, the difficulty in interpreting statistical model results) can be compensated by the strengths of other approaches (i.e., ocean predictions at all locations and times from numerical models, the fundamental physical balances found using simple dynamical models). This is the approach which has been taken in this thesis.

Future work following on from this thesis may include the following. The long reconstructed MJO index can be used to examine low-frequency changes in the observed MJO connections in long station records (e.g., Alaska SAT). These low frequency changes may shed light on interactions, possibly nonlinear, between the MJO and other climate phenomena such as El Niño / La Niña, the Pacific Decadal Oscillation or the Indian Ocean dipole. Second, a series of process studies using a general circulation model could be performed to test the sensitivity of the MJO-response in the northeastern Indian Ocean to bathymetry. This sensitivity may be critical in generating the reflected Rossby waves seen in the observed sea level signal. Finally, the Madden-Julian Oscillation provides predictability in certain regions of the oceans. A sound MJO prediction system could potentially lead to useful forecasting systems for both coastal communities and the deep ocean. For example, the detection of sea level anomalies in the western equatorial Pacific associated with an MJO event could act as a signal to forecasters of the possibility of predictable coastal anomalies at a later date in the Americas. The passage of coastally trapped waves can lead to anomalies in temperature, salinity, and nutrients near the surface (i.e., in the euphotic zone) due to upwelling and downwelling which will have significant impacts on biological productivity and important human activities such as fisheries or recreation.

APPENDIX A

A MONTE CARLO METHOD FOR THE CALCULATION OF STATISTICAL SIGNIFICANCE

A worked example is outlined here for determining the statistical significance of the calculated proportion of variance of an environmental variable time series that is accounted for by the MJO index ($\bar{\kappa}$, see Section 2.2.3) using a Monte Carlo method based on the assumption of no relationship between the two time series.

To illustrate the technique we calculate the proportion of San Diego sea level variance that can be predicted by the MJO index. An hourly time series of sea level measured by a tide gauge in San Diego, USA was obtained for the period 1/1/1979 to 31/12/2008 and the inverse barometer effect was removed using daily 20th Century Reanalysis mean sea level pressure (see Section 7.2.2). The adjusted sea level was de-tided using a Doodson X0 filter (*Doodson*, 1928), detrended, and subsampled to daily values. The annual cycle and its first two harmonics were removed by linear regression.

The multiple coherence between the MJO index and San Diego sea level (thin line, Figure A.1a) was modified (thick line) by adding a small constant to the spectral density of the MJO index (shaded area). This constant was equal to 2% of the maximum spectral density of the MJO index. Using the modified coherence, the proportion of variance accounted for by the MJO index over this period was found, using Equation 2.18, to be $\bar{\kappa} = 0.39$ (the unmodified coherence gave a value of $\bar{\kappa} = 0.41$ and so the results are not

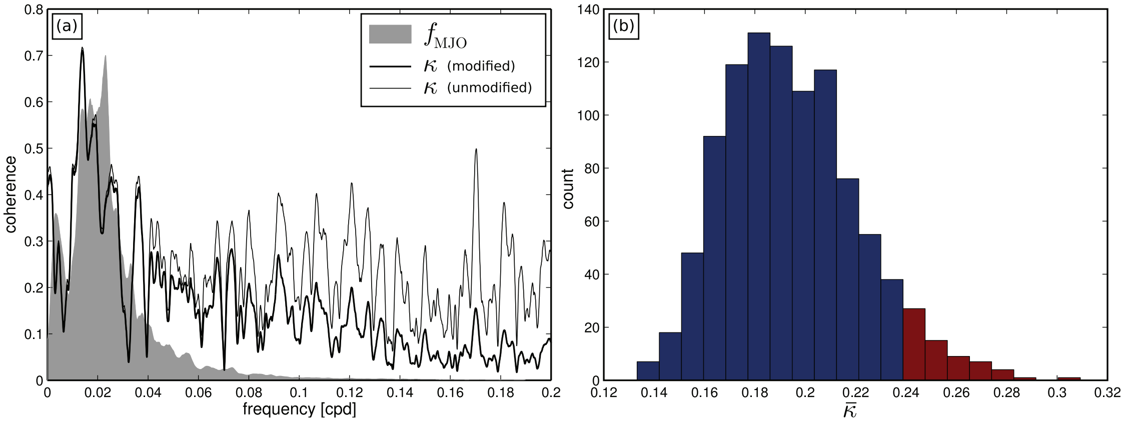

Figure A.1: Illustration of the calculation of statistical significance of $\bar{\kappa}$ between the MJO index and San Diego sea level. (a) Coherence between the MJO index and San Diego sea level without modification (thin line) and modified (thick line) by adding a small constant to the spectral density of the MJO index (shaded area). (b) Distribution of $\bar{\kappa}$ under the assumption of no relationship between the MJO index and San Diego sea level (calculated using a sample of 1000 cloned MJO indices). The values above the 5% significance level are shown in red ($\bar{\kappa}_{5\%} = 0.24$).

strongly sensitive to this modification). Given this value of $\bar{\kappa}$ what can we say about its statistical significance?

The 5% significance level, $\bar{\kappa}^2_{5\%}$, was calculated by first generating 1000 clones of the MJO index with the same mean, variance and spectral density but randomized phases. The proportion of San Diego sea level standard deviation accounted for (i.e., $\bar{\kappa}$) by each one was then calculated. This yielded a distribution of $\bar{\kappa}$ under the assumption of no relationship between the MJO index and San Diego sea level (Figure A.1b). The value for which 95% of the samples fall below, $\bar{\kappa}_{5\%}$, is the 5% significance level. It was found that $\bar{\kappa}_{5\%} = 0.24$ and therefore the value of $\bar{\kappa}$ quoted above (0.39) is statistically significant at the 5% significance level.

APPENDIX B

EQUATIONS FOR INCOMPRESSIBLE AND INVISCID FLOW

The equations governing an incompressible and inviscid fluid on a sphere observed with respect to a rotating system of coordinates are (*Kundu*, 1990)

$$\frac{\partial \boldsymbol{u}}{\partial t} + \boldsymbol{u} \cdot \nabla \boldsymbol{u} + 2\boldsymbol{\Omega} \times \boldsymbol{u} = -\frac{1}{\rho} \boldsymbol{\nabla} p - \boldsymbol{g} \tag{B.1}$$

$$\boldsymbol{\nabla} \cdot \boldsymbol{u} = 0. \tag{B.2}$$

where $\boldsymbol{u}(x, y, z, t) = u\hat{\mathbf{x}} + v\hat{\mathbf{y}} + w\hat{\mathbf{z}}$ is the fluid velocity, $\boldsymbol{\Omega}$ is a vector with magnitude equal to the rotation rate and direction along the axis of rotation, $\rho(x, y, z, t)$ is the fluid density, $p(x, y, z, t)$ is the fluid pressure, and $\boldsymbol{g} = g\hat{\mathbf{z}}$ is gravitational acceleration. A hat indicates a unit vector in the stated direction. Equation B.1 is known as the *momentum equation* and Equation B.2 as the *continuity equation*.

B.1 Three Dimensional Equations of Motion

The rotation vector is written $\boldsymbol{\Omega} = \Omega(\cos\phi\hat{\mathbf{x}} + \sin\phi\hat{\mathbf{y}})$ where Ω is the angular frequency of the Earth's rotation and ϕ denotes latitude. The Coriolis term in Equation B.1 can now be written $2\boldsymbol{\Omega} \times \boldsymbol{u} = 2\Omega[(w\cos\phi - v\sin\phi)\hat{\mathbf{x}} + u\sin\phi\hat{\mathbf{y}} - u\cos\phi\hat{\mathbf{z}}]$. If the thin shell approximation is made (i.e., the vertical scale of motion is much smaller than the horizontal scale of motion) and noting that gravity dominates the Coriolis effect in the vertical, the Coriolis term simplifies to $2\boldsymbol{\Omega} \times \boldsymbol{u} = -fv\hat{\mathbf{x}} + fu\hat{\mathbf{y}}$ where $f(\phi) = 2\Omega\sin\phi$ is called the

Coriolis parameter.

In the vertical, the momentum equation is now

$$\frac{\partial w}{\partial t}+u\frac{\partial w}{\partial x}+v\frac{\partial w}{\partial y}+w\frac{\partial w}{\partial z}=-\frac{1}{\rho}\frac{\partial p}{\partial z}-g. \tag{B.3}$$

In the ocean, large-scale motions in the vertical are dominated by the gravitational acceleration and the pressure gradient terms (*Gill*, 1982). Therefore, it is useful to define an equilibrium pressure $p_0(z)$ and density $\rho_0(z)$ that satisfy this dominant balance

$$\frac{dp_0}{dz}=-g\rho_0. \tag{B.4}$$

Perturbations from this equilibrium state are denoted $p_\mathrm{p}(x,y,z,t)$ and $\rho_\mathrm{p}(x,y,z,t)$ and are defined by

$$p=p_0+p_\mathrm{p}, \quad \rho=\rho_0+\rho_\mathrm{p}. \tag{B.5}$$

Assuming the horizontal scale of motion is much larger than the vertical scale of motion, the perturbation pressure and density also satisfy the hydrostatic equation (*Gill*, 1982):

$$\frac{\partial p_\mathrm{p}}{\partial z}=-g\rho_\mathrm{p}. \tag{B.6}$$

This effectively neglects the acceleration and nonlinear terms in the vertical momentum equation governing perturbations to the equation of state. The result is known as the *hydrostatic approximation*.

The equations governing perturbations to the equilibrium state reduce to

$$\begin{aligned}
\frac{\partial u}{\partial t}+u\frac{\partial u}{\partial x}+v\frac{\partial u}{\partial y}+w\frac{\partial u}{\partial z}-fv &= -\frac{1}{\rho_0}\frac{\partial p_\mathrm{p}}{\partial x} && \text{(B.7)}\\
\frac{\partial v}{\partial t}+u\frac{\partial v}{\partial x}+v\frac{\partial v}{\partial y}+w\frac{\partial v}{\partial z}+fu &= -\frac{1}{\rho_0}\frac{\partial p_\mathrm{p}}{\partial y} && \text{(B.8)}\\
\frac{\partial p}{\partial z} &= -g\rho && \text{(B.9)}\\
\frac{\partial u}{\partial x}+\frac{\partial v}{\partial y}+\frac{\partial w}{\partial z} &= 0, && \text{(B.10)}
\end{aligned}$$

where the *Boussinesq approximation* has been made so that density is replaced by the equilibrium density everywhere except in Equation B.9. This approximation is valid if the fluid is incompressible and if the vertical scale of motion is small compared with the vertical scale over which density varies.

B.2 The Shallow Water Equations

Consider an ocean of uniform density $\rho_0 = \text{const}$. Let the ocean bottom lie at $z = -H(x, y)$ and the free surface at $z = \eta(x, y, t)$. Uniform density leads to the expression $p_0 = -g\rho_0 z$ from Equation B.4. The atmospheric pressure at the surface is assumed constant and so we have a perturbation pressure $p_\text{p}(z = \eta) = -p_0(z = \eta) = g\rho_0\eta$. Since density is uniform everywhere, $\rho_\text{p} = 0$ and so Equation B.6 implies that $p_\text{p} = g\rho_0\eta$ for all z. Therefore, the pressure gradient terms in Equations B.7–B.8 can be written in terms of the height of the free surface η and the momentum equations become

$$\frac{\partial u}{\partial t} + u\frac{\partial u}{\partial x} + v\frac{\partial u}{\partial y} + w\frac{\partial u}{\partial z} - fv = -g\frac{\partial \eta}{\partial x} \tag{B.11}$$

$$\frac{\partial v}{\partial t} + u\frac{\partial v}{\partial x} + v\frac{\partial v}{\partial y} + w\frac{\partial v}{\partial z} + fu = -g\frac{\partial \eta}{\partial y}. \tag{B.12}$$

The fluid velocity is now only a function of x and y since η is not a function of depth.

Integrating the continuity equation with respect to depth from $-H$ to η leads to

$$\frac{\partial \eta}{\partial t} + \frac{\partial}{\partial x}\left[(H + \eta)u\right] + \frac{\partial}{\partial y}\left[(H + \eta)v\right] = 0,$$

where the surface boundary condition $w(z = \eta) = d\eta/dt$ has been used. Furthermore, ignoring nonlinear terms leads to

$$\frac{\partial \eta}{\partial t} + \frac{\partial}{\partial x}(Hu) + \frac{\partial}{\partial y}(Hv) = 0. \tag{B.13}$$

Equations B.11–B.13 are known as the *shallow water equations*.

APPENDIX C

REFLECTION AND TRANSMISSION OF EQUATORIAL WAVES AT AN EASTERN BOUNDARY

The treatment given here follows *Clarke and Shi* (1991) and the same results can also be found in *Clarke* (1992) and *Grimshaw and Allen* (1988).

Consider fluid motion on an equatorial β-plane (Equations 3.18–3.20)

$$\boldsymbol{u}_t + y\hat{\mathbf{z}} \times \boldsymbol{u} = -\boldsymbol{\nabla}\phi \tag{C.1}$$

$$\phi_t + \boldsymbol{\nabla} \cdot \boldsymbol{u} = 0 \tag{C.2}$$

where the equations of motion have been expressed in vector form and the primes have been dropped, a subscript denotes a partial derivative, $\boldsymbol{u}(x, y, t) = u\hat{\mathbf{x}} + v\hat{\mathbf{y}}$ is the depth-averaged fluid velocity, $\phi(x, y, t)$ is the height of the free surface expressed as geopotential height, and a hat indicates a unit vector in the stated direction. All variables have been nondimensionalized as described in Section 3.3.1.

Performing the operation $\left(\frac{\partial}{\partial t} - \hat{\mathbf{z}}\times\right)$ on Equation C.1 leads to

$$\boldsymbol{u} + \frac{1}{y^2}\boldsymbol{u}_{tt} = -\frac{1}{y^2}\boldsymbol{\nabla}\phi_t + \frac{1}{y}\hat{\mathbf{z}} \times \boldsymbol{\nabla}\phi. \tag{C.3}$$

If a wave solution with low frequency ($\omega^2/y^2 \ll 1$) is assumed then $\frac{1}{y^2}\boldsymbol{u}_{tt}$ is small

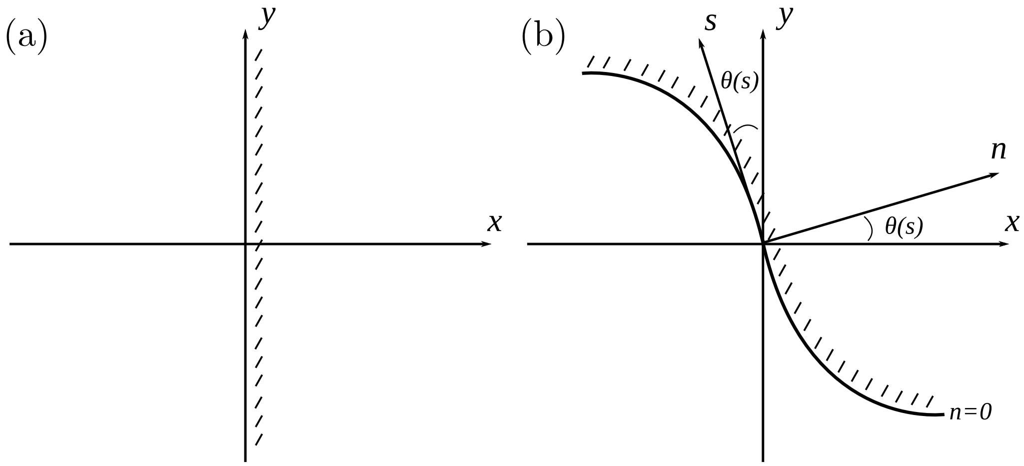

Figure C.1: Coordinate systems at eastern ocean boundaries. Two boundaries are considered: (a) meridional and (b) non-meridional. Normal and tangential coordinates (n, s) used for nonmeridional boundary are shown with their relationship to the eastward and northward coordinates (x, y).

compared to $\boldsymbol{u}$ and Equation C.3 simplifies to

$$\boldsymbol{u} = -\frac{1}{y^2}\boldsymbol{\nabla}\phi_t + \frac{1}{y}\hat{\mathbf{z}} \times \boldsymbol{\nabla}\phi. \tag{C.4}$$

Substituting this expression for $\boldsymbol{u}$ into Equation C.2 leads to

$$\phi_{xxt} + \phi_{yyt} - \frac{2}{y}\phi_{yt} + \phi_x - y^2\phi_t = 0. \tag{C.5}$$

This equation is subject to boundary conditions that depend on the geography. The cases of a meridional boundary and a nonmeridional boundary are presented below.

C.1 Meridional boundary

Consider a meridional eastern boundary at $x = 0$ (Figure C.1a). Along this boundary the flow must be zero and the boundary condition (using Equation C.4) at $x = 0$ is

$$0 = -\frac{1}{y^2}\boldsymbol{\nabla}\phi_t + \frac{1}{y}\hat{\mathbf{z}} \times \boldsymbol{\nabla}\phi.$$

Assuming a wave solution of the form $\phi \sim e^{i\omega t}$, this equation leads to

$$-i\omega\phi_x - y\phi_y = 0$$

which implies that the ratio of the length scale in x to the length scale in y is ω/y. Using this relationship between length scales allows us to neglect ϕ_{tyy} with respect to ϕ_{txx} and ϕ_{yt}/y with respect to ϕ_x in Equation C.5, to an error of order ω^2/y^2. Near the boundary, this yields the governing equation

$$\phi_{xxt} + \phi_x - y^2\phi_t = 0.$$

Assuming a wave solution of the form $\phi = A(y)e^{\lambda x - i\omega t}$ leads to the following dispersion relation

$$\lambda^2 - \frac{i}{\omega}\lambda - y^2 = 0.$$

If λ is imaginary, then waves will propagate offshore in the x direction; if λ is complex, then the real part will cause the wave amplitude to decay offshore such that waves are trapped near the coast. Solving for λ gives two cases. The first case, for $\omega < 1/2y$, yields a completely imaginary solution

$$\lambda = i\frac{1}{2\omega}\left[1 \pm \sqrt{1-(2y\omega)^2}\right] \tag{C.6}$$

and the second case, for $\omega > 1/2y$, yields a complex solution

$$\lambda = i\frac{1}{2\omega} \pm y\sqrt{1-\frac{1}{(2y\omega)^2}}. \tag{C.7}$$

At a fixed frequency a critical latitude can be defined, $y_{\mathrm{c}} = 1/2\omega$, equatorward of which waves radiate offshore (Equation C.6) and poleward of which waves remain trapped to the boundary and are able to propagate along the coast (Equation C.7). Similarly, at a fixed latitude a critical frequency can also be defined, $\omega_{\mathrm{c}} = 1/2y$, above which waves are trapped to the boundary and below which they radiate offshore.

C.2 Nonmeridional boundary

Consider the case of a nonmeridional eastern boundary (Figure C.1b). The dispersion relation, which now includes the effect of coastline angle, is given by

$$\lambda^2 - \frac{i}{\omega}\cos\theta\lambda - y^2 = 0. \tag{C.8}$$

The derivation of Equation C.8 can be found in *Clarke and Shi* (1991). As above, solving for λ gives two cases. The first case, for $\omega < \cos\theta/2y$, yields a completely imaginary solution

$$\lambda = i\frac{\cos\theta}{2\omega}\left[1 \pm \sqrt{1 - \left(\frac{2y\omega}{\cos\theta}\right)^2}\right] \tag{C.9}$$

and the second case, for $\omega > \cos\theta/2y$, yields a complex solution

$$\lambda = i\frac{\cos\theta}{2\omega} \pm y\sqrt{1 - \left(\frac{\cos\theta}{2y\omega}\right)^2}. \tag{C.10}$$

Thus, at a fixed frequency, a critical latitude can be defined

$$y_{\mathrm{c}} = \frac{\cos\theta}{2\omega}, \tag{C.11}$$

equatorward of which waves radiate offshore (Equation C.9) and poleward of which waves remain trapped to the boundary and are able to propagate along the coast (Equation C.10). Similarly, at a fixed latitude the critical frequency is defined as $\omega_{\mathrm{c}} = \cos\theta/2y$. Above this critical frequency waves are trapped to the boundary and below this frequency they radiate offshore. Note that for $\theta = 0$ these results simplify to those given above for a perfectly meridional boundary.

APPENDIX D

RESTRICTION OF PRESSURES FOR INCLUSION IN THE HISTORICAL RECONSTRUCTION

Three restrictions limiting the number of predictors in the regression model (Chapter 7) are outlined below.

D.1 Strength of Linear Relationship with the MJO

The strength of the linear relationship between surface pressure and $\boldsymbol{I}_t^{\mathrm{WH}}$ is measured by

$$\bar{\kappa}_p^2 = \frac{\int \left[\kappa_{1,p}^2(\omega) f_1(\omega) + \kappa_{2,p}^2(\omega) f_2(\omega)\right] d\omega}{\int \left[f_1(\omega) + f_2(\omega)\right] d\omega}, \tag{D.1}$$

where $\kappa_{1,p}^2$ and $\kappa_{2,p}^2$ are the squared coherence between p_{ijt}^a and the first and second components of $\boldsymbol{I}_t^{\mathrm{WH}}$ respectively, and f_1 and f_2 are the corresponding power spectral densities of the first and second components of $\boldsymbol{I}_t^{\mathrm{WH}}$. The integral of f_1 is the variance of the first component of $\boldsymbol{I}_t^{\mathrm{WH}}$; the integral of the product of f_1 and $\kappa_{1,p}^2$ is the variance of the first component of $\boldsymbol{I}_t^{\mathrm{WH}}$ that can be accounted for by p_{ijt}^{a}. The statistic $\bar{\kappa}$ is a number between zero and one representing the proportion of the total standard deviation of $\boldsymbol{I}_t^{\mathrm{WH}}$ that is accounted for by p_{ijt}^a (see Section 2.2.3 for details).

This statistic is a function of latitude and longitude and is strongest in the tropical

Indo-Pacific where $\bar{\kappa}$ is about 0.65 (Figure 7.1). There are also indications of the eastward-propagating nature of the MJO in the broad region of influence across the open Pacific Ocean as well as the blocking produced by the western slopes of the Andes and the East African Highlands. This pattern is consistent with *Donald et al.* (2006) who showed similar global behaviour using composites of sea level pressure based on MJO phase. All potential pressure predictors are required to have $\bar{\kappa} \geq 0.33$.

D.2 Accuracy of the Reanalysis Pressure

The standard deviation of the 56-member ensemble at a given grid point and time (Δp_{ijt}) is a measure of the quality of the hindcast pressure. The following relative measure of the quality of the hindcast pressure has been calculated:

$$\Delta_{ijt} = \frac{\Delta p_{ijt}}{s_{ij}}, \tag{D.2}$$

where s_{ij} represents the standard deviation of p^a_{ijt} through time. This normalization allows for the fact that pressure is more variable at some locations. Time series of Δ_{ijt} for selected locations are shown in Figure D.1.

To measure the overall level, and trend, of Δ_{ijt} it is approximated by the model

$$\Delta_{ijt} = \alpha_{0ij} - \alpha_{1ij}(t - t_{\mathrm{h}}) + \epsilon_t \tag{D.3}$$

where t denotes time, t_{h} represents the midway point between 1905 and 2008, and ϵ_t is an error term representing effects not included in the model. (Note the negative sign for α_{1ij} was introduced because it is anticipated that the trend in relative error will be negative, reflecting more accurate hindcasts in later years). The coefficient α_0 measures the relative error in the middle of the last century (i.e., $t = t_{\mathrm{h}}$). As expected it is generally low in regions with a large number of observations over 1905–2008 (top panel, Figure D.2). The coefficient α_1 reflects local changes in the observing system and tends to be low where the number of observations have been consistent over time (bottom panel, Figure D.2). Predictors are rejected from regions where $\alpha_0 > 0.8$ and $\alpha_1 > 1.76 \cdot 10^{-5}$ days^{-1} (thick contours, Figure D.2). The critical value for α_1 represents a change in Δ_{ijt} of 67% over 1905–2008. The thick contour in Figure 7.1 shows the intersection of the rejection regions

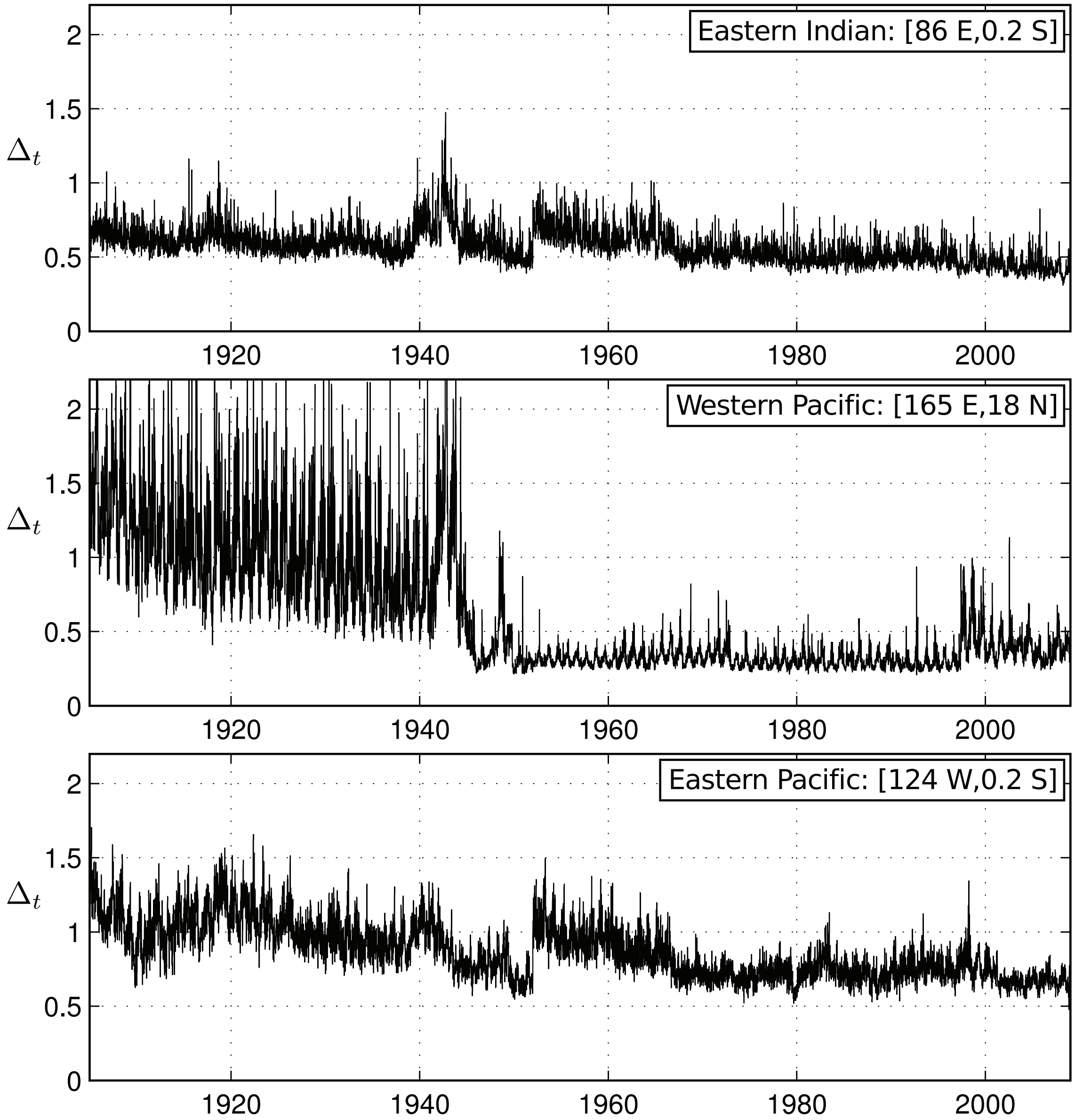

Figure D.1: Relative error of Twentieth Century Reanalysis pressure at selected locations. The relative error Δ_t is calculated following Equation D.2. Pressure series from the Western Pacific and Eastern Pacific locations shown above would be rejected due to excessive trend and mean relative error, respectively, based on the restrictions outlined in Section D.2. Pressure from the Eastern Indian location would not be rejected.

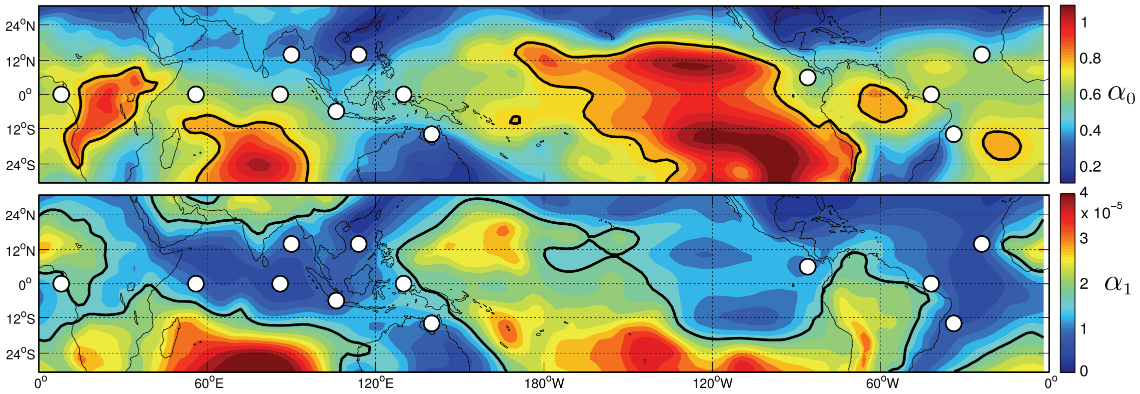

Figure D.2: Mean and trend in the relative error of surface pressure Δ_{ijt}. Top: mean of Δ_{ijt} (α_{0ij}) with thick contour showing the critical value (0.8). Bottom: trend of Δ_{ijt} (α_{1ij}) with thick contour showing critical value ($1.76 \cdot 10^{-5}$ days^{-1}). White circles show the chosen locations of predictors used in the regression model.

based on the critical values of $\bar{\kappa}$, α_0, and α_1.

D.3 Pressure Decorrelation Lengthscales

A set of sensitivity studies was carried out to determine the effect of spatial separation on the choice of pressures for inclusion as predictors in the regression model. In one experiment the zonal and meridional separation of equispaced pressures along the equator, and two adjacent zonal lines, were varied and the impact on the fit of the regression was assessed. The regressions were trained onto the first half of the WH04 period (1/1/1979–28/2/1994) and validated on the second half (1/3/1994–31/12/2008). A two-dimensional plot of the total error variance over the validation period as a function of longitudinal and latitudinal separation distance was constructed (not shown). As the longitudinal spacing decreases, more predictors are included; the regression is eventually overfit to the pressure data over the training period, and the skill reduces over the validation period. The error variance over the validation period reaches a minimum with a longitudinal separation of 18° and a latitudinal separation of 14° (see Figure D.3, thick line). Excluding the Hilbert transform of each predictor significantly reduced the skill of the regression model for both components (Figure D.3, thin line). Switching the training and validation periods yielded essentially the same results.

	Indian	Pacific	Atlantic
14°N	20°	20-30°	20°
Equator	25-30°	40-50°	50°
14°S	20°	20-30°	40°

Table D.1: Longitudinal decorrelation lengthscales of p^{a}_{ijt} in each basin along the equator, 14°N, and 14°S. The lengthscale is a function of latitude and ocean basin and is given as a single values or range for each region. The basins are defined as lying between the three major topographic features in the tropics: the Andes, the East African Highlands, and the Maritime Continent.

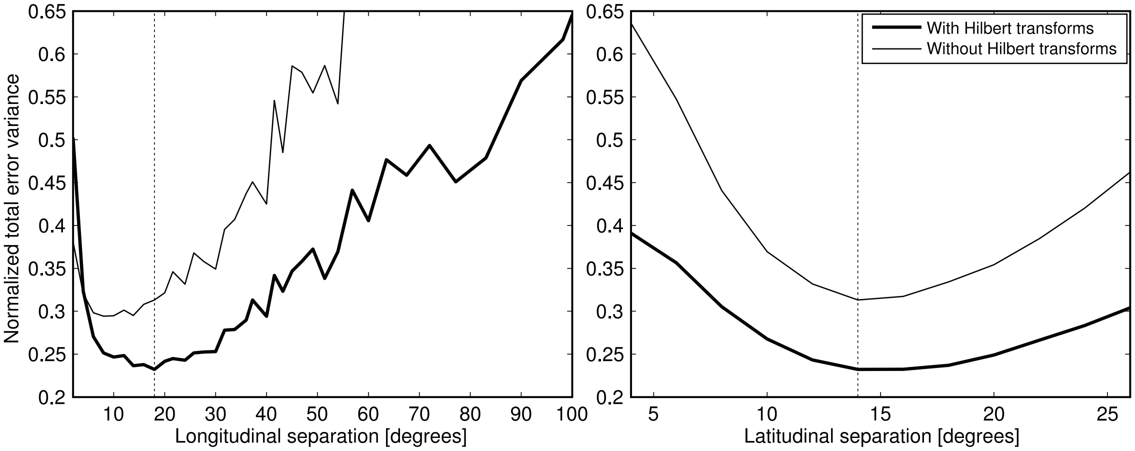

Figure D.3: Fit of the regression model to $\boldsymbol{I}_t^{\mathrm{WH}}$ over the validation period (1/3/1994–31/12/2008). Left: the total error variance is shown as a function of east-west spacing assuming a north-south spacing (of three lines) of 14°. Right: the total error variance is shown as a function of north-south spacing (of three lines) assuming an east-west spacing of 18°. Note that the total error variance has been normalized by the total variance of $\boldsymbol{I}_t^{\mathrm{WH}}$ over the validation period.

Although the above sensitivity study is straightforward, it does not allow for geographically varying decorrelation scales. If the pressure decorrelation lengthscale is defined as the distance required for the correlation of pressure to drop to 0.5 then the north-south decorrelation scale is fairly homogenous with values between 14° and 18°. The east-west decorrelation scale however depends on both latitude and longitude (Table D.1). When choosing the predictors included in the model, no two locations (white circles, Figures 7.1 and D.2) were chosen closer than the decorrelation scales defined in Table D.1.

APPENDIX E

CALCULATING THE POSTERIOR DISTRIBUTION

In accordance with the multivariate autoregressive model for a stochastically forced, damped harmonic oscillator presented in Chapter 2, assume the oscillator and associated forcing at time t_0 are stored in the first and last pair of elements of the four dimensional state vector $\boldsymbol{x}$ respectively. Further assume that the prior distribution for $\boldsymbol{x}$ at time t_0 is normal with zero mean and covariance matrix $\boldsymbol{\Sigma}_{\text{prior}}$. In the notation of Chapter 2, $\boldsymbol{\Sigma}_{\text{prior}} = \boldsymbol{\Sigma}_{\infty}$.

Assume a multivariate observation becomes available at time t_0 and it is related to the state vector by $\boldsymbol{y}_{\text{obs}} = \boldsymbol{x} + \nu$ where ν is the observation error which is taken to be normally distributed with zero mean and covariance matrix $\boldsymbol{\Sigma}_{\text{obs}}$. It is straightforward to show that the posterior distribution of the state given this observation is also normal with mean and covariance

$$\begin{aligned} \boldsymbol{\mu}_{\text{post}} &= \boldsymbol{\Sigma}_{\text{prior}} \left(\boldsymbol{\Sigma}_{\text{prior}} + \boldsymbol{\Sigma}_{\text{obs}}\right)^{-1} \boldsymbol{\mu}_{\text{obs}} && \text{(E.1)} \\ \boldsymbol{\Sigma}_{\text{post}} &= \left(\boldsymbol{\Sigma}_{\text{prior}}^{-1} + \boldsymbol{\Sigma}_{\text{obs}}^{-1}\right)^{-1} && \text{(E.2)} \end{aligned}$$

These results follow directly from the product of a pair of normal probability densities which is also normal.

Assume $\boldsymbol{y}_{\text{obs}}$ and the observation error covariance matrix take the form

$$\boldsymbol{y}_{\text{obs}} = \begin{bmatrix} \boldsymbol{y}_{\text{obs}}^{\text{osc}} \\ \boldsymbol{y}_{\text{obs}}^{\text{for}} \end{bmatrix} \qquad \boldsymbol{\Sigma}_{\text{obs}} = \begin{bmatrix} \sigma_{\text{obs}}^2 \mathrm{I} & 0 \\ 0 & \alpha \mathrm{I} \end{bmatrix} \tag{E.3}$$

where α represents the variance of the uncertainty of the observed forcing. We will consider the case in which the uncertainty on the observed forcing becomes very large ($\alpha \to \infty$). This implies that we only have observational information on the oscillator and not on the associated forcing. What are the implications of the new observation? Can we say something about the forcing despite not observing it?

In the limit $\alpha \to \infty$ the mean of the posterior distribution is given by

$$\boldsymbol{\mu}_{\text{post}} = \frac{1}{1+\sigma_{\text{obs}}^2} \begin{bmatrix} \mathrm{I} \\ \boldsymbol{\Sigma}_{21}\boldsymbol{\Sigma}_{11}^{-1} \end{bmatrix} \boldsymbol{y}_{\text{obs}}^{\text{osc}}, \tag{E.4}$$

where $\boldsymbol{\Sigma}_{ij}$ refers to the ij^{th} block of $\boldsymbol{\Sigma}_{\text{prior}}$ when arranged in four 2×2 blocks. Note that as σ_{obs}^2 tends to infinity the posterior mean reverts to the prior mean as expected; as σ_{obs}^2 tends to zero the posterior mean for the oscillator is simply the observation itself and the mean forcing comes from a linear regression of the forcing components onto the oscillator components. This tells us that, even in the absence of any observation of the forcing, an observation of the oscillator can be used along with the prior to infer the mean of the forcing.

The covariance of the posterior distribution is given by

$$\boldsymbol{\Sigma}_{\text{post}} = \frac{1}{1+\sigma_{\text{obs}}^2} \left[\sigma_{\text{obs}}^2 \boldsymbol{\Sigma}_{\text{prior}} + \begin{bmatrix} 0 & 0 \\ 0 & \boldsymbol{\Sigma}_{22} - \boldsymbol{\Sigma}_{21}\boldsymbol{\Sigma}_{11}^{-1}\boldsymbol{\Sigma}_{12} \end{bmatrix} \right] \tag{E.5}$$

In the limit σ_{obs}^2 tends to infinity the posterior covariance reverts to the prior covariance as expected; in the limit σ_{obs}^2 tends to zero, the posterior covariance of the forcing is simply the variance of the residuals from a linear regression of the forcing components onto the oscillator components.

BIBLIOGRAPHY

Arief, D., and S. Murray, Low-frequency fluctuations in the Indonesian throughflow through Lombok Strait, *Journal of Geophysical Research*, *101*, 12,455, 1996.

Bellenger, H., and J. Duvel, Intraseasonal convective perturbations related to the seasonal march of the Indo-Pacific monsoons, *Journal of Climate*, *20*, 2853, 2007.

Bessafi, M., and M. Wheeler, Modulation of South Indian Ocean tropical cyclones by the Madden–Julian oscillation and convectively coupled equatorial waves, *Monthly Weather Review*, *134*, 638–656, 2006.

Blumberg, A., and G. Mellor, A description of a three-dimensional coastal ocean circulation model, *Three-dimensional coastal ocean models*, *4*, 1–16, 1987.

Bond, N., and G. Vecchi, The Influence of the Madden–Julian Oscillation on precipitation in Oregon and Washington, *Weather and Forecasting*, *18*, 600–613, 2003.

Bougeault, P., and P. Lacarrere, Parameterization of orography-induced turbulence in a mesobeta-scale model, *Monthly weather review*, *117*, 1872–1890, 1989.

Brillinger, D., *Time Series: Data Analysis and Theory*, Holden-Day, 1981.

Brillinger, D., *Time Series: Data Analysis and Theory*, Society for Industrial Mathematics, 2001.

Brink, K., A comparison of long coastal trapped wave theory with observations off Peru, *Journal of Physical Oceanography*, *12*, 897–913, 1982.

Cane, M., and E. Sarachik, The response of a linear baroclinic equatorial ocean to periodic forcing, *Journal of Marine Research*, *39*, 651–693, 1981.

Cassou, C., Intraseasonal interaction between the Madden-Julian Oscillation and the North Atlantic Oscillation, *Nature*, *455*, 523, 2008.

Cazenave, A., A. Lombard, and W. Llovel, Present-day sea level rise: A synthesis, *Comptes rendus-Geoscience*, *340*, 761–770, 2008.

Chelton, D., R. deSzoeke, M. Schlax, K. El Naggar, and N. Siwertz, Geographical variability of the first baroclinic Rossby radius of deformation, *Journal of Physical Oceanography*, *28*, 433–460, 1998.

Chelton, D., M. Schlax, J. Lyman, and G. Johnson, Equatorially trapped Rossby waves in the presence of meridionally sheared baroclinic flow in the Pacific Ocean, *Progress in Oceanography*, *56*, 323–380, 2003.

Chen, D., M. Cane, A. Kaplan, S. Zebiak, and D. Huang, Predictability of El Niño over the past 148 years, *Nature*, *428*, 733–736, 2004.

Church, J., and A. Forbes, Circulation in the Gulf of Carpentaria. i direct observations of currents in the south-east corner of the Gulf of Carpentaria, *Australian Journal of Marine and Freshwater Research*, *34*, 1–10, 1983.

Clarke, A., Wind-forced linear and nonlinear Kelvin waves along an irregular coastline, *Journal of Fluid Mechanics*, *83*, 337–348, 1977.

Clarke, A., On the reflection and transmission of low-frequency energy at the irregular western Pacific Ocean boundary, *Journal of Geophysical Research*, *96*, 3289–3305, 1991.

Clarke, A., Low-frequency reflection from a nonmeridional eastern ocean boundary and the use of coastal sea level to monitor eastern Pacific equatorial Kelvin waves, *Journal of Physical Oceanography*, *22*, 163–183, 1992.

Clarke, A., *An introduction to the dynamics of El Niño and the Southern Oscillation*, Academic Press: London, UK, 2008.

Clarke, A., and R. Ahmed, Dynamics of remotely forced intraseasonal oscillations off the western coast of South America, *Journal of Physical Oceanography*, *29*, 240–258, 1999.

Clarke, A., and X. Liu, Observations and dynamics of semiannual and annual sea levels near the eastern Equatorial Indian Ocean boundary, *Journal of Physical Oceanography*, *23*, 386–399, 1993.

Clarke, A., and X. Liu, Interannual sea level in the northern and eastern Indian Ocean, *Journal of Physical Oceanography*, *24*, 1224–1235, 1994.

Clarke, A., and C. Shi, Critical frequencies at ocean boundaries, *Journal of Geophysical Research-Oceans*, *96*, 1991.

Compo, G., et al., The twentieth century reanalysis project, *Quarterly Journal of the Royal Meteorological Society*, *137*, 1–28, 2011.

Diky, L., and G. Golitsyn, Calculation of the Rossby wave velocities in the Earth's atmosphere, *Tellus*, *20*, 314–317, 1968.

Donald, A., H. Meinke, B. Power, M. Wheeler, A. Maia, R. Stone, J. Ribbe, and N. White, Near-global impact of the Madden-Julian Oscillation on rainfall, *Geophysical Research Letters*, *33*, 2006.

Doodson, A., The analysis of tidal observations, *Philosophical Transactions of the Royal Society of London. Series A, Containing Papers of a Mathematical or Physical Character*, *227*, 223–279, 1928.

Durland, T., R. Samelson, D. Chelton, and R. de Szoeke, Modification of long equatorial Rossby wave phase speeds by zonal currents, *Journal of Physical Oceanography*, *41*, 1077–1101, 2011.

Enfield, D., The intraseasonal oscillation in Eastern Pacific sea levels: How is it forced?, *Journal of Physical Oceanography*, *17*, 1860–1876, 1987.

Farrell, B., and P. Ioannou, Generalized stability theory. part i: Autonomous operators, *Journal of the atmospheric sciences*, *53*, 2025–2025, 1996.

Finney, B., *Voyage of rediscovery: a cultural odyssey through Polynesia*, Univ of California Press, 1994.

Forbes, A., and J. Church, Circulation in the Gulf of Carpentaria. ii residual currents and mean sea level, *Australian Journal of Marine and Freshwater Research*, *34*, 11–22, 1983.

Fu, L., Wind-forced intraseasonal sea level variability of the extratropical oceans, *Journal of Physical Oceanography*, *33*, 436–449, 2003.

Fu, L., E. Christensen, C. Yamarone Jr, M. Lefebvre, Y. Ménard, M. Dorrer, and P. Escudier, TOPEX/POSEIDON mission overview, *Journal of Geophysical Research*, *99*, 24,369–24,382, 1994.

Gaspar, P., Y. Grégoris, and J. Lefevre, A simple eddy kinetic energy model for simulations of the oceanic vertical mixing: Tests at Station Papa and long-term upper ocean study site, *Journal of Geophysical Research*, *95*, 16,179–16, 1990.

Gill, A., *Atmosphere-Ocean Dynamics*, Academic. San Diego. US, 1982.

Girishkumar, M., M. Ravichandran, M. McPhaden, and R. Rao, Intraseasonal variability in barrier layer thickness in the south central Bay of Bengal, *Journal of Geophysical Research*, *116*, C03,009, 2011.

Gottschalck, J., et al., A framework for assessing operational model MJO forecasts: A project of the CLIVAR Madden-Julian Oscillation Working Group, *Bulletin of the American Meteorological Society*, 2010.

Grabowski, W., Impact of explicit atmosphere–ocean coupling on MJO-like coherent structures in idealized aquaplanet simulations, *Journal of the Atmospheric Sciences*, *63*, 2289–2306, 2006.

Grimshaw, R., and J. Allen, Low-frequency baroclinic waves off coastal boundaries, *Journal of Physical Oceanography*, *18*, 1124–1143, 1988.

Haines, J., K. Thompson, and D. Wiens, The detection of coastal-trapped waves, *Journal of Geophysical Research*, *96*, 2593–2597, 1991.

Hall, J., A. Matthews, and D. Karoly, The modulation of tropical cyclone activity in the Australian region by the Madden–Julian Oscillation, *Monthly Weather Review*, *129*, 2970–2982, 2001.

Han, W., Origins and dynamics of the 90-day and 30-60-day variations in the equatorial Indian Ocean, *Journal of physical oceanography*, *35*, 708–728, 2005.

Han, W., D. Lawrence, and P. Webster, Dynamical response of equatorial Indian Ocean to intraseasonal winds: zonal flow, *Geophysical Research Letters*, *28*, 4215–4218, 2001.

Harrison, D., and G. Vecchi, Westerly wind events in the Tropical Pacific, 1986–1995, *J. Climate*, *10*, 3131–3156, 1997.

Harvey, A., *Forecasting, structural time series models and the Kalman filter*, Cambridge University Press, 1991.

Hendon, H., Impact of air–sea Coupling on the Madden–Julian Oscillation in a general circulation model, *Journal of the Atmospheric Sciences*, *57*, 3939–3952, 2000.

Hendon, H., B. Liebmann, and J. Glick, Oceanic Kelvin waves and the Madden–Julian Oscillation, *Journal of the Atmospheric Sciences*, *55*, 88–101, 1998.

Hidayat, R., and S. Kizu, Influence of the Madden-Julian Oscillation on Indonesian rainfall variability in austral summer, *International Journal of Climatology*, 2009.

Ho, C., J. Kim, J. Jeong, H. Kim, and D. Chen, Variation of tropical cyclone activity in the South Indian Ocean: El Niño–Southern Oscillation and Madden-Julian Oscillation effects, *Journal of Geophysical Research*, *111*, D22,101, 2006.

Iskandar, I., W. Mardiansyah, Y. Masumoto, and T. Yamagata, Intraseasonal Kelvin waves along the southern coast of Sumatra and Java, *J. Geophys. Res*, *110*, 2005.

Jiang, X., D. Waliser, M. Wheeler, C. Jones, M. Lee, and S. Schubert, Assessing the skill of an all-season statistical forecast model for the Madden–Julian Oscillation, *Monthly Weather Review*, *136*, 1940–1956, 2008.

Jin, E., et al., Current status of ENSO prediction skill in coupled ocean–atmosphere models, *Climate Dynamics*, *31*, 647–664, 2008.

Johnson, R., and D. Wichern, *Applied Multivariate Statistical Analysis*, Prentice Hall Upper Saddle River, NJ, 2002.

Jones, C., and L. Carvalho, Stochastic simulations of the Madden–Julian oscillation activity, *Climate Dynamics*, pp. 1–18, 2009.

Jones, C., L. Carvalho, R. Higgins, D. Waliser, and J. Schemm, A statistical forecast model of tropical intraseasonal convective anomalies, *Journal of Climate*, *17*, 2078–2095, 2004.

Kalnay, E., et al., The NCEP/NCAR 40-year reanalysis project, *Bulletin of the American Meteorological Society*, *77*, 437–471, 1996.

Kanamitsu, M., W. Ebisuzaki, J. Woollen, S. Yang, J. Hnilo, M. Fiorino, and G. Potter, NCEP-DOE AMIP-II Reanalysis (R-2), *Bulletin of the American Meteorological Society*, *83*, 1631–1643, 2002.

Kang, I., and H. Kim, Assessment of MJO predictability for Boreal Winter with various statistical and dynamical models, *Journal of Climate*, 2010.

Kasahara, A., Normal modes of ultralong waves in the atmosphere, *Monthly Weather Review*, *104*, 669–690, 1976.

Kessler, W., *Intraseasonal Variability in the Atmosphere–Ocean Climate System*, chap. The Oceans, pp. 176–222, Springer, 2005.

Kessler, W., M. McPhaden, and K. Weickmann, Forcing of intraseasonal Kelvin waves in the equatorial Pacific, *Journal of Geophysical Research-Oceans*, *100*, 1995.

Kim, H., C. Hoyos, P. Webster, and I. Kang, Ocean–atmosphere coupling and the boreal winter MJO, *Climate Dynamics*, pp. 1–14, 2009.

Kleeman, R., Measuring dynamical prediction utility using relative entropy, *Journal of the Atmospheric Sciences*, *59*, 2057–2072, 2002.

Kleeman, R., Stochastic theories for the irregularity of enso, *Philosophical Transactions of the Royal Society A: Mathematical, Physical and Engineering Sciences*, *366*, 2509, 2008.

Kundu, P., *Fluid Mechanics*, Academic Press, 1990.

Large, W., and S. Pond, Open ocean momentum flux measurements in moderate to strong winds, *Journal of Physical Oceanography*, *11*, 324–336, 1981.

Large, W., and S. Yeager, The global climatology of an interannually varying air–sea flux data set, *Climate dynamics*, *33*, 341–364, 2009.

LeBlond, P., and L. Mysak, *Waves in the Ocean*, Elsevier Oceanography Series, Amsterdam, 1978.

Lin, H., and G. Brunet, The influence of the Madden–Julian Oscillation on Canadian wintertime surface air temperature, *Monthly Weather Review*, *137*, 2250–2262, 2009.

Lin, H., G. Brunet, and J. Derome, Forecast skill of the Madden-Julian Oscillation in two Canadian atmospheric models, *Monthly Weather Review*, *136*, 4130–4149, 2008.

Lin, H., G. Brunet, and J. Derome, An observed connection between the North Atlantic oscillation and the Madden–Julian oscillation, *Journal of Climate*, *22*, 364–380, 2009.

Lo, F., and H. Hendon, Empirical extended-range prediction of the Madden–Julian Oscillation, *Monthly Weather Review*, *128*, 2528–2543, 2000.

Lorenz, E., Deterministic Nonperiodic Flow., *Journal of Atmospheric Sciences*, *20*, 130–148, 1963.

Lorenz, E., A study of the predictability of a 28-variable atmospheric model, *Tellus*, *17*, 321–333, 1965.

Luyten, J., and D. Roemmich, Equatorial currents at semi-annual period in the Indian Ocean, *J. Phys. Oceanogr.;(United States)*, *12*, 1982.

Madden, R., and P. Julian, Detection of a 40–50 Day oscillation in the zonal wind in the Tropical Pacific, *Journal of the Atmospheric Sciences*, *28*, 702–708, 1971.

Madden, R., and P. Julian, Description of global-scale circulation cells in the tropics with a 40–50 day period, *Journal of the Atmospheric Sciences*, *29*, 1109–1123, 1972.

Madden, R., and P. Julian, Observations of the 40–50-day tropical oscillation - A review, *Monthly Weather Review*, *122*, 814–837, 1994.

Madden, R., and P. Julian, *Intraseasonal Variability in the Atmosphere–Ocean Climate System*, chap. Historical perspective, pp. 1–18, Springer, 2005.

Madec, G., *NEMO ocean engine*, Institut Pierre-Simon Laplace (IPSL), France, 2008.

Madec, G., P. Delecluse, M. Imbard, and C. Lévy, *OPA 8.1 Ocean general circulation model reference manual*, LODYC/IPSL, 1998.

Maharaj, E., and M. Wheeler, Forecasting an index of the Madden-Julian Oscillation, *Int. J. Climatol*, *25*, 1611–1618, 2005.

Maloney, E., and D. Hartmann, Modulation of Eastern North Pacific hurricanes by the Madden–Julian Oscillation, *Journal of Climate*, *13*, 1451–1460, 2000a.

Maloney, E., and D. Hartmann, Modulation of hurricane activity in the Gulf of Mexico by the Madden-Julian Oscillation, *Science*, *287*, 2002, 2000b.

Maloney, E., D. Chelton, and S. Esbensen, Subseasonal SST Variability in the Tropical Eastern North Pacific during Boreal Summer, *Journal of Climate*, *21*, 4149–6167, 2008.

Mantua, N., and S. Hare, The Pacific decadal oscillation, *Journal of Oceanography*, *58*, 35–44, 2002.

Marion, J., and S. Thornton, Classical Mechanics of Particles and Systems, *Holt Rinehart & Winston*, 1995.

Matsuno, T., Quasi-geostrophic motions in the equatorial area, *J. Meteor. Soc. Japan*, *44*, 25–42, 1966.

McBride, J., and W. Frank, Relationships between stability and monsoon convection, *Journal of the Atmospheric Sciences*, *56*, 1999.

McPhaden, M., Variability in the central equatorial Indian Ocean. Part I: Ocean dynamics, *J. Mar. Res*, *40*, 157–176, 1982.

Meehl, G., G. Kiladis, K. Weickmann, M. Wheeler, D. Gutzler, and G. Compo, Modulation of equatorial subseasonal convective episodes by tropical-extratropical interaction in the Indian and Pacific Ocean regions, *J. Geophys. Res.*, *101*, 15–15, 1996.

Mellor, G., and T. Yamada, Development of a turbulence closure model for geophysical fluid problems, *Reviews of geophysics and space physics*, *20*, 851–875, 1982.

Moore, D., and J. McCreary, Excitation of intermediate-frequency equatorial waves at a western ocean boundary: With application to observations from the Indian Ocean, *J. Geophys. Res*, *95*, 5219–5231, 1990.

Nerem, R., D. Chambers, E. Leuliette, G. Mitchum, and B. Giese, Variations in global mean sea level associated with the 1997–1998 ENSO event: Implications for measuring long term sea level change, *Geophysical research letters*, *26*, 3005–3008, 1999.

Newman, M., P. Sardeshmukh, and C. Penland, How important is air-sea coupling in ENSO and MJO evolution?, *Journal of Climate*, *22*, 2958–2977, 2009.

Oliver, E., and K. Thompson, Madden-Julian Oscillation and sea level: Local and remote forcing, *Journal of Geophysical Research*, *115*, C01,003, 2010.

Oppenheim, A., R. Schafer, J. Buck, et al., *Discrete-time signal processing*, vol. 1999, Prentice hall Englewood Cliffs, NJ:, 1989.

Pariwono, J., J. Bye, and G. Lennon, Long-period variations of sea-level in Australasia, *Geophysical Journal of the Royal Astronomical Society*, *87*, 43–54, 1986.

Pawlowicz, R., B. Beardsley, and S. Lentz, Classical tidal harmonic analysis including error estimates in MATLAB using T_TIDE, *Computers and Geosciences*, *28*, 929–937, 2002.

Pearce, A., and B. Phillips, ENSO events, the Leeuwin Current, and larval recruitment of the western rock lobster, *ICES Journal of Marine Science*, *45*, 13, 1988.

Pedlosky, J., *Geophysical Fluid Dynamics*, Springer-Verlag, 1987.

Penland, C., A stochastic model of IndoPacific sea surface temperature anomalies, *Physica D: Nonlinear Phenomena*, *98*, 534–558, 1996.

Perez, R., D. Chelton, and R. Miller, The effects of wind forcing and background mean currents on the latitudinal structure of equatorial Rossby waves, *Journal of physical oceanography*, *35*, 666–682, 2005.

Pohl, B., and A. Matthews, Observed changes in the lifetime and amplitude of the Madden–Julian Oscillation associated with interannual ENSO sea surface temperature anomalies, *Journal of Climate*, *20*, 2659–2674, 2007.

Potemra, J., Contribution of equatorial Pacific winds to southern tropical Indian Ocean Rossby waves, *Journal of Geophysical Research*, *106*, 2407–2422, 2001.

Priestley, M., Spectral analysis and time series, *New York*, 1981.

Reppin, J., F. Schott, J. Fischer, and D. Quadfasel, Equatorial currents and transports in the upper central Indian Ocean: Annual cycle and interannual variability, *Journal of geophysical research*, *104*, 15,495–15, 1999.

Risbey, J., M. Pook, P. McIntosh, M. Wheeler, and H. Hendon, On the remote drivers of rainfall variability in Australia, *Monthly Weather Review*, *137*, 3233–3253, 2009.

Ristic, B., S. Arulampalam, and N. Gordon, *Beyond the Kalman filter: Particle filters for tracking applications*, Artech House Publishers, 2004.

Ropelewski, C., and M. Halpert, North American precipitation and temperature patterns associated with the El Niño/Southern Oscillation (ENSO), *Mon. Weather Rev.;(United States)*, *114*, 1986.

Ropelewski, C., and M. Halpert, Global and regional scale precipitation patterns associated with the El Niño/Southern Oscillation, *Monthly Weather Review*, *115*, 1606–1626, 1987.

Roundy, P., C. Schreck III, and M. Janiga, Contributions of convectively coupled equatorial Rossby waves and Kelvin waves to the real-time multivariate MJO indices, *Monthly Weather Review*, *137*, 469–478, 2009.

Saji, N., and T. Yamagata, Possible impacts of Indian Ocean dipole mode events on global climate, *Climate Research*, *25*, 151–169, 2003.

Saji, N., B. Goswami, P. Vinayachandran, and T. Yamagata, A dipole mode in the tropical Indian Ocean, *Nature*, *401*, 360–363, 1999.

Salby, M., and H. Hendon, Intraseasonal behavior of clouds, temperature, and motion in the Tropics, *Journal of the Atmospheric Sciences*, *51*, 2207–2224, 1994.

Schlesinger, M., and N. Ramankutty, An oscillation in the global climate system of period 65–70 years, *Nature*, *367*, 723–726, 1994.

Schneider, T., and S. Griffies, Conceptual framework for predictability studies, *Journal of climate*, *12*, 3133–3155, 1999.

Sengupta, D., R. Senan, and B. Goswami, Origin of intraseasonal variability of circulation in the tropical central Indian Ocean, *Geophys. Res. Lett*, *28*, 1267–1270, 2001.

Shinoda, T., H. Hendon, and J. Glick, Intraseasonal variability of surface fluxes and sea surface temperature in the tropical Western Pacific and Indian Oceans, *Journal of Climate*, *11*, 1685–1702, 1998.

Shumway, R., and D. Stoffer, *Time Series Analysis and Its Applications*, Springer, 2000.

Slingo, J., et al., Intraseasonal oscillations in 15 atmospheric general circulation models: results from an AMIP diagnostic subproject, *Climate Dynamics*, *12*, 325–357, 1996.

Smagorinsky, J., Some historical remarks on the use of nonlinear viscosities, *Large Eddy Simulation of Complex Engineering and Geophysical Flows*, *1*, 69–106, 1993.

Smith, W., and D. Sandwell, Global sea floor topography from satellite altimetry and ship depth soundings, *Science*, *277*, 1956, 1997.

Spall, M., and J. Pedlosky, Reflection and transmission of equatorial Rossby waves, *Journal of Physical Oceanography*, *35*, 363–373, 2005.

Spillane, M., D. Enfield, and J. Allen, Intraseasonal oscillations in sea level along the west coast of the Americas, *Journal of Physical Oceanography*, *17*, 313–325, 1987.

Thompson, K., R. Marsden, and D. Wright, Estimation of low-frequency wind stress fluctuations over the open ocean, *Journal of Physical Oceanography*, *13*, 1003–1011, 1983.

Tregoning, P., K. Lambeck, and G. Ramillien, GRACE estimates of sea surface height anomalies in the Gulf of Carpentaria, Australia, *Earth and Planetary Science Letters*, *271*, 241–244, 2008.

Vance, D., D. Staples, and J. Kerr, Factors affecting year-to-year variation in the catch of banana prawns (Penaeus merguiensis) in the Gulf of Carpentaria, Australia, *ICES Journal of Marine Science*, *42*, 83, 1985.

Vecchi, G., and N. Bond, The Madden-Julian Oscillation (MJO) and northern high latitude wintertime surface air temperatures, *Geophys. Res. Lett.*, *31*, 2004.

Vialard, J., S. Shenoi, J. McCreary, D. Shankar, F. Durand, V. Fernando, and S. Shetye, Intraseasonal response of the northern Indian Ocean coastal waveguide to the Madden-Julian Oscillation, *Geophysical Research Letters*, *36*, 14, 2009.

Vitart, F., S. Woolnough, M. Balmaseda, and A. Tompkins, Monthly forecast of the Madden-Julian Oscillation using a coupled GCM, *Monthly Weather Review*, *135*, 2700–2715, 2007.

von Neumann, J., Some remarks on the problem of forecasting climatic fluctuations, *Dynamics of Climate*, pp. 9–11, 1960.

Waliser, D., *Intraseasonal Variability in the Atmosphere–Ocean Climate System*, chap. Predictability and Forecasting, pp. 389–423, Springer, 2005.

Wallace, J., and R. Dickinson, Empirical orthogonal representation of time series in the frequency domain. part i: Theoretical considerations, *Journal of Applied Meteorology*, *11*, 887–892, 1972.

Wang, B., *Intraseasonal Variability in the Atmosphere–Ocean Climate System*, chap. Theory, pp. 307–360, Springer, 2005.

Webber, B., A. Matthews, and K. Heywood, A dynamical ocean feedback mechanism for the Madden-Julian Oscillation, *Quarterly Journal of the Royal Meteorological Society*, *136*, 740–754, 2010.

Webster, P., et al., The joint air-sea monsoon interaction experiment (jasmine): Exploring intraseasonal variability in the south asian monsoon, *Bull. Amer. Meteor. Soc*, 2002.

Wedi, N., and P. Smolarkiewicz, A reduced model of the Madden-Julian oscillation, *International Journal for Numerical Methods in Fluids*, *56*, 1583, 2008.

Wheeler, M., and H. Hendon, An all-season real-time multivariate MJO index: Development of an index for monitoring and prediction, *Monthly Weather Review*, *132*, 1917–1932, 2004.

Wheeler, M., and G. Kiladis, Convectively coupled equatorial waves: Analysis of clouds and temperature in the wavenumber–frequency domain, *Journal of the Atmospheric Sciences*, *56*, 374–399, 1999.

Wheeler, M., and K. Weickmann, Real-time monitoring and prediction of modes of coherent synoptic to intraseasonal tropical variability, *Monthly Weather Review*, *129*, 2677–2694, 2001.

Wheeler, M., G. Kiladis, and P. Webster, Large-scale dynamical fields associated with convectively coupled equatorial waves, *Journal of Atmospheric Sciences*, *57*, 613–640, 2000.

Wheeler, M., H. Hendon, S. Cleland, H. Meinke, and A. Donald, Impacts of the Madden–Julian oscillation on Australian rainfall and circulation, *Journal of Climate*, *22*, 1482–1498, 2009.

Wijffels, S., and G. Meyers, An intersection of oceanic waveguides: Variability in the Indonesian throughflow region, *Journal of Physical Oceanography*, *34*, 2004.

Woolnough, S., J. Slingo, and B. Hoskins, The relationship between convection and sea surface temperature on intraseasonal timescales, *Journal of Climate*, *13*, 2086–2104, 2000.

Woolnough, S., F. Vitart, and M. Balmaseda, The role of the ocean in the Madden–Julian Oscillation: Implications for MJO prediction, *Quarterly Journal of the Royal Meteorological Society*, *133*, 117–128, 2007.

Yin, X., B. Gleason, G. Compo, N. Matsui, and R. Vose, *The International Surface Pressure Databank (ISPD) land component version 2.2*, National Climatic Data Center. Asheville, NC, US, 2008.

Yuan, Y., and C. Li, Decadal variability of the IOD-ENSO relationship, *Chinese Science Bulletin*, *53*, 1745–1752, 2008.

Zhang, C., Madden-Julian Oscillation, *Rev. Geophys*, *43*, 1–36, 2005.

Zhang, C., and M. Dong, Seasonality in the Madden–Julian Oscillation, *Journal of Climate*, *17*, 3169–3180, 2004.

Zhang, C., M. Dong, S. Gualdi, H. Hendon, E. Maloney, A. Marshall, K. Sperber, and W. Wang, Simulations of the Madden–Julian oscillation in four pairs of coupled and uncoupled global models, *Climate Dynamics*, *27*, 573–592, 2006.

Zhang, X., Y. Lu, and K. Thompson, Sea Level variations in the tropical Pacific Ocean and the Madden–Julian Oscillation, *Journal of Physical Oceanography*, *39*, 2009.